Functional Diversity of Vascular Macrophages in Atherosclerosis

Inhye Park

Kennedy Institute of Rheumatology
&
Wolfson College

University of Oxford



A thesis submitted for the degree of Doctor of Philosophy
In Molecular and Cellular Medicine

Michaelmas Term 2018

Abstract

Functional Diversity of Vascular Macrophages in Atherosclerosis

Inhye Park
Wolfson College
Submitted for the degree of Doctor of Philosophy in Molecular and Cellular Medicine
Michaelmas Term 2018

Atherosclerosis is a multifactorial chronic inflammatory disease of the artery. Diverse macrophage subsets in the atherosclerotic artery contribute to the pathogenesis of the disease. The dendritic cell immunoreceptor (DCIR) 1 is a C-type lectin receptor that inhibits immune responses in myeloid cells. DCIR1 plays both protective and detrimental roles in autoimmune diseases and pathogen-induced infections, respectively. However, to date, the role of DCIR1 in macrophage biology and atherosclerosis remains unknown.

In this thesis, I identified six macrophage subsets by single cell technologies in the murine atherosclerotic aorta. These consist of three “resident” and three “recruited” subsets, which include two novel subpopulations (CD209b+ resident and CCR2+ recruited macrophages). DCIR1 is preferentially expressed by resident vascular macrophages and maintains the balance between resident and recruited macrophage subsets. A novel mouse strain *LysM*^{Cre} *Dcir1*-DTR^{flox} enables ablation of vascular resident macrophages, together with the majority of tissue macrophages. DCIR1-mediated macrophage ablation opens the niche to Ly6C+ monocytes which can re-acquire DCIR1. This indicates that DCIR1 expression defines tissue resident macrophages.

A comparative study using apolipoprotein E (*ApoE*)$^{-/-}$ and *ApoE*$^{-/-}$ *Dcir1*$^{-/-}$ mice showed that DCIR1 protects against atherosclerosis by maintaining the resident vascular macrophage niche in the aorta. The loss of DCIR1 alters the myeloid cell dynamics in the atherosclerotic aorta, promoting the recruitment of monocytes and macrophages and exacerbating disease evolution.

In conclusion, DCIR1 is a potent regulator of myeloid homeostasis which acts to sustain the resident macrophage niche in the majority of organs. In atherosclerosis, DCIR1 alleviates the disease progression by sustaining the survival of two vascular resident macrophage subsets and limiting monocyte influx to the artery.

Table of contents

CHAPTER 1. Introduction 1
1.1. Macrophage biology and their functional diversity 2
1.1.1. Macrophage ontogeny and the local micro-environment 2
1.1.2. Macrophage heterogeneity and activation 6
1.2. Introduction to atherosclerosis 7
1.2.1. The pathogenesis of atherosclerosis 8
1.2.2. Murine models of atherosclerosis 12
1.2.3. The role of the myeloid lineage in atherosclerosis 13
1.3. C-type lectin receptors and dendritic cell immunoreceptors (DCIR) 19
1.3.1. Human dendritic cell immunoreceptors (DCIR) 20
1.3.2. Murine Dendritic Cell Immunoreceptors (DCIR) isoforms and DCAR 21
1.3.3. The role of DCIR1, DCIR2 and DCAR2 in murine experimental diseases 24
1.4. Hypothesis and Aims 27

CHAPTER 2. Characterisation of aortic macrophage subsets using single cell technologies 28
2.1. Introduction 29
2.2. Mass cytometry reveals the atlas of immune cells in the healthy and atherosclerotic aorta 30
2.2.1. Mass cytometry and high dimensional viSNE analysis identifies sixteen leucocyte populations in the atherosclerotic aorta 35
2.2.2. Atherosclerosis alters the immune cell composition of murine aortas 39
2.3. Spatial distribution of lesional and resident macrophage subsets in atherosclerosis 42
2.4. Single cell RNA sequencing of aortic macrophage subsets 47
2.5. Morphology of lesional and adventitial macrophages in the atherosclerotic aorta 52
2.6. Discussion 54

CHAPTER 3. Investigation of human DCIR and murine DCIR1 expression in the immune system 58
3.1. Introduction 59
3.2. Investigation of human DCIR and murine DCIR1 expression in *in vitro* macrophages 61
3.2.1. Murine macrophage activation and *Dcir* isoforms 61
3.2.2. Human monocyte-derived macrophage subsets differentially express DCIR 65
3.3. DCIR1 maintains tissue macrophage marker CD206 in bone marrow-derived macrophages 68
3.4. Studies on the expression of human DCIR and murine DCIR1 in the immune system 73
3.4.1. Human DCIR is expressed by monocytes and neutrophils in the blood 73
3.4.2. Tissue resident macrophages and DCIR1 expression 75
3.4.3. Macrophages express high levels of *Dcir1* in the aorta and the lung 79
3.4.4. Local micro-environment in the cardiovascular system and alveoli induces *Dcir1* expression in a murine macrophage cell line 81
3.5. Discussion 87

CHAPTER 4. A novel mouse strain for ablation of aortic macrophages 90

4.1. Introduction 91
4.2. Generation and characterisation of the *LysM*^{Cre} *Dcir1*-DTR^{flox} mouse strain 93
4.2.1. The detection of eGFP expressing cells from the *LysM*^{Cre} *Dcir1*-DTR^{flox} mice 95
4.2.2. Analysis of the gene expression of *egfp* (eGFP) and *Hbegf* (DTR) in macrophages 97
4.2.3. Levels of DCIR1 in leucocytes by mass cytometry 100
4.2.4. Intravenous delivery of diphtheria toxin induces cell ablation in macrophages and neutrophils in *LysM*^{Cre} *Dcir1*-DTR^{flox} mice 102
4.2.5. Intraperitoneal delivery of diphtheria toxin selectively ablates tissue macrophage 108
4.2.6. Full characterisation of the DCIR1-mediated depletion in the aorta, heart, lungs and spleen using mass cytometry 114
4.2.7. Ablated macrophages are bone marrow-derived in the post-irradiation setting 123
4.3. DCIR1-mediated macrophage ablation in acute arterial injury model and atherosclerosis. 129
4.3.1. The effect of macrophage depletion on acute arterial injury model 129
4.3.2. Lethality of long term macrophage depletion in atherosclerotic mice 133
4.4. Discussion 139

CHAPTER 5. Dendritic cell immunoreceptor 1 (DCIR1) protects against atherosclerosis by sustaining the vascular macrophage niche 143
5.1. Introduction 144
5.2. Atherosclerosis increases *Dcir/Dcir1* expression by recruitment of monocytes and macrophages 145
5.3. Generation of a *Dcir1*-deficient *ApoE*$^{-/-}$ mouse strain 149
5.4. *Dcir1* deficiency exacerbates lesion formation during atherogenesis 152
5.5. *Dcir1* deficiency promotes the development of atherosclerotic plaques with a vulnerable phenotype 156
5.6. DCIR1 sustains the resident macrophage population and limits monocyte influx in the aorta 167
5.7. The effect of DCIR1 on the cellular composition of spleen and para-aortic lymph nodes 174
5.8. Characterisation of aortic myeloid cells from *Dcir1*-competent and *Dcir1*-deficient *ApoE*$^{-/-}$ mice using single cell RNA sequencing 178
5.9. Discussion 183

CHAPTER 6. Final Discussion 187
6.1. Characterisation of macrophage subsets in the atherosclerotic aorta 189
6.2. DCIR1 expression levels define tissue resident macrophages 193
6.3. DCIR1 protects against atherosclerosis by maintaining the resident macrophage niche in the aorta 195
6.4. Future perspectives 196
6.5. Concluding remarks 197

CHAPTER 7. Materials and Methods 200
7.1. List of antibodies 201
7.2. Mice 205
7.2.1. Maintenance of Mice 205
7.2.2. Generation of mouse strains 206

7.2.3. Genotyping 212
7.2.4. *In vivo* Experimental procedures 217
7.2.5. Single cell dissociation from murine tissues 219
7.3. *In vitro* cell culture 223
7.3.1. Murine bone marrow cell culture 223
7.3.2. Human monocyte-derived macrophage culture 223
7.3.3. Ligand assay 224
7.4. Nucleic acid assays 224
7.4.1. Quantitative Real Time Polymerase Chain Reaction (qRT-PCR) 224
7.4.2. Single cell RNA sequencing 226
7.5. Protein assays 227
7.5.1. Flow cytometry 227
7.5.2. Mass cytometry 228
7.5.3. Mass cytometry data processing and analysis 228
7.5.4. Enzyme-linked immunosorbent assay (ELISA) 230
7.5.5. Immunoblotting 230
7.6. Serum cholesterol assay 231
7.7. Histology 231
7.7.1. May-Grünwald Giemsa stain 231
7.7.2. Perivascular cast-treated carotid artery analysis 232
7.7.3. Elastin Van Gieson (EVG) 232
7.7.4. Aorta *en face* analysis and Sudan IV staining 233
7.7.5. Aortic root section 233
7.7.6. Oil Red O (ORO) 233
7.7.7. Haematoxylin and Eosin staining 234
7.7.8. Picro-sirius Red 234
7.7.9. Avidin-Biotin Complex (ABC) staining 235
7.7.10. Immunofluorescence (IF) 236
7.7.11. Imaging and analysis of the cryosectioned tissue 236
7.8. Statistical analysis 237

Appendix 1: Supplemental data 238

Appendix 2: Abbreviations 247

Appendix 3: Published material 250

Appendix 4: Bibliography 251

Acknowledgements 268

List of figures

Figure 1.1 The origin and activation of macrophages. 5
Figure 1.2 The pathogenesis of atherosclerosis. 11
Figure 1.3 Macrophage subsets in the atherosclerotic lesion..... 17
Figure 2.1 Schematic of sample processing and mass cytometry. 33
Figure 2.2 The atlas of leucocyte populations in the atherosclerotic aorta using mass cytometry and viSNE analysis..... 38
Figure 2.3 Atherosclerosis alters the immune cell composition in the aorta. 41
Figure 2.4 Spatial distribution of aortic macrophages in the atherosclerotic aorta. 44
Figure 2.5 Heterogeneity of aortic macrophages in the atherosclerotic aorta. 45
Figure 2.6 Spatial distribution of leucocytes from intima-media and adventitia of atherosclerotic aorta by mass cytometry. 46
Figure 2.7 Single cell RNA sequencing and unbiased high-dimensional analysis ivis identifies 6 clusters in CD11b+ CD64$^{low-high}$ cells from atherosclerotic aortas. 50
Figure 2.8 Comparative analysis of lesional and adventitial macrophages by single cell RNA sequencing and unbiased high-dimensional analysis ivis. 51
Figure 2.9 Photomicrography of macrophage subsets and dendritic cells (DCs) from the atherosclerotic aorta. 53
Figure 3.1 The differential expression of *Dcir1* in murine bone marrow-derived macrophages. 62
Figure 3.2 The expression pattern of *Dcir* isoforms and *Dcar2* in macrophages. 64
Figure 3.3 The differential expression of DCIR in human macrophages. 67
Figure 3.4 The phenotype of bone marrow-derived macrophages cultured with MCSF in wild type and *Dcir1*$^{-/-}$ mice. 71
Figure 3.5 The cell surface expression of DCIR in non-leucocytes, lymphocytes, monocytes and neutrophils from human blood. 74
Figure 3.6 The cell surface expression of DCIR1 in leucocyte populations in the aorta and heart. 77
Figure 3.7 The cell surface expression of DCIR1 in leucocyte populations in the lung and the BM. 78
Figure 3.8 The relative gene expression of *Dcir1* in macrophages, dendritic cells and monocytes in the aorta and the lung. 80
Figure 3.9 The differential expression of *Dcir1* and *Mrc1* in murine macrophage cell line RAW264.7 by treatment with extracts from the heart, aorta, broncho-alveolar lavage (BAL) and lungs. 83
Figure 3.10 The effect of the heart extract on the relative gene expression of *Dcir* isoforms and *Dcar2* in murine macrophage cell line RAW264.7. 84
Figure 3.11 Surfactant protein (SP)-D does not regulate the expression of *Dcir1* in murine macrophage cell line RAW264.7. 86
Figure 4.1 *Dcir1* gene alteration to trace and ablate DCIR1 expressing cells. 94
Figure 4.2 The detection of eGFP in myeloid cells from *LysM*^{Cre} *Dcir1*-DTR^{flox} mice by utilising a GFP antibody. 96
Figure 4.3 The detection of gene expression of *Dcir1*, *egfp*, *Hbegf* (DTR) in myeloid cell populations from *LysM*^{Cre} *Dcir1*-DTR^{flox} mice. 99

Figure 4.4 Comparative expression of DCIR1 in leucocytes from the aorta, heart, lungs and spleen of the *LysM*^{Cre} *Dcir1*-DTR^{flox} strain by mass cytometry..... 101
Figure 4.5 The DTR-mediated macrophage ablation by intravenous injection of diphtheria toxin (DT) in the BM, spleen and lungs of *LysM*^{Cre} *Dcir1*-DTR^{flox} mice..... 103
Figure 4.6 The DTR-mediated neutrophil ablation by intravenous injection of DT in the BM, spleen and lungs of *LysM*^{Cre} *Dcir1*-DTR^{flox} mice..... 104
Figure 4.7 Monocyte ablation by intravenous injection of DT in the BM, spleen and lungs of *LysM*^{Cre} *Dcir1*-DTR^{flox} mice..... 105
Figure 4.8 The DTR-mediated cell ablation by intravenous injection of DT in a murine model of peritonitis in *LysM*^{Cre} *Dcir1*-DTR^{flox} mice..... 107
Figure 4.9 The DTR-mediated neutrophil ablation by intraperitoneal injection of DT in the BM, lungs and aorta of *LysM*^{Cre} *Dcir1*-DTR^{flox} mice..... 110
Figure 4.10 The DTR-mediated macrophage ablation by intraperitoneal injection of DT in the BM, lungs, aorta, heart, peritoneum, colon, liver and brain of *LysM*^{Cre} *Dcir1*-DTR^{flox} mice. 112
Figure 4.11 The effect of intraperitoneal injection of DT on monocytes from the BM, lungs, aorta, peritoneum, colon and liver of *LysM*^{Cre} *Dcir1*-DTR^{flox} mice..... 113
Figure 4.12 In-depth characterisation of macrophage depletion in the aorta of the *LysM*^{Cre} *Dcir1*-DTR^{flox} strain by mass cytometry..... 117
Figure 4.13 In-depth characterisation of macrophage depletion in the heart of the *LysM*^{Cre} *Dcir1*-DTR^{flox} strain by mass cytometry..... 120
Figure 4.14 In-depth characterisation of macrophage depletion in the lungs of the *LysM*^{Cre} *Dcir1*-DTR^{flox} strain by mass cytometry..... 121
Figure 4.15 In-depth characterisation of macrophage depletion in the spleen of the *LysM*^{Cre} *Dcir1*-DTR^{flox} strain by mass cytometry..... 122
Figure 4.16 Ablation of macrophages from the aorta, heart, lungs and BM of the chimera mice that received the BM from *LysM*^{Cre} *Dcir1*-DTR^{flox} mice..... 126
Figure 4.17 Ablation of aortic macrophages of the chimera mice that received the BM from *LysM*^{Cre} *Dcir1*-DTR^{flox} or *Dcir1*-DTR^{flox} mice..... 128
Figure 4.18 The effect of macrophage depletion on perivascular collar-induced injury model using *LysM*^{Cre} *Dcir1*-DTR^{flox} mice..... 130
Figure 4.19 Macrophage depletion on perivascular collar-induced injury model using *LysM*^{Cre} *Dcir1*-DTR^{flox} mice..... 132
Figure 4.20 The effect of macrophage depletion using *ApoE*$^{-/-}$ mice with the bone marrow of *ApoE*$^{-/-}$ *LysM*^{Cre} *Dcir1*-DTR^{flox} mice..... 135
Figure 4.21 Schematic of macrophage depletion in atherosclerotic mice..... 138
Figure 5.1 The expression of murine *Dcir1* and human *Dcir* in the atherosclerotic tissue... 148
Figure 5.2 Schematic of experimental design and sample processing..... 150
Figure 5.3 Atherosclerotic lesion formation in the aortic root of 20-week old *ApoE*$^{-/-}$ and *ApoE*$^{-/-}$ *Dcir1*$^{-/-}$ mice..... 153
Figure 5.4 Atherosclerotic lesion formation in the whole aorta of *ApoE*$^{-/-}$ and *ApoE*$^{-/-}$ *Dcir1*$^{-/-}$ mice..... 155
Figure 5.5 The size of aortic roots of 20-week old *ApoE*$^{-/-}$ and *ApoE*$^{-/-}$ *Dcir1*$^{-/-}$ mice..... 157
Figure 5.6 Formation of necrotic core in the lesion of 20-week old *ApoE*$^{-/-}$ and *ApoE*$^{-/-}$ *Dcir1*$^{-/-}$ mice..... 159
Figure 5.7 Smooth muscle cell content in the aortic root of HFD-fed 20-week old *ApoE*$^{-/-}$ and *ApoE*$^{-/-}$ *Dcir1*$^{-/-}$ mice..... 161

Figure 5.8 Collagen content in the aortic root of HFD-fed 20-week old *ApoE*$^{-/-}$ and *ApoE*$^{-/-}$ *Dcir1*$^{-/-}$ mice. 163
Figure 5.9 Myeloid cell content in the aortic root of HFD-fed 20-week old *ApoE*$^{-/-}$ and *ApoE*$^{-/-}$ *Dcir1*$^{-/-}$ mice. 165
Figure 5.10 The immune cell composition of aortas from 20-week old *ApoE*$^{-/-}$ and *ApoE*$^{-/-}$ *Dcir1*$^{-/-}$ mice by mass cytometry. 170
Figure 5.11 The phenotypic changes in macrophages from the aorta of 20-week old HFD-fed *ApoE*$^{-/-}$ and *ApoE*$^{-/-}$ *Dcir1*$^{-/-}$ mice by mass cytometry. 172
Figure 5.12 The phenotype of macrophages from the aorta of 20-week old HFD-fed *ApoE*$^{-/-}$ and *ApoE*$^{-/-}$ *Dcir1*$^{-/-}$ mice by flow cytometry..... 173
Figure 5.13 Single cell RNA sequencing identifies 9 myeloid populations in CD11b+ cells from aorta of *ApoE*$^{-/-}$ and *ApoE*$^{-/-}$ *Dcir1*$^{-/-}$ mice. 182
Figure 6.1 Macrophage subsets in the atherosclerotic aorta. 192
Figure 6.2 The proposed role of DCIR1 in vascular macrophages and atherosclerosis..... 199
Figure 7.1 Breeding strategy to generate an *ApoE*$^{-/-}$ *Dcir1*$^{-/-}$ mouse colony. 206
Figure 7.2 Generation of *Dcir1*-DTR^{flox} knock-in and *LysM*^{Cre} *Dcir1*-DTR^{flox} mice for *Dcir1*-mediated cell ablation..... 208
Figure 7.3 Breeding strategy to generate an *ApoE*$^{-/-}$ *LysM*^{Cre} *Dcir1*-DTR^{flox} littermate. 210
Figure 7.4 Breeding strategy to produce *Ldlr*$^{-/-}$ mice on a CD45.1 background. 211
Figure 7.5 Genotyping of *ApoE*$^{-/-}$ *Dcir1*$^{+/-}$ littermate mice. 214
Figure 7.6 Genotyping of *Dcir1*-DTR^{flox} knock-in and *LysM*^{Cre}*Dcir1*-DTR^{flox} mice..... 215
Figure 7.7 Genotyping of *Ldlr*$^{-/-}$ mice on a CD45.1 background. 216
Figure 7.8 Surgical placement of a Tygon collar on a mouse carotid artery. 218

Appendix Figure 8. 1 Gating strategy for myeloid cell populations in the healthy aorta and heart. 239
Appendix Figure 8. 2 Gating strategy for leucocyte populations in the atherosclerotic aorta. 240
Appendix Figure 8. 3 Gating strategy for myeloid cell populations in the lungs. 241
Appendix Figure 8. 4 Gating strategy for myeloid cell populations in the BM and blood.... 241
Appendix Figure 8. 5 Gating strategy for myeloid cell populations in the spleen..... 242
Appendix Figure 8. 6 Gating strategy for myeloid cell populations in the colon. 242
Appendix Figure 8. 7 Gating strategy for myeloid cell populations in the brain. 243
Appendix Figure 8. 8 Gating strategy for myeloid cell populations in the liver. 243
Appendix Figure 8. 9 Gating strategy for myeloid cell populations in the peritoneum. 244
Appendix Figure 8. 10 Gating strategy for leucocyte cell populations in the perivascular fibrotic tissue..... 244

List of tables

Table 1.1 Summary of the DCIR family. 23
Table 1.2 The effect of *Dcir1* deficiency on murine experimental diseases. 26
Table 2.1 The percentage of live CD45+ leucocytes in the healthy and atherosclerotic aorta. 34
Table 2.2 The percentage of endothelial and smooth muscle cells in the healthy and atherosclerotic aorta. 34
Table 3.1 The percentage of cell population in bone marrow-derived myeloid cells. 70
Table 3.2 The percentage of cell population in polarised bone marrow-derived macrophages. 70
Table 3.3 The effect of *Dcir1* deficiency on phagocytic activity of bone marrow-derived macrophages. 71
Table 3.4 The effect of *Dcir1* deficiency on the phosphorylation of STAT5 and STAT6 of bone marrow-derived macrophages. 71
Table 3.5 The effect of *Dcir1* deficiency on the production of IL-6 and IL-10 in bone marrow-derived macrophages. 72
Table 4.1 Body weight of chimeric *ApoE*$^{-/-}$ mice transplanted by the bone marrow of *ApoE*$^{-/-}$ *LysM*^{Cre} *Dcir1*-DTR^{flox} mice or non-irradiated *ApoE*$^{-/-}$ *LysM*^{Cre} *Dcir1*-DTR^{flox} mice. Unit: gram. 10ng/g n=4-5, 25ng/g n=2, 30ng/g n=6. N/A stands for not applicable. 136
Table 4.2 The rates of macrophage depletion by DT treatment in the aorta, spleen, para-aortic lymph nodes (PALN) and lungs in relative to the saline-treated group. 136
Table 4.3 Characterisation of the aortic root section of chimera *ApoE*$^{-/-}$ mice transplanted by the BM of *ApoE*$^{-/-}$ *LysM*^{Cre} *Dcir1*-DTR^{flox} mice. 136
Table 5.1 Body weight of 20-week old *ApoE*$^{-/-}$ and *ApoE*$^{-/-}$ *Dcir1*$^{-/-}$ mice on a chow or high fat diet. 151
Table 5.2 Serum cholesterol levels of 20-week old *ApoE*$^{-/-}$ and *ApoE*$^{-/-}$ *Dcir1*$^{-/-}$ males on a chow or high fat diet. 151
Table 5.3 Summary of the phenotype of the aortic root lesion from 20-week old *ApoE*$^{-/-}$ and *ApoE*$^{-/-}$ *Dcir1*$^{-/-}$ mice on a high fat diet. 166
Table 5.4 Cell numbers from the aorta, spleen and para-aortic lymph nodes (PALN) of 20-week old *ApoE*$^{-/-}$ and *ApoE*$^{-/-}$ *Dcir1*$^{-/-}$ mice on a chow or high fat diet. 167
Table 5.5 The percentage of immune cell populations in the aorta of 20-week old *ApoE*$^{-/-}$ and *ApoE*$^{-/-}$ *Dcir1*$^{-/-}$ mice on chow and high fat diet by mass cytometry. 171
Table 5.6 The percentage of immune cell populations in the spleen of 20-week old *ApoE*$^{-/-}$ and *ApoE*$^{-/-}$ *Dcir1*$^{-/-}$ mice on chow or high fat diet by mass cytometry. 175
Table 5.7 The percentage of immune cell populations in the para-aortic lymph nodes (PALN) of 20-week old *ApoE*$^{-/-}$ and *ApoE*$^{-/-}$ *Dcir1*$^{-/-}$ mice on chow or high fat diet by mass cytometry. 177
Table 7.1 Antibodies used in experiments. 202
Table 7.2 Buffers and solutions made in-house. 204
Table 7.3 List of mouse strains used in experiments. 205
Table 7.4 Sequences of primers used for genotyping. 213
Table 7.5 Parameters for reverse transcription PCR of genotyping assays. 213
Table 7.6 Concentrations of enzymes for tissue dissociation. 222
Table 7.7 List of TaqMan assays used for quantitative real time PCR in this study. 225
Table 7.8 List of antibodies used for mass cytometry. 229

Appendix Table 8. 1 The percentage of leucocyte populations in the aorta, lungs, spleen and BM of wild type and *Dcir1*$^{-/-}$ mice at 12 weeks old..... 245
Appendix Table 8. 2 The percentage of leucocyte populations in the aorta and lungs of wild type and *Dcir1*$^{-/-}$ mice at 24 weeks old..... 246

Word count: 42,863

CHAPTER 1. Introduction

1.1. Macrophage biology and their functional diversity

The mononuclear phagocyte system is defined as a family of blood monocytes, tissue resident macrophages and monocyte-derived dendritic cells (DCs) (van Furth, 1981). Macrophages are distributed throughout the majority of organs of vertebrates that are to maintain tissue homeostasis (Gordon et al., 2014). Macrophages exhibit remarkable heterogeneity, which enables specialisation in the tissue micro-environment (Davies et al., 2013). The major functions of macrophages range from defence against pathogens to tissue repair (Mantovani et al., 2013).

The precursors of tissue resident macrophages were initially thought to be monocytes from the bone marrow (BM) (van Furth and Cohn, 1968). However, recent studies discovered that tissue resident macrophages arise from embryonic precursors and maintain their niche in the host tissue by self-renewal through local cytokines or growth factors (Ginhoux et al., 2010, Guilliams et al., 2013, Yona et al., 2013, Bain et al., 2014, Epelman et al., 2014) **(Figure 1.1)**.

1.1.1. Macrophage ontogeny and the local micro-environment

In the central nervous system, macrophages (also known as microglia) play a role as the immune sentinel by defending against pathogens and phagocytosing apoptotic neurons and synapses (Ajami et al., 2007, Ginhoux et al., 2010). Microglia originate from yolk sac macrophages and maintain their niche via interleukin (IL)-1 signalling independent of monocyte contribution. In the lung, alveolar macrophages provide immune surveillance and clearance of surfactant in the airspace called alveoli (Lambrecht, 2006, Guilliams et al., 2013). Foetal liver monocytes give rise to alveolar macrophages, which then sustain their niche via granulocyte-macrophage colony

stimulating factor (GMCSF) from the local milieu (Schneider et al., 2014). Although macrophages in the lungs, liver and BM are of embryonic origin and are capable of self-renewal in the adult, when the niche is challenged by infection or tissue damage such as irradiation, monocytes can replenish the niche and fully replicate the tissue-specific signature (Guilliams et al., 2013, Hashimoto et al., 2013, Yona et al., 2013, Scott et al., 2016, van de Laar et al., 2016).

On the contrary, macrophages in the cardiovascular system have dual origin in which both embryonically-derived and monocyte-derived macrophages co-exist in the steady state (Epelman et al., 2014, Molawi et al., 2014, Ensan et al., 2016). Cardiac macrophages perform cardiac remodelling, clearance of damaged cardiomyocytes and facilitate cardiac conduction (Pinto et al., 2012, Hulsmans et al., 2017). In the adult heart, monocyte-derived macrophages outnumber the niche with age (Molawi et al., 2014). The healthy aorta harbours macrophages in the outmost layer, namely adventitia, which maintain the integrity of the artery through crosstalk with smooth muscle cells (SMCs) (Lim et al., 2018). Embryonic C-X3-C motif chemokine receptor (CX3CR) 1+ precursors and fms like tyrosine kinase (flt) 3+ foetal liver monocytes give rise to tissue resident macrophages in the aorta before birth and are postnatally replenished by monocytes (Ensan et al., 2016). Proliferation of vascular macrophages is dependent on the local supply of C-X3-C motif chemokine ligand (CX3CL) 1 and macrophage colony stimulating factor (MCSF), and their niche is open to the monocyte influx in the steady state (Ensan, 2016 #63;Lim, 2018 #253).

In the intestinal mucosa, macrophages phagocytose bacteria and apoptotic cells (Smythies et al., 2005). Since intestinal macrophages are less capable of self-renewal,

they are rapidly repopulated by monocytes throughout the life (Hashimoto et al., 2013, Bain et al., 2014). However, a recent study showed the mixed origin of intestinal macrophages by introducing three subsets of macrophages, one of which is long-lived and is independent of monocyte replenishment (Shaw et al., 2018).

While the origin of macrophages plays a part in determining macrophage functions, the tissue micro-environment can shape the unique macrophage identity through transcriptomic and epigenetic modifications regardless of their origin (Lavin et al., 2014). Guilliams and colleagues demonstrated that both foetal and bone marrow monocytes can effectively colonise the empty niche of alveolar and hepatic macrophages, and can acquire tissue-specific gene expression signatures and functional capacity (Scott et al., 2016, van de Laar et al., 2016). However, fully differentiated macrophages from other organs were unable to fully replicate the identity of alveolar macrophages, indicating the limited plasticity in mature macrophages (van de Laar et al., 2016).

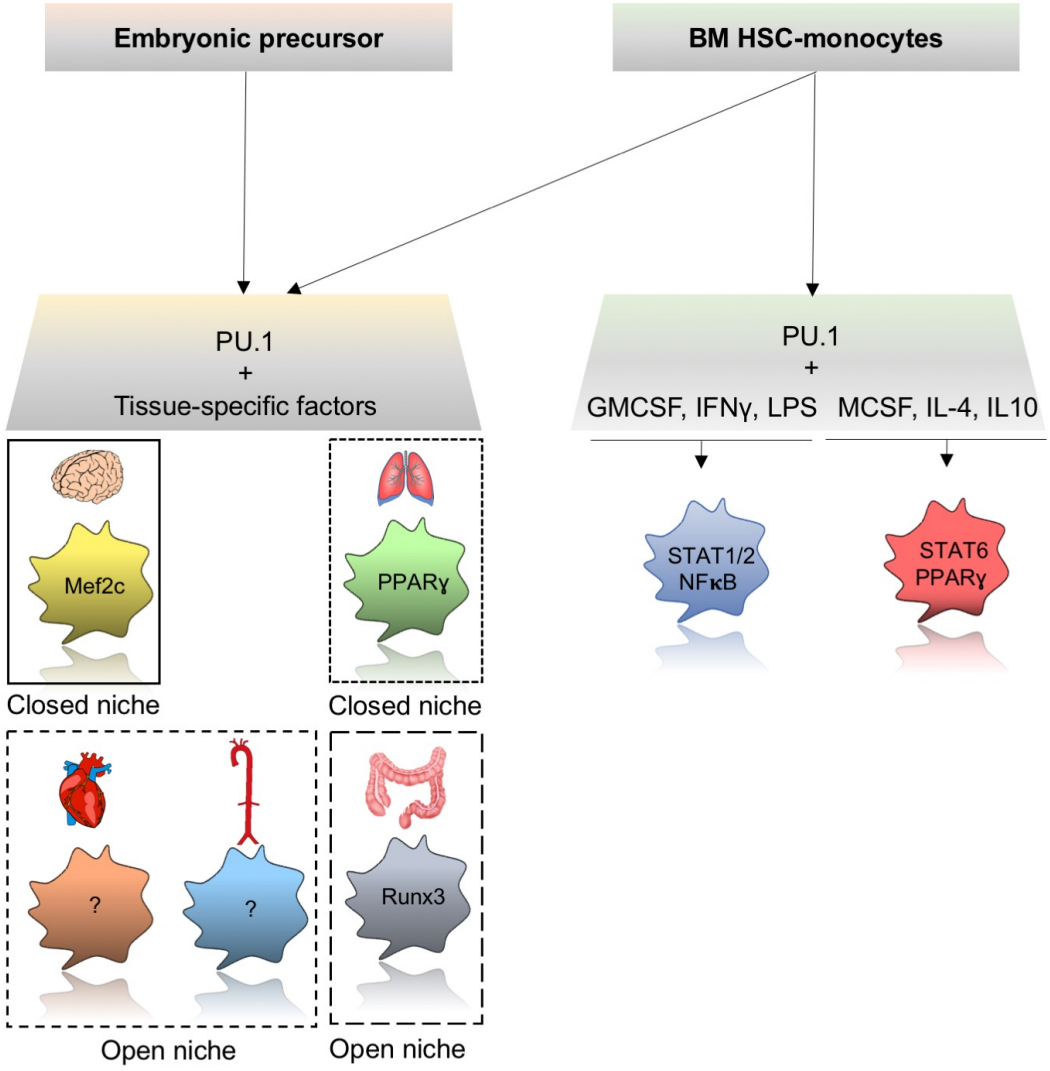


Figure 1.1 The origin and activation of macrophages.

The embryonic precursors give rise to tissue macrophages and haematopoietic stem cell (HSC)-derived monocytes from the bone marrow (BM) can replenish the macrophage niche throughout the life depending on the niche accessibility, availability and competition with the local progenitors. Macrophages in the brain and the lungs are independent of monocyte contribution in the steady state (closed niche) while macrophages in the heart, aorta and intestine can be continuously replenished by monocytes (open niche). BM-derived macrophages can be activated by granulocyte-macrophage colony stimulating factor (GMCSF), interferon (IFN) γ or lipopolysaccharide (LPS) and exhibit the pro-inflammatory phenotype. Macrophage colony stimulating factor (MCSF), Interleukin (IL)- 4 or IL-13 shapes macrophages specialised for anti-fungal and helminth infection. The transcription factor PU.1 directs stimulus-specific transcription factors to regulate gene expression in response to environmental challenges. The figure is modified from Lavin et al., 2014, Guilliams et al., 2014, Martinez and Gordon, 2014.
Abbreviations: myocyte enhancer factor 2c (mef2c). peroxisome proliferator-activated receptor (PPAR) γ, runt-related transcription factor 3 (runx3), nuclear factor kappa-light-chain-enhancer of activated B cells (NFκB), signal transducer and activator of transcription (STAT).

1.1.2. Macrophage heterogeneity and activation

Macrophages undergo classical activation (M1) in response to T helper (Th) 1 cell-derived cytokine interferon (IFN) γ, and become adept in destroying microorganism by producing pro-inflammatory mediators such as inducible nitric oxide synthase (iNOS) (Mills et al., 2000, Mantovani et al., 2002). The phenotype of macrophages can be switched towards anti-parasitic in response to Th2 cytokine IL-4 (Stein et al., 1992, Mills et al., 2000). The alternatively-activated (M2) macrophages show enhanced mannose receptor activity and produce arginase 1, an enzyme responsible for reducing excessive nitric oxide (NO) production (Mills et al., 2000). The concept of M1-M2 dichotomy was popularly adopted and informed much of the current understanding of macrophage biology, however, the M1-M2 paradigm does not fully reflect a continuum of macrophage activation states *in vivo* (Mosser and Edwards, 2008).

The master transcription factor PU.1 plays a central role in myeloid lineage development and macrophage differentiation (Olson et al., 1995, Nerlov and Graf, 1998). Tissue micro-environmental cues shape the distinct gene expression signature of macrophages by promoting the ability of PU.1 to bind tissue-specific enhancers and transcription factors (Lawrence and Natoli, 2011, Gautier et al., 2012, Gosselin et al., 2014, Lavin et al., 2014). The functional state of macrophages is influenced by individual or combined signals, which leads transcriptional and epigenetic modifications in macrophages (Xue et al., 2014). Pro-inflammatory macrophage states are generated via the activation of transcription factors such as signal transducer and activator of transcription (STAT) 1/2, nuclear factor kappa-light-chain-enhancer of activated B cells (NFκB), STAT5 and interferon regulatory factor (IRF) 5 (Lawrence

and Natoli, 2011, Martinez and Gordon, 2014). Alternative or anti-inflammatory macrophage states are induced through STAT6, peroxisome proliferator-activated receptors (PPAR) γ, jumonji domain-containing protein (JMJD) 3 and IRF4 (Satoh et al., 2010).

1.2. Introduction to atherosclerosis

Cardiovascular disease (CVD) is the most common cause of global mortality, and the number of people with high risk CVD is predicted to grow worldwide (Kearney et al., 2005). The risk factors for cardiovascular events include hypertension, smoking, high levels of cholesterol, diabetes, obesity and a sedentary lifestyle (Dahlof, 2010). Atherosclerosis is a multifactorial chronic disease of the vessel wall characterised by hypercholesterolaemia, immune cell accumulation and vascular remodelling, and is the underlying cause of CVD and stroke (Ross, 1999, Lloyd-Jones, 2010).

Currently treatment for atherosclerosis largely focusses on surgeries and lowering cholesterol, and suppressing inflammation has recently emerged as a therapeutic target (Back and Hansson, 2015). Statins, a lipid lowering drug, lowered 50% of cardiovascular events including stroke and myocardial infarction (MI) (Ridker, 2010). Proprotein convertase subtilisin/kexin type (PCSK) 9 monoclonal antibody successfully reduced 60% of low-density lipoprotein (LDL) cholesterol levels and 15% of cardiovascular events in patients with atherosclerotic CVD (Sabatine et al., 2017). Anti-inflammatory treatment with methotrexate, a folic acid antagonist, achieved an 18% reduction in MI incidence in patients with systemic inflammation such as rheumatoid arthritis (RA) and psoriasis (Micha et al., 2011). Recently, canakinumab,

a monoclonal antibody that neutralises IL-1β activity, was shown to lower cardiovascular risk by 15%, together with reducing cardiovascular risk marker high-sensitivity C-reactive protein (hsCRP) in patients who had suffered from a heart attack (Ridker et al., 2017). Despite currently available treatments, cardiovascular events continue to grow and there is a need for more effective anti-inflammatory therapies (Charo and Taub, 2011).

1.2.1. The pathogenesis of atherosclerosis

The first stage of atherosclerosis in humans is intimal thickening characterised by the deposition of lipids and extracellular matrix in the sub-endothelial space (Virmani et al., 2000) (**Figure 1.2**). Endothelial dysfunction and perturbation of the endothelial cell junctions, together with the expression of vascular cell adhesion molecule (VCAM) 1 and chemokines by endothelial cells, promotes infiltration of blood-borne leucocytes within the intima (Cybulsky and Gimbrone, 1991, Cybulsky et al., 2001). Recruited monocytes in the sub-endothelium give rise to macrophages via local supply of MCSF (Clinton et al., 1992, Rosenfeld et al., 1992). Macrophages acquire the expression of scavenger receptors (SR)-A and CD36 and ingest excessive LDLs, which exist as various active modified forms such as oxidised LDLs (oxLDLs) (Kunjathoor et al., 2002). Lipid-laden macrophages undergo apoptosis and can be cleared by other phagocytes.

Impaired clearance of apoptotic cells leads to formation of the necrotic core, acellular regions within the plaque (Tabas, 2005). Production of “don’t eat me” signal CD47 by apoptotic cells interferes with efferocytosis (apoptotic cell removal) in the plaque (Kojima et al., 2016). In the normal condition, apoptotic cells express pro-efferocytic

ligands such as milk fat globule-EGF factor (MFGE) 8 which facilitates efferocytosis. Toll-like receptor (TLR) activation-derived pro-inflammatory cytokine tumour necrosis factor (TNF) α drives upregulation of CD47 in the apoptotic cells. Furthermore, oxLDLs may play a role in masking “eat me” signals in the dying cells, resulting in formation of necrotic core in the plaque.

At the later stage, SMCs migrate from the medial space to the intimal lesion where they form a fibrous cap surrounding the necrotic and lipid core (Virmani et al., 2000). As disease progresses, degradation of matrix metalloproteinases (MMPs) and calcification within the plaque, together with the mechanical force from the circulation, increases the risk of rupture of the fibrous cap or plaque erosion triggering fatal cardiovascular events.

Post-mortem studies identified a strong correlation between coronary mortality and plaque rupture (Virmani et al., 2000). The “vulnerable” plaque is characterised by thin fibrous cap, large necrotic core, high macrophage content, high micro-vessel density and intraplaque haemorrhage (van Lammeren et al., 2011). Plaque vulnerability increases risks of rupture, resulting in cardiovascular death.

Geometric re-construction in the atherosclerotic artery comprises restrictive or expansive arterial remodelling (Pasterkamp et al., 2000). Expansive arterial remodelling was considered to be protective as it prevents narrowing of the lumen in comparison with the restrictive remodelling which induces luminal narrowing (Glagov et al., 1987). However, arterial enlargement allows the outward growth of the plaque and also triggers the rupture in the external laminal side. The lesion rich with

macrophage and T cell populations is also a causal factor for plaque rupture, especially, macrophages are one of the main sources of MMPs that degrade the component of the vascular wall (Johnson, 2017).

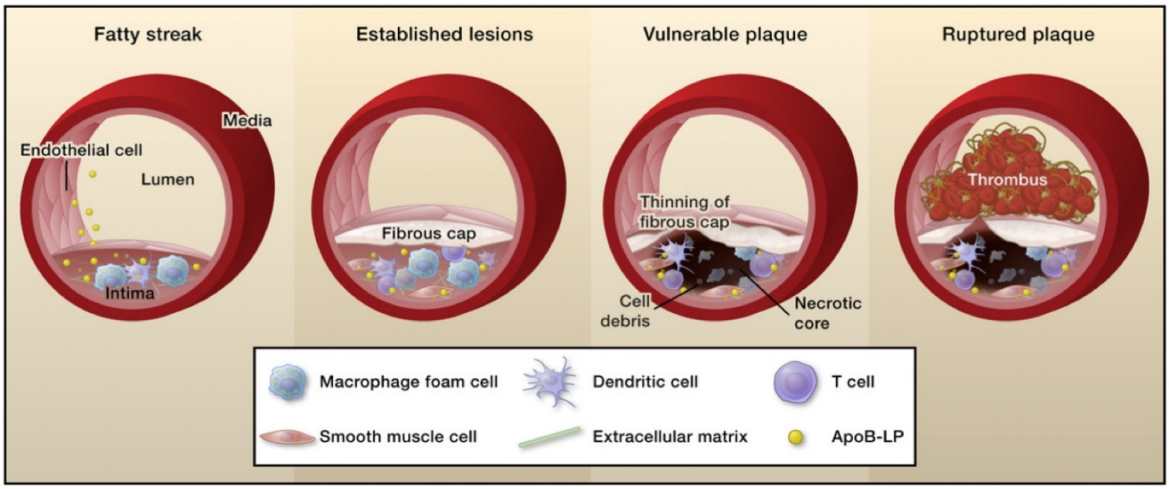


Figure 1.2 The pathogenesis of atherosclerosis.

Disturbance of cholesterol homeostasis can trigger the development of atherosclerotic lesions in the intima of blood vessels. The lesion progresses with the recruitment of myeloid cells and the formation of a fibrous cap. Initiation of the immune response leads to the accumulation of dendritic cells and T cells resulting in chronic inflammation. In the vulnerable plaque, risk of thrombosis stems from necrosis and thinning of fibrous cap. The figure is adapted from Moore and Tabas, 2011.

1.2.2. Murine models of atherosclerosis

Murine models of atherosclerosis were generated by genetic deletion in apolipoprotein E (*ApoE*) and low-density lipoprotein receptor (*Ldlr*) on a C57BL/6 background, by disturbing lipid metabolism and, consequently driving hypercholesterolaemia in mice (Plump et al., 1992, Zhang et al., 1992, Ishibashi et al., 1993). The *ApoE* $^{-/-}$ strain exhibits the similar lipid profile as humans and spontaneously develops atherosclerosis while *Ldlr* $^{-/-}$ mice show no lesion development on a normal chow diet, thus requiring feeding with high cholesterolaemic diet to establish atherosclerosis (Nakashima et al., 1994, Daugherty, 2002). Genetic polymorphism in the *Ldlr* gene in humans is strongly associated with familial hypercholesterolaemia (Hobbs et al., 1992). Both strains have been extensively employed for investigating aetiology and pathophysiology of atherosclerosis (Getz and Reardon, 2016).

In *ApoE* $^{-/-}$ mice which develop robust lesion similar to humans, monocyte adhesion to the vessel wall starts at the age of 8 weeks and foam cell formation is observed in the lesion at the age of 10-weeks (Nakashima et al., 1994). Fatty streaks and lesions are established in the intima of the artery after 12 weeks and SMCs migrate into intima to form a fibrous cap after 20 weeks. Vascular remodelling and calcification occur in the lesion of *ApoE* $^{-/-}$ mice older than 32 weeks. The *Ldlr* $^{-/-}$ strain is a popular model for bone marrow transplantation studies since *Ldlr*-competent macrophages do not interfere with atherogenesis whilst ApoE-producing macrophages can rescue the atherosclerotic phenotype (Boisvert et al., 1995, Linton et al., 1995).

1.2.3. The role of the myeloid lineage in atherosclerosis

1.2.3.1 Monocytes

Hypercholesterolaemia promotes monocyte mobilisation to the circulation and their recruitment to the artery (Averill et al., 1989, Back et al., 1995, Murphy et al., 2011). Two broad monocyte subsets are detected in human and murine blood. Classical monocytes are $CD14^{high}$ CD16- in humans and Ly6C+ CCR2+ in mice whist non-classical monocytes are $CD14^{low}$ $CD16^{high}$ and Ly6C- CCR2- respectively (Passlick et al., 1989, Geissmann et al., 2003, Ingersoll et al., 2010). Intermediate monocytes are observed in human blood, which are defined by co-expression of CD14 and CD16 (Wong et al., 2012).

Classical Ly6C+ monocytes promote progression of atherosclerosis, which is a precursor for macrophages in the atherosclerotic plaque (Swirski et al., 2007). Ly6C- monocytes are derived from Ly6C+ monocytes via a nuclear receptor subfamily 4 group A member 1a (Nr4a1) pathway and patrol the vasculature, but do not migrate into the intima (Hanna et al., 2011, Yona et al., 2013). The high prevalence of intermediate and non-classical monocytes is associated with patients with a higher cardiovascular risk (Thomas et al., 2017).

The chemokine receptors, CCR2, CX3CR1 and CCR5, have been implicated in the recruitment of monocytes within atherosclerotic lesions. CCR2 and CX3CR1 are highly expressed by Ly6C+ monocytes and are essential in monocyte trafficking (Tacke et al., 2007). Deletion of CCR2, CX3CR1 or both genes in *ApoE* $^{-/-}$ mice abolishes monocyte counts in the blood as well as lesion formation (Boring et al., 1998,

Combadiere et al., 2003, Lesnik et al., 2003, Combadiere et al., 2008). CCR5 is used by Ly6C- monocytes to enter the atherosclerotic plaque (Combadiere et al., 2008).

Blockade of monocyte recruitment in the lesion is beneficial in the early lesion, but it is less effective in the established lesion since macrophages can self-renew via SR-A (Guo et al., 2005, Robbins et al., 2013). However, the role of monocytes in late atherosclerosis was demonstrated by Rahman et al. showing that Ly6C+ monocytes give rise to CD206 and arginase 1 expressing macrophages in the regressive atherosclerotic aorta (Rahman et al., 2017). These macrophages are driven in a STAT6-dependent manner and are thought to play a role in the resolution of inflammation.

1.2.3.2 Macrophages

The importance of macrophages in atherosclerosis was demonstrated by several studies, showing that ablation of CD11b+ myeloid cells and deficiency in MCSF abolished lesion formation in the *ApoE* $^{-/-}$ strain (Qiao et al., 1997, Rajavashisth et al., 1998, Stoneman et al., 2007). The atherosclerotic plaque generates myriads of tissue and stress signals including oxLDLs, inflammatory mediators and haem, which can induce heterogeneity of macrophages (Park et al., 2017) (**Figure1.3**). A number of studies in human and murine atherosclerosis have identified several macrophage subsets by utilising immunohistochemistry, gene expression quantitation and cytometry. Pro-inflammatory macrophages were predominantly detected in the plaque shoulder, close to necrotic cores and in carotid endarterectomies from patients with symptomatic disease (Stoger et al., 2012, Cho et al., 2013). In the healthy murine aorta, CD11c+ myeloid cells are detected in the intimal space and can ingest LDLs upon the initiation of hypercholesterolaemia (Jongstra-Bilen et al., 2006). The

transcription factor IRF5 is a master regulator in inflammatory macrophages and directly controls the expression of CD11c in macrophages (Seneviratne et al., 2017). CD11c+ macrophages are detected in murine atherosclerotic lesions and their content increases with high fat diet (Cole et al., 2018). *Irf5* deficiency reduces CD11c+ macrophages in the atherosclerotic lesion and alleviates the disease severity through reducing necrotic core formation (Seneviratne et al., 2017). A recent study reported that plaque CD11c+ macrophages are heterogeneous and comprise foam cells and a non-foamy inflammatory subset. (Kim et al., 2018). Macrophages that ingested LDLs have foamy morphology and display pro-fibrotic properties (Hayes et al., 2014, Thomas et al., 2015).

Alternatively-activated macrophages are also observed in the vascular adventitial tissue and can be identified by the expression of CD68, CD206, CD163 and Dectin-1 (Chinetti-Gbaguidi et al., 2011, Stoger et al., 2012). This subset is highly represented in the asymptomatic plaque relative to the plaque from symptomatic patients (Cho et al., 2013). These macrophages are driven by transcriptional factors including PPARγ and krüppel-like factor 4 (KLF4) (Jiang et al., 1998, Ricote et al., 1998, Liao et al., 2011). PPARγ or KLF4 deficiency in atherosclerotic models exacerbates atherosclerosis and PPARγ activation alleviates lesion formation (Li et al., 2000, Collins et al., 2001, Babaev et al., 2005, Sharma et al., 2012). PPARγ expression in macrophages colocalise with CD206 in the human atherosclerotic lesion and PPARγ activation drives the anti-inflammatory phenotype in macrophages *in vitro* and *in vivo* (Bouhlel et al., 2007).

Oxidised phospholipids are derived from the oxidation process of accumulated LDLs in the atherosclerotic plaque and are capable of inducing the distinct phenotype of macrophages (Kadl et al., 2010). This subset, known as Mox, is characterised by the expression of haem oxygenase (HO) 1 and exhibits the different transcriptomic profile in comparison to pro-inflammatory and anti-inflammatory macrophages. Mox lack phagocytic properties and promote chemotaxis of monocytes, which are driven by nuclear factor erythroid 2-related factor 2 (Nrf2). Two research groups concomitantly identified that macrophages under the influence of intraplaque haemorrhage undergo a distinct phenotypic transition. These subsets, Mhem identified by Boyle et al. or M(Hb) identified by Finn et al., display the anti-inflammatory phenotype and reduced lipid ingestion activity via activation of activating transcription factor (ATF) 1, liver X receptor (LXR) α, ATP-binding cassette transporter (ABCA) 1, HO1, Nrf2 (Boyle et al., 2011, Boyle et al., 2012, Finn et al., 2012). Finally, C-X-C motif ligand (CXCL) 4, also known as platelet factor 4, is a prognostic predictor for atherosclerosis and is widely observed in human carotid endarterectomies (Pitsilos et al., 2003, Gleissner et al., 2010). Macrophages exposed to CXCL4 stimulation display a reduced phagocytic capability, together with low expression of CD163.

Recently, several research groups have identified and characterised macrophage subsets in the murine atherosclerotic aorta by utilising mass cytometry and single cell RNA sequencing (scRNAseq). Cochain et al. described three aortic macrophage subsets within the plaques comprising resident-like, inflammatory and triggering receptor expressed on myeloid cells (Trem) 2 expressing macrophage subpopulations by scRNAseq (Cochain et al., 2018). Concomitantly, mass cytometry also identified 2 resident and 2 recruited subsets in atherosclerotic aortas (Cole et al., 2018).

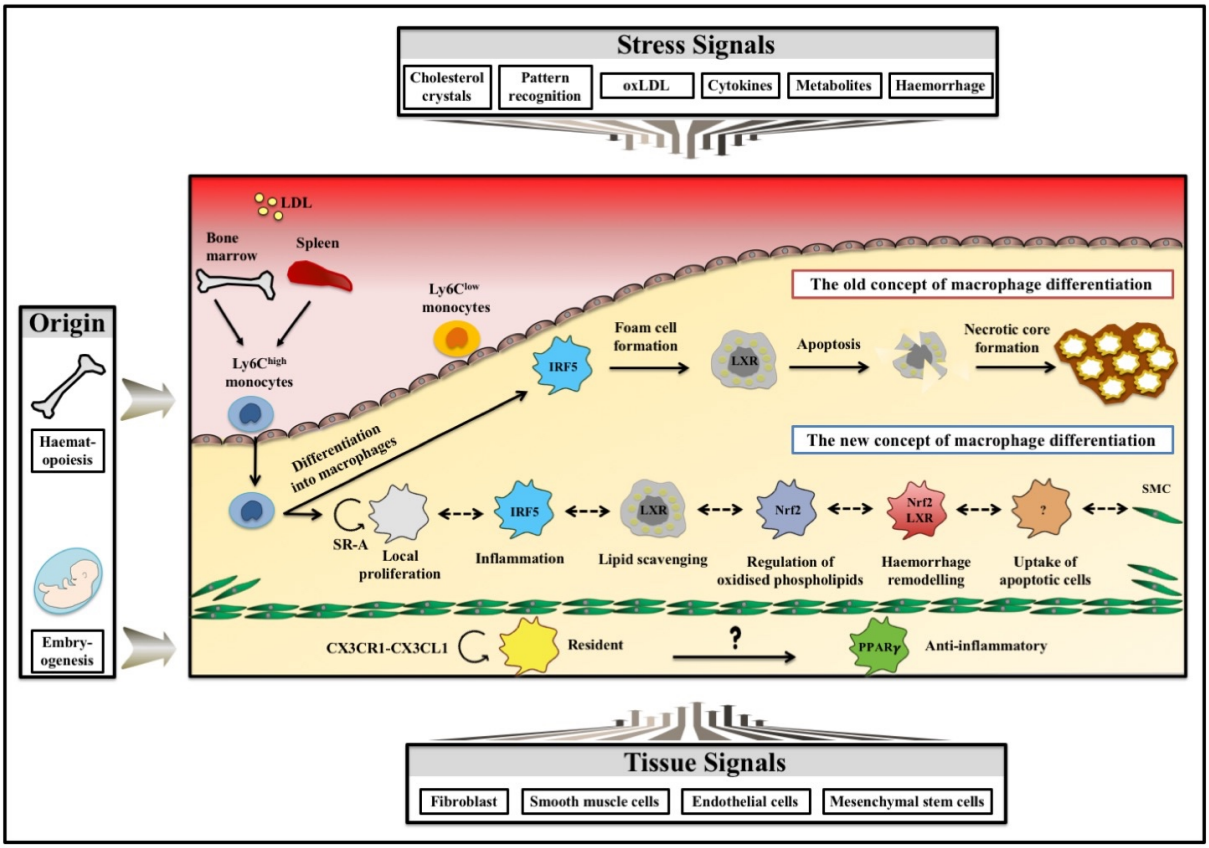


Figure 1.3 Macrophage subsets in the atherosclerotic lesion.

Ly6C+ monocytes give rise to macrophages within the lesion. It was thought that monocyte-derived macrophages solely ingest lipids, become foam cells, and eventually undergo apoptosis. However, recent evidence suggests that the recruited macrophages sustain local proliferation via scavenger receptor (SR)-A and differentiate into several subsets in response to environmental cues: these include lipid derivatives, inflammatory mediators and haemorrhage. The dynamic transition of the macrophage function results from activation of specific transcription factors. Tissue resident macrophages in adventitia are thought to be derived during embryogenesis and may contribute to the tissue homeostasis.
Abbreviations: low-density lipoproteins (LDLs), oxidised LDLs (oxLDLs), interferon regulatory factor (IRF) 5, nuclear factor kappa-light-chain-enhancer of activated B cells (NFκB), liver X receptor (LXR), nuclear factor erythroid 2-related factor (Nrf) 2, activating transcription factor (ATF) 1, C-X3-C motif chemokine receptor 1 (CX3CR) 1, chemokine C-X3-C motif ligand (CX3CL) 1, peroxisome proliferator-activated receptor (PPAR) γ. The figure is adapted from Park et al., 2017.

1.2.3.3 Dendritic Cells

DCs are antigen presenting cells that are subdivided into conventional DCs (cDCs) and plasmacytoid DCs (pDCs) based on their origin; cDCs are derived from common myeloid progenitors whereas pDCs are from common lymphoid progenitors (Guilliams et al., 2014). Two types of cDCs, cDC1 and cDC2, perform different functions in association with T lymphocytes, in which cDC1 prime CD8+ T cells and cDC2 activate $CD4^+$ T cell differentiation (Merad et al., 2013).

cDC1, cDC2 and pDCs are detected in the atherosclerotic aorta in mice (Cole et al., 2018). cDC1 play a protective role through promoting regulatory T cell (Treg) activation while CCL17 expressing DCs in the atherosclerotic lesion reduces Treg expansion (Liu et al., 2008, Choi et al., 2011, Weber et al., 2011). Several research groups reported opposing roles of pDCs in atherosclerosis (Daissormont et al., 2011, Macritchie et al., 2012, Yun et al., 2016).

1.2.3.4 Neutrophils

Neutrophils belong to the family of polymorphonuclear cells (PMN), together with eosinophils and basophils, and are the first responder to injury and infection (Kolaczkowska and Kubes, 2013). Although neutrophils have a short life span, they are largely instrumental in eliminating pathogens through secretion of anti-microbial granule proteins, phagocytosis and release of nuclear materials called neutrophil extracellular traps (NETs) (Brinkmann et al., 2004).

Neutrophils play a detrimental role in atherogenesis, by producing NETs which prime macrophages to produce IL-1β in the murine atherosclerotic plaque (Warnatsch et al., 2015). In a murine MI model, neutrophils may play a protective role by promoting

macrophage activation into the raparative phenotype via producing neutrophil gelatinase-associated lipocalin (Horckmans et al., 2017).

1.3. C-type lectin receptors and dendritic cell immunoreceptors (DCIR)

The innate immune system is the frontline defence against pathogens and is mediated by myeloid populations and natural killer (NK) cells (Janeway, 1999). Innate immune cells sense the molecular signatures that are derived from microbes through the pattern recognition receptor (PPR) family (Akira et al., 2006). PPRs comprise four broad receptor families including TLRs, Retinoic acid-inducible gene (RIG)-I-like receptors (RLRs), NOD-like receptors (NLRs) and C-type lectin receptors (CLRs) (Takeuchi and Akira, 2010). CLRs are preferentially expressed by the myeloid lineage and recognise pathogen-associated molecular patterns (PAMPs) and damage-associated molecular patterns (DAMPs), dependent or independent of Ca^{2+} influx (Sancho and Reis e Sousa, 2012, Hoving et al., 2014).

The extracellular domain of CLRs consists of one or multiple carbohydrate recognition domains (CRDs) or C-type lectin-like domains (CTLDs) (Hoving et al., 2014). CLRs carry either an immunoreceptor tyrosine-based activation motif (ITAM) or immunoreceptor tyrosine-based inhibition motif (ITIM) in the cytoplasmic domain (Billadeau and Leibson, 2002). These motifs mediate signals upon activation of CLRs and their regulation provides a balance in cellular activation in the immune system. Some CLRs including dendritic cell-specific intercellular adhesion molecule-3-grabbing non-integrin (DC-SIGN) lack both ITAM and ITIM domains and can

undertake antigen presentation and endocytosis through other signalling motif domains including tyrosine-independent motifs (Del Fresno et al., 2018).

1.3.1. Human dendritic cell immunoreceptors (DCIR)

Bates et al. first identified human dendritic cell immunoreceptor (DCIR) and murine DCIR1 in DCs, monocytes, macrophages, B lymphocytes, and granulocytes, and showed that DCIR carries the ITIM domain (Bates et al., 1999) (**Table 1.1**). Human DCIR is located on chromosome 12p13 in close proximity to the NK gene complex. Human DCIR expression is reduced by treating monocyte-derived DCs with stimulatory signals including CD40 ligand, LPS and TNFα. Richard et al. later discovered two different forms of DCIR in human neutrophils, a full length and a short form lacking the site for oligomerisation of CLRs (Richard et al., 2002). Neutrophils down-regulate gene expression of the short DCIR in response to GM-CSF, IL-3, IL-4, or IL-13 whilst the full length DCIR is not observed in resting neutrophils. Richard et al. also showed that treating neutrophils with pro-inflammatory signals (LPS, TNFα and IL-1α), and GMCSF reduces cell surface levels of DCIR (Richard et al., 2003). Collective evidence suggests that down-regulation of DCIR in myeloid cells is required to perform inflammatory responses.

The inhibitory role of DCIR on TLR-mediated cytokine production was demonstrated in DCs, showing that DCIR internalisation upon activation using its monoclonal antibody suppresses TLR9-induced IFNα production in human pDCs and TLR8-induced IL-12 and TNFα production in monocyte-derived DCs (Meyer-Wentrup et al., 2009, Meyer-Wentrup et al., 2008). In addition, DCIR-mediated antigen presentation enhances CD8+ T cell activation (Klechevsky et al., 2010). Lambert et al. showed that

human immunodeficiency virus (HIV) 1 utilises DCIR in DCs as an attachment protein for transmission to CD4+ T cells (Lambert et al., 2008). Endogenous and pathogenic ligands for DCIR were identified by Bloem et al.; these include glycans (mannotriose, sulfo-Lewis^a, Lewis^a, Lewis^b) and HIV1-derived gp140 glycoprotein (Bloem et al., 2014, Bloem et al., 2013). Several polymorphisms in the *Dcir* gene are strongly associated with susceptibility to rheumatoid arthritis, systemic lupus erythematosus and primary Sjogren's syndrome (Lorentzen et al., 2007, Guo et al., 2012, Liu et al., 2015).

1.3.2. Murine Dendritic Cell Immunoreceptors (DCIR) isoforms and DCAR

In mice, DCIR has 4 different isoforms: DCIR1 (Clec4a2), DCIR2 (Clec4a4), DCIR3 (Clec4a3) and DCIR4 (Clec4a1) (Flornes et al., 2004) (**Table 1.1**). Of these forms, DCIR1 and DCIR2 carry the ITIM domain whilst no signalling domains are found in DCIR3 and DCIR4. The sequence of human DCIR and DCIR1 shares 65% homology (Bates et al., 1999). DCIR1 is widely expressed by macrophages, DCs, neutrophils and eosinophils in lymphatic organs, which resemble the expression pattern of human DCIR (Kanazawa et al., 2002, Kishimoto et al., 2015). However, DCIR2 is exclusively found in CD8- cDCs and DCIR3 and DCIR4 are detected at high levels in Ly6C- monocytes and at low levels in Ly6C+ monocytes (Uto et al., 2016, Kameda et al., 2016, Hsu et al., 2017). DCIR4 can also be expressed by Ly6C+ monocyte-derived macrophages. Despite known ligands for human DCIR, to date, little is known about endogenous and exogenous ligands for DCIR in mice. However, given that DCIR1 and DCIR2 signal through the ITIM domain, it is thought to counteract ITAM-mediated responses through sensing self-derived damage-associated molecular patterns (DAMPs) (Del Fresno et al., 2018).

Interestingly, dendritic cell immunoactivating receptor (DCAR) was first reported as a putative partner with DCIR, whose cytoplasmic domain is composed of ITAM and whose homology in the CRD is 91% (Kanazawa et al., 2003). Two isoforms of DCAR were identified DCAR1 (*Clec4b2*) and DCAR2 (*Clec4b1*) (Flornes et al., 2004). However, the human homolog of DCAR has not been reported (Toyonaga et al., 2016). DCAR is expressed by subpopulations of cDCs in lymph nodes (LN) and monocyte-derived macrophages in the peritoneum and spleen (Toyonaga et al., 2016). The same study also reported mycobacteria-derived phosphatidyl-inositol mannosides (PIM) as a pathogenic ligand for DCAR2, which then promotes the production of monocyte chemoattractant protein (MCP) 1 for the recruitment of monocytes during tuberculosis.

Species	Human	Murine				
Protein name	**DCIR**	**DCIR1**	**DCIR2**	**DCIR3**	**DCIR4**	**DCAR1**	**DCAR2**
Gene name	***Clec4a***	***Clec4a2***	***Clec4a4***	***Clec4a3***	***Clec4a1***	***Clec4b2***	***Clec4b1***
Signalling motif	**ITIM**	**ITIM**	**ITIM**	**NF**	**NF**	**ITAM**	**ITAM**
Signalling partners	SHP1/ SHP2	SHP1/ SHP2					
Ligands	Lewis-type glycans, gp140	SA-IVIg	d-mannose, l-fucose, GlcNAc, GalNAc	Not known	Not known	Not known	Ac-Phosphatidyl-inositol mannosid-es
Functions	Inhibition of TLR 8/9-mediated cytokine production in DCs	Myeloid homeostasis, BCR-mediated-Ca2+ mobilisation	Inhibition of TLR-mediated cytokine production in DCs	Not known	Not known	Not known	Induction of MCP-1 production
The expression pattern	Neut, Mono, DCs B cells	Neut, Mono, cDCs, Mac	CD8a-cDCs (spleen)	High in Ly6C-mono, Low in Ly6C+ mono	High in Ly6C-mono, Low in Ly6C+ mono	CD8a-cDCs, CD11b+ myeloid cells	cDCs, Splenic Mac, Mono-derived cells
References	Bates et al., 1999, Richard et al., 2002, Meyer-Wentrup et al., 2008 & 2009, Bloem et al., 2014	Kanazawa et al., 2002, Massoud et al., 2014, Fujikado et al., 2008, Kishimoto et al., 2015	Utoet al., 2015	Kameda et al., 2016, Hsu et al., 2017	Kameda et al., 2016, Hsu et al., 2017	Flornes et al., 2004	Kanazawa et al., 2003, Toyonaga et al., 2016

Table 1.1 Summary of the DCIR family.

Abbreviations: immunoreceptor tyrosine-based activation motif (ITAM), immunoreceptor tyrosine-based inhibition motif (ITIM), Src homology region 2 domain-containing phosphatase (SHP), monocyte chemoattractant protein (MCP), neutrophils (Neut), monocytes (Mono), dendritic cells (DCs) and macrophages (Mac).

1.3.3. The role of DCIR1, DCIR2 and DCAR2 in murine experimental diseases

Several studies using the *Dcir1*$^{-/-}$ mouse strain have demonstrated the role of DCIR1 *in vivo* in murine models of autoimmune diseases and pathogen-driven infection models (**Table 1.2**). Fujikado et al. first reported that DCIR1 maintains DC homeostasis and global deletion of DCIR1 induces DC expansion in lymph nodes, resulting in aggravation of collagen-induced arthritis (Fujikado et al., 2008). In addition, *Dcir1*$^{-/-}$ mice are more susceptible to experimental autoimmune encephalomyelitis (EAE), because of increased infiltration of DCs and CD4+ T cells in the inflamed spinal cord (Seno et al., 2015).

DCIR1 plays a detrimental role in pathogen-associated inflammation. *Dcir1*$^{-/-}$ mice are more resistant to the incidence of cerebral malaria, hepatitis and tuberculosis. *Dcir1* deficiency protects from malaria by limiting TNFα production from CD8+ T cell activation (Maglinao et al., 2013). In a model of hepatitis, the mortality rate was shown to be reduced in *Dcir1*$^{-/-}$ mice via a reduction of TNFα in serum and neutrophil influx in the liver (Ishiguro et al., 2017). In a murine model of tuberculosis, levels of type I IFN in DCs of *Dcir1*$^{-/-}$ mice is reduced, resulting in enhanced Th 1 responses (Troegeler et al., 2017). Troegeler et al. also suggested that the absence of DCIR1 triggers accumulation of active Src homology region 2 domain-containing phosphatase (SHP)-2 in DCs, which then activates CD4+ T cells. The role of DCIR1 in murine colitis models is unclear with opposing effects on leukocyte recruitment (Hutter et al., 2014, Tokieda et al., 2015). The discrepancies could be due to the use of different colitis models.

Uto et al. reported that DCIR2 inhibits TLR-mediated inflammation and its deficiency results in enhanced CD4+ T and CD8+ T cell responses in mice (Uto et al., 2016). However, little is known about the role of DCIR3 and DCIR4 in myeloid cells. Toyonaga et al. identified that DCAR promotes production of MCP-1and MCP-2 in monocyte-derived inflammatory cells upon sensing PIM and drives IFNγ in Th1 cells during mycobacterial infection (Toyonaga et al., 2016).

Collectively, the studies suggested that DCIR1 plays an immuno-inhibitory role in DCs and protects against autoimmune diseases such as rheumatoid arthritis (RA). To date, no studies have investigated the role of DCIR1 in macrophage biology or in atherosclerosis. Human *Dcir* is present in alternatively-activated macrophages and murine *Dcir1* is also expressed by some tissue macrophages (Krausgruber et al., 2011) (Immunological Genome Project (www.immgen.org)). This indicates that DCIR1 potentially plays an inhibitory role in macrophages and also contributes to the regression of atherosclerosis.

Experimental model	Phenotypes of *Dcir1*$^{-/-}$ mice	The role of DCIR1	References
Collagen-induced arthritis (CIA)	• Increased CD11c+ DCs in lymph nodes	• Protective	Fujikado et al., 2008
Experimental autoimmune encephalomyelitis (EAE)	• Increased CD11c+ DCs and CD4+ T cells in spinal cords	• Protective	Seno et al., 2015
Cerebral malaria (CM) (*Plasmodium berghei* ANKA infection)	• Less incidence of CM • Lower TNFα in serum • Less IFNγ +CD8+T cells in the brain • Less CD4+T and CD8+T cells in the spleen	• Detrimental	Maglinao et al., 2013
Endotoxemic hepatitis	• Lower mortality • Lower TNFα, CXCL1&2, IL-6, IL-10 and CCL2 • Less neutrophils, CD4+ and CD8+ T cells, monocytes in the liver	• Detrimental	Ishiguro et al., 2017
Tuberculosis	• Enhanced bacteria clearance • Decreased IFNα in DCs • Increased IFNγ+Th1, CD8+T, B cells, macrophages, DCs in the lungs • Pro-inflammatory phenotype in the lungs • Increased IL-12p70 in the lungs	• Detrimental	Troegeler et al., 2017
Colitis (Dextran sulfate sodium-induced)	• Increased cell infiltration in the colon • Less neutrophils in the colon • Low MCP2 levels in the colon • Less ROS in *Dcir1*$^{-/-}$ neutrophils	• Limited effect • Detrimental	Hutter et al., 2014, Tokeida et al., 2015

Table 1.2 The effect of *Dcir1* deficiency on murine experimental diseases.

1.4. Hypothesis and Aims

In this thesis, I hypothesise that DCIR1 could play a regulatory role in macrophage responses and could protect against atherosclerosis.

The aims for this thesis are:

1) To decipher macrophage heterogeneity in the healthy and atherosclerotic aorta (Chapter 2).
2) To explore the expression pattern of DCIR1 in macrophages (Chapter 3).
3) To study the role of vascular resident macrophages in the steady state and atherosclerosis (Chapter 4).
4) To study the effect of *Dcir1* deficiency in atherosclerosis (Chapter 5).

CHAPTER 2. Characterisation of aortic macrophage subsets using single cell technologies

2.1. Introduction

The aorta is the largest artery that supplies oxygenated blood from the left ventricle to the body. The arterial wall is divided structurally into three layers: the intima, the media and the adventitia. The intima, the innermost layer of artery, is composed of endothelial cells and facilitates the blood flow (Lum and Malik, 1994). The middle section of the artery, known as the media, comprises smooth muscle cells (SMC), elastic fibres and collagen, which provides integrity to the artery (Wolinsky and Glagov, 1967). The adventitia is the outermost layer that surrounds the artery and provides stability to the artery (Coen et al., 2011).

The healthy aorta harbours various immune cell populations including lymphocytes and myeloid cells (Butcher et al., 2011). Macrophages are the most abundant leucocyte population in the healthy aorta and they predominantly reside in the adventitia and maintain tissue homeostasis (Ensan et al., 2016, Lim et al., 2018). Hypercholesterolaemia promotes the production of monocytes in the BM and their mobilisation to the artery where they differentiate into macrophages (Swirski et al., 2007). The tissue micro-environment, together with stress factors produced within the inflamed artery, drives the phenotypic diversity in macrophages (Park et al., 2017). Several subsets of macrophages have been described in the atherosclerotic plaque. Pro-inflammatory macrophages are located in the plaque shoulder in close proximity to necrotic core (Stoger et al., 2012). Lipid-laden macrophages, also known as foam cells, constitute lesional immune cells and perform lipid clearance (Kunjathoor et al., 2002). Macrophages activated by oxidised phospholipids express haem oxygenase (HO) 1 and regulate redox status in the lesion (Kadl et al., 2010). Macrophages observed at the site of intraplaque haemorrhage are less phagocytic but specialised

for clearance of iron and erythrocytes (Boyle et al., 2011, Finn et al., 2012). Platelet factor 4 also drives the unique phenotype of lesional macrophages, associated with plaque destabilisation (Gleissner et al., 2010). The athero-protective phenotype of macrophages is also observed in the lesion and adventitia (Chinetti-Gbaguidi et al., 2011, Stoger et al., 2012).

Recent studies using single cell genomics and mass cytometry delineated several subsets in the murine atherosclerotic aorta, proposing 3 “recruited” macrophages (an inflammatory subset, foam cells, triggering receptor expressed on myeloid cells 2 (Trem2)+ cells) and 2 “resident” macrophages (Lyve1+, CD209b+) (Chinetti-Gbaguidi et al., 2011, Stoger et al., 2012, Cochain et al., 2018, Cole et al., 2018, Kim et al., 2018, Lim et al., 2018, Winkels et al., 2018).

In this chapter, I sought to identify and characterise immune cells, particularly in macrophage subsets, in the healthy and atherosclerotic aorta in mice. Single cell approaches, using cytometry by time of flight (CyTOF) and single cell RNA sequencing (scRNAseq), were utilised to achieve the aim.

2.2. Mass cytometry reveals the atlas of immune cells in the healthy and atherosclerotic aorta.

Mass cytometry (CyTOF) with multi-dimensional analysis provides a step change in the resolution of single cell biology and identification of the immune cell compartment (Bendall et al., 2011). To better characterise the landscape of immune cell populations in the healthy and atherosclerotic aortas, I used CyTOF with a panel of antibodies

recognising 36 surface and intracellular markers, together with the high dimensional analysis tSNE algorithm. Age-matched C57BL/6J (wild type; WT) and *ApoE*$^{-/-}$ mice were used for this analysis. WT mice were maintained on a normal chow diet until sacrifice and *ApoE*$^{-/-}$ mice were fed either a chow or high cholesterolaemic diet (also called high fat diet (HFD)) from the age of 12-week for a further 12 weeks (**Figure 2.1a**). At 24 weeks of age, aortas were dissected from these mice. For each sample, aortas from 2 mice of the same group were combined to obtain sufficient cell numbers. Single cells were retrieved from combined aortas by enzymatic digestion. Individual samples were stained with a Rhodium-based DNA intercalator for viability and were labelled with the Palladium-based barcoding kit. Barcoded cells were then combined together for staining with metal-conjugated antibodies and were finally labelled with an Iridium DNA intercalator. This work was performed collaboratively with Dr Jennifer Cole.

Data were acquired with a Helios mass cytometer and were analysed on Cytobank. Iridium-positive events were gated as cells. Cells negative for rhodium were designated as the live population (**Figure 2.1b**). Live cells expressing CD45 were gated as leucocytes. T cells expressing both CD4 and CD8 were considered contamination from the close proximity of the thymus (Mohanta et al., 2016). viSNE clustering was performed on the live CD45+ leucocyte population excluding CD4+ CD8+ T cells. The percentages of aortic live leucocytes increased with severity of atherosclerosis: 24.1±1.2% (WT), 35.2±3.2% (*ApoE*$^{-/-}$ chow) and 51.0±2.2% (*ApoE*$^{-/-}$ HFD) (WT vs. Chow p=0.023, WT vs. HFD p=0.0007 and Chow vs. HFD p=0.004) (**Table 2.1**).

Markers for endothelial cells and smooth muscle cells (SMC) were also included; endothelial cells were defined as live CD45- CD31+ and SMC as live CD45- alpha smooth muscle actin (ACTA)+ (**Table 2.2**). The proportion of endothelial cells was 4.1±0.3% in the WT, 3.3±0.3% in the chow-fed *ApoE*$^{-/-}$ and 4.0±0.2 in HFD-*ApoE*$^{-/-}$ mice. The SMC content significantly declined from 3.1±0.3% in the WT to 1.6±0.2% in the Chow and 1.3±0.1% in the HFD-fed mice (WT vs. Chow p=0.0018 and WT vs. HFD p=0.0016).

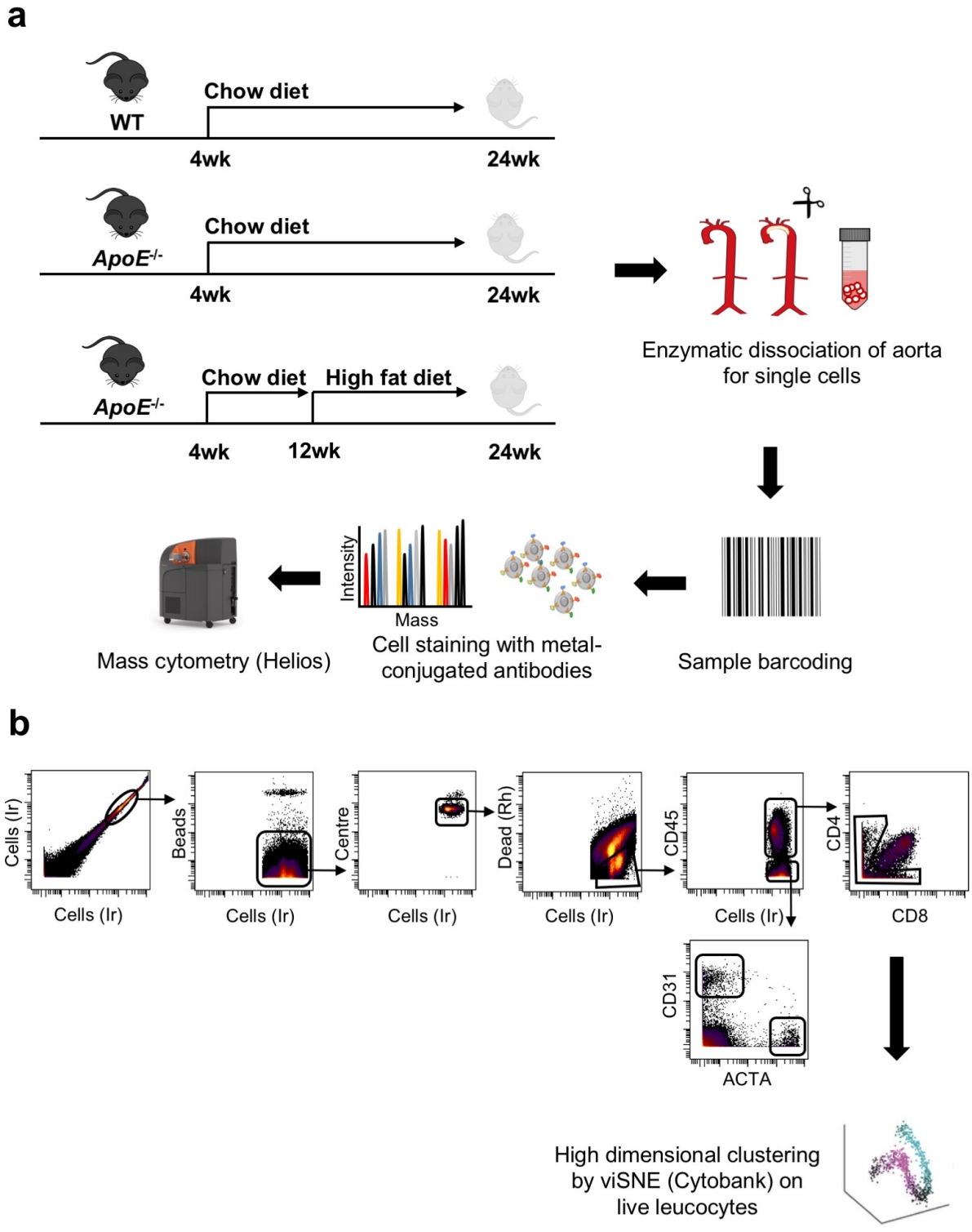


Figure 2.1 Schematic of sample processing and mass cytometry.

a) C57BL/6J (wild type; WT) mice were fed on a normal chow and *ApoE*$^{-/-}$ mice were fed on a chow or a high fat diet for 12 weeks. Single cells dissociated from aortas of these mice were barcoded and stained with metal-conjugated antibodies. The data were then acquired on a Helios mass cytometer. **b)** Live CD45+ cells were gated and analysed by viSNE clustering (Cytobank).

% of live cells	WT (Chow)	*ApoE*$^{-/-}$ (Chow)	*ApoE*$^{-/-}$ (HFD)	P values
Leucocytes (CD45+)	24.1±1.2	35.2±3.2	51.0±2.2	WT vs. Chow 0.023 WT vs. HFD 0.0007 Chow vs. HFD 0.004

Table 2.1 The percentage of live CD45+ leucocytes in the healthy and atherosclerotic aorta.

WT: n= 6, *ApoE*$^{-/-}$ (Chow): n=10, *ApoE*$^{-/-}$ (HFD): n=8. Data are presented as mean±SEM. Mann-Whitney t test.

% of live cells	WT (Chow)	*ApoE*$^{-/-}$ (Chow)	*ApoE*$^{-/-}$ (HFD)	P values
Endothelial cells (CD45- CD31+)	4.1±0.3	3.3±0.3	4.0±0.2	WT vs. Chow 0.0553 WT vs. HFD 0.7242 Chow vs. HFD 0.0155
Smooth muscle cells (CD45- ACTA+)	3.1±0.3	1.6±0.2	1.3±0.1	WT vs. Chow 0.0018 WT vs. HFD 0.0016 Chow vs. HFD 0.4546

Table 2.2 The percentage of endothelial and smooth muscle cells in the healthy and atherosclerotic aorta.

WT: n= 6, *ApoE*$^{-/-}$ (Chow): n=10, *ApoE*$^{-/-}$ (HFD): n=8. Data are presented as mean±SEM. Mann-Whitney t test.

2.2.1. Mass cytometry and high dimensional viSNE analysis identifies sixteen leucocyte populations in the atherosclerotic aorta

Next, live CD45+ cells were examined in greater detail to determine the landscape of immune cell populations in the aorta. The viSNE analysis allowed identification of a total of 16 populations including 8 myeloid populations and 8 lymphocyte populations (**Figure 2.2a**). These populations include macrophages ("resident" and "recruited"), monocytes (Ly6C+ and Ly6C-), type 1 and 2 conventional DCs (cDC1 and cDC2), granulocytes (neutrophils and eosinophils), B cells (B1 B and B2 B), T cells ($\boldsymbol{\gamma\delta}$+, CD4+ and CD8+), natural killer (NK) cells, innate lymphoid cells (ILCs), plasmacytoid dendritic cells (pDCs) and two unknown clusters. (**Figure 2.2b**)

Myeloid populations were the most abundant, accounting for 77.5±1.0% of total leucocytes in all groups. Macrophages were defined as CD11b+ CD68+ CD64+ and comprise 58.5±1.5% of all leucocytes in both WT and *ApoE*$^{-/-}$ strains. Macrophages can be divided into CD206+ (resident-like) and CD11c+ (recruited) subsets (**Figure 2.2b**). Monocytes were defined by expression of common mononuclear cell markers CD11b+ and CD68+ but lacked expression of the macrophage marker CD64 and DC markers. Monocytes can be further separated into classical Ly6C+ CCR2+ and non-classical Ly6C- CCR2- CX3CR1+ subsets.

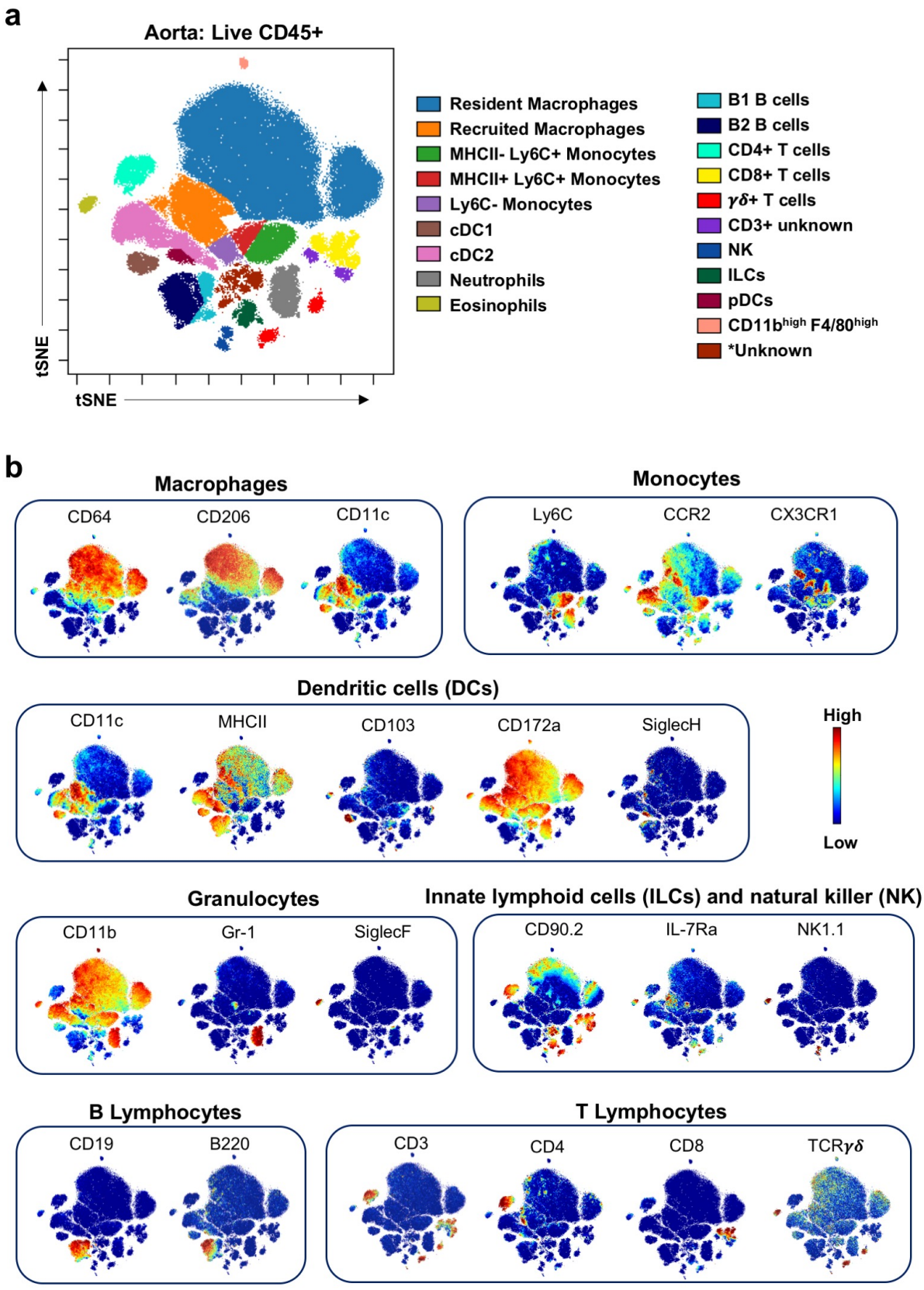
In this analysis, cells expressing high levels of CD11b and F4/80 were often observed in some murine aortas. This subset lacked expression of major macrophage markers such as CD64, CD206 and CD169 and may come from contamination from peri-adventitial fat or serosal macrophages (Davies et al., 2013, Cho et al., 2014). The last

unknown cluster was thought to be the myeloid population as these cells expressed myeloid markers including Ly6C, CCR2, XCR1, CD172a and CD90.2.

viSNE analysis enabled delineation of two subsets of cDCs (CD68+ CD11c+ MHCII+ CD64-) from macrophages. cDC1 were identified by high expression levels of CD103, XCR1 and CD24 whilst cDC2 were defined by CD11b+ and CD172a+ expression (**Figure 2.2b**). Two granulocyte populations, neutrophils and eosinophils, were identifiable by their distinct markers: CD11b+ Gr1+ and CD11b+ SiglecF+ F4/80+ respectively.

B lymphocytes expressed high levels of CD19 and MHCII (**Figure 2.2b**). B cells can be subdivided by the expression of B220: B220- B1 B cells and B220+ B2 B cells. T lymphocytes were defined by their expression of CD3. Cells that co-expressed CD3 and TCRβ can be broadly divided into two T cell populations on the basis of expression of CD4 and CD8; these are CD4+ T cells (T helper) and cytotoxic CD8+ T cells. Of CD3+ TCRβ- cells, TCR$\boldsymbol{\gamma\delta}$ expressing cells were referred to as $\boldsymbol{\gamma\delta}$+ T cells. A CD3+ T cell population which did not express TCR$\boldsymbol{\gamma\delta}$, CD4 or CD8, was also identified, which I referred to as CD3+ unknown. Other small lymphoid populations were also identified including ILCs (Lin- CD90.2+ IL-7Ra+), NK cells (NK1.1+) and pDCs (SiglecH+ B220+ MHCII+).

The heatmap in **Figure 2.2c** summarises the differential marker expression in all leucocyte populations.



(Continued on the next page)

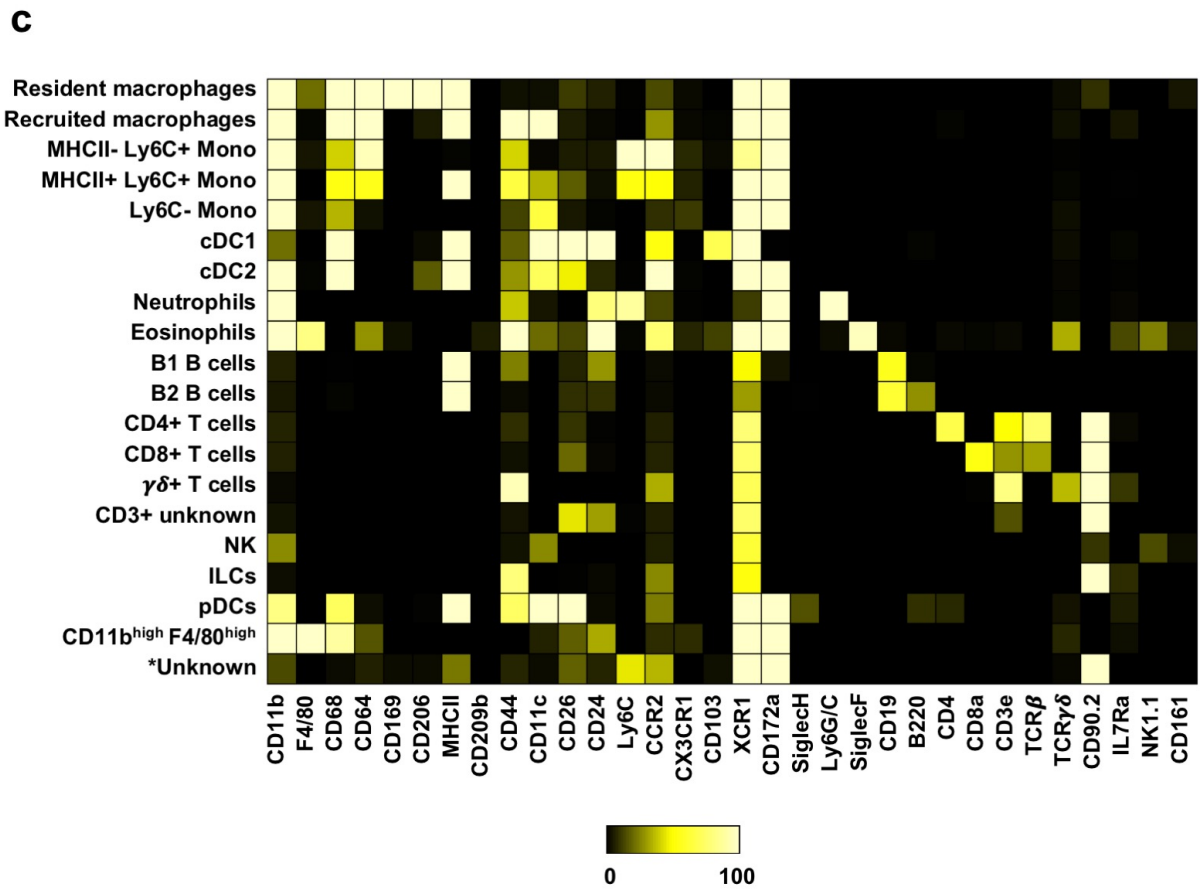


Figure 2.2 The atlas of leucocyte populations in the atherosclerotic aorta using mass cytometry and viSNE analysis.

a) The viSNE plot showing 20 cell clusters of live CD45+ cells in the aorta of *ApoE*$^{-/-}$ mice (chow and HFD groups; n=13). **b)** Marker expressions of selected clusters by viSNE. **c)** The heatmap of marker expression in 20 clusters.

2.2.2. Atherosclerosis alters the immune cell composition of murine aortas

To gain an insight into how chronic inflammation affects the leucocyte composition in the aortas, I compared individual samples from WT mice and *ApoE*$^{-/-}$ mice fed either a chow or HFD. The most striking difference in the immune cell composition between healthy and atherosclerotic aortas is the emergence of macrophage subsets that express CD11c, along with a decrease in the proportion of "resident" macrophages (**Figure 2.3a)**. The percentage of CD11c+ "recruited" macrophages in the healthy aorta accounted for 2.4±0.3% of the live CD45+ cells and their proportion increased with atherosclerosis to 4.9±0.3% in the aorta of chow diet-fed *ApoE*$^{-/-}$ mice and 11.3±1.0% in the aorta of HFD-fed *ApoE*$^{-/-}$ mice (WT vs. Chow p= 0.001, WT vs. HFD p=0.0007 and Chow vs. HFD p<0.0001) (**Figure 2.3b)**. Conversely, the percentage of resident aortic macrophages declined from 61.1±0.9% in the WT mice to 55.4±2.6% in chow-fed *ApoE*$^{-/-}$ mice and 41.4±1.9% HFD-fed *ApoE*$^{-/-}$ mice (WT vs. Chow p= 0.0934, WT vs. HFD p=0.0007 and Chow vs. HFD p=0.0005). The data suggest that the arterial inflammation skews macrophage towards the recruited phenotype.

Monocytosis is one of the key features of hypercholesterolaemia, where Ly6C+ monocyte count increases in the blood and mobilise into the inflamed artery (Swirski et al., 2007). In **Figure 2.3b**, viSNE clustering divided monocytes into three distinct populations based on the expression of Ly6C and MHCII. All three subsets of monocytes increased with disease severity**.** MHCII- Ly6C+ monocytes increased from 0.5±0.1% of live CD45+ cells in WT mice to 4.9±1.5% in HFD-fed *ApoE*$^{-/-}$ mice (p=0.0007) and MHCII+ Ly6C+ monocytes accounted for 2.7±0.4% of live CD45+ cells in HFD-fed *ApoE*$^{-/-}$ mice compared to 0.4±0.03% in WT mice (p=0.0007). The

proportion of Ly6C- monocytes went from 0.6±0.1% in WT mice to 3.0±0.3% in HFD-fed *ApoE*$^{-/-}$ mice (p=0.0007). Atherosclerosis also increased the influx of other leucocytes into the murine aorta (Galkina et al., 2006). I observed a two-fold increase in the proportion of cDC1 and neutrophils in aortas of HFD-fed *ApoE*$^{-/-}$ mice compared to the WT mice (cDC1: 1.1±0.1% (WT) vs. 2.0±0.1% (HFD) p=0.0007 and neutrophils: 2.1±0.7% (WT) vs. 4.1±0.7% (HFD) p=0.0127).

High fat-fed *ApoE*$^{-/-}$ mice exhibited features of advanced atherosclerosis and had a significantly increased T cell compartment (CD4+ T and CD8+ T cells) compared to the WT group (CD4+T: 1.4±0.3% (WT) vs. 3.9±0.6% (HFD) p=0.008 and CD8+T: 1.3±0.3% (WT) vs. 4.6±0.5% (HFD) p=0.0007; **Figure 2.3b**). Albeit the role of pDCs in atherosclerosis remained unclear (Daissormont et al., 2011, Macritchie et al., 2012), the data showed that their proportion increased with disease severity (0.6±0.1% (WT), 0.7±0.1% (Chow) and 1.3±0.1% (HFD); WT vs. HFD p=0.0047 and Chow vs. HFD p=0.0219). B cells can be divided by the expression of B220 into two broad subsets: atheroprotective B1 B cells and atherogenic B2 B cells (Srikakulapu and McNamara, 2017). B 1B cell compartment did not increase with the severity of the disease, however, their percentage in chow-fed *ApoE*$^{-/-}$ mice was almost 2-fold higher than WT and HFD-fed *ApoE*$^{-/-}$ mice (Chow vs. WT p=0.0312 and Chow vs. HFD p=0.0343). The proportion of cDC2, B2 B cells, NK cells and ILC was not affected by inflammation in the aorta.

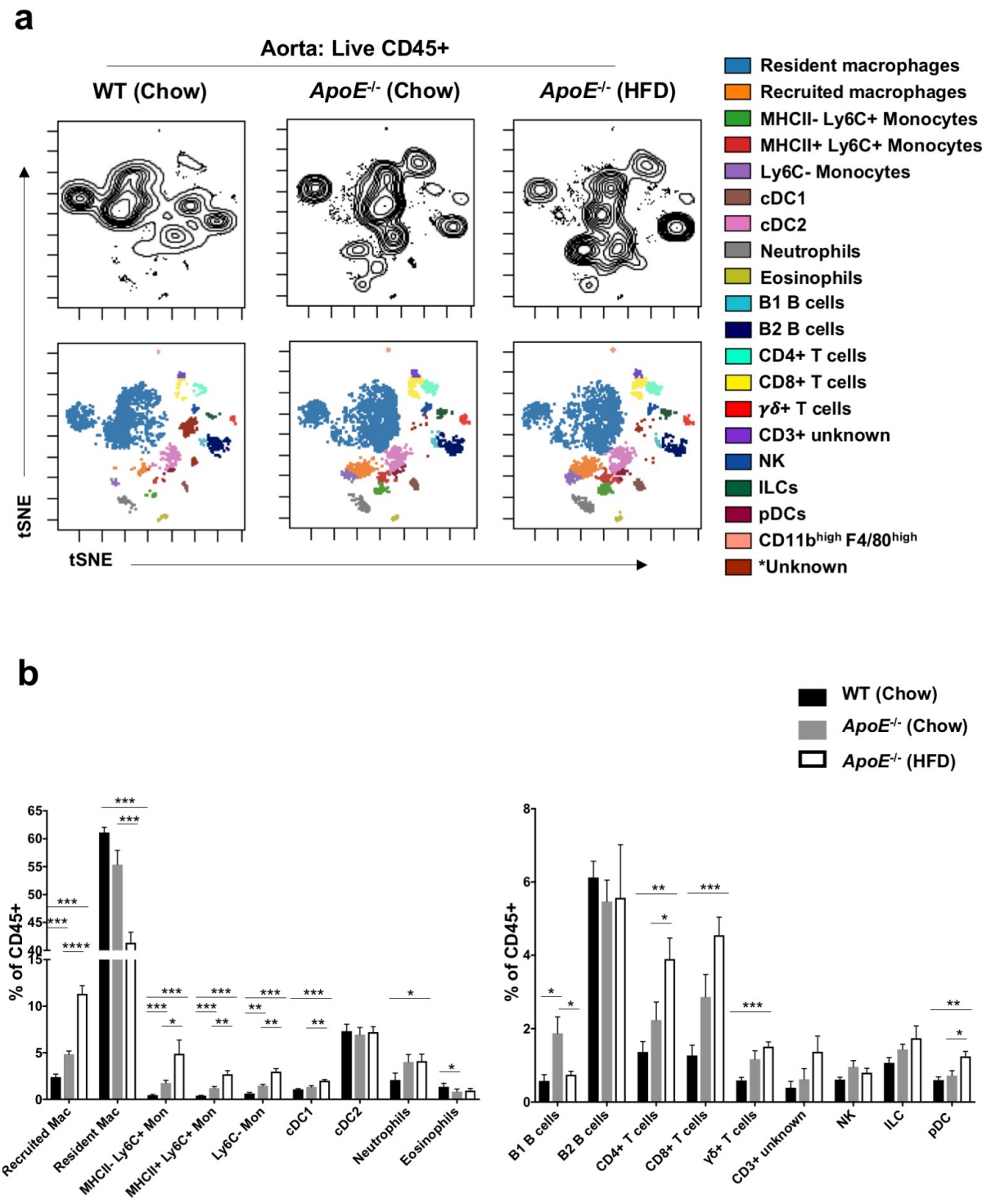


Figure 2.3 Atherosclerosis alters the immune cell composition in the aorta.

a) 20 clusters of aortic leucocytes in three groups WT, *ApoE*$^{-/-}$ (chow) and *ApoE*$^{-/-}$ (HFD) are presented by density and overlay. 19 clusters were identified and 1 cluster remains unknown. An individual sample from each group is selected for representation. **b)** Percentages of each population in each group are displayed in bar graphs. WT: n= 6, *ApoE*$^{-/-}$ (Chow): n=10, *ApoE*$^{-/-}$ (HFD): n=8. Data are presented as mean±SEM. Mann-Whitney t test. **P<0.01, ***P<0.001, ****P<0.0001

2.3. Spatial distribution of lesional and resident macrophage subsets in atherosclerosis

Having identified that CD11c+ recruited macrophages were positively associated with arterial inflammation, I sought to visualise the spatial distribution of macrophage subsets in the aortic root of HFD-fed *ApoE*$^{-/-}$ mice by performing immunohistochemistry. Aortic root sections were stained with a combination of antibodies against CD11c and CD206 or CD11c and CD64. CD11c expression was exclusively located in the lesion and the media, whilst the tissue resident macrophage marker CD206 was widely expressed in the adventitia (**Figure 2.4a**). The image of the aortic root section showed co-localisation of CD11c with CD64, which demonstrated that lesional macrophages expressed CD11c. It is likely that this novel subset of macrophages, that was abundant in the atherosclerotic aorta, were the recruited macrophages that were found in Figure 2.2 and 2.3.

To further understand the spatial distribution of vascular leucocytes, aortas from 12 *ApoE*$^{-/-}$ mice were mechanically separated after enzymatic digestion into adventitia and intima/media portions that were then further dissociated into single cells. Samples were then processed as described in Figure 2.1. In a combined analysis three broad clusters of macrophages were identified: 1) CD206+ CD209b+, 2) CD206+ CD209b- and 3) CD11c+ CD44+ (**Figure 2.5a**). The expression of CD11c and CD44 defined a cluster which lacked the expression of CD206 and CD169 (**Figure 2.5b**). This subset was detected exclusively in the intima-media where atherosclerotic lesions were located. The other two macrophage clusters expressed high levels of CD206 and CD169. One of clusters was characterised by the additional expression of CD209b,

highly expressed by marginal zone macrophages in the spleen. Both clusters can be further separated by the expression of Lyve1 and MHCII.

Live CD45+ cells from each tissue compartment were clustered using the viSNE algorithm. The plot in **Figure 2.6a** presents 14 leucocyte subsets that were identified in the combined data of the intima/media and adventitia. The proportion of each population in the two compartments of the vessel was shown in doughnut charts, whereby the percentages were the mean of two independent experiments (**Figure 2.6b**). Notably, the data suggested that recruited macrophages predominantly resided in the intima-media, accounting for 40.8±4.2 of total live leucocytes. In contrast, tissue resident macrophages consisted of 77.5±5.3% of live CD45+ in the adventitia and 18.9±0.4% in the intima-media (**Figure 2.6b,c**). Blood borne cells such as neutrophils, monocytes and cDC2 were predominantly located in the intima-media whereas a higher percentage of $\boldsymbol{\gamma\delta}$+ T cells and B cells was observed in the adventitia. CD4+ and CD8+ T cell subsets, cDC1, B cells, NK and ILCs were equally distributed in both tissues. However, I was unable to identify pDCs and B1 B in these two independent experiments. It may be that an additional enzymatic digestion and mechanical dissociation of the intima-media and adventitia may have caused loss of small populations such as pDCs.

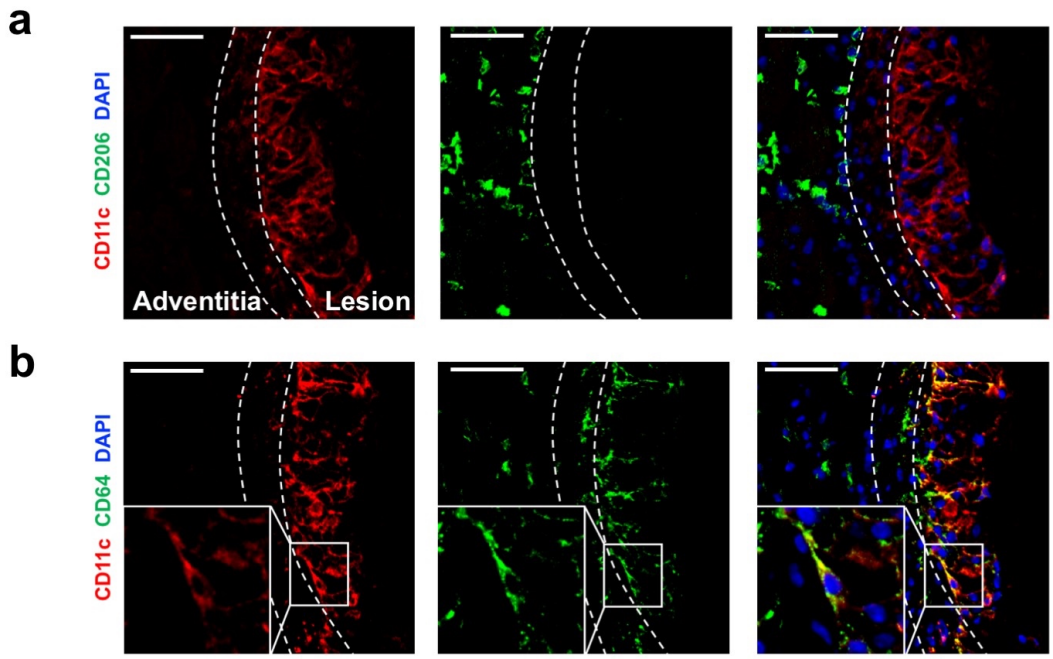


Figure 2.4 Spatial distribution of aortic macrophages in the atherosclerotic aorta.

a) CD11c+ cells (red) are located in the lesion and CD206+ macrophages (green) are widely distributed in the adventitia of the aortic root section. The area stained in blue indicates nuclei. **b)** Overlay with CD11c (red), CD64 (green) and DAPI represents CD11c+ macrophages in the lesion of the aortic root. The images are the representation of 6 high fat fed *ApoE*$^{-/-}$ mice and were taken at X10 magnification. Scale bars denote 200 μm.

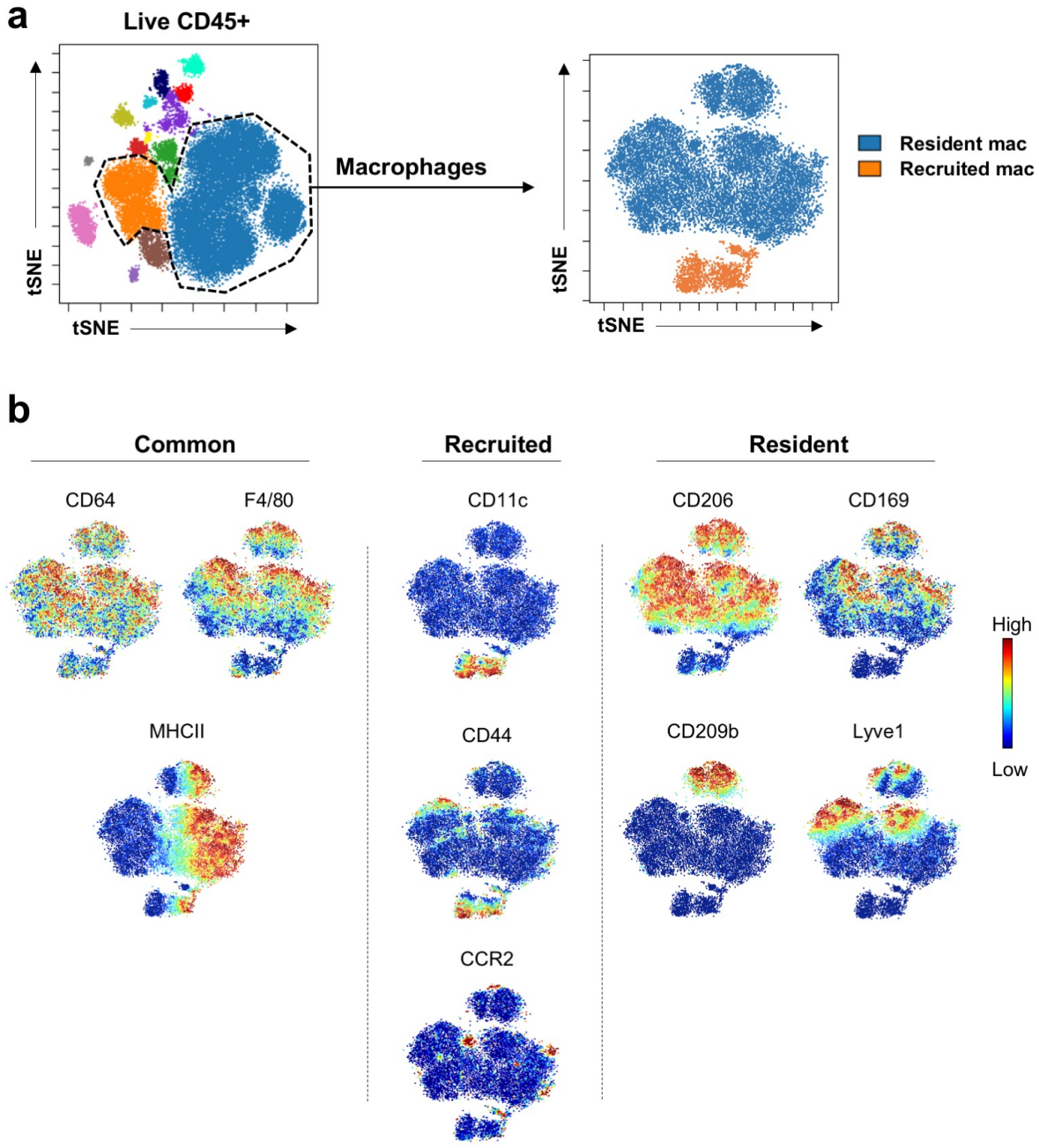


Figure 2.5 Heterogeneity of aortic macrophages in the atherosclerotic aorta.

a) Macrophages (CD11b+ CD68+ CD64+) from aortas of *ApoE*$^{-/-}$ mice were gated and were clustered by viSNE analysis on the basis of the 19 myeloid marker expression. Two major subsets are indicated. **b)** The expression profile of selected markers is displayed in the viSNE plot.

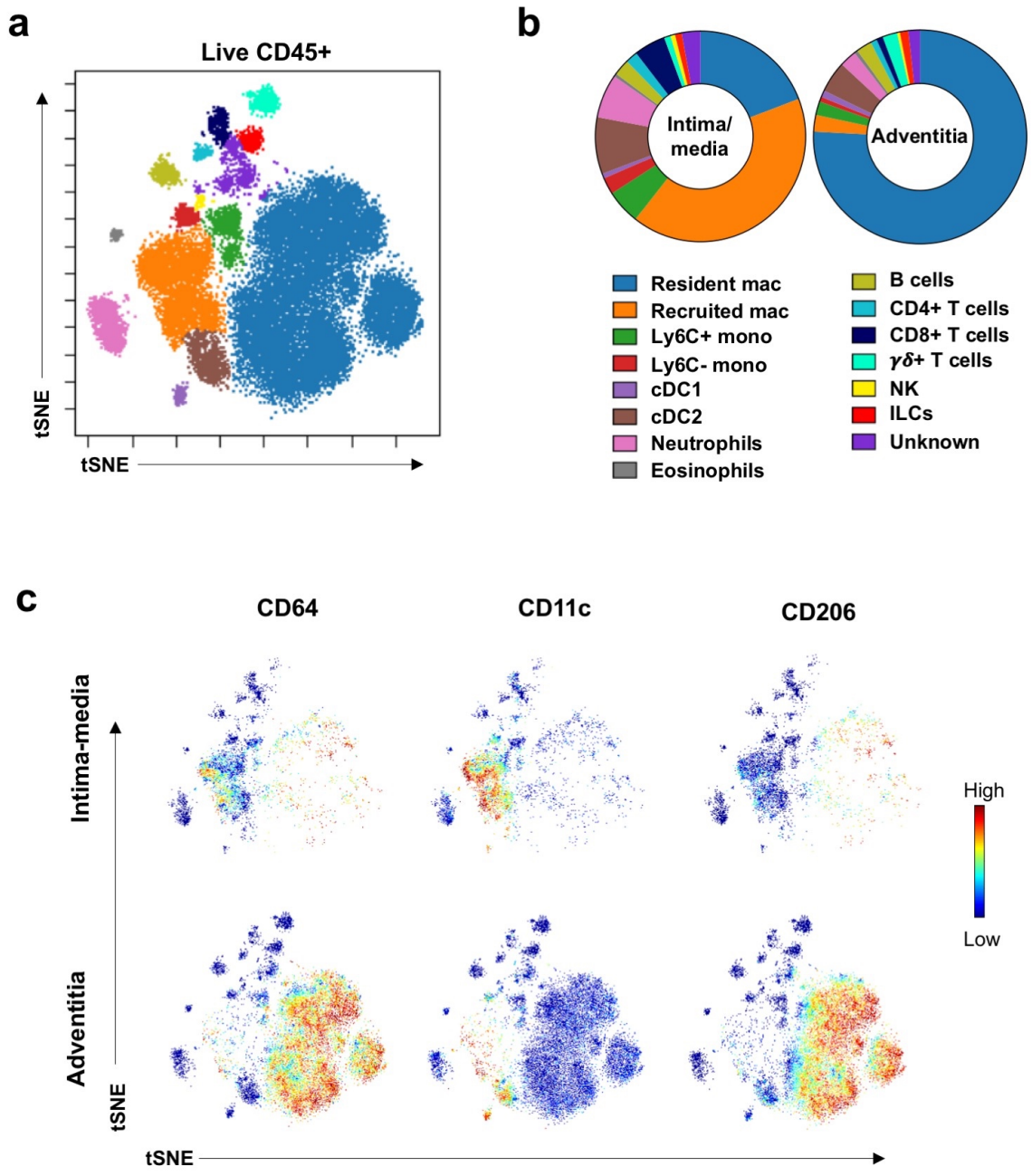


Figure 2.6 Spatial distribution of leucocytes from intima-media and adventitia of atherosclerotic aorta by mass cytometry.

a) Live CD45+ cells from intima/media and adventitia of 12 *ApoE*$^{-/-}$ mice were concatenated and were analysed by viSNE clustering. The analysis identifies 14 leucocyte populations. **b)** The proportion of each population in intima-media and adventitia is shown in the doughnut plots. **c)** The expression of CD64, CD11c and CD206 is displayed in intima/media and adventitia. The viSNE plots from a) c) are the representative of two independent experiments and b) The percentage is the mean of two experiments.

2.4. Single cell RNA sequencing of aortic macrophage subsets

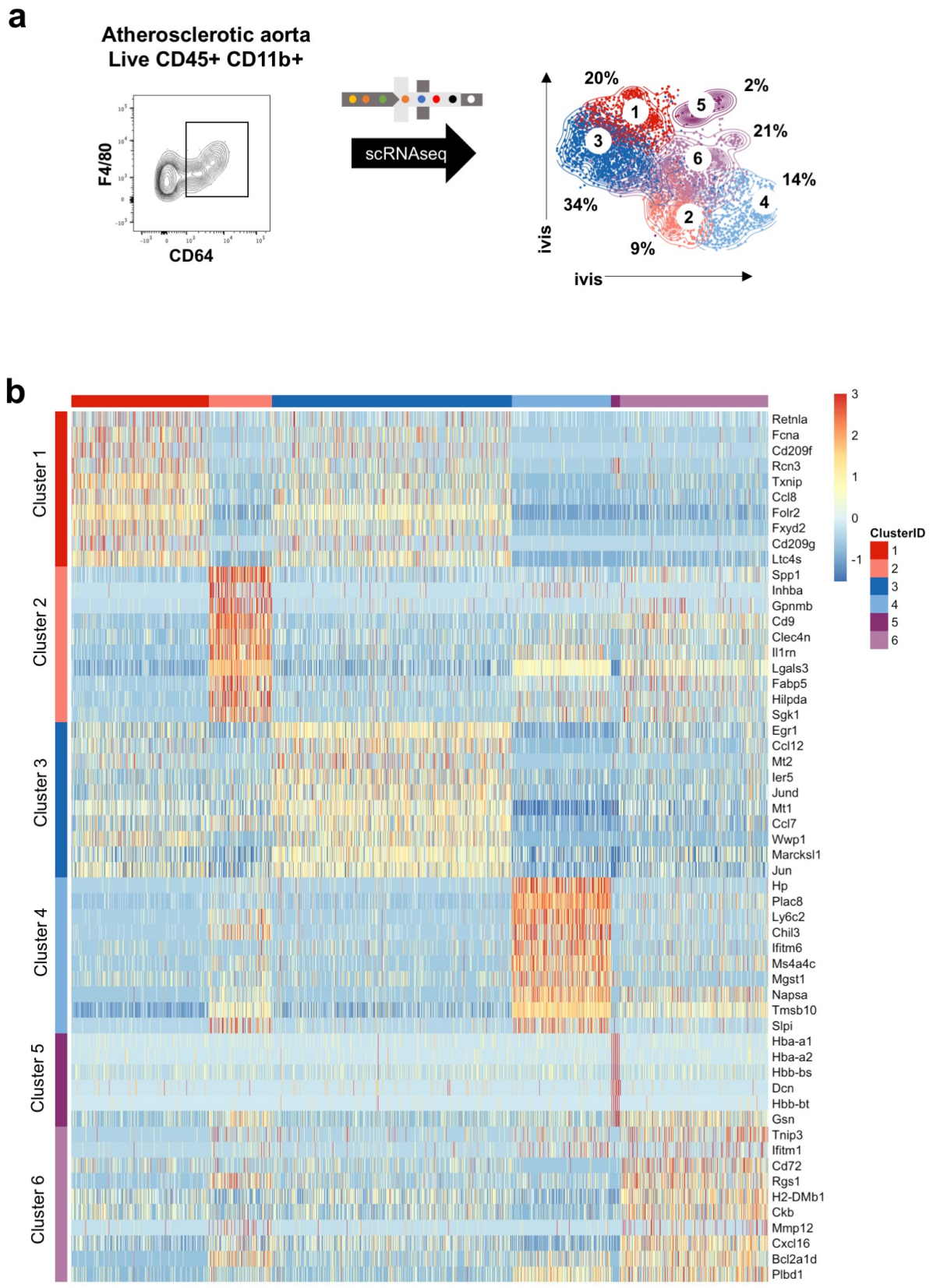
Next, I sought to gain an insight into the potential function of aortic macrophage subsets using single-cell RNA sequencing (scRNAseq). CD11b+ CD64$^{low\ to\ high}$ cells from aortas of high fat fed-*ApoE*$^{-/-}$ mice were sorted by fluorescence-activated cell sorting (FACS) and gene expression data from single cells acquired using 10X Genomics and the HiSeq4000 platform (**Figure 2.7a**). A novel dimensionality reduction framework, namely the ivis algorithm (developed in collaboration with Dr Ignat Drozdov from Bering Ltd), tSNE and LargeVis were adopted for clustering input cells based on their transcriptomic profile. Gene ontology analysis of biological processes (GO analysis) was also performed to comprehend the functional profiling of the cell clusters.

The data analysis identified 6 subsets of myeloid cells including 2 resident clusters (cluster 1 (20%) and cluster 3 (34%)), 2 recruited clusters (cluster 2 (9%) and cluster 4 (14%)), cDC2 (cluster 6 (21%)) and a small population of Ly6C+ monocytes (cluster 5 (2%)). The heatmap in **Figure 2.7b** shows the top 10 genes expressed by each cluster.

The GO analysis segregated the clusters into groups associated with specific functions (**Figure 2.7c**). The gene expression profile of 6 clusters suggested that cluster 1 (CD206+ CD209b+ resident macrophages) was specialised in protein activation cascade, immune responses and complement activation. Cluster 3 (CD206+ HO1+ resident macrophages) was associated with wound healing and extracellular signal–regulated kinases (ERK) signalling. Cluster 2 (CD11c+ recruited macrophages) expressed genes associated with lipid handling and chemotaxis.

Cluster 4 (CCR2+ recruited macrophages) may perform wound healing, phagocytosis and reactive oxygen metabolism. Cluster 5 and 6 were compatible with monocytes and DCs, respectively.

Further analysis excluding clusters 5+6 and grouping clusters 1 and 3 or clusters 2 and 4 was performed. The top 20 genes expressed by each cluster were shown in the heatmap (**Figure 2.8a**). Clusters 1 and 3 expressed high levels of resident macrophage markers including *Cd163, Lyve1, Mrc1* (CD206), *Jun, Csf1r* and *Clec4a2* (*Dcir1*) (**Figure 2.8b**). In contrast, clusters 2 and 4 displayed the gene expression signature of recruited macrophages, showing high levels of *Ly6C2, Il1b, Cd44, Clec4e, Csf2rb and Irf5*.



(Continued on the next page)

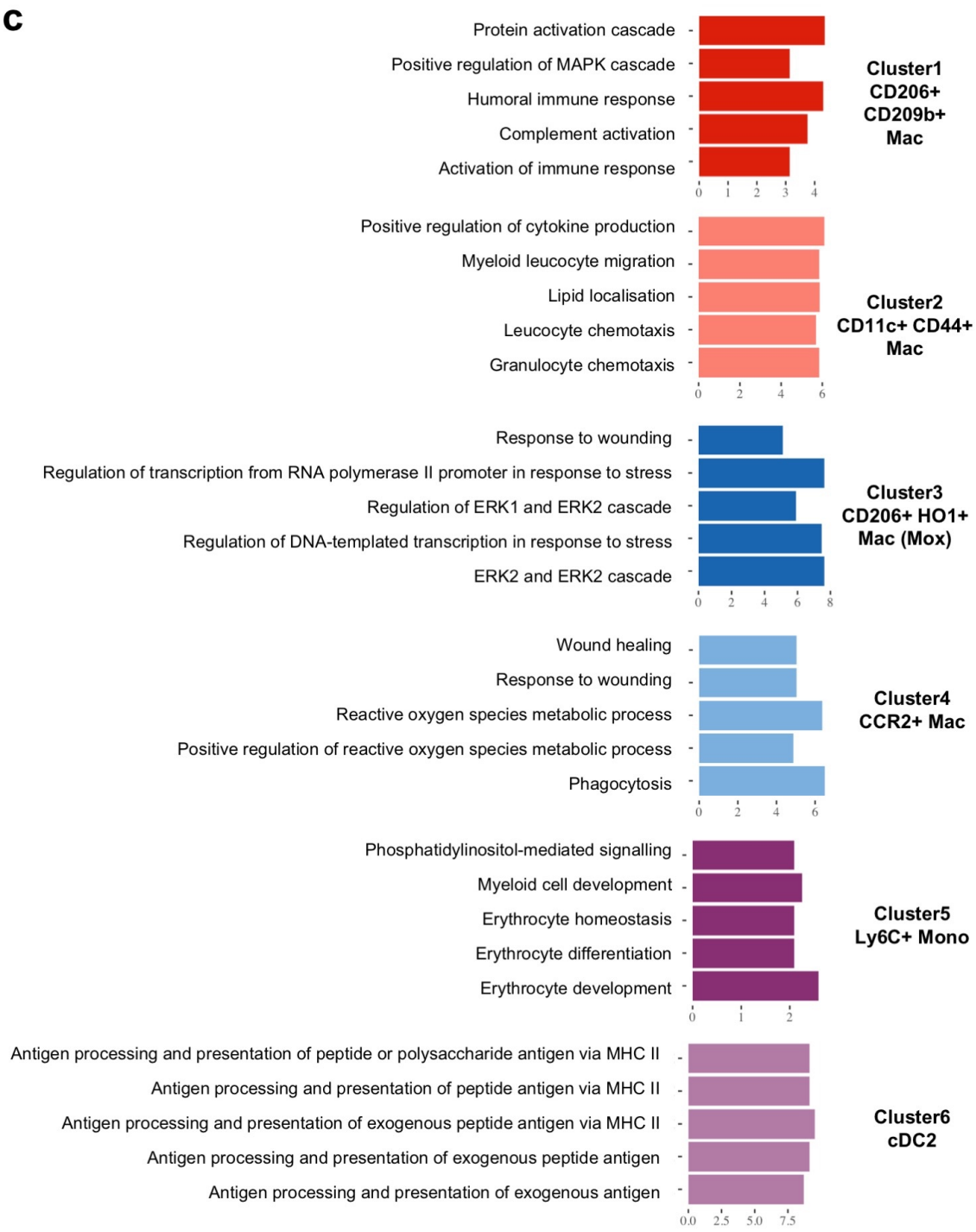


Figure 2.7 Single cell RNA sequencing and unbiased high-dimensional analysis ivis identifies 6 clusters in CD11b+ CD64$^{low-high}$ cells from atherosclerotic aortas.

a) Live CD45+ CD11b+ CD64$^{low-high}$ cells were isolated from aortas of 9 *ApoE*$^{-/-}$ females fed on a HFD. Single cells were then sequenced by using 10X Genomics platform. The transcriptomic data from single cells were analysed using ivis, which identifies 6 clusters. **b)** The heatmap of 6 clusters showing top 10 genes each. **c)** Gene ontology analysis of biological processes (GO analysis) was applied to 6 clusters to relate the gene expression profile to cellular functions. Data were analysed in collaboration with Dr Ignat Drozdov from Bering Ltd.

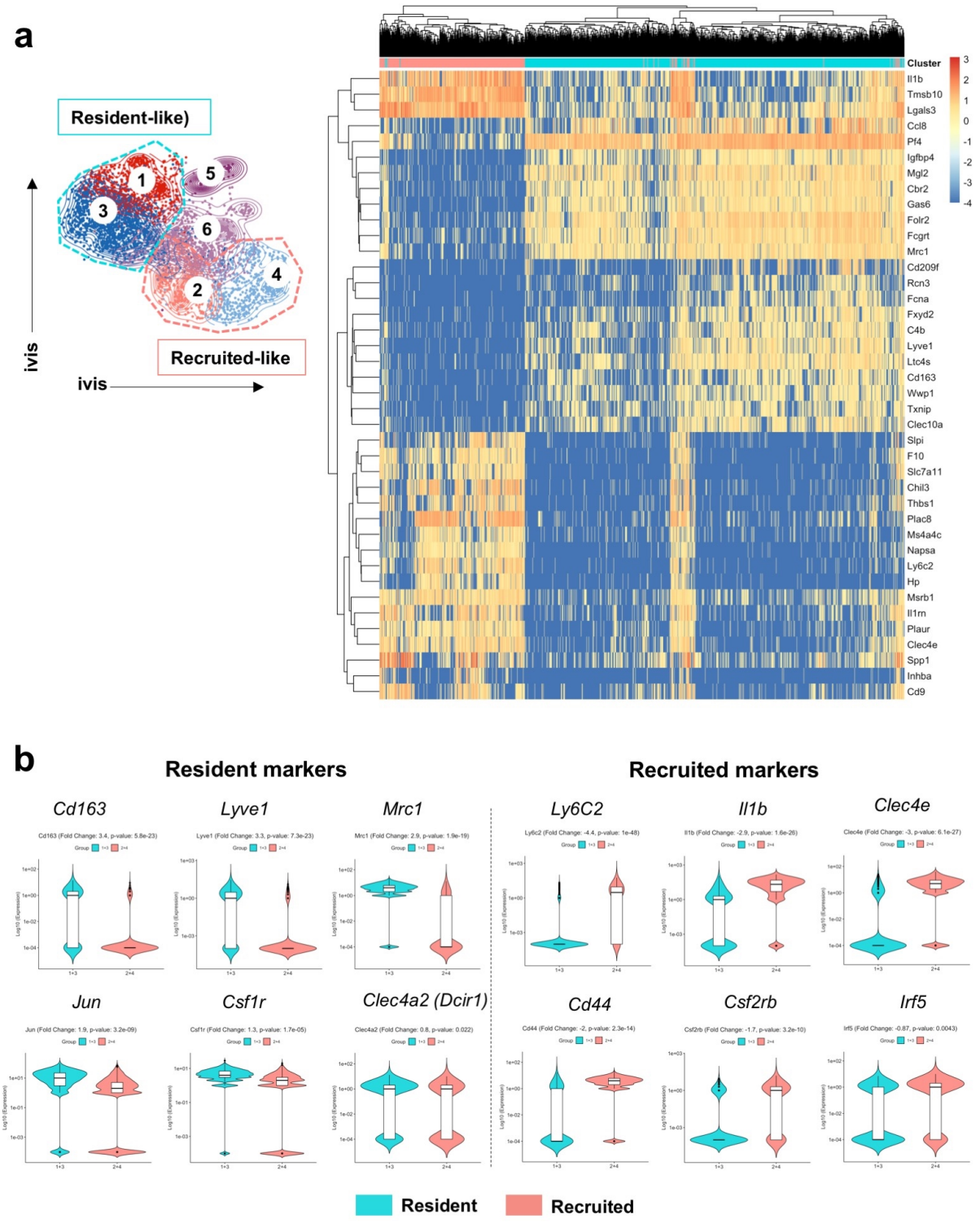


Figure 2.8 Comparative analysis of lesional and adventitial macrophages by single cell RNA sequencing and unbiased high-dimensional analysis ivis.

a) 4 clusters from Figure 2.7 are selected as bona fide macrophages and were grouped as resident-like (cluster 1+3) and recruited-phenotype (cluster 2+4). The heatmap of 2 groups is displayed by top 20 genes each. **b)** Selected violin plots of log-scale gene expression of 2 macrophage groups. The selected genes are statistically different.

2.5. Morphology of lesional and adventitial macrophages in the atherosclerotic aorta

To assess how lesional and adventitial macrophages differ in their morphology, macrophages from aortas of high fat fed-*ApoE*$^{-/-}$ mice were sorted as live CD45+ CD11b+ F4/80+ CD64+ and then further separated into CD11c+ or CD206+ subsets. Again, CD206+ macrophages were divided by their expression of MHCII. In addition to this, DCs (defined as live CD45+ CD11c+ MHCII+ CD64-) were also included to compare with macrophage subsets.

Overall, CD206+ macrophages lacking MHCII expression displayed a round shape while the majority of MHCII+ CD206+ macrophages develop dendrites (**Figure 2.9**). CD11c+ macrophages exhibited both foamy and non-foamy features. DCs presented extended dendrites, as a result of antigen presentation.

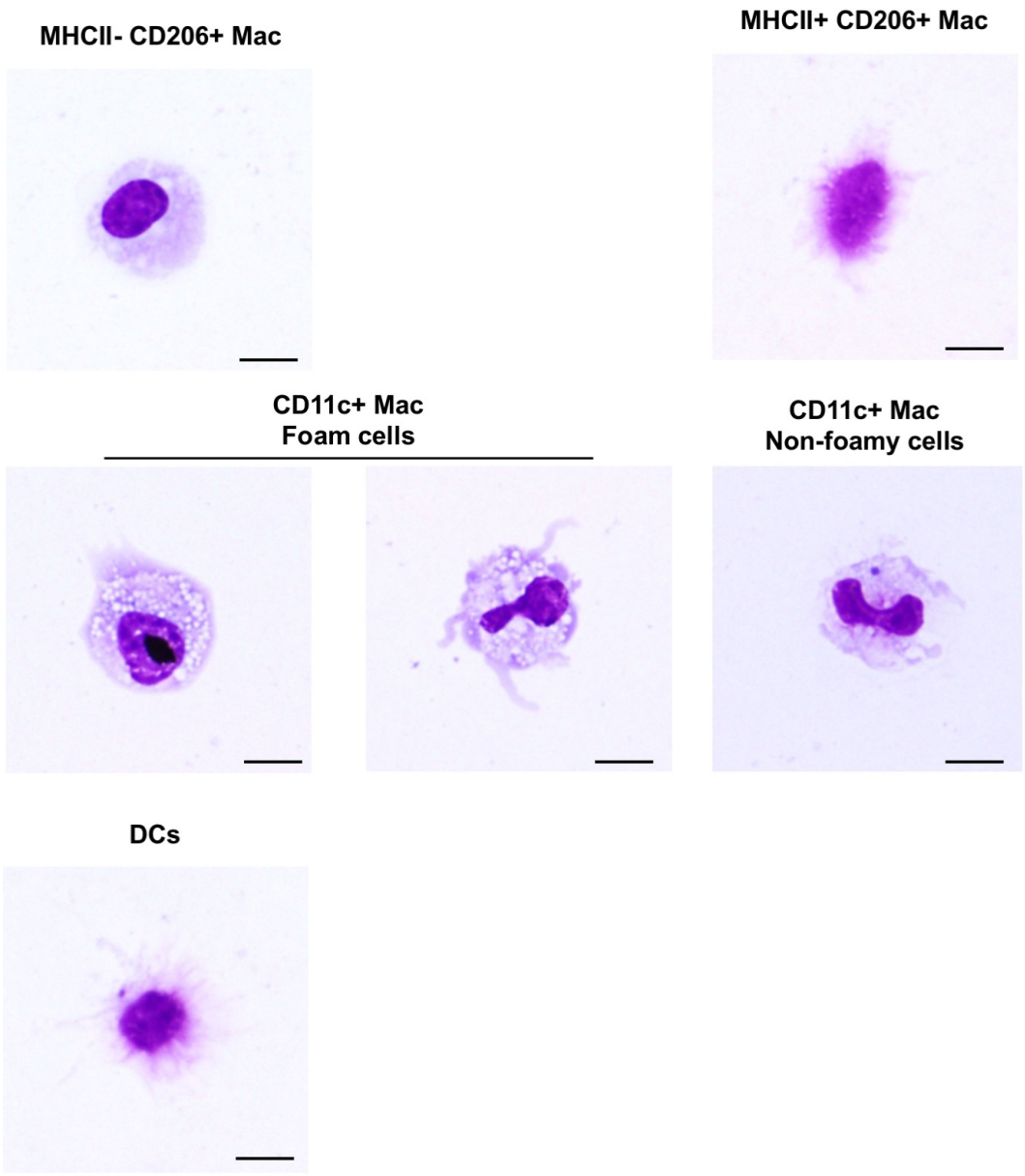


Figure 2.9 Photomicrography of macrophage subsets and dendritic cells (DCs) from the atherosclerotic aorta.

Aortic single cells from 9 *ApoE*$^{-/-}$ females fed on a HFD were FACS-sorted into four types: resident macrophages (live CD45+ CD11b+ F4/80+ CD64+ CD206+ MHCII- and live CD45+ CD11b+ F4/80+ CD64+ CD206+ MHCII+), recruited macrophages (live CD45+ CD11b+ F4/80+ CD64+ CD206- CD11c+) and DCs (live CD45+ CD64- CD11c+ MHCII+). Four cell types were stained with May-Grünwald Giemsa dye. Images were taken at X40 magnification. Scale bars denote 100 μm.

2.6. Discussion

In this chapter, I utilised mass cytometry and multi-dimensional analysis viSNE to compare the diversity of immune cells in the healthy and the atherosclerotic aorta. Single cell genomics were used for identification of macrophage subsets in the atherosclerotic aorta. The viSNE algorithm identified 16 broad leucocyte populations in the aorta. Arterial inflammation altered the immune cell landscape and high fat feeding accelerated the differences compared to the healthy aorta. The recruitment of monocyte subsets and the enrichment of CD11c+ “recruited” macrophage subsets were the most prominent feature of atherosclerosis. This trend is in line with the well-studied literature (Swirski et al., 2006, Kim et al., 2000, Rajavashisth et al., 1998, Lessner et al., 2002, Swirski et al., 2007). The representation of “resident” CD206+ macrophages declined during arterial inflammation. In contrast, a study by Winkels et al. showed using CyTOF that HFD feeding reduced monocytes in *ApoE*$^{-/-}$ mice (Winkels et al., 2018). The discrepancies might originate from the fact that the frequency and resolution of monocytes and macrophages in their study were very low relative to my data and others (Cochain et al., 2018, Kim et al., 2018).

The diversity of aortic macrophages during atherosclerosis was further analysed by both CyTOF and scRNAseq. The two techniques revealed both 4 main macrophage subsets comprising 2 “recruited” and 2 “resident” subpopulations. Recruited macrophages consist of CD11c+ CD44+ and CCR2+ subsets. CD11c+ macrophages can be further divided into 2 subpopulations based on MHCII expression. CD11c+ macrophages are thought to be inflammatory macrophages producing cytokines, handling lipid and mediating chemotaxis. My results showed two morphologically distinct subsets amongst CD11c+ macrophages. A very recent study also reported

that lesional macrophages express CD11c and are divided into two subsets comprising foam cells and non-foamy inflammatory macrophages (Kim et al., 2018). The CCR2+ “recruited” macrophages performed wound healing and reactive oxygen metabolism, demonstrating the presence of the reparative macrophage phenotype in the lesion. Fate mapping techniques or parabiosis experiments will be required to ascertain if recruited lesional macrophages originate from monocytes, and if so, which subsets of monocytes differentiate into this population.

The resident macrophage subset predominantly reside in the adventitia of the aorta. This population was divided into 2 subsets based on their function comprising CD206+ CD209b+ and CD206+ CD209b-. Although mass cytometry and scRNAseq did not provide two identical resident subsets, the GO analysis suggested that resident macrophages perform protein activation cascade, immune responses and complement activation and the other subset is associated with wound healing and oxygen metabolism. Macrophages induced by oxidised phospholipids (also known as Mox) are defined by the expression of HO1 (Kadl et al., 2010). CD206+ CD209b- resident macrophages expressed higher levels of *hmox1* compared to other 3 macrophage subsets, appointing that this subset could represent Mox. This macrophage subset might reside in the intima-media since HO1 expression was predominantly found in the lesion (Kadl et al., 2010). Furthermore, Rahman et al. also showed the presence of CD206+ macrophages in the regressive lesion, which may serve an anti-inflammatory role (Rahman et al., 2017).

Interestingly, my data corroborated the recent finding by Lim et al. that Lyve1 is broadly expressed by resident macrophages and that MCSF sustains adventitial resident

macrophages (Lim et al., 2018). In addition, my results also indicated that recruited macrophages may be driven by the granulocyte-macrophage colony-stimulating factor (GMCSF) pathway, by showing high levels of *Csf2rb* expression. GMCSF regulates expression of the pro-inflammatory transcription factor IRF5, which directly binds to the CD11c gene loci when stimulated by lipopolysaccharide (LPS) (Krausgruber et al., 2011, Seneviratne et al., 2017).

Cochain et al. recently described 3 different macrophage subsets including resident, recruited and TREM2^{high} macrophages in the murine aorta using scRNAseq. However, my data did not single out a macrophage subset expressing high levels of Trem2 (Cochain et al., 2018). This might be due to the fact that this subset may lack CD64 expression as cells expressing CD11b and CD64 were used for this analysis. However, this subset was later identified in Chapter 5.

Although the study of the separate layers of aortas by CyTOF provided an insight into the spatial-distribution of leucocytes, there were technical limitations. The procedure of separating aortic layers requires an additional digestion step with collagenase II and elastase, which may have caused cell loss. I observed that live CD45+ populations account for 7-17.6% of cells in the intima/media and 16.4-22.7% of cells in the adventitia. In general, the average percentage of leucocytes is 35-51% in atherosclerotic aortas. Despite the fact that the additional digestion step may have reduced the proportion of immune cells, macrophage populations were enriched within the live CD45+ cells. Finally, in two individual experiments performed comparing the intima-media versus adventitia, I was unable to detect the pDCs and B1 B population seen when whole aortas were examined.

In summary, in this chapter, I described 16 leucocyte populations in the murine atherosclerotic aorta using mass cytometry and demonstrated the dynamic change in the immune cell composition that occurs during development of atherosclerosis. I revealed the spatial distribution of recruited and resident macrophages in the aorta, and described distinct markers for each subset, by using immunofluorescence and mass cytometry. I showed that recruited macrophages are located in the intima and the media whilst resident macrophages predominantly reside in the adventitia. The data from mass cytometry and scRNAseq on macrophage subsets in this chapter complement the current understanding of the diverse phenotype of macrophages and their potential role in atherosclerosis.

CHAPTER 3. Investigation of human DCIR and murine DCIR1 expression in the immune system

3.1. Introduction

The immune system is a key host defence mechanism and comprises innate and adaptive immunity (Janeway, 1999). The innate immune response is mediated by cells of the myeloid lineage and innate lymphoid cells (ILCs) cells which perform the frontline defence against pathogens. The myeloid lineage, which can be subdivided by the morphology of their nucleus, includes polymorphonuclear cells (PMN) and mononuclear cells (MNC). Macrophages, a type of MNC, are highly versatile phagocytes that are distributed in most tissues throughout the body (Gordon and Pluddemann, 2017). Their major function is the maintenance of organ homeostasis in the host by phagocytosing apoptotic cells and debris, repairing the injured tissue and performing immune surveillance (Mantovani et al., 2013).

Studies on the phenotypic and functional states of macrophages under polarising conditions have shaped the current understanding of macrophage biology. However, the concept of M1-M2 dichotomy does not fully reflect the heterogeneity of macrophages *in vivo*, where their activated states rather resemble a continuous spectrum (Mosser and Edwards, 2008).

In tissues, macrophages sense endogenous and exogenous ligands through pattern recognition receptors (PRRs) and become adapted to the organ micro-environment. C type lectin receptors (CLR) are members of the pattern recognition receptor (PRR) family and are predominantly expressed by myeloid populations (Sancho and Reis e Sousa, 2012). The CLR family carry one or multiple carbohydrate recognition domains (CRDs) which recognise ligands derived from self and pathogens, dependent or independent of Ca^{2+} influx (Hoving et al., 2014).

Dendritic cell immunoreceptor (DCIR; also known as *clec4a*) is a rare type of the CLR family member, which signals through an ITIM in the cytoplasmic domain (Bates et al., 1999). The phosphorylated ITIM recruits Src homology region 2 domain-containing phosphatase (SHP)-1 and SHP2. Human DCIR recognises glycoprotein of human immunodeficiency virus (HIV) 1, which is utilised by the virus to attach to DCs (Lambert et al., 2008). Bloem et al. identified that DCIR strongly binds to gp140 of HIV-1 and the endogenous ligand sulfo-Lewis^a extracted from keratinocytes (Bloem et al., 2014).

The roles of DCIR in DCs include endocytosis, antigen presentation and control of TLR-mediated cytokine production (Meyer-Wentrup et al., 2008, Meyer-Wentrup et al., 2009, Massoud et al., 2014). In human macrophages, DCIR is upregulated by Th2 cytokines, indicating its regulatory role (Krausgruber et al., 2011). However, its expression pattern and function in macrophages remain in question. The first aim of this chapter is to investigate the expression profile of human DCIR and murine DCIR isoforms in differentially activated macrophages using gene expression and protein assays. I also sought to assess if *Dcir1* deficiency affects macrophage functions *in vitro*. This chapter also aims to determine the expression of DCIR1 in leucocyte populations from murine tissues including aortas, hearts, lungs and bone marrow (BM) by utilising flow cytometry. Finally, I provide preliminary evidence that potential endogenous ligands for DCIR1 may be present in the aorta, heart and lung.

3.2. Investigation of human DCIR and murine DCIR1 expression in *in vitro* macrophages

3.2.1. Murine macrophage activation and *Dcir* isoforms

3.2.1.1. Inflammatory stimuli reduce the expression of *Dcir1* in murine macrophages

First, I sought to determine how the expression of *Dcir1* is regulated in murine macrophages. Murine BM cells were cultured with granulocyte-macrophage colony-stimulating factor (GMCSF) or macrophage colony-stimulating factor (MCSF) and were then further activated by treatment with LPS+ IFNγ or IL-4+IL-13 for 18 hours. The gene expression profile of *Dcir1* was determined by quantitative real time-polymerase chain reaction (qRT-PCR) (**Figure 3.1a**). *Dcir1* expression was higher in GMCSF-macrophages than in their MCSF-cultured counterparts (M (GMCSF) vs. M (MCSF) $p=0.0004$) (**Figure 3.1b**). In both cases, treatment with LPS+ IFNγ significantly inhibited the expression of *Dcir1* (M (GMCSF) vs. M (LPS+ IFNγ) $p=0.0238$; M (MCSF) vs. M (LPS+ IFNγ) $p<0.0001$) (**Figure 3.1b**). *Dcir1* expression was not increased in alternatively activated macrophages in the GMCSF group, however, there was a slight but statistically significant increase in the expression level of *Dcir1* in MCSF-derived macrophages treated with IL-4+IL-13 (M (MCSF) vs. M (IL-4+IL-13) $p<0.0229$).

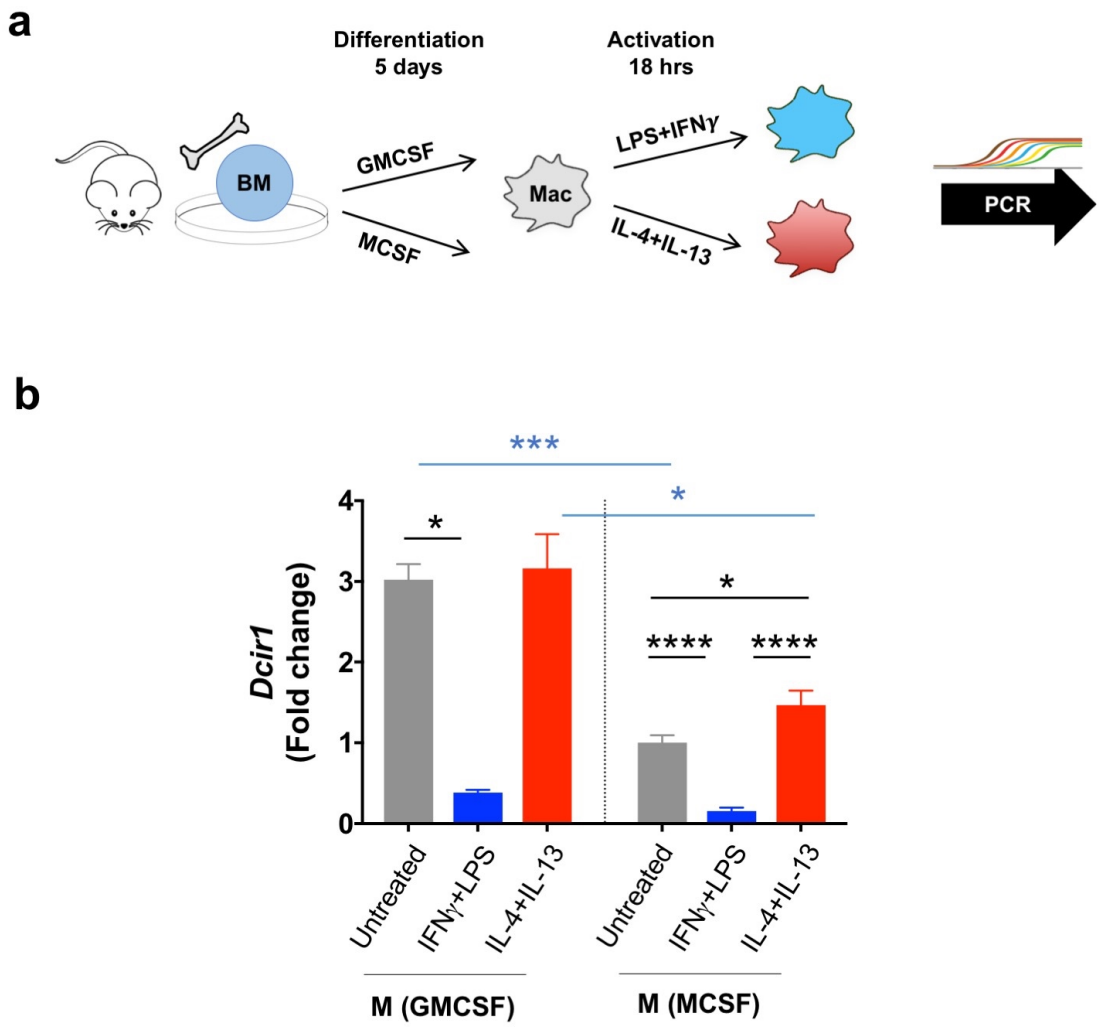


Figure 3.1 The differential expression of *Dcir1* in murine bone marrow-derived macrophages.

a) Bone marrow cells were cultured with GMCSF or MCSF for 5 days to allow their differentiation into macrophages. The macrophages were then primed with LPS+IFNγ or IL-4+IL-13 for a further 18 hours. qRT-PCR was performed on these cells to measure the expression of *Dcir1*. **b)** Graphs display gene expression levels of *Dcir1* relative to the housekeeping gene *18S rRNA*. Values are normalised against M (MCSF). Data are presented as mean±SEM. M (GMCSF) n=3 or M (MCSF) n=9, Mann-Whitney test. *P<0.05, ***P<0.001, ****P<0.0001.

3.2.1.2. *Dcir* isoforms and *Dcar2* in murine macrophages

qRT-PCR was used to determine the expression of other *Dcir* isoforms and its putative partner *Dcar2* in differentially activated macrophages. Notably, gene expression of *Dcir2* and *Dcar2* was not detected in any macrophage types (**Figure 3.2**). The expression of *Dcir3* was generally higher than *Dcir1* and *Dcir4* in all macrophage types. Its expression decreased upon stimulation with LPS+ IFNγ and increased following IL-4+IL-13 treatment. In terms of its gene expression pattern, *Dcir3* was similar to *Dcir1*, despite the fact that it lacks the ITIM motif. The expression level of *Dcir4* did not change with treatment in the GMCSF-cultured macrophages, however, it was attenuated in both M (LPS+ IFNγ) and M (IL-4+IL-13). Taken together, *in vitro* macrophages expressed *Dcir1*, *Dcir3* and *Dcir4* and the expression of *Dcir1* and *Dcir3* is down-regulated by inflammatory stimuli.

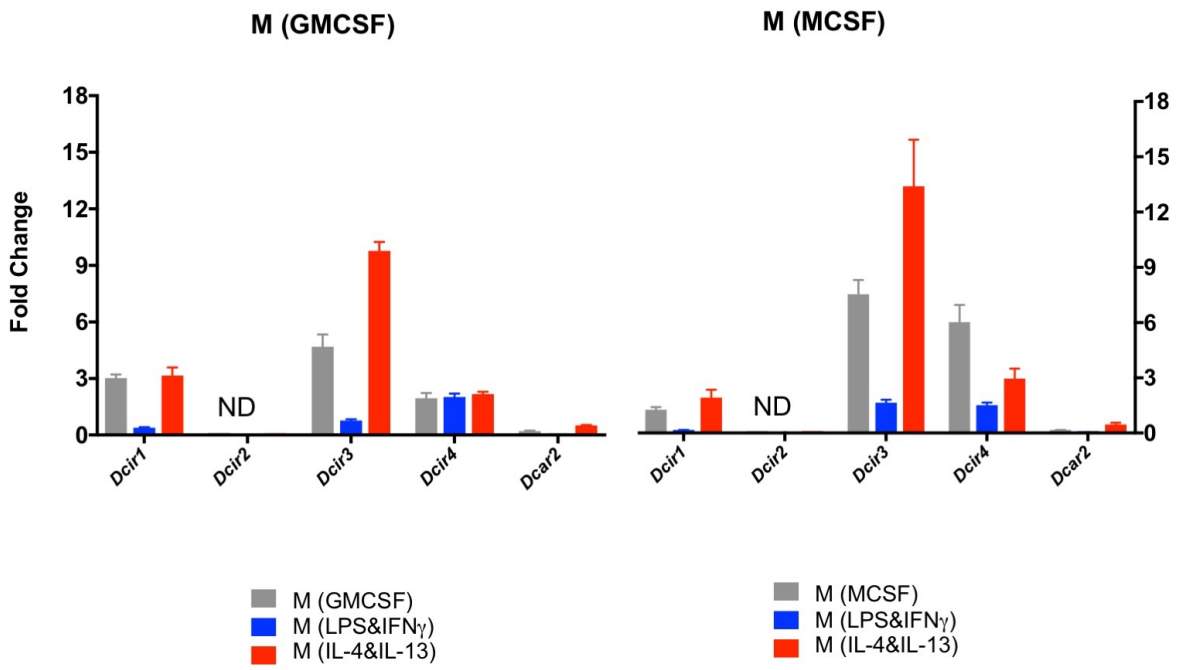


Figure 3.2 The expression pattern of *Dcir* isoforms and *Dcar2* in macrophages.

Bone marrow cells were cultured with GMCSF or MCSF for 5 days to allow their differentiation into macrophages. The macrophages were then primed with LPS+IFNγ or IL-4+IL-13 for a further 18 hours. qRT-PCR was performed on these cells to measure the gene expression of 4 *Dcir* isoforms *and Dcar2*. The graphs present the gene expression levels relative to the housekeeping gene *18S rRNA* in three differentially activated macrophage types. Values are normalised against *Dcir1* gene expression of M (MCSF). Data are presented as mean±SEM. n= 3 each group. Mann-Whitney test. ND stands for not detected.

3.2.2. Human monocyte-derived macrophage subsets differentially express DCIR

To determine the levels of *Dcir* mRNA and DCIR protein in human macrophages, monocytes were isolated from the blood by the density-based centrifugal elutriation method and were cultured with GMCSF or MCSF for 5 days (**Figure 3.3a**). MCSF-cultured macrophages were then further activated with various stimuli including cytokines (IFNγ, LPS+ IFNγ, IL-4+IL-13, IL-10 and CXCL4) and TLR ligands (FSL-1 for TLR2, poly I:C high molecular weight for TLR3, LPS for TLR4 and CpG ODN for TLR9) for 18 hours. Cells from different conditions were divided and were analysed by qRT-PCR and flow cytometry. The data are the representation of 2 independent experiments.

Dcir gene expression was higher in GMCSF (both in DC (GMCSF) and M (GMCSF)) and M (IL-4+IL-13) than in M (MCSF) (**Figure 3.3b**). Notably, IFNγ and LPS inhibited the gene expression levels of *Dcir* in MCSF-cultured macrophages and the combined treatment synergistically reduced *Dcir* expression. Treatment with the anti-inflammatory cytokine IL-10 or platelet factor 4 CXCL4, known to differentiate macrophages into a distinct phenotype, did not alter *Dcir* expression, nor did ligands for TLR2, TLR3 and TLR9.

A similar pattern was also seen in the protein level of DCIR (**Figure 3.3c**). Treating MCSF-cultured macrophages with IL-4+IL-13 induced remarkably high levels of DCIR protein expression whilst LPS+IFNγ treatment reduced DCIR levels. In other conditions, including stimulation with TLR ligands, there were no apparent differences in the MFI of DCIR.

In order to confirm if macrophages exhibit a pro-inflammatory or anti-inflammatory phenotype, I concomitantly measured expression levels of CD40 (an inflammatory marker) and CD163 (a marker for alternatively activated macrophages) in these cell types. Graphs in **Figure 3.3d** and **3.3e** demonstrated that high expression levels of CD40 were detected in GMCSF-cultured DC and macrophages as well as MCSF-cultured macrophages that were treated with IFNγ, LPS or their combination. Conversely, MCSF-cultured cells expressed higher levels of CD163 than GMCSF-treated cells, and inflammatory stimuli (IFNγ, LPS or both) decreased its expression.

In summary, human DCIR was expressed in both GMCSF- and MCSF-cultured macrophages and its expression was inhibited by pro-inflammatory conditions whilst IL-4+IL-13 treatment up-regulated DCIR expression.

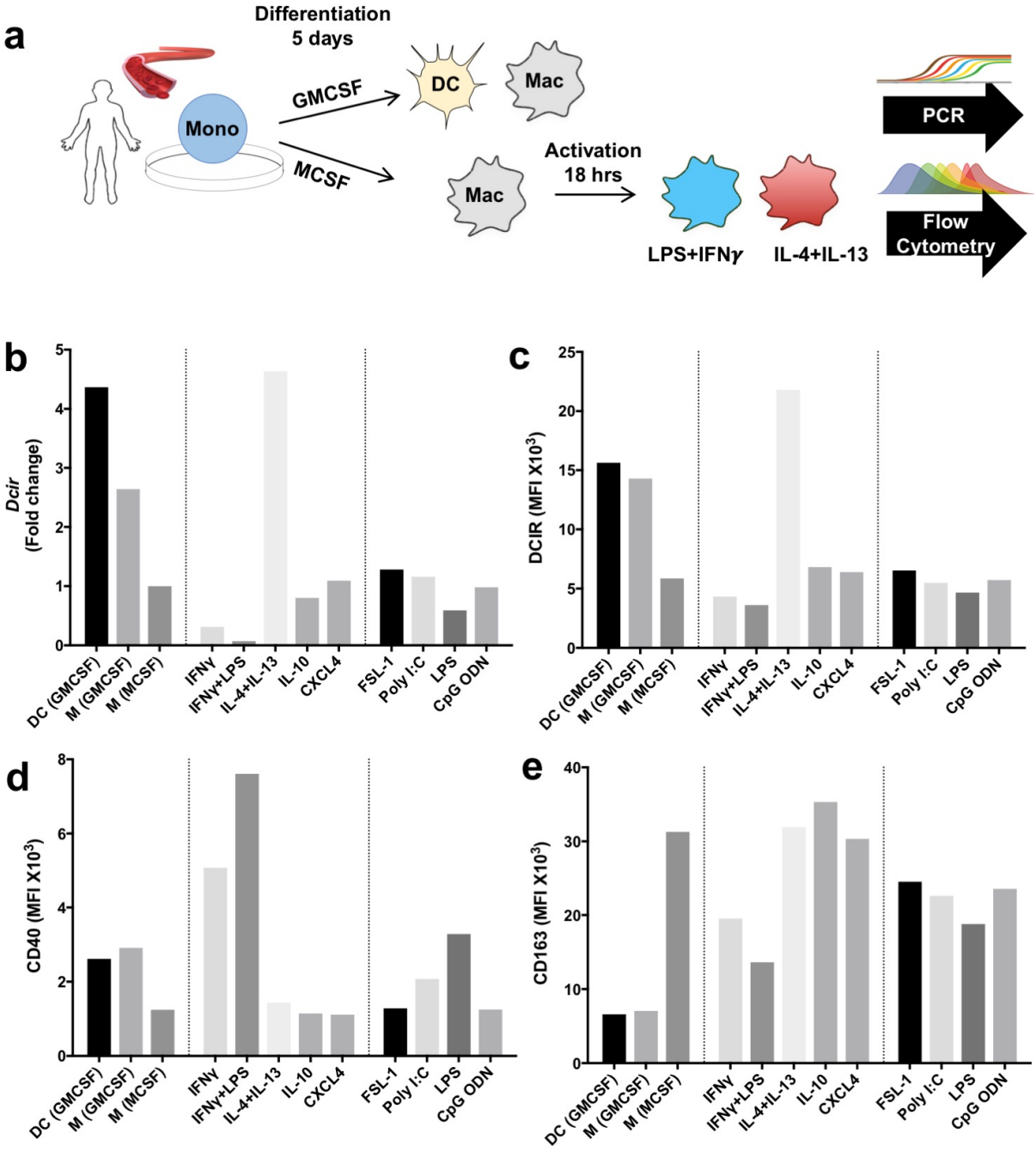


Figure 3.3 The differential expression of DCIR in human macrophages.

a) Monocytes from human blood were cultured with GMCSF or MCSF for 5 days to allow their differentiation into macrophages. In the GMCSF-treated cells, adherent cells were considered as macrophages and the suspension cells were referred as to DC. Adherent MCSF-derived macrophages were primed with cytokines or Toll-like receptor (TLR) ligands for a further 18 hours. Gene expression of *Dcir* was determined by using qRT-PCR and cell surface expression of DCIR, CD40 and CD163 was measured by using flow cytometry. Graphs display **b)** *Dcir* gene expression relative to the housekeeping gene*18S rRNA*. Values are normalised against M (MCSF). **c)** mean fluorescence intensity (MFI) of DCIR. **d)** The MFI of CD40. **e)** The MFI of CD163. This is a representation of 2 independent experiments.

3.3. DCIR1 maintains tissue macrophage marker CD206 in bone marrow-derived macrophages

To investigate how *Dcir1* deficiency contributes to the differentiation of the BM cells, I used BM-derived macrophages (BMDM) using WT and *Dcir1*$^{-/-}$ mice. The BM cells were cultured with either GMCSF or MCSF for 6 days or 10 days and the phenotype of cells was analysed by flow cytometry with myeloid markers. I compared the phenotype of these macrophages from WT and KO mice and found that there were no significant differences in cellular composition or cell numbers (**Table 3.1**). However, tissue resident marker CD206 expression was declined in the MCSF macrophages of the KO relative to the WT at Day 6 and Day 10 (**Figure 3.4**). When macrophages were cultured with MCSF for 10 days, CD206 expression was significantly diminished, showing 83±3% in the WT and 69±4% in the KO ($P<0.05$). Given that CD206 is a marker for tissue resident and alternatively activated macrophages, I additionally tested if DCIR1 regulates macrophage polarisation in the BMDM. Surprisingly, *Dcir1* deficiency did not alter in percentages of polarised macrophages M1 and M2 in response to LPS&IFNγ and IL-4&IL-13 (**Table 3.2**). However, CD206 expression was consistently lower in M1 and M2 macrophages of the KO mice compared to the WT.

To identify if DCIR1 regulates phagocytic activity in BMDM, I also performed assays for phagocytosis using fluorescent latex microsphere beads. No significant differences in phagocytic capacity were observed in the *Dcir1*$^{-/-}$ mice (**Table 3.3**). Fujikado et al. reported that DCIR1 delayed phosphorylation of signal transducer and activator of transcription (STAT) 5 in BM-derived DCs in response to GMCSF (Fujikado et al., 2008). However, *Dcir1* deficiency had no impact on activation of STAT5 and STAT6 in GMCSF- and MCSF-cultured macrophages (**Table 3.4**). Additionally, I also tested

whether DCIR1 regulates cytokine production in BMDM in response to TLR activation. Macrophages lacking DCIR1 produced higher pro-inflammatory cytokine IL-6 upon TLR9 activation while *Dcir1* deficiency did not affect the production of IL-10 in GMCSF- and MCSF- cultured BMDM upon stimulation with TLR 2,3,4,7/8,9 ligands, LPS+IFNγ or IL-4+IL-13 (**Table 3.5**).

Collectively, *Dcir1* deficiency impaired the maintenance of the tissue resident marker CD206 in MCSF-cultured BMDM, although it did not affect phagocytosis, phosphorylation of STAT5 and STAT6. The data also suggested the potential interaction between DCIR1 with TLR9 in macrophages.

	Population	WT	KO	P value
Day 6	DC (GMCSF)	5.8±0.8	7.5±0.5	0.6733
	M (GMCSF)	17.4±1.1	20.0±1.6	0.7485
Day 10	DC (GMCSF)	48.8±1.5	47.5±2.7	0.9655
	M (GMCSF)	17.9±1.3	17.7±1.3	0.9882
Day 6	M (MCSF)	96.4±0.3	96.4±0.3	0.9795
Day 10	M (MCSF)	97.0±0.6	96.9±1.1	0.9882

Table 3.1 The percentage of cell population in bone marrow-derived myeloid cells.

Percentages are calculated per live cells. Day 6 n=3, Day 10 n=5. Mann-Whitney test.

	Population	WT	KO	P value
M (MCSF)	CD11b+ F4/80+	96.4±0.3	96.4±0.3	>0.9999
	CD11b+ F4/80+ CD206+	83.6±0.4	73.6±4.4	0.1000
M (LPS+IFNγ)	CD11b+ F4/80+	88.0±0.9	92.0±1.0	0.1000
	CD11b+ F4/80+ CD206+	73.3±0.6	66.9±4.2	0.4000
M (IL-4+IL-13)	CD11b+ F4/80+	96.2±0.3	95.5±0.2	0.2000
	CD11b+ F4/80+ CD206+	84.2±0.4	76.0±1.3	0.1000

Table 3.2 The percentage of cell population in polarised bone marrow-derived macrophages.

Percentages are calculated per live cells. n=3. Mann-Whitney test.

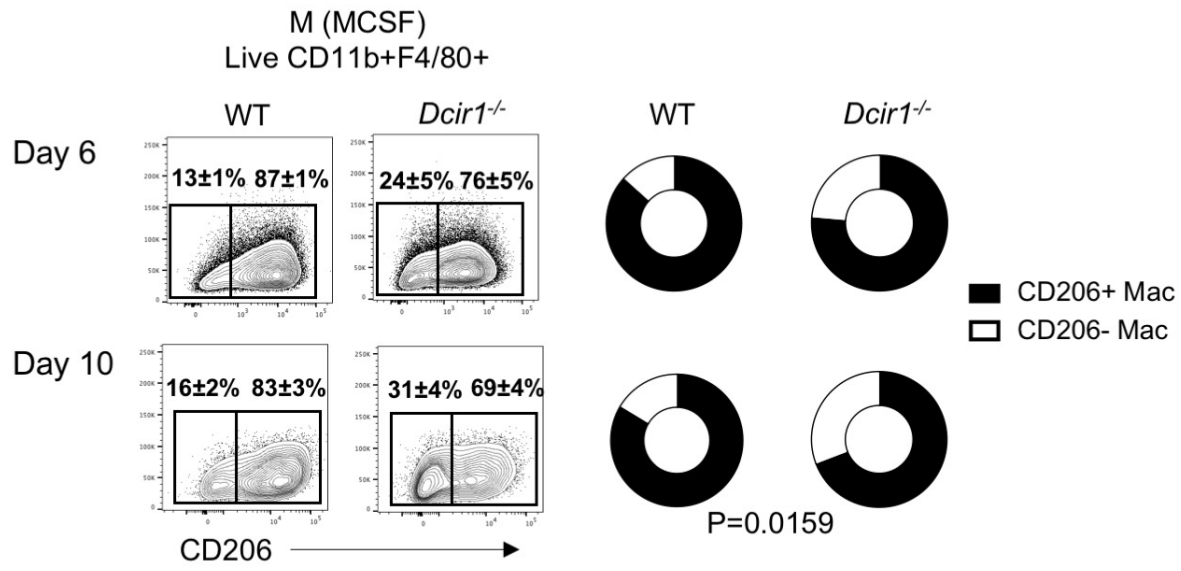


Figure 3.4 The phenotype of bone marrow-derived macrophages cultured with MCSF in wild type and *Dcir1*$^{-/-}$ mice.

The bone marrow of wild type (WT) and *Dcir1*$^{-/-}$ mice was cultured with MCSF for 6 days or 10 days. Cells were then analysed by flow cytometry. The live CD11b+ F4/80+ population is displayed in contour plots by the expression of CD206. The average percentage of CD206+ and CD206- macrophages is presented in doughnut charts by genotype. Day 6: n=3. Day 10: n=5. Mann-Whitney test.

		WT	KO	P value
Phagocytosis	M (GMCSF)	8.7±1.8	7.0±0.6	0.8413
	M (MCSF)	12.0±1.6	11.2±1.7	0.6905

Table 3.3 The effect of *Dcir1* deficiency on phagocytic activity of bone marrow-derived macrophages.

The data are presented as percentages in live macrophages and mean±SEM. n=5. Mann-Whitney test.

		WT	KO	P value
pSTAT5	M (GMCSF)	46.0±2.5	49.3±4.2	0.5476
	M (MCSF)	35.9±1.9	39.9±3.1	0.4206
pSTAT6	M (GMCSF)	60.3±2.2	62.5±4.7	0.4206
	M (MCSF)	36.3±2.5	33.7±3.5	>0.9999

Table 3.4 The effect of *Dcir1* deficiency on the phosphorylation of STAT5 and STAT6 of bone marrow-derived macrophages.

The data are presented as percentages in live macrophages and mean±SEM. n=5. Mann-Whitney test.

IL-6 (pg/ml)	WT	KO	P value	WT	KO	P value
Stimuli	**M (GMCSF)**			**M (MCSF)**		
FSL-1	43709±15202	45246±17760	n.s.	39617±13115	36035±10644	n.s.
Poly I:C HMW	142±24	532±370	n.s.	1777±178	2219±226	n.s.
LPS	81020±11199	87510±13047	n.s.	5742±982	6629±1082	n.s.
R848	110796±19829	87510±13047	n.s.	31771±7883	31729±7476	n.s.
CpG ODN	428±317	1381±1210	n.s.	**128±34**	**339±13**	**0.0364**
IFNɣ + LPS	73781±16927	75782±11501	n.s.	5125±781	5505±673	n.s.
IL-4+ IL-13	327±12	3671±3409	n.s.	181±49	193±18	n.s.

IL-10 (%)	WT	KO	P value	WT	KO	P value
Stimuli	**M (GMCSF)**			**M (MCSF)**		
FSL-1	443±37	343±37	n.s.	251±28	211±23	n.s.
Poly I:C HMW	101±1	105±3	n.s.	243±27	240±31	n.s.
LPS	392±42	349±46	n.s.	724±109	626±89	n.s.
R848	718±103	560±82	n.s.	452±68	387±46	n.s.
CpG ODN	113±7	125±10	n.s.	103±1	109±4	n.s.
IFNɣ + LPS	350±20	321±26	n.s.	558±80	451±68	n.s.
IL-4+ IL-13	106±5	130±22	n.s.	103±5	114±8	n.s.

Table 3.5 The effect of *Dcir1* deficiency on the production of IL-6 and IL-10 in bone marrow-derived macrophages.

The data are presented as mean±SEM. n=3 each. Multiple t test.

3.4. Studies on the expression of human DCIR and murine DCIR1 in the immune system

3.4.1. Human DCIR is expressed by monocytes and neutrophils in the blood

To determine the cell surface expression of DCIR, I performed flow cytometry on human peripheral blood cells using an anti-human DCIR antibody. Four populations of cells were separated based on their granularity and size, together with surface marker expression (**Figure 3.5**). Cells lacking CD45 expression were thought to include platelets and erythrocytes, which lacked DCIR expression as shown in a histogram plot. Lymphocytes, which expressed CD45 and were smaller in size, were gated as CD45+ SSC^{low} and showed no expression of DCIR. On the other hand, monocytes gated as CD45+ $SSC^{intermediate}$ expressed high levels of DCIR as did CD45+ SSC^{high} CD15+ CD16+ neutrophils.

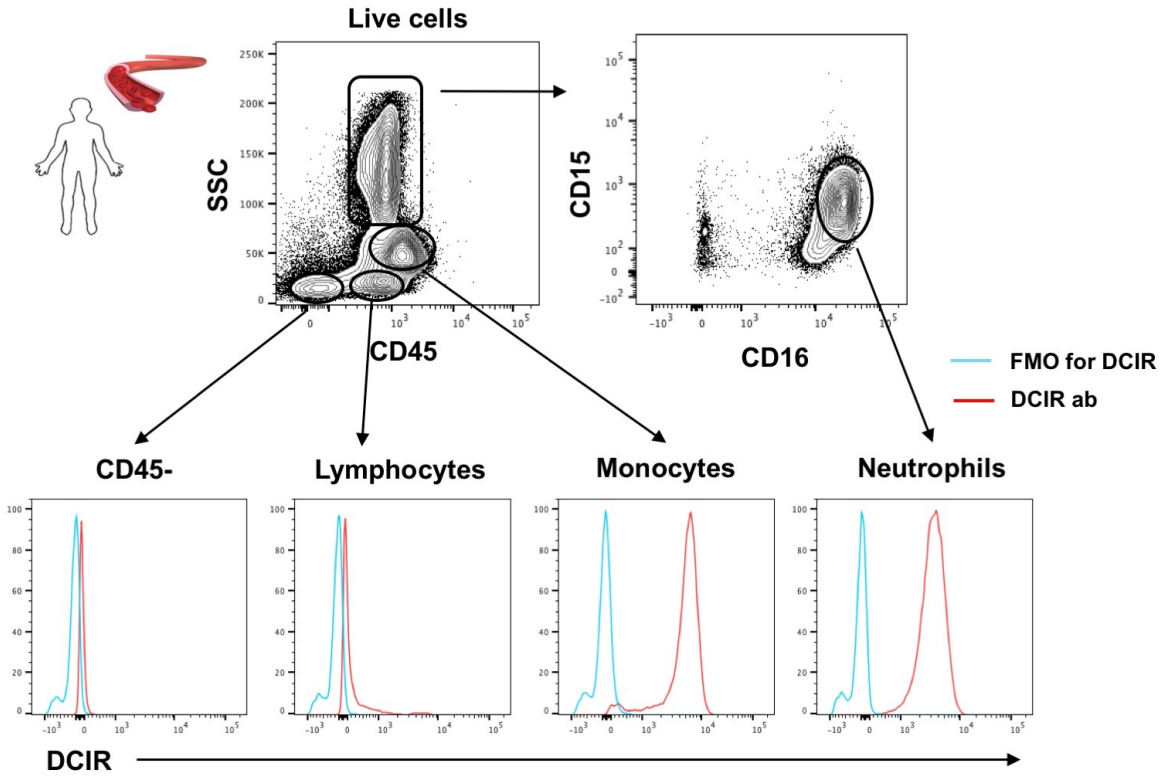


Figure 3.5 The cell surface expression of DCIR in non-leucocytes, lymphocytes, monocytes and neutrophils from human blood.

The expression of DCIR in leucocytes from human blood was measured by flow cytometry. Four cell populations were approximately gated based on their granularity (side scatter; SSC) and the marker expression. The mean fluorescence intensity (MFI) of DCIR in four cell populations is displayed in histogram plots. FMO stands for fluorescence minus one control, in this experiment, FMO includes all markers except DCIR antibody. n=2.

3.4.2. Tissue resident macrophages and DCIR1 expression

Kishimoto et al. originally found that DCIR1 expression was remarkably high in neutrophils, monocytes and eosinophils in the BM, blood and spleen (Kishimoto et al., 2015). In addition, the Immunological Genome project (ImmGen) database also suggested that *Dcir1* expression in BM neutrophils was strikingly higher than in other myeloid populations in the immune system, despite the fact that the dataset on tissue macrophages in various organs was largely unknown.

Having shown that *Dcir1* was present in BMDM, I investigated whether DCIR1 protein can be also detected in macrophages that reside in murine tissues. Single cells from the aorta, heart, lungs and BM were retrieved from mice in the steady state and were analysed by flow cytometry. All leucocyte populations were gated on live CD45+ cells. In aortas, DCIR1 was widely expressed by myeloid cells comprising macrophages, type 2 cDCs (cDC2), neutrophils and Ly6C+ monocytes. In contrast, lymphocytes (T cells and B cells) lacked DCIR1 expression (**Figure 3.6a**). A similar observation was also found in cardiac leucocytes, showing that myeloid cells expressed DCIR1 whereas its expression was not found in lymphocytes (**Figure 3.6b**). In both aortas and the heart, macrophages and cDC2 displayed the highest levels of DCIR1 expression and neutrophils and monocytes expressed lower levels compared to the other myeloid counterparts.

Healthy lungs harbour a number of leucocytes that can be identified using 11 surface markers (**Figure 3.7a**). Two types of macrophages in the lung are named after their location; alveolar macrophages (AM) originate from foetal monocytes and self-renew in the alveoli while monocytes continuously replenish macrophages in the interstitial

space of the lungs (Lehnert et al., 1985, Guilliams et al., 2013). High levels of DCIR1 expression were found in these two macrophage populations, cDC2, neutrophils, Ly6C+ monocytes and eosinophils. cDC1, and Ly6C- monocytes moderately expressed DCIR1 (**Figure 3.7a**).

I also confirmed that BM neutrophils expressed high levels of DCIR1 and monocytes also expressed DCIR1 (**Figure 3.7b**). Collectively, it is consistent that DCIR1 is exclusively expressed by myeloid cell populations in the aorta, heart, lungs and BM.

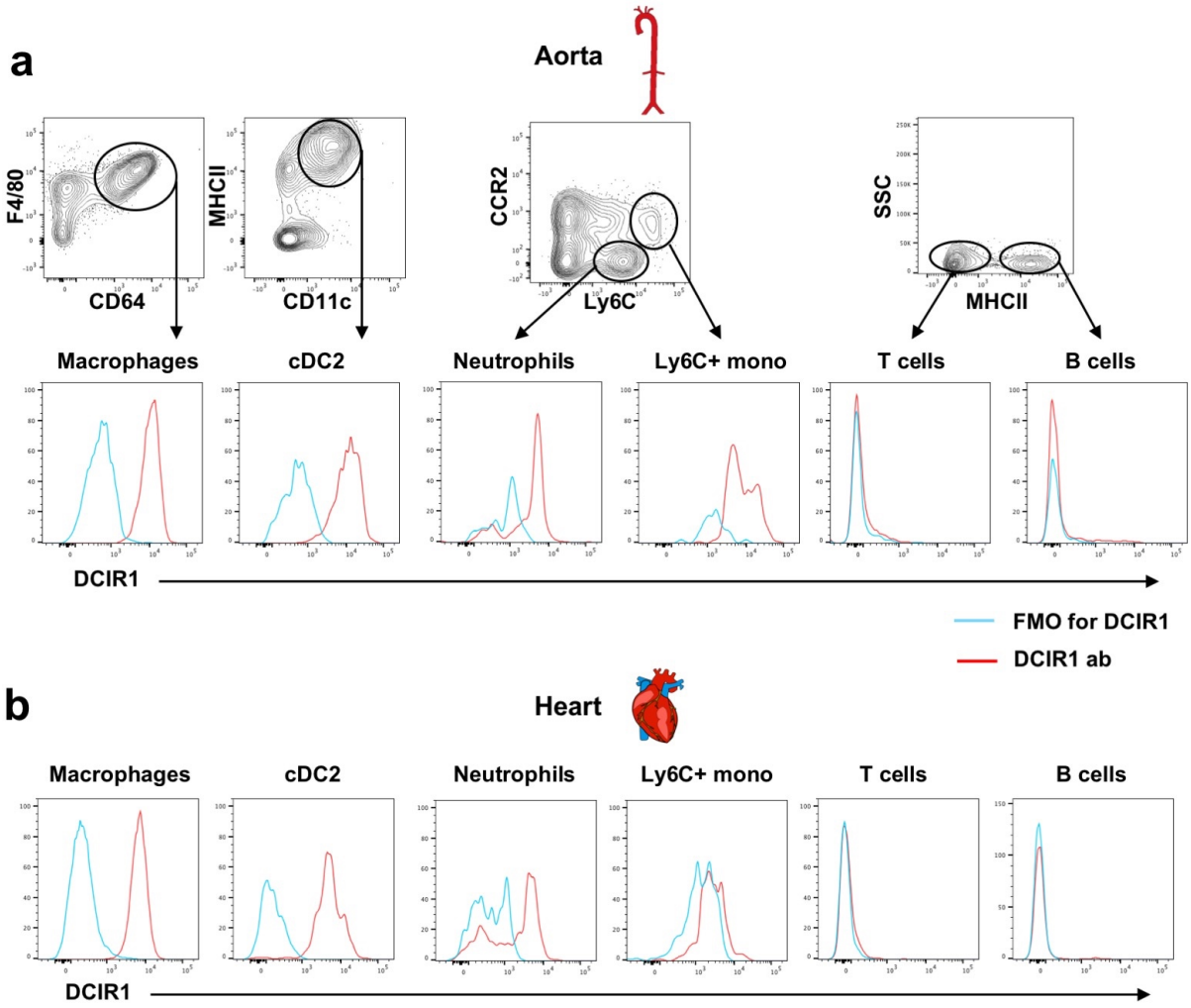


Figure 3.6 The cell surface expression of DCIR1 in leucocyte populations in the aorta and heart.

Single cells from the aorta and the heart of wild type mice were analysed by flow cytometry. For further details of gating strategy, see Appendix 1 Figure 8.1. An antibody against murine DCIR1 (TKKT clone) was utilised to measure DCIR1 expression. The MFI of DCIR1 in macrophages, cDC2, neutrophils, Ly6C+ monocytes, T cells and B cells is displayed in a histogram plot **a)** in the aorta and **b)** in the heart. n=3.

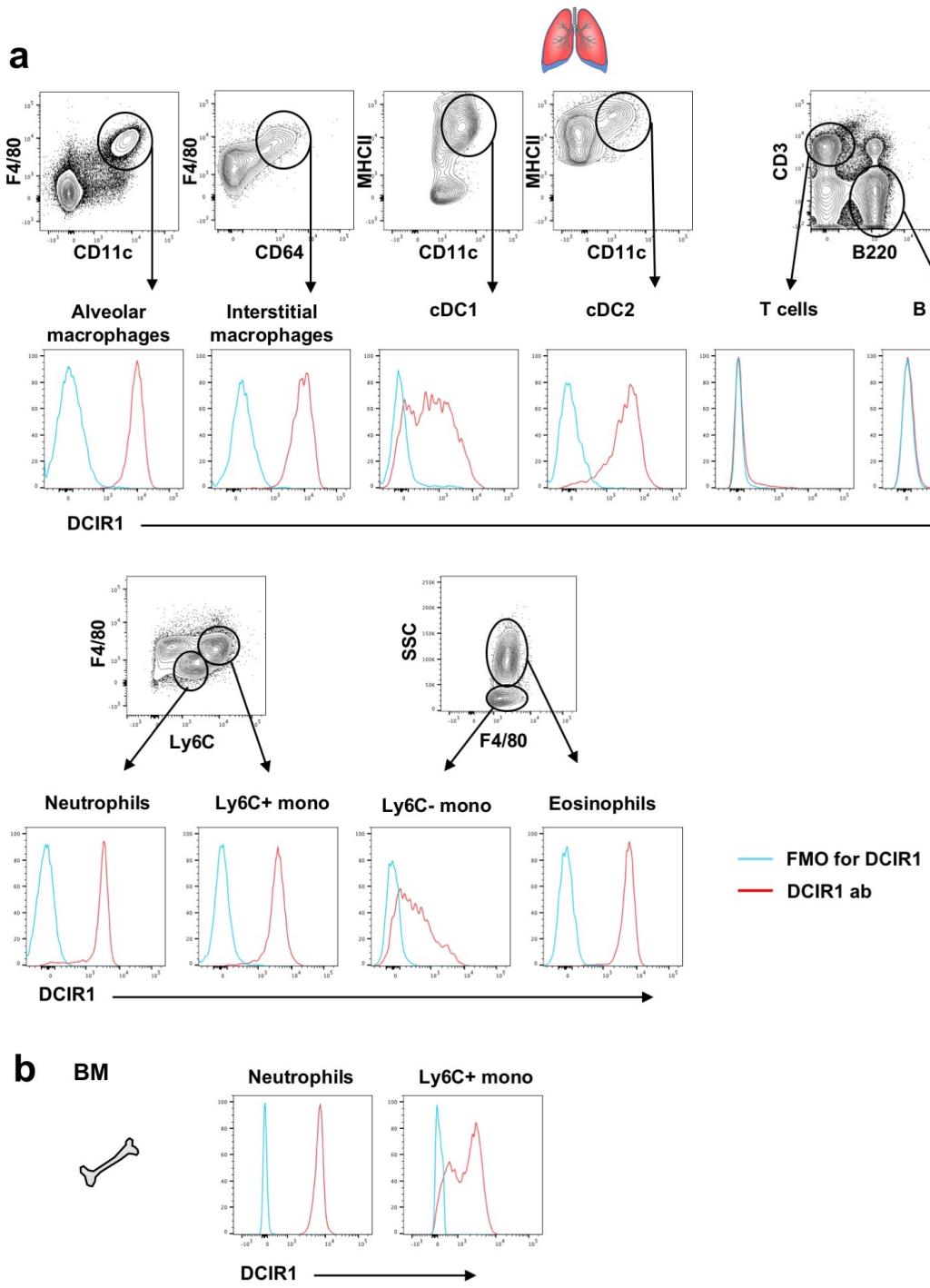


Figure 3.7 The cell surface expression of DCIR1 in leucocyte populations in the lung and the BM.

Single cells from the lung and the BM of wild type mice were analysed by flow cytometry. For further details of gating strategy, see Appendix 1 Figure 8.3 and 8.4. **a)** The mean fluorescence intensity (MFI) of DCIR1 in alveolar macrophages, interstitial macrophages, cDC1, cDC2, T cells, B cells, neutrophils, Ly6C+ monocytes, Ly6C- and eosinophils is displayed in a histogram plot. **b)** The MFI in neutrophils and Ly6C+ monocytes from the BM. n=3.

3.4.3. Macrophages express high levels of *Dcir1* in the aorta and the lung

Although the protein level of DCIR1 can be measured using an antibody, autofluorescence in tissue-derived macrophages can interfere with the accurate measurement of protein levels using fluorescence-mediated methods. Thus, I utilised fluorescence-activated cell sorting (FACS) to separate populations and gene expression of *Dcir1* was then determined on macrophages and DCs from the aorta and on alveolar macrophages, interstitial macrophages, Ly6C+ monocytes and DCs from the lung. In aortas, macrophages were selected as live CD45+ CD11b+ F4/80+ CD64+ and DCs were defined by the positive expression of CD45 CD11c MHCII and lack of F4/80 and CD64 expression. Four populations of cells from the lung were sorted as follows: AM: live CD45+ CD11c+ F4/80+ CD64+ CD11b-, interstitial macrophages (IM): live CD45+ CD11b+ F4/80+ CD64+ MHCII+ CD11c-, Ly6C+ monocytes: live CD45+ CD11b+ Ly6C+ CD64-, DC: CD45+ CD11c+ MHCII+ F4/80- CD64-.

The gene expression of *Dcir1* in both aorta and lung was remarkably higher in aortic macrophages and AM compared to other populations in their myeloid family (**Figure 3.8**). This suggested that DCIR1 was widely expressed on the surface of myeloid populations but the gene expression of *Dcir1* was highly up-regulated in macrophages from the aorta and the lung. The results may indicate that *Dcir1* expression was sustained in macrophages, presumably through crosstalk with the tissue micro-environment.

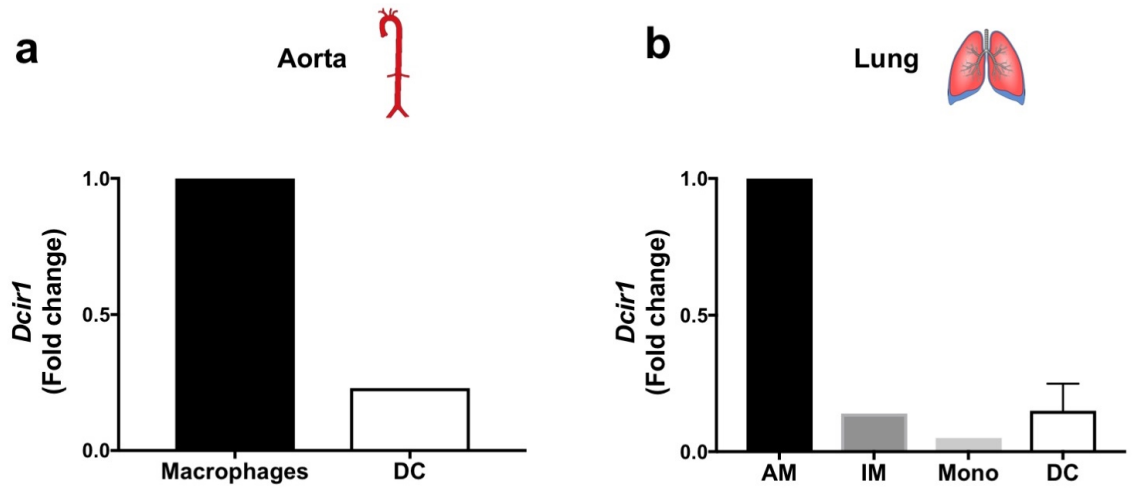


Figure 3.8 The relative gene expression of *Dcir1* in macrophages, dendritic cells and monocytes in the aorta and the lung.

Myeloid popualtions from the aorta and the lung of wild type mice were sorted based on the fluorescence-activated cell sorting method. *Dcir1* expression of each cell population was measured by using qRT-PCR. The expression is relative to the housekeeping gene *18S rRNA*. **a)** *Dcir1* expression levels in macrophages (CD45+ CD11b+ F4/80+ CD64+) and DCs (CD45+ CD11c+ MHCII+ F4/80- CD64-) in aortas. **b)** *Dcir1* expression in alveolar macrophages (AM; CD45+ CD11c+ F4/80+ CD64+ CD11b-), interstitial macrophages (IM; CD45+ CD11b+ F4/80+ CD64+ MHCII+ CD11c-), monocytes (CD45+ CD11b+ Ly6C+ CD64-) and DCs (CD45+ CD11c+ MHCII+ F4/80- CD64-). Data are presented as mean±SEM. Aortic macrophages, AM and lung DC: n=3, other cells n=1.

3.4.4. Local micro-environment in the cardiovascular system and alveoli induces *Dcir1* expression in a murine macrophage cell line

Next, I sought to determine whether tissue-derived factors maintain or enhance the expression of *Dcir1* in macrophages. Aortas, hearts, lungs and broncho-alveolar lavage (BAL) were harvested from wild type mice and were then cut into small pieces. Tissues or BAL and macrophage cell line RAW264.7 were co-cultured for 24 hours as described in **Figure 3.9a**. The relative expression of *Dcir1* and the tissue resident macrophage marker *Mrc1* (CD206) was examined by qRT-PCR.

Tissue extract from the heart elevated the expression of *Dcir1* 4-fold relative to the untreated cells ($p=0.0238$) and the level of *Mrc1* in macrophages was also increased (**Figure 3.9b,c**). Aortic tissues and BAL were also capable of enhancing the expression of *Dcir1* 2-fold compared to the untreated cells. Treating cells with lung-extract, GMCSF and MCSF for 24 hours did not affect the expression of *Dcir1*. This preliminary experiment provides insights into the shaping of macrophages towards a tissue-resident phenotype by factors produced by tissues including hearts, aortas and alveoli. Moreover, it suggested that *Dcir1* might be a marker for tissue resident macrophages alongside *Mrc1*.

I also examined how the supernatant from the heart influenced the gene expression of other *Dcir* isoforms and *Dcar2* in the same experimental set-up. Having previously shown that the expression pattern of *Dcir3* was in line with *Dcir1* in BMDM, I also observed that the heart extract significantly induced *Dcir3* expression 4-fold relative to untreated cells, which was the same degree of change as was found for *Dcir1* (**Figure 3.10**). Although the baseline level of *Dcir4* expression was very low relative to *Dcir1*

(*Dcir4* vs. *Dcir1*: 0.17 vs. 1), the expression of *Dcir4* rose by 2.23 following treating with the heart extract. In line with the fact that *Dcir2* and *Dcar2* were not detected in BMDM, expression of these two genes was also not detected in RAW264.7 cells and their expression did not increase following exposure to the heart extract.

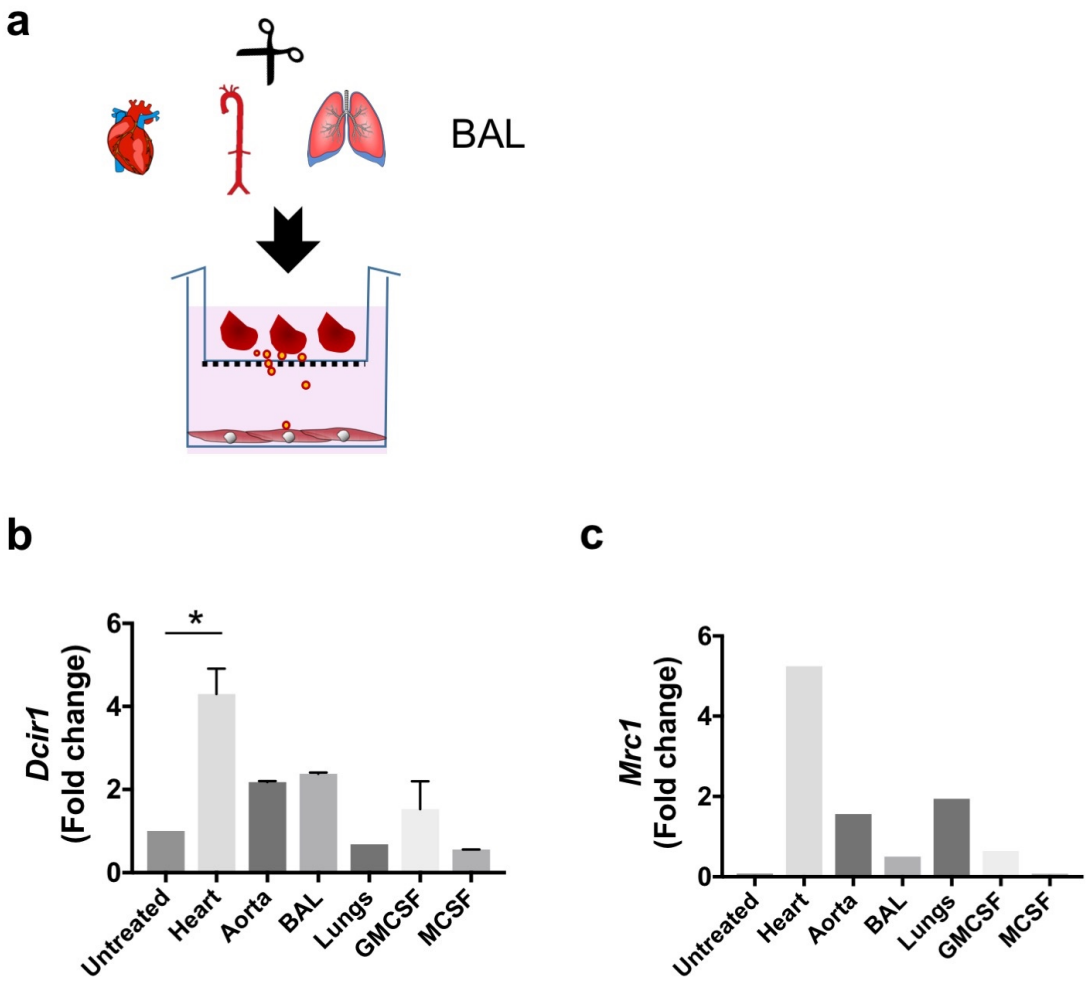


Figure 3.9 The differential expression of *Dcir1* and *Mrc1* in murine macrophage cell line RAW264.7 by treatment with extracts from the heart, aorta, broncho-alveolar lavage (BAL) and lungs.

RAW264.7 cells were treated with medium, GMCSF, MCSF or finely cut tissue pieces on the membrane with 0.5μm pores, where small particles such as cytokines can pass through, for 24 hours. The mRNA levels of *Dcir1* and *Mrc1* was measured by using qRT-PCR. The gene expression is relative to the housekeeping gene *18S rRNA* and is normalised against the *Dcir1* expression in untreated cells. The relative expression of *Dcir1* by treatment with extracts from the heart, aorta, BAL, lungs, GMCSF or MCSF. Medium treated cells were included as a negative control. Data are presented as mean±SEM. *Dcir1*: the untreated: n=3, heart: n=6, aorta/BAL/GMCSF/MCSF: n=2, lung: n=1. *Mrc1*: n=1 in all group. Mann-Whitney test. *P<0.05.

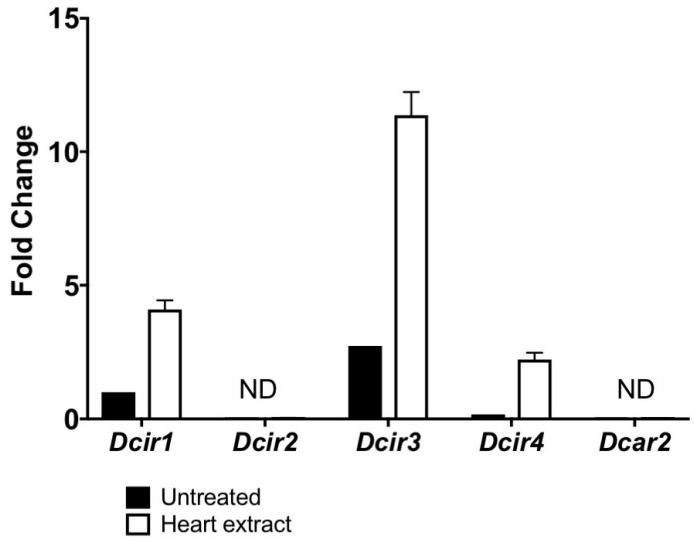


Figure 3.10 The effect of the heart extract on the relative gene expression of *Dcir* isoforms and *Dcar2* in murine macrophage cell line RAW264.7.

RAW264.7 cells were co-cultured with heart extracts from 4 wild type mice or medium for 24 hours. The transcriptomic levels of 4 *Dcir* isoforms and *Dcar2* were determined by using qRT-PCR and is relative to the level of the housekeeping gene *18S rRNA*. Fold change is normalised against *Dcir1* expression of the untreated sample. Data are presented as mean±SEM. The untreated: n=1, heart: n=4.

In the search for endogenous ligands for DCIR1, I tested whether *Dcir1* expression was altered by surfactant proteins (SP) whose interaction with alveolar macrophages has been extensively studied. SP are produced by type II alveolar epithelial cells in the lining of the alveoli sac (Pattle, 1955). SP-A and SP-D, members of the C type lectin family, called collectin, bind to the carbohydrate recognition domain of CLRs and play a role in host defence against pathogens (McCormack and Whitsett, 2002). Given the finding that BAL increased *Dcir1* expression in macrophages, I determined whether BAL contains SP-A and SP-D and also tested in RAW264.7 macrophages to see if SP-D itself increases *Dcir1* expression.

SP-A and SP-D were present in whole lung extract and BAL fluid as determined by Western blotting (**Figure 3.11**). Due to the difference in the level of total protein, a direct comparison between lungs and BAL was not plausible. Although SP-A seemed to be abundant in the BAL, murine recombinant SP-A was not commercially available at the time of conducting the experiment. Therefore, I treated macrophages with three different concentrations of SP-D for 24 hours, and the results showed that the serial treatment had no impact on the expression of *Dcir1*. Further work is required to determine if SP-A or other lectins in the BAL have the potential to enhance the expression of *Dcir1* in macrophages.

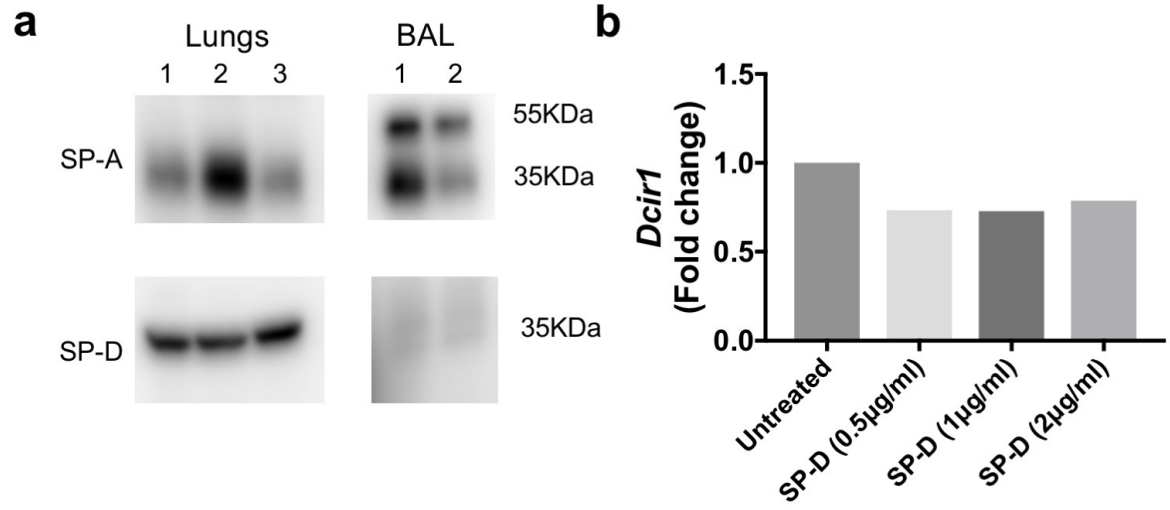


Figure 3.11 Surfactant protein (SP)-D does not regulate the expression of *Dcir1* in murine macrophage cell line RAW264.7.

a) SP-A and SP-D are detected in the lung extract and brocho-alveolar lavage (BAL) of WT mice. **b)** RAW264.7 cells were co-cultured with SP-D (0.5, 1 or 2μg/ml) for 24 hours. Levels of *Dcir1* were determined by using qRT-PCR and is relative to the level of the housekeeping gene *18S rRNA*. n=1.

3.5. Discussion

This chapter highlighted that an inflammatory challenge supressed the expression of human *Dcir* and murine *Dcir1* in *in vitro* macrophages and DCIR1 was highly expressed by tissue macrophages. Treating GMCSF- and MCSF-treated macrophages with bacterial LPS and pro-inflammatory cytokine IFNγ significantly inhibited the expression of human *Dcir* and murine *Dcir1*. It is still to be determined whether down-regulation of *Dcir/Dcir1* is the result of direct interaction with LPS and IFNγ, or due to exposure to inflammatory mediators that are produced through TLR4 and IFNγ receptor activation. In human and murine macrophages, there was a disparate effect on the expression of *Dcir/Dci1* in response to the T helper (Th) 2 cytokines IL-4 and IL-13. In the human system, *Dcir* expression levels significantly increased in the M2 macrophages whilst *Dcir1* expression moderately increased in mice. Thus, human DCIR and murine DCIR1 may play a different role in macrophages in response to Th2 cytokines.

Dcir2 and *Dcar2* were not detected in both GMCSF- and MCSF-macrophages nor were they expressed in the RAW264.7. In contrast, the expression of *Dcir3* and *Dcir4* decreased along with *Dcir1* expression upon inflammatory stimuli in MCSF-macrophages whilst levels of *Dcir1* and *Dcir3* were also attenuated by the same condition in GMCSF-macrophages. These data were the first to show the comparative expression of *Dcir* isoforms in differentially activated macrophages, and highlighted that functions of *Dcir1, Dcir3* and *Dcir4* may be associated with each other in macrophage biology. The expression pattern of *Dcir/Dcir1* suggested that *Dcir/Dcir1* may play a modulatory role in the immune response.

DCIR1 was detected *in vivo* in macrophages from the aorta, heart and lung. DCIR1 was widely expressed by macrophages, cDC2, neutrophils and Ly6C+ monocytes in the aorta and heart. In the lung, high levels of DCIR1 was detected in alveolar and interstitial macrophages, cDC2, neutrophils and Ly6C+ monocytes, and lower levels were found in Ly6C- monocytes and eosinophils. Gene expression analysis of *Dcir1* in sorted macrophages and DCs in aortas and lungs confirmed that *Dcir1* expression was highly up-regulated in aortic and alveolar macrophages relative to other cells of the myeloid lineage. Taken together, these data suggest that macrophages are capable of sustaining *Dcir1* expression possibly via communication tissue micro-environments.

In support of this possibility, co-culturing of the macrophage cell line RAW264.7 with tissue extracts from aortas, hearts, lungs and BAL elevated the expression of *Dcir1* along with *Mrc1* (CD206), a marker for tissue macrophages. When macrophages were deficient in *Dcir1*, CD206 expression was not effectively sustained in the culture with MCSF. Since *Dcir1* deficiency did not affect phagocytic activity in BMDM, loss of CD206 in the absence of DCIR1 is probably associated with survival or identity of macrophages. Additionally, the heart extract also increased levels of *Dcir3* and *Dcir4,* whilst expression of *Dcir2* and *Dcar2* was not detected in this cell line. The results are in accordance with a study showing that DCIR2 is exclusively expressed by splenic CD8- cDCs and is a marker for DCs (Uto et al., 2016).

A search for candidates for DCIR1 ligands was performed on RAW264.7 cells by treating them with surfactant protein, which is a C type lectin also known as collectin, that is abundant in the alveoli space of the lung. Although murine recombinant SP-D

was unable to induce *Dcir1* expression, other collectins could still be candidates for *Dcir1* ligands. By utilising lectin purification chromatography in combination with mass spectrometry, identification of DCIR1 ligands in tissue extracts would be feasible.

In summary, human *Dcir* and murine *Dcir1* and *Dcir3* were down-regulated by inflammatory signals in macrophages. However, GMCSF and tissue-derived factors from the aorta, the heart and alveoli enhanced the expression of *Dcir1* and *Mrc1* in macrophages. *Dcir1*-null macrophages were impaired in sustaining CD206 expression in response to MCSF. Taken together, DCIR1 may define tissue resident macrophages in those tissues.

CHAPTER 4. A novel mouse strain for ablation of aortic macrophages

4.1. Introduction

The heathy artery harbours resident macrophages in the adventitia which performs tissue homeostasis (Lim et al., 2018). During arterial inflammation, monocytes are recruited in the intimal layer of the artery where they differentiate into macrophages that plays a role in progression and regression of atherosclerosis (Swirski et al., 2007). Pathological signals from the atherosclerotic lesion can shape macrophages into various subsets by altering transcriptional and epigenetic regulations (Chinetti-Gbaguidi et al., 2015). However, these subsets have not been characterised simultaneously, in part due to technical challenges. Thus, characterisation of macrophage subsets and understanding their role in atherosclerosis would be of importance for potential use of macrophages as a therapeutic target.

In the chapter 2, I have shown 4 macrophage subsets in the aorta of *Apolipoprotein E (ApoE)*$^{-/-}$ mice, two of which resembled resident macrophages. My data from single cell RNA sequencing (scRNAseq) and gene expression assays also demonstrated that dendritic cell immunoreceptor 1 (*Dcir1;* gene name: *clec4a2*) was preferentially expressed by vascular resident macrophages. Taking all of this evidence into account, utilising *Dcir1* may provide a tool for ablating the resident adventitial macrophage subset in arterial inflammation.

Cre/*loxP* recombination derived from P1 bacteriophages is a popular tool for genetic alteration in mice. Cre recombinase recognises *loxP* sequences in genome, which then preferentially deletes the *loxP* sites (Sternberg and Hamilton, 1981). Mice carrying the inserted *loxP* sites in the gene of interest can be crossed with cell specific Cre expressing mice to initiate genetic modification. This system has been extensively

utilised in cell-specific conditional knock-out (KO) or knock-in (KI) mouse models (Shi et al., 2018b). Diphtheria toxin receptor (DTR)-mediated conditional cell ablation has been applied in a number of murine models as rodent heparin-binding EGF-like growth factor (HB-EGF precursor; also known as DTR) has the lesser affinity to bind to DT subunit B (DT-B) whilst the interaction between DT-B and DTR in primates is exponentially stronger (Naglich et al., 1992, Mitamura et al., 1997, Saito et al., 2001). Therefore, introducing human DTR in murine cells under the specific promoter facilitates inducible apoptosis in cells expressing the gene of interest by administering DT-B. Combination of Cre/*loxP* recombination and DTR-mediated cell ablation enhances specificity in targeting cells, by crossing mice carrying DTR with Cre-expressing mice (Buch et al., 2005). Nonetheless, a number of DTR-Cre mouse models such as CD11b, CD11c, CD68, CX3CR1 and F4/80 for ablation of macrophages have been generated, some of which can result in depletion of other myeloid populations (Shi et al., 2018a). *LysM*^{Cre} mice whose Cre recombinase is under the control of lysozyme M (*LysM*; gene name: Lyz2), show the high efficacy of Cre activity in macrophages and neutrophils and less in DC (Clausen et al., 1999).

To this end, *LysM*^{Cre} mice were bred with Cre-inducible *Dcir1*-DTR^{flox} KI mouse strain to establish a novel mouse strain for ablation of tissue resident macrophages in the aorta. The aim of the work in this chapter is to optimise macrophage ablation in this strain and, ultimately, is to establish studies on the *in vivo* function of aortic resident macrophages in the steady state and atherosclerosis.

4.2. Generation and characterisation of the *LysM^{Cre} Dcir1*-DTR^{flox} mouse strain

A Cre-inducible *Dcir1*-DTR^{flox} KI mouse strain was generated in concert with Gen0way (France). A construct containing neomycin, human diphtheria toxin receptor (DTR; gene name: *Hbegf*), and enhanced green fluorescence protein (*egfp*) was introduced upstream of exon 8 of the *Dcir1* gene (**Figure 4.1**). The neomycin gene includes stop codon sequences which prevent the transcription of the inserted genes in the absence of Cre recombinase, and a pair of *LoxP* sequences are located in each end of the neomycin gene to enable the deletion of neomycin and a stop codon. Once the *Dcir1*-DTR^{flox} mouse is crossed with the Cre expressing strain, Cre recombinases preferentially deletes the *loxP* sites in the modified *Dcir1* gene which allows the transcription of *Hbegf* and *egfp* under the *Dcir1* promoter. In order to enhance specificity of ablating macrophages, *LysM^{Cre}* mice were crossed with *Dcir1*-DTR^{flox} KI mice. Therefore, cells co-expressing *LysM* (gene name: *Lyz2*) and *Dcir1* can be monitored by eGFP as a reporter protein and can undergo apoptosis by administering DT-B (hereafter referred to as DT).

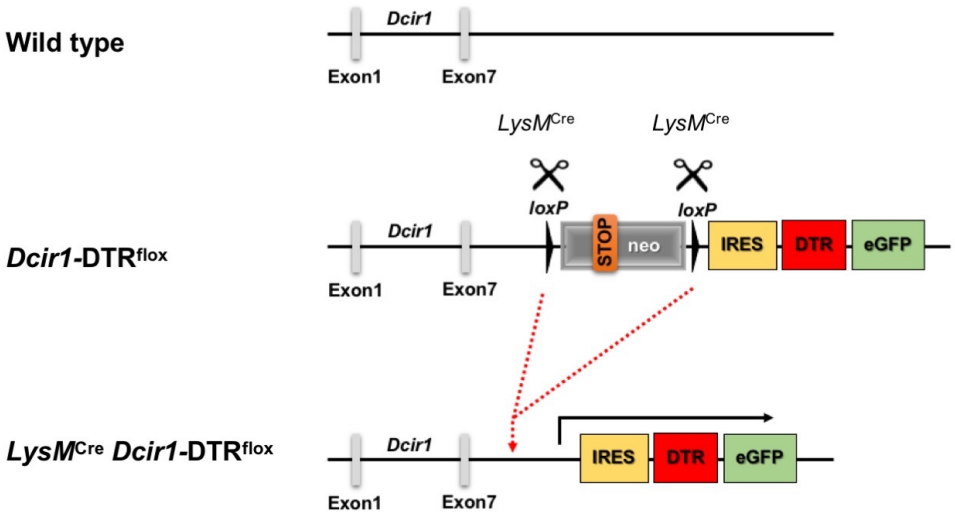


Figure 4.1 *Dcir1* gene alteration to trace and ablate DCIR1 expressing cells.

A construct containing *loxP* sequences, neomycin, internal ribosome entry site (IRES), diphtheria toxin receptor (DTR) and eGFP is inserted upstream of exon 8 of the *Dcir1* gene. The transcription of DTR and eGFP is initiated by crossing with Cre expressing mice via *loxP*-Cre recombination. The *LysM*^{Cre} strain was selected to ablate macrophages. This gene modification does not affect the function of DCIR1 as the transcription terminates at exon 7.

4.2.1. The detection of eGFP expressing cells from the *LysM*^{Cre} *Dcir1*-DTR^{flox} mice

Having established the *LysM*^{Cre} *Dcir1*-DTR^{flox} mouse strain, endogenous levels of eGFP in myeloid cells of this strain were traced by using flow cytometry. First, I sought to compare levels of eGFP in neutrophils, monocytes and macrophages from the bone marrow (BM), blood, spleen, aorta and lungs as well as BM-derived macrophages (BMDM) of *Dcir1*-DTR^{flox} and *LysM*^{Cre} *Dcir1*-DTR^{flox} mice. Levels of eGFP were illustrated in a histogram by mean fluorescence intensity (MFI) (**Figure 4.2**). Endogenous expression of eGFP was detected in neutrophils from the BM of *LysM*^{Cre} *Dcir1*-DTR^{flox} mice while it was not monitored in monocytes and macrophages in the BM (**Figure 4.2a,b,c**). Both *in vitro* and *in vivo* macrophages are renowned for their strong autofluorescence, which restrains the detection of fluorescent protein used in the green channel (Edelson et al., 1985, Njoroge et al., 2001). To avoid this issue, biotinylated antibody against GFP was utilised in combination with streptavidin antibody conjugated with allophycocyanin (APC) in the red channel. Neutrophils, monocytes and macrophages from the same organs were intracellularly stained with GFP antibody and streptavidin-APC antibody. GFP expression was detected in neutrophils from 5 organs (**Figure 4.2a**). Consistently, eGFP was also not observed in monocytes and macrophages from these tissues of *LysM*^{Cre} *Dcir1*-DTR^{flox} mice by antibody-mediated eGFP detection (**Figure 4.2b,c**). Furthermore, the detection of eGFP using an antibody against GFP in BMDM cultured with macrophage colony stimulating factor (MCSF) or granulocyte macrophage colony stimulating factor (GMCSF) was not possible.

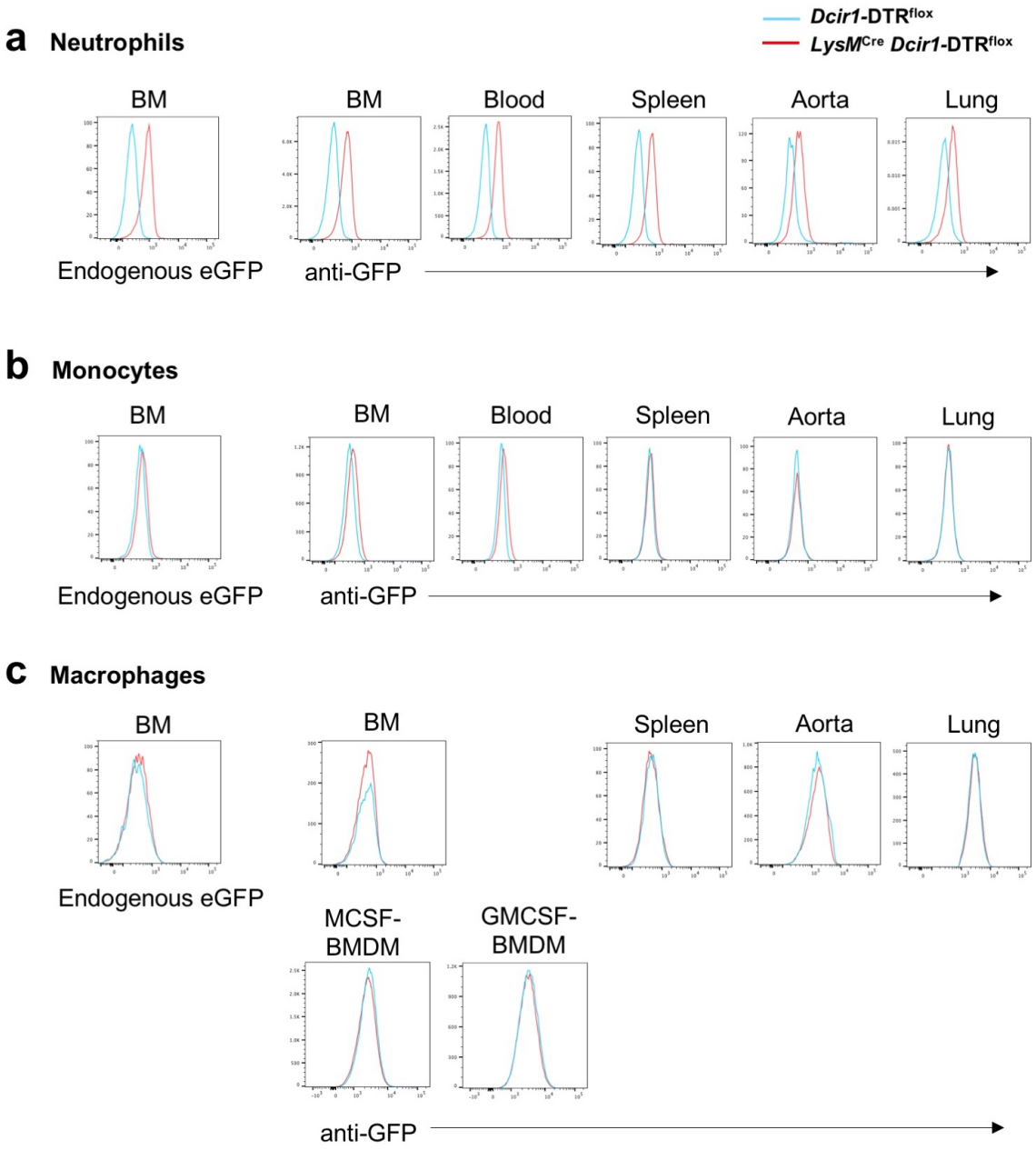


Figure 4.2 The detection of eGFP in myeloid cells from *LysM*^{Cre} *Dcir1*-DTR^{flox} mice by utilising a GFP antibody.

eGFP in neutrophils, monocytes and macrophages from the aorta, lungs, spleen, BM and blood or BM-derived macrophages (BMDM) was measured by flow cytometry using antibody against GFP. The histogram plots present the mean fluorescence intensity (MFI) of GFP in **a)** neutrophils, **b)** Ly6C+ monocytes and **c)** macrophages.

4.2.2. Analysis of the gene expression of *egfp* (eGFP) and *Hbegf* (DTR) in macrophages

To ensure if gene expression of *egfp* (eGFP) and *Hbegf* (DTR) was present in macrophages and other myeloid cells of *LysM*^{Cre} *Dcir1*-DTR^{flox} and *Dcir1*-DTR^{flox} mice, gene expression of *Dcir1, egfp* and *Hbegf* in these cells was determined by using qRT-PCR in the BM cells cultured with MCSF, GMCSF or granulocyte colony stimulating factor (GCSF). Gene expression levels of *Dcir1, egfp* and *Hbegf* were detected in MCSF-treated macrophages, GMCSF-treated dendritic cells (DCs)-macrophages and GCSF-treated neutrophils of *LysM*^{Cre} *Dcir1*-DTR^{flox} (**Figure 4.3a,b,c**). As expected, expression levels of *egfp* and *Hbegf* were not detected in cells from the *Dcir1*-DTR^{flox} mice while *Dcir1* was expressed in all *in vitro* myeloid cells in both strains.

To determine the levels of *egfp* and *Hbegf* in the myeloid cells that reside in the aorta and lungs, macrophages, DCs, monocytes, cells were dissociated from these tissues and were separated based on their marker expression by fluorescence-activated cell sorting (FACS). All populations were gated on live CD45+ cells: aortic macrophages were defined as CD11b+ F4/80+ CD64+, aortic DC as CD11c+ MHCII+ CD64-, alveolar macrophages (AM) as CD11c+ F4/80+ CD64+ CD11b-, interstitial macrophages (IM) as CD11b+ F4/80+ CD64+ CD11c- and Ly6C+ monocytes as CD11b+ Ly6C+ CD64- (gating strategy is depicted in Appendix 1 Figure 8.3). Aortic macrophages were divided into two subpopulations by the expression of MHCII. Gene expression in the isolated populations was then measured by using qRT-PCR. Transcription levels of *Dcir1, egfp* and *Hbegf* were relatively higher in two aortic macrophage subsets compared to DCs (**Figure 4.3d**). In the lungs, gene expression of *Dcir1, egfp* and *Hbegf* was found in macrophage subpopulations at the higher level

while showing very low levels in Ly6C+ monocytes and DCs (**Figure 4.3e**). Noticeably, it was apparent that AM expressed higher levels of these three genes than IM. Although eGFP was not detected at the protein level in aortic and alveolar macrophages, transcription levels of *egfp* and *Hbegf* were present in these macrophages (**Figure 4.2c; Figure 4.3d,e**). Collective data indicate two potential hypotheses; first, the *egfp* transcript is not translated at the protein level or expression levels of endogenous eGFP is too low to detect by flow cytometry.

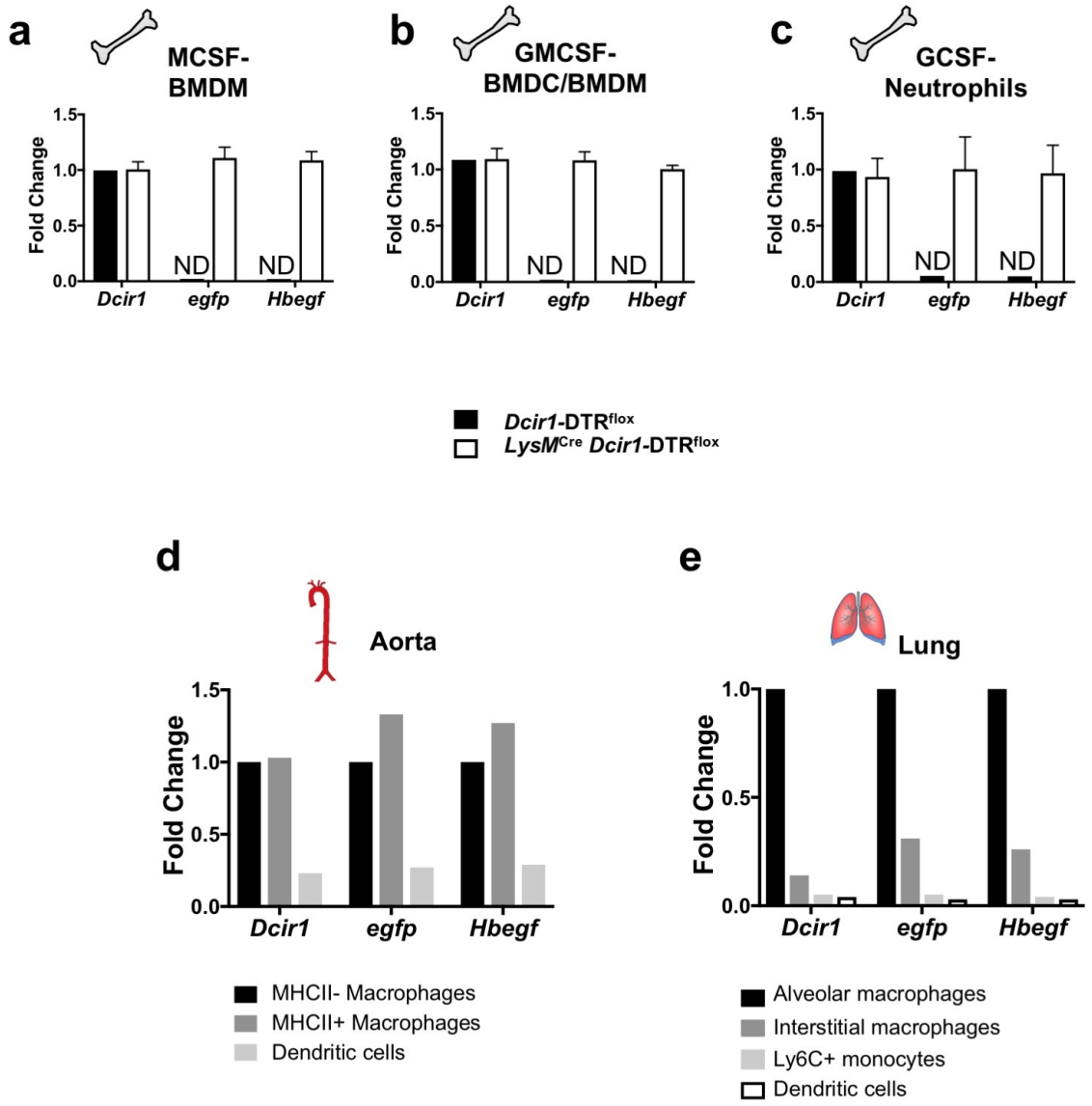


Figure 4.3 The detection of gene expression of *Dcir1*, *egfp*, *Hbegf* (DTR) in myeloid cell populations from *LysM*^{Cre} *Dcir1*-DTR^{flox} mice.

The BM cells of *LysM*^{Cre} *Dcir1*-DTR^{flox} mice were cultured with MCSF, GMCSF or GCSF for 6 days. Macrophage subtypes, DC and Ly6C+ monocytes from aortas and lungs of the *LysM*^{Cre} *Dcir1*-DTR^{flox} mice were separated by the fluorescence-activated cell sorting technique. Gene expression of *Dcir1*, *egfp*, *Hbegf* (DTR) was analysed by qRT-PCR. Gene expression is relative to the housekeeping gene 18S rRNA. The graphs show fold change of three genes in **a)** MCSF-cultured BM-derived macrophages (BMDM), **b)** GMCSF-cultured BM-derived DCs (BMDC) and BMDM, **c)** GCSF-treated BM (neutrophils). **d)** aortic cells and **e)** myeloid cells from lungs. Data are presented as mean±SEM. a,b,c) n=3 each, d,e) n=1. ND stands for not-detected.

4.2.3. Levels of DCIR1 in leucocytes by mass cytometry

Previously, I have shown the levels of DCIR1 in myeloid cell populations from the aorta, heart, lungs and the BM by flow cytometry using biotinylated antibody against DCIR1 in Chapter 2. The data showed that DCIR1 was broadly expressed by macrophages, neutrophils, DCs, and monocytes in those tissues. However, since the detection of DCIR1 levels was based on a secondary antibody, the direct comparison was not difficult. Therefore, I conjugated DCIR1 antibody with a metal tag to measure DCIR1 levels in leucocytes by mass cytometry (CyTOF). Here, I presented the relative expression of DCIR1 in leucocyte populations from the aorta, heart, lungs and spleen of *LysM*^{Cre} *Dcir1*-DTR^{flox} mice by CyTOF (**Figure 4.4a,b,c,d**). As shown, DCIR1 was widely expressed by the myeloid family comprising macrophages, neutrophils, Ly6C+ monocytes and cDC2 in the aorta, heart, lungs and spleen. In line with the gene expression data, DCIR1 expression was markedly higher in macrophages from the aorta and heart compared to the other myeloid populations.

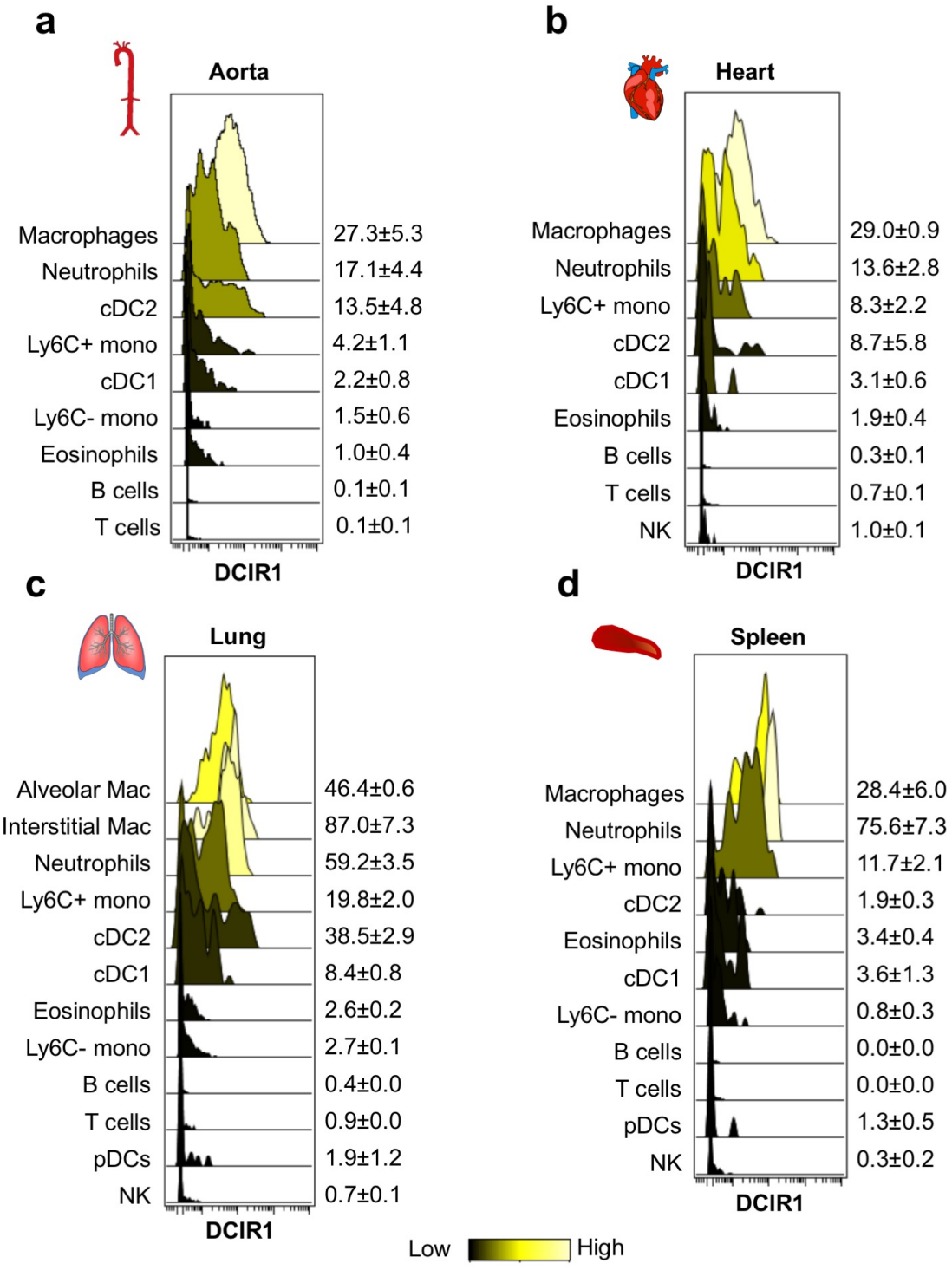


Figure 4.4 Comparative expression of DCIR1 in leucocytes from the aorta, heart, lungs and spleen of the *LysM*^{Cre} *Dcir1*-DTR^{flox} strain by mass cytometry.

The mean of DCIR1 expression in leucocyte populations that were identified by viSNE clustering is displayed in histogram plots. The plots present levels of DCIR1 expression in **a)** the aorta, **b)** heart, **c)** lungs and **d)** spleen. The histogram is the representative of 8 *LysM*^{Cre} *Dcir1*-DTR^{flox} mice in the aorta, lungs and spleen and 4 mice in the heart.

4.2.4. Intravenous delivery of diphtheria toxin induces cell ablation in macrophages and neutrophils in *LysM*^{Cre} *Dcir1*-DTR^{flox} mice

Having shown that neutrophils and macrophages from tissues of *LysM*^{Cre} *Dcir1*-DTR^{flox} mice expressed *egfp* and *Hbegf* (DTR) at the gene level, I then tested these mice whether they could respond to the DT treatment. Initially, these mice were subjected to an intravenous injection of DT for 24 hours or two injections within 72 hours. The BM, spleen and lungs were analysed by flow cytometry.

Macrophages from the BM, spleen and lungs were significantly ablated at 24 hours from injection with DT while no cell loss was observed in the control mice and saline-treated mice (ablation rates: BM: 92.0±1.4% ($P<0.001$), spleen: 88.4±2.3% ($P<0.01$), lungs: 88.1±1.5% ($P<0.00001$); **Figure 4.5a,b,c**). BM and alveolar macrophages from *LysM*^{Cre} *Dcir1*-DTR^{flox} mice were depleted by DT at 72 hours (BM: 89.0±0.5% ($P<0.001$), lungs: 56.5±4.9% ($P<0.05$). In addition, significant ablation of neutrophils in the BM was also achieved in the DT-treated *LysM*^{Cre} *Dcir1*-DTR^{flox} mice at 24 and 72 hours (ablation rates: 24 hours: 69.2±1.9% ($P<0.001$), 72 hours: BM: 70.6±1.8% ($P<0.0001$); **Figure 4.6a**). A moderate depletion of splenic and lung neutrophils was observed at two time points, however, it did not reach statistical significance (**Figure 4.6b,c**). Of note, monocytes from the BM, spleen and lungs of *LysM*^{Cre} *Dcir1*-DTR^{flox} mice were not depleted by DT treatment but increased in these organs at 72 hours (**Figure 4.7a,b,c**).

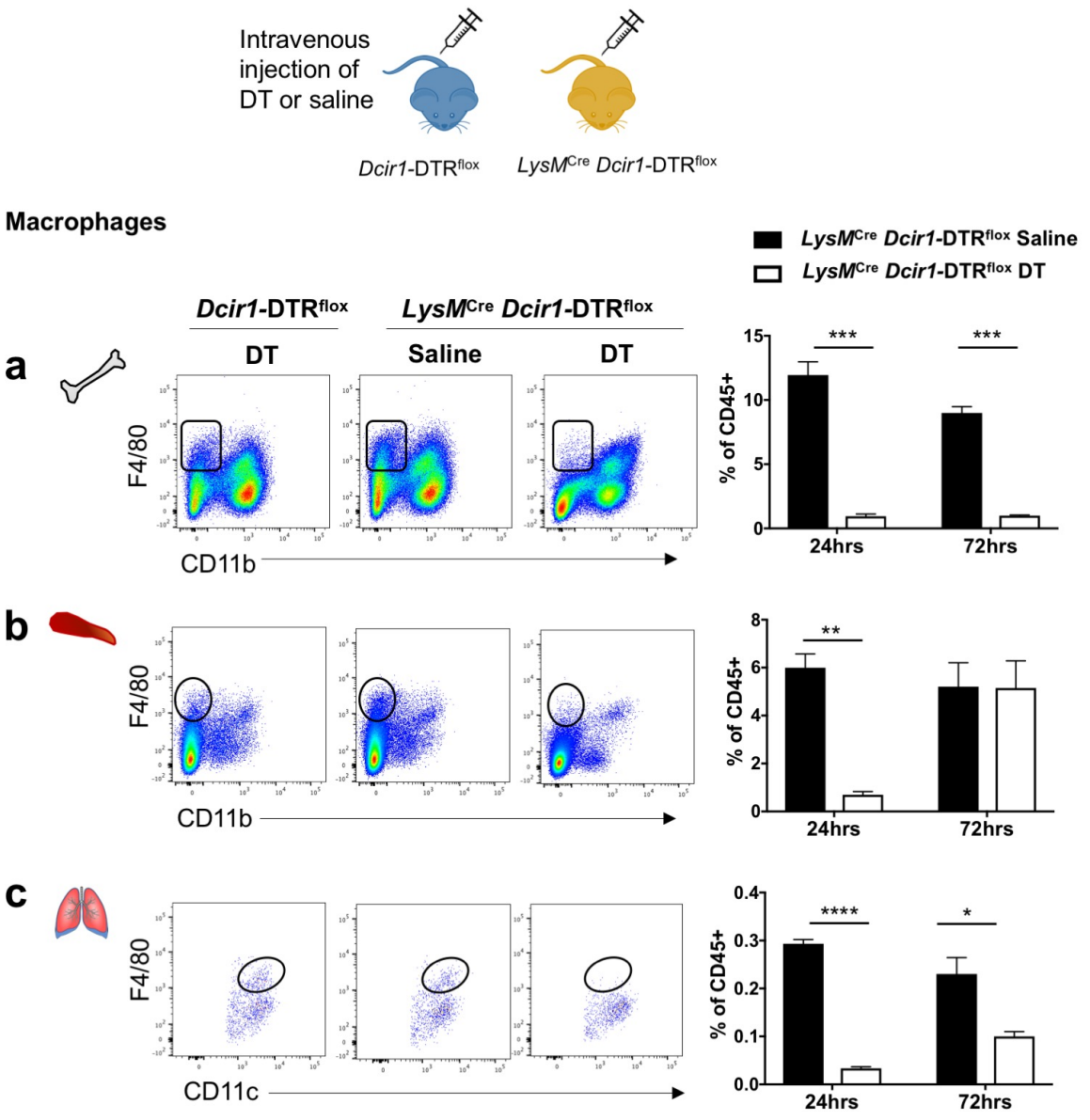


Figure 4.5 The DTR-mediated macrophage ablation by intravenous injection of diphtheria toxin (DT) in the BM, spleen and lungs of *LysM*^{Cre} *Dcir1*-DTR^{flox} mice.

LysM^{Cre} *Dcir1*-DTR^{flox} and *Dcir1*-DTR^{flox} mice were subjected to intravenous injection of 1.5 µg/mouse DT or saline for 24 and 72 hours. Mice received one injection for 24- hour time points and two injections were given at Day0 and Day2 for 72-hour time point. The cells from the BM, spleen and lungs of all mice were analysed by flow cytometry. The graphs present the percentage of macrophages in **a)** the BM, **b)** spleen and **c)** lungs. The representative images show gating for macrophages at 24-hour time point. Data are presented as mean±SEM. n=3. Multiple t test. *P<0.05, **P<0.01, ***P<0.001 and ****P<0.0001.

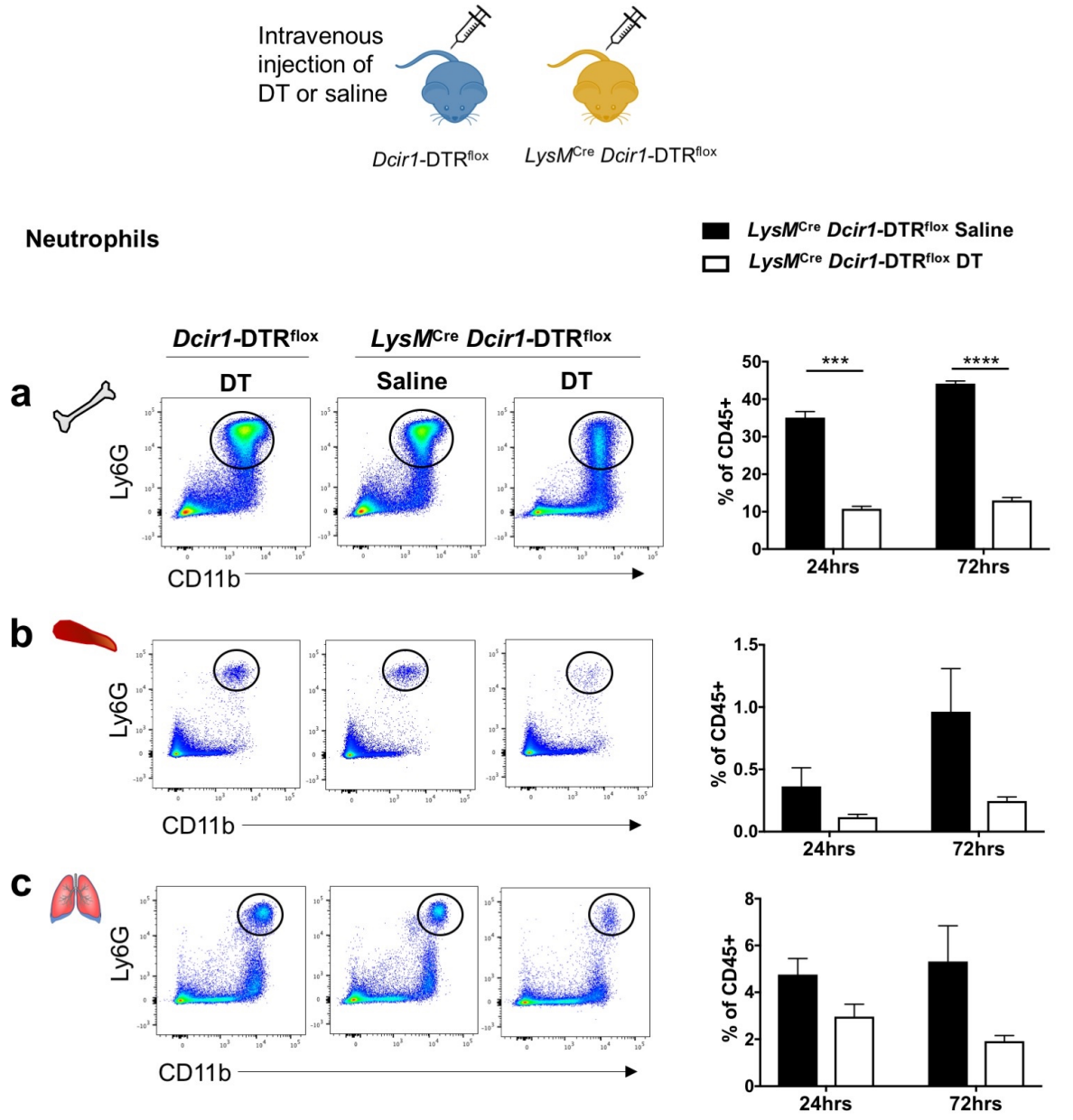


Figure 4.6 The DTR-mediated neutrophil ablation by intravenous injection of DT in the BM, spleen and lungs of *LysM*^{Cre} *Dcir1*-DTR^{flox} mice.

LysM^{Cre} *Dcir1*-DTR^{flox} and *Dcir1*-DTR^{flox} mice were subjected to intravenous injection of 1.5 µg/mouse DT or saline for 24 and 72 hours. Mice received one injection for 24- hour time points and two injections were given at Day0 and Day2 for 72-hour time point. The cells from the BM, spleen and lungs of all mice were analysed by flow cytometry. The graphs present the percentage of neutrophils in **a)** the BM, **b)** spleen and **c)** lungs. The representative images show gating for neutrophils at 72-hour time point. Data are presented as mean±SEM. n=3. Multiple t test. ***P<0.001 and ****P<0.0001.

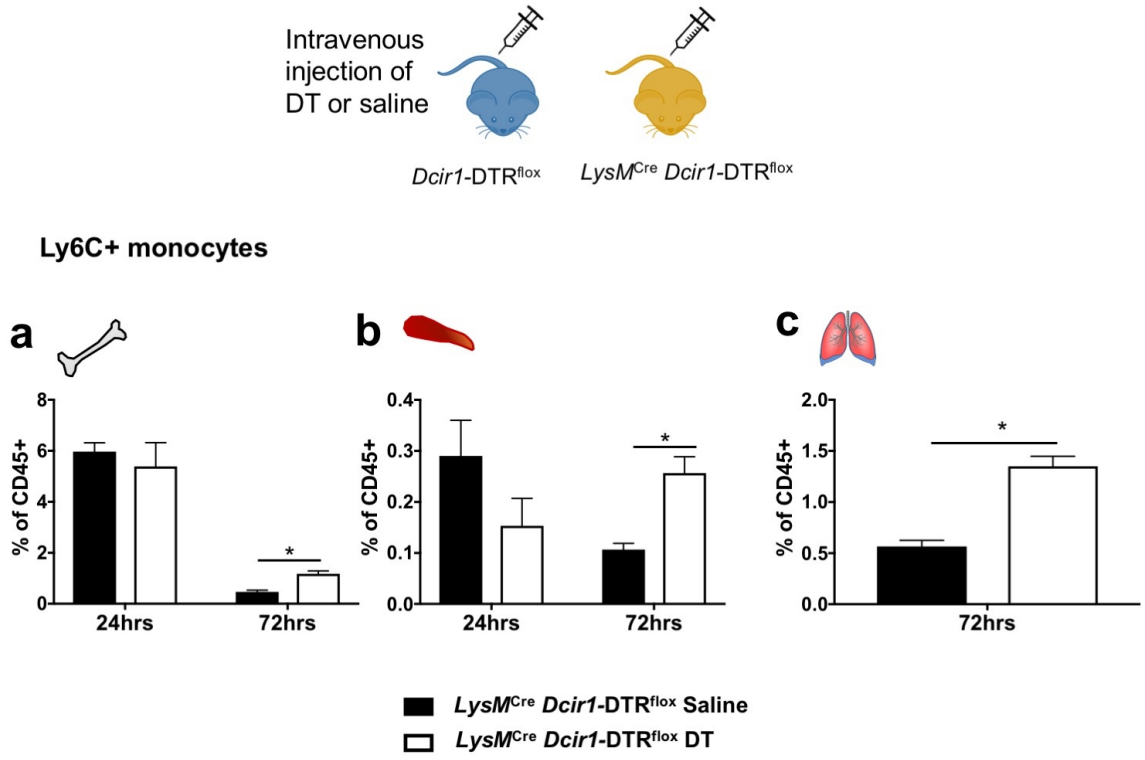


Figure 4.7 Monocyte ablation by intravenous injection of DT in the BM, spleen and lungs of *LysM*^{Cre} *Dcir1*-DTR^{flox} mice.

LysM^{Cre} *Dcir1*-DTR^{flox} and *Dcir1*-DTR^{flox} mice were subjected to intravenous injection of 1.5 µg/mouse DT or saline for 24 and 72 hours. Mice received one injection for 24- hour time points and two injections were given at Day0 and Day2 for 72-hour time point. The cells from the BM, spleen and lungs of all mice were analysed by flow cytometry. The graphs present the percentage of monocytes in **a)** the BM, **b)** spleen and **c)** lungs. Data are presented as mean±SEM. n=3. Multiple t test. *P<0.05.

Having shown the efficacy of ablation of macrophages and neutrophils in these organs, I sought to test if cell depletion could be achieved in a murine model of peritonitis induced by thioglycollate (TG). Firstly, *LysM*^{Cre} *Dcir1*-DTR^{flox} mice were infected by injecting TG in the peritoneum for 4 hours to facilitate the recruitment of neutrophils and were subjected to an intravenous injection of DT overnight. In the second experiment, *LysM*^{Cre} *Dcir1*-DTR^{flox} mice received an intravenous injection of DT overnight and on the following day peritonitis was induced for a further 4 hours. Single cells from the BM and peritoneum were collected and were analysed by flow cytometry. DT treatment enabled depletion of neutrophils in the BM of *LysM*^{Cre} *Dcir1*-DTR^{flox} mice with peritonitis whereas neutrophils, monocytes and macrophages in the peritoneum were not affected by the DT injection (saline vs. DT: BM-neutrophils: 46.5% vs. 15.7% P<0.01, BM-macrophages: 4.2% vs. 0.8% P<0.01; **Figure 4.8a**). In the mice that received DT injections followed by TG, neutrophils and macrophages in the BM and peritoneum were successfully ablated (saline vs. DT: BM-neutrophils: 38.7% vs. 4.9% P<0.0001, BM-macrophages: 5.8% vs. 1.1% P<0.0001, peritoneal neutrophils: 63.5% vs. 9.0% P<0.05, peritoneal macrophages: 18.9% vs. 4.7% P<0.05; **Figure 4.8b**). In contrast, the monocyte proportion was increased by 2-fold in the peritoneum of these mice, which did not reach statistical significance. Collectively, these data suggest that local inflammation rescued depletion of neutrophils and macrophages in the peritoneum. This can be explained by that the inflammatory insult alleviated *Dcir1* expression in these cells, which consequently dampened DTR expression. This trend is in line with the data in Chapter 3 (Figure 3.1) showing that pro-inflammatory signals, lipopolysaccharide (LPS) and interferon (IFN) γ, reduced *Dcir1* levels in macrophages.

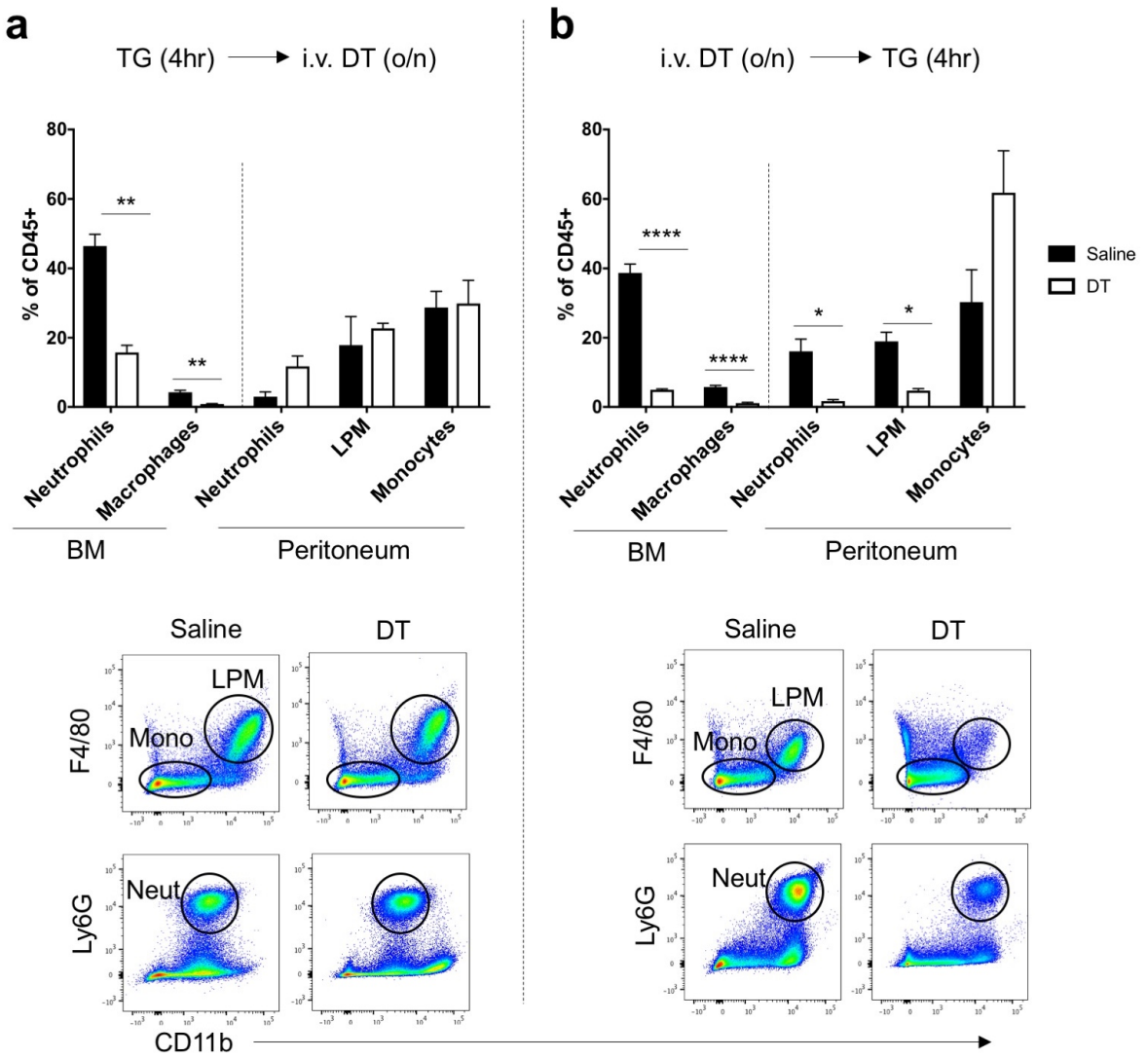


Figure 4.8 The DTR-mediated cell ablation by intravenous injection of DT in a murine model of peritonitis in *LysM*^{Cre} *Dcir1*-DTR^{flox} mice.

a) Peritonitis was induced by injecting thioglycollate (TG) into the peritoneum of *LysM*^{Cre} *Dcir1*-DTR^{flox} mice. After 4 hours, the mice received an intravenous injection of 1.5 µg/mouse DT or saline for 18 hours. Cells from the the BM and peritoneum were analysed by flow cytometry. The graph displays the percentage of neutrophils, macrophages, monocytes in these organs. **b)** An intravenous injection of DT or saline was administered in the mice overnight and peritonitis was induced next day. Cells from the BM, blood and peritoneum were collected 4 hours after TG injection. The graph presents the percentage of neutrophils, macrophages, monocytes in these tissues. Flow cytometry images show gating for monocytes, large peritoneal macrophages (LPM) and neutrophils from peritoneum. Data are presented as mean±SEM. n=3. Multiple t test. *P<0.05, **P<0.01 and ****P<0.0001.

4.2.5. Intraperitoneal delivery of diphtheria toxin selectively ablates tissue macrophage

To establish long term treatment with DT, intraperitoneal administration of DT was devised. First, I introduced saline or 30 ng/g DT intraperitoneally three times for a week in *LysM*^{Cre} *Dcir1*-DTR^{flox} and *Dcir1*-DTR^{flox} mice. Single cells form the BM, lungs, aorta, heart, peritoneum, colon, liver and brain of these mice were retrieved and were analysed by flow cytometry.

In sharp contrast with the intravenous delivery, intraperitoneal injection of DT did not ablate neutrophils in *LysM*^{Cre} *Dcir1*-DTR^{flox} mice (**Figure 4.9a,b,c**). However, intraperitoneal DT injections delivered significant ablation in macrophages in the BM, alveoli of the lungs, aorta, heart and peritoneum (ablation rates: BM: 70.4±7.0% (P<0.0001), alveolar Mac: 97.4±0.9% (P<0.0001), MHCII+ aortic Mac: 65.8±10.1% (P<0.0001), MHCII+ cardiac Mac: 69.8±3.1% (P<0.01), large peritoneal Mac: 97.8±0.5 (P<0.01) and small peritoneal Mac: 58.0±4.1% (P<0.01); **Figure 4.10a,b,c,d,e**). Percentages of interstitial, colonic and liver macrophages were significantly increased in the DT-treated *LysM*^{Cre} *Dcir1*-DTR^{flox} mice compared to the saline-treated and the DT-treated *Dcir1*-DTR^{flox} controls (saline vs. DT: Interstitial Mac: 0.8±0.1% vs. 1.6±0.3 (P<0.05), colonic Mac: 11.2±3.5% vs. 20.5±3.2% (P<0.05), liver Mac: 2.4±0.5% vs. 8.6±1.6 (P<0.01); **Figure 4.10b,f,g**). Brain macrophages, also known as microglia, from *LysM*^{Cre} *Dcir1*-DTR^{flox} mice were resistant against DT treatment (**Figure 4.10h**). Consistent with the results from intravenous delivery of DT, monocytes in the BM, lungs, peritoneum and colon were significantly expanded in the DT-treated *LysM*^{Cre} *Dcir1*-DTR^{flox} mice relative to two control groups (saline vs. DT: BM: 12.6±1.6% vs. 22.9±2.1% (P<0.01), lungs: 5.7±1.1% vs. 11.3±1.6% (P<0.01), peritoneum: 4.0±1.5%

vs. 31.7±1.8% (P<0.01), colon: 1.8±0.7% vs. 11.5±2.7% (P<0.01); (**Figure 4.11a,b,d,e**). Although there was an increasing trend in the percentage of monocytes in the aorta and liver of the DT-treated mice, this did not reach statistical significance (**Figure 4.11c, f**).

The efficacy of DT in *LysM*^{Cre} *Dcir1*-DTR^{flox} mice was clearly different by the administration route, possibly due to their different kinetics. Intravenous delivery depleted neutrophils and macrophages while intraperitoneal injection exclusively ablated the macrophage population. DT by intravenous administration may reach rapidly to the BM and other organs at the high concentration than the intraperitoneal method since DT in the peritoneum is slowly absorbed by tissues. This can be speculated by that neutrophils may be less sensitive to DT treatment.

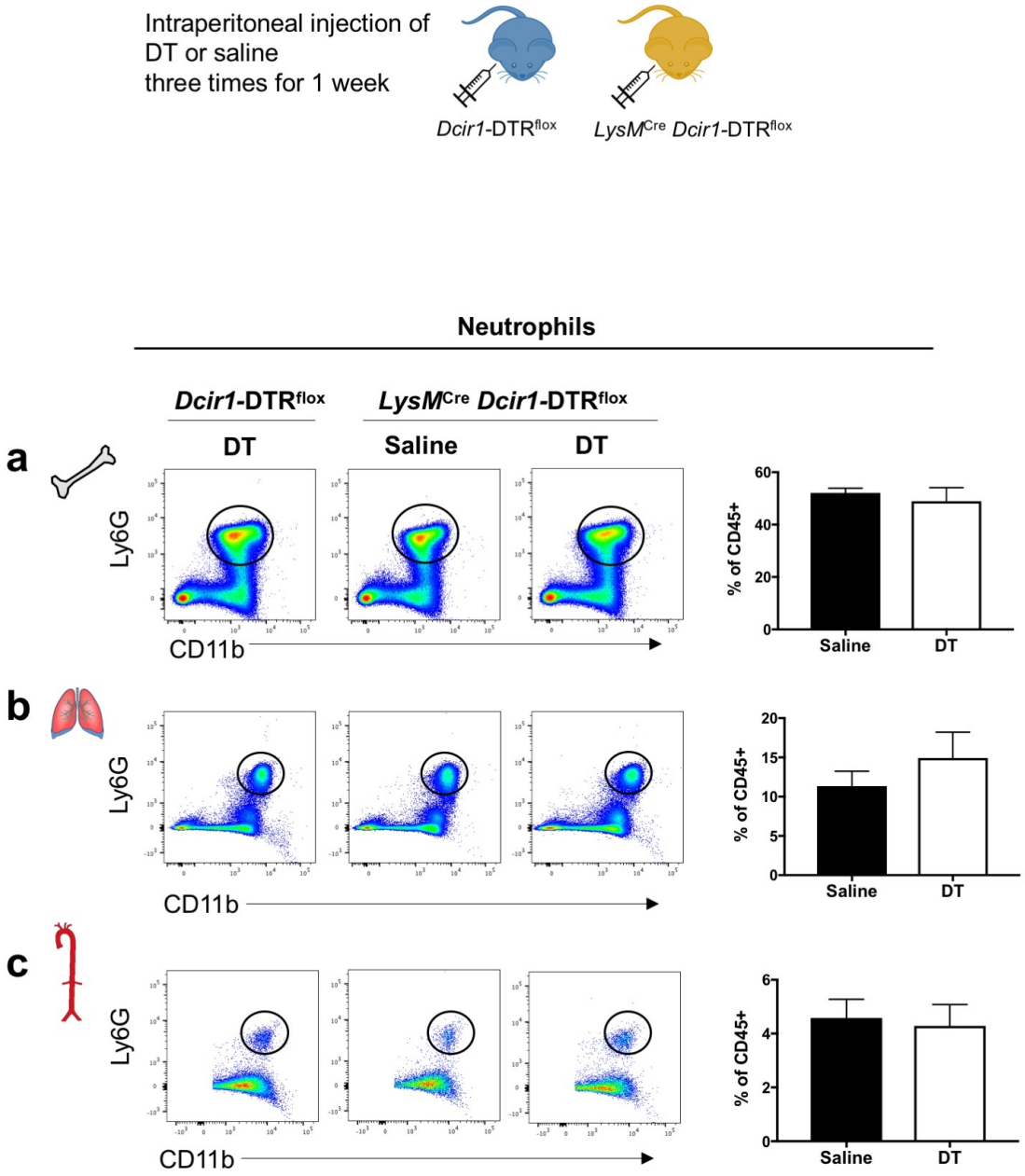
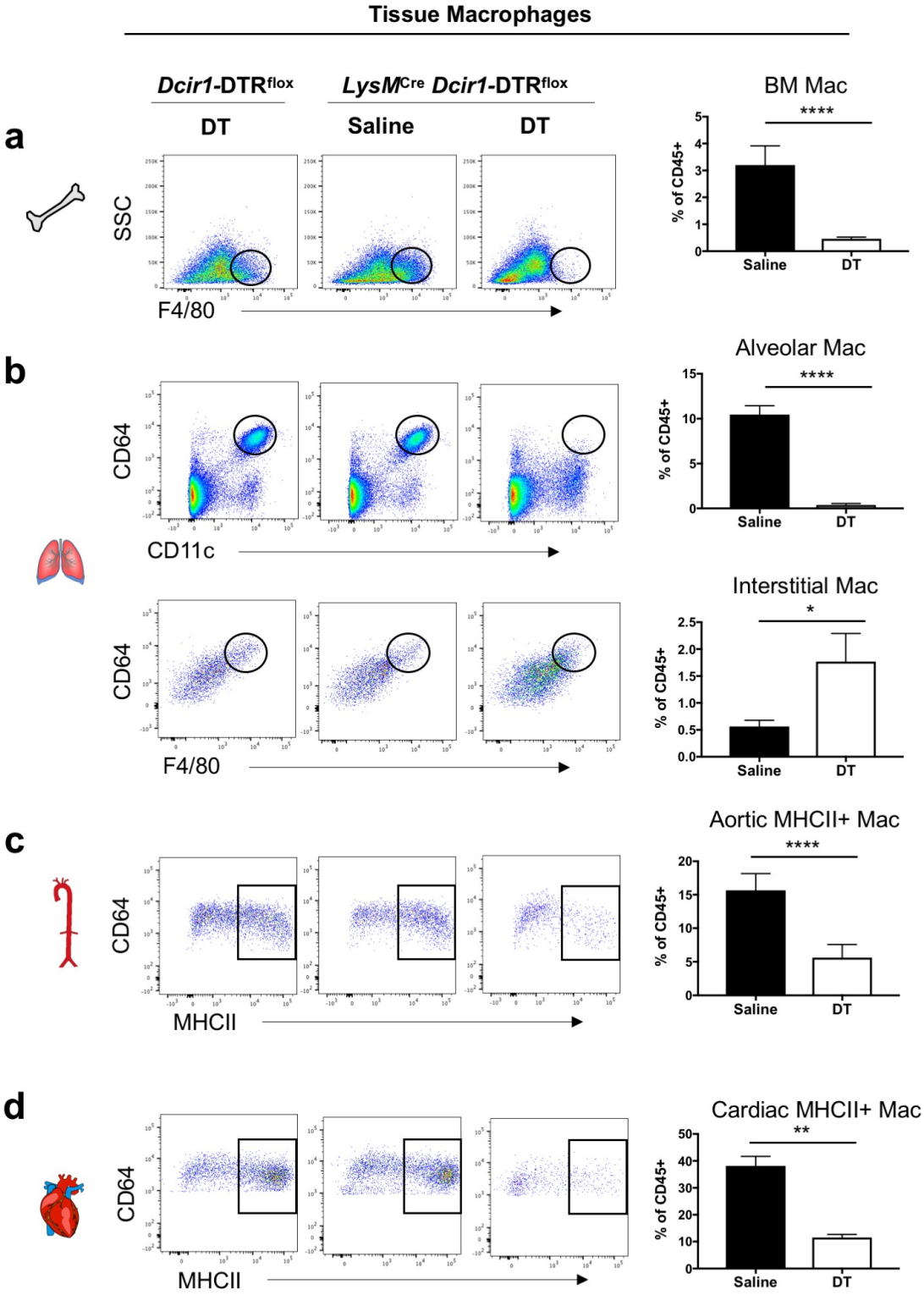


Figure 4.9 The DTR-mediated neutrophil ablation by intraperitoneal injection of DT in the BM, lungs and aorta of *LysM*^{Cre} *Dcir1*-DTR^{flox} mice.

LysM^{Cre} *Dcir1*-DTR^{flox} and *Dcir1*-DTR^{flox} mice were subjected to intravenous injection of 30ng/g diphtheria toxin (DT) or saline three times for a week. The cells from the BM, lungs and aorta of all mice were analysed by flow cytometry. The graphs present the percentage of neutrophils in **a)** the BM, **b)** lungs and **c)** aorta. The representative images show gating for neutrophils. Data are presented as mean±SEM. n=13. Mann-Whitney test.



(Continued on the next page)

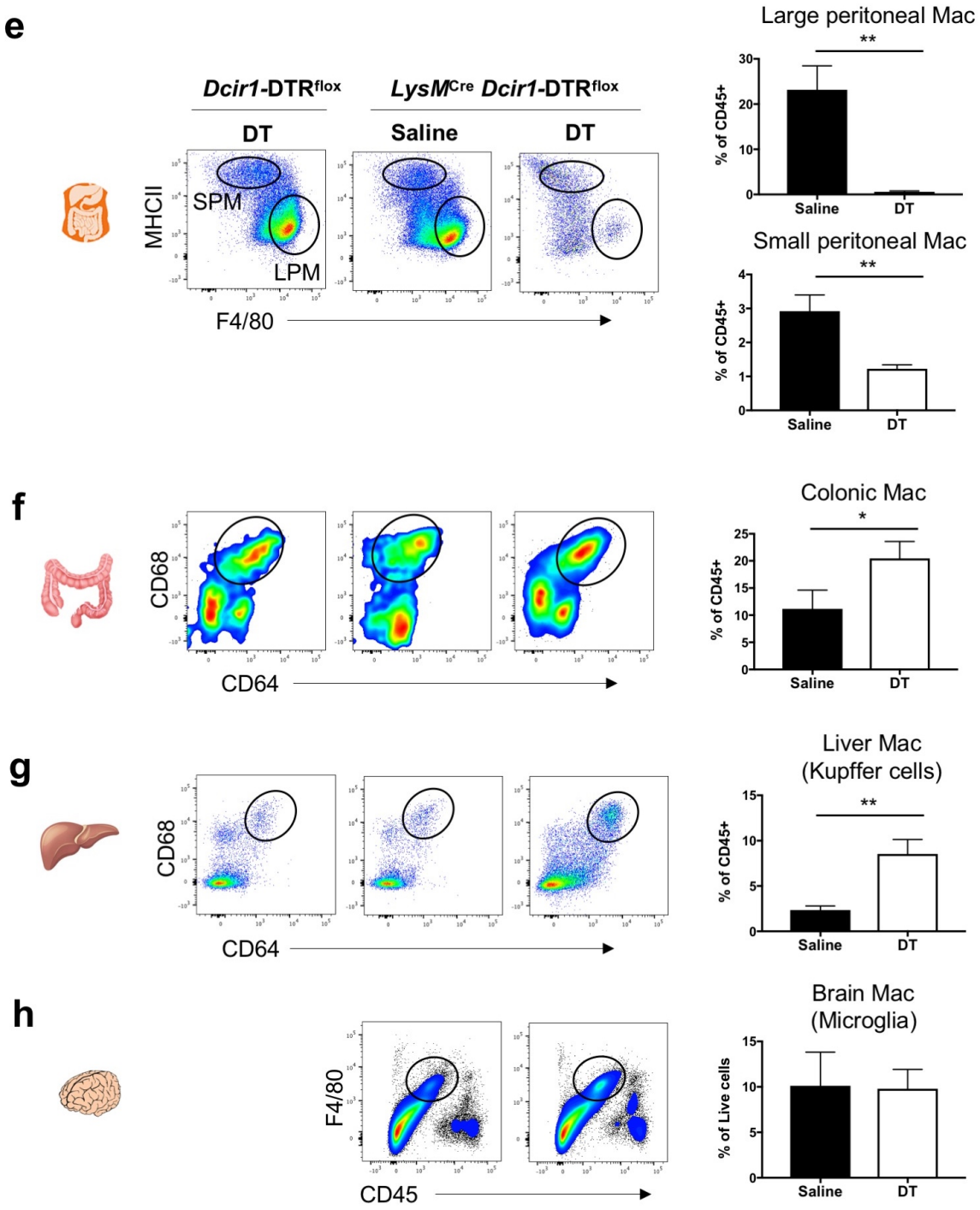


Figure 4.10 The DTR-mediated macrophage ablation by intraperitoneal injection of DT in the BM, lungs, aorta, heart, peritoneum, colon, liver and brain of *LysM*^{Cre} *Dcir1*-DTR^{flox} mice.

LysM^{Cre} *Dcir1*-DTR^{flox} and *Dcir1*-DTR^{flox} mice were subjected to intravenous injection of 30ng/g diphtheria toxin (DT) or saline three times for a week. The graphs present the percentage of macrophages in **a)** the BM, **b)** lungs and **c)** aorta, **d)** heart, **e)** peritoneum, **f)** colon, **g)** liver and **h)** brain. The representative images show gating for macrophages. Data are presented as mean±SEM. a-c) n=13-15, d-g) n=6-10, h) n=3. Mann-Whitney test. *P<0.05, **P<0.01 and ****P<0.0001.

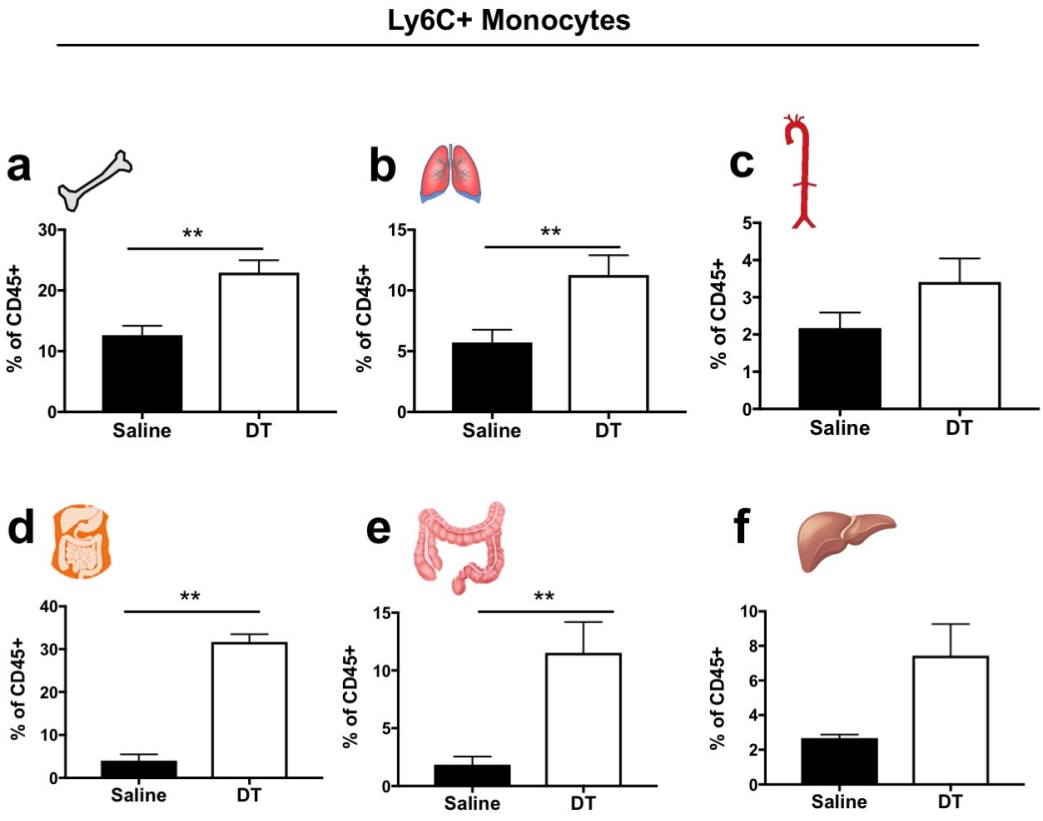


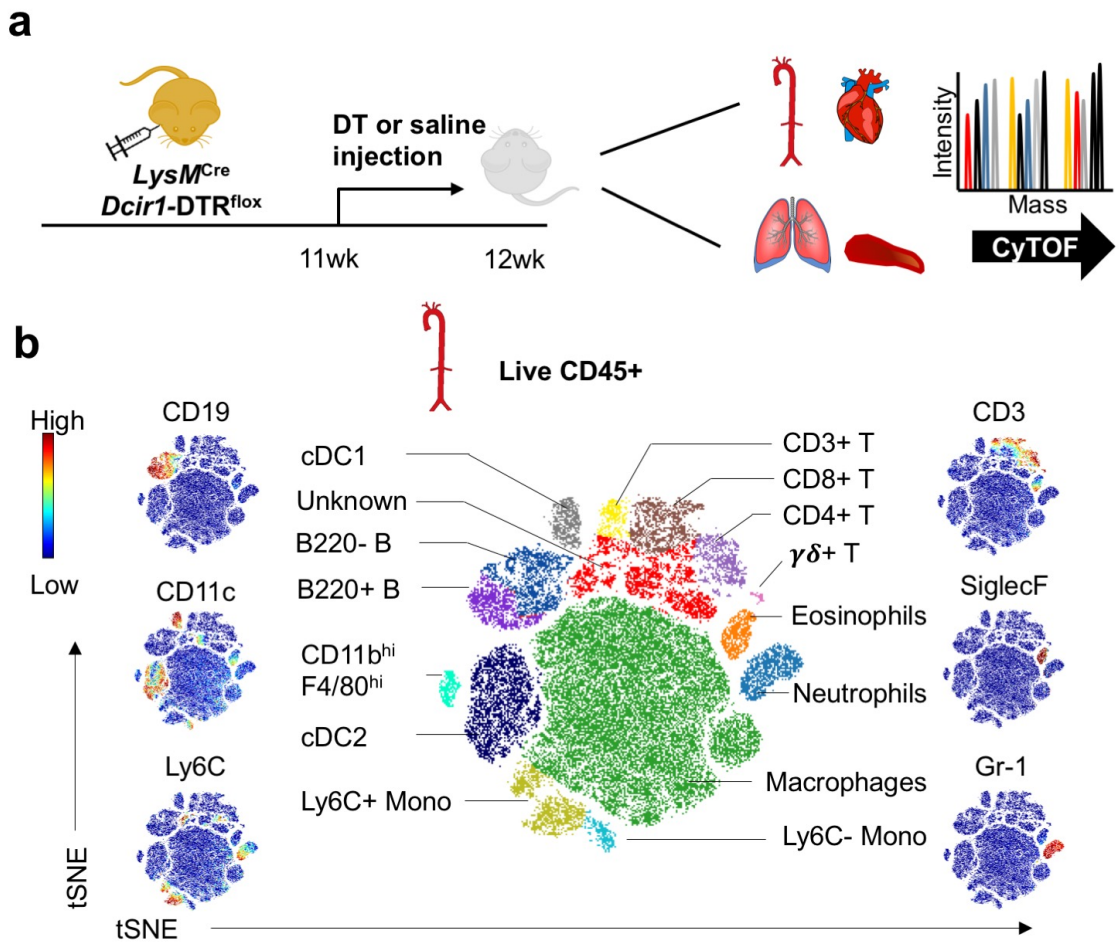
Figure 4.11 The effect of intraperitoneal injection of DT on monocytes from the BM, lungs, aorta, peritoneum, colon and liver of *LysM*^{Cre} *Dcir1*-DTR^{flox} mice.

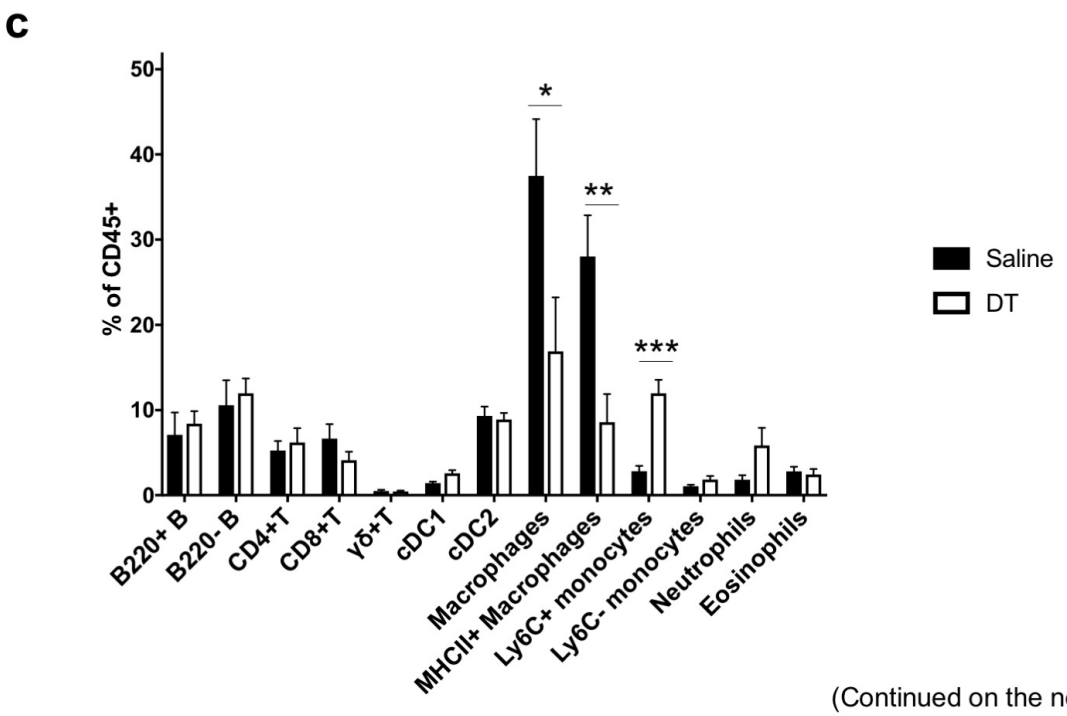
LysM^{Cre} *Dcir1*-DTR^{flox} and *Dcir1*-DTR^{flox} mice were subjected to intravenous injection of 30ng/g DT or saline three times for a week. The cells from the BM, lungs and aorta of all mice were analysed by flow cytometry. The graphs present the percentage of monocytes in **a)** the BM, **b)** lungs, **c)** aorta, **d)** peritoneum, **e)** colon and **f)** liver. Data are presented as mean±SEM. BM, peritoneum, colon n=7, lungs n=13, aorta: n=16, liver n=3. Mann-Whitney test. **P<0.01.

4.2.6. Full characterisation of the DCIR1-mediated depletion in the aorta, heart, lungs and spleen using mass cytometry

To fully characterise the DCIR1-LysM-mediated cell ablation, I utilised CyTOF with a panel of 35 markers and a multi-dimensional clustering algorithm, viSNE. *LysM*^{Cre} *Dcir1*-DTR^{flox} mice were subjected to saline or DT treatment three times for a week (**Figure 4.12a**). viSNE clustering identified 11 leucocyte populations in aortas of saline- and DT-treated mice; these include B220+ B cells (B1 B), B220+ B cells (B2 B), CD4+ T, CD8+ T, γδ+ T, type 1 conventional dendritic cells (cDC1), cDC2, macrophages, Ly6C+ monocytes, Ly6C- monocytes, neutrophils and eosinophils (**Figure 4.12b**). Administration of DT halved the total aortic macrophage population and significantly reduced MHCII expressing macrophages in *LysM*^{Cre} *Dcir1*-DTR^{flox} mice (saline vs. DT: total Mac: 37.5±6.7% vs. 16.9±6.3% ($P<0.05$), MHCII+ Mac: 28.0±4.8 vs. 8.6±3.3% ($P<0.01$); **Figure 4.12c**). Ly6C+ monocytes were increased by DT treatment in *LysM*^{Cre} *Dcir1*-DTR^{flox} mice relative to the saline group (saline vs. DT: 2.8±0.6% vs. 12.0±1.6% ($P<0.001$)). As shown in Chapter 2, aortic resident macrophages defined by positive expression of CD206 can be further separated into three subpopulations on the basis of the expression of CD209b and MHCII, comprising CD209b+ MHCII+, CD209b- MHCII+ and CD209b- MHCII-. Here, I showed that DT-mediated cell depletion was observed in CD209b+ MHCII+ and CD209b- MHCII+ subpopulations (**Figure 4.12d**). Surprisingly, macrophages that expressed CD44, an adhesion receptor that recognises hyaluronan, were resistant to DT treatment (**Figure 4.12e**). This new subset expressed low levels of DCIR1 and lacked MHCII expression. The concept of “monocyte waterfall” illustrates the differentiation of monocytes into macrophages by expression of Ly6C and MHCII or CD64, which was originally described in a murine model of colitis (Tamoutounour et al., 2012). I adopted the

monocyte waterfall gate to describe the monocyte differentiation, and showed Ly6C+ monocytes acquiring macrophage marker CD64 in the DT group (**Figure 4.12f)**. Taken together, Ly6C+ CD64+ cells in the DT-treated group also expressed CD44, demonstrating the potential link that monocytes can differentiate into CD44+ macrophages in the aorta.





(Continued on the next page)

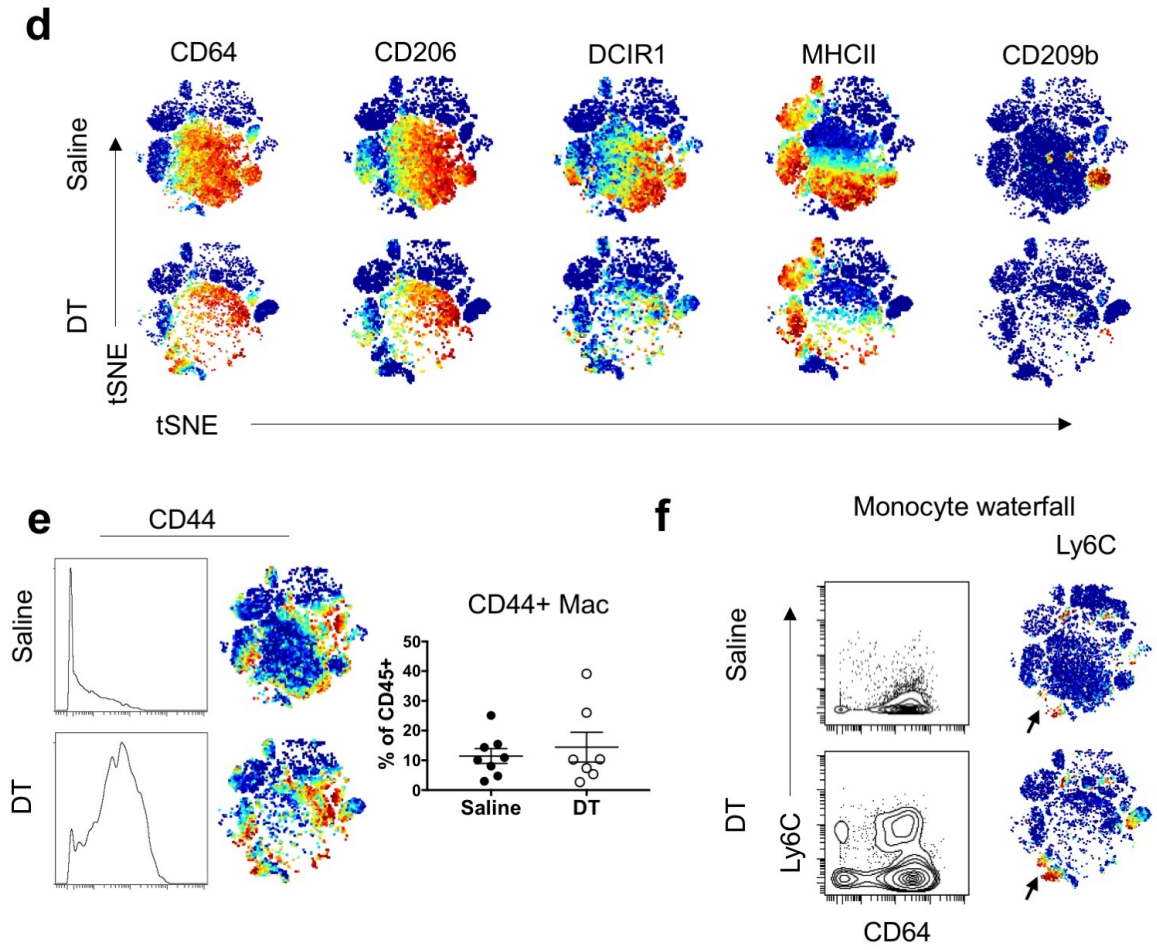


Figure 4.12 In-depth characterisation of macrophage depletion in the aorta of the *LysM*^{Cre} *Dcir1*-DTR^{flox} strain by mass cytometry.

a) *LysM*^{Cre} *Dcir1*-DTR^{flox} mice were subjected to saline or 30 ng/g DT treatment for a week and single cells from the aorta, heart, lungs and spleen of these mice were analysed by mass cytometry (CyTOF). **b)** The viSNE plots of live CD45+ aortic cells from the saline and DT-treated mice showing 15 cell clusters and selected marker expression. **c)** The graph displaying the percentage of identified populations by treatment group. **d)** The expression of DCIR1, MHCII and CD209b. **e)** CD44 expression by histogram plots in macrophages and by viSNE in live CD45+ cells. The graph shows the proportion of CD44+ macrophages. **f)** Monocyte waterfall is illustrated in contour plots by the expression of Ly6C and CD64 in the CD11b+ CD68+ DC- cells. Ly6C expression is presented in viSNE plots of live CD45+ cells. Data are presented as mean±SEM. Mann-Whitney test. *P<0.05, **P<0.01, ***P<0.001.

In-depth immunophenotyping of leucocytes from the heart, lungs and spleen from saline- or DT-treated *LysM*^{Cre} *Dcir1*-DTR^{flox} mice was also performed using CyTOF and viSNE. In the live CD45+ cells from the heart, 12 leucocyte populations were identified, comprising B1 B, B2 B, CD4+ T, CD8+ T, γδ+ T, natural killer (NK), cDC1, cDC2, macrophages, Ly6C+ monocytes, neutrophils and eosinophils (**Figure 4.13a**). Following DT treatment, cardiac macrophages were ablated by 63.9±9.3% and MHCII+ subset was also significantly depleted by 81.1±9.0% (**Figure 4.13b**). Unexpectedly, eosinophils were also ablated by DT treatment ($P<0.05$) despite their low expression of DCIR1 (**Figure 4.13b; Figure 4.4**). The B and T cell compartment, together with cDC2 was increased by DT treatment.

In the lungs, 13 leucocyte populations were identified, and these are B cells, CD4+ T, CD8+ T, γδ+ T, NK, cDC1, cDC2, AM, IM, Ly6C+ monocytes, Ly6C- monocytes, neutrophils and eosinophils (**Figure 4.14a)**. Over 70% of AM were ablated by DT treatment ($P<0.001$) (**Figure 4.14b**). B cells and eosinophils were also ablated, which was not observed in the data by flow cytometry. Since B cells and eosinophils do not express DCIR1, the proportion of these populations may have been affected by the secondary response to DT-mediated cell death (**Figure 4.14b; Figure 4.4**).

Finally, viSNE clustering identified 14 immune cell populations in the spleen consisting of B1 B, B2 B, CD4+ T, CD8+ T, γδ+ T, NK, pDCs, cDC1, cDC2, macrophages, Ly6C+ monocytes, Ly6C- monocytes, neutrophils and eosinophils (**Figure 4.15a**). There might be a mild effect of DT on T cell populations, showing a reduction in both CD4+ and CD8+ T lymphocytes in the DT group (both $P<0.05$; **Figure 4.15c**). DT treatment

significantly ablated the macrophage population from 5.1±0.7% to 2.1±0.5% of total myeloid cells (P<0.01; **Figure 4.15c**).

Notably, ablation of macrophages in the aorta and lungs promotes Ly6C+ monocyte recruitment to the tissue. This observation was consistent with the data from flow cytometry and was also detected in the BM, peritoneum, colon and liver (**Figure 4.12, Figure 4.14; Figure 4.11**).

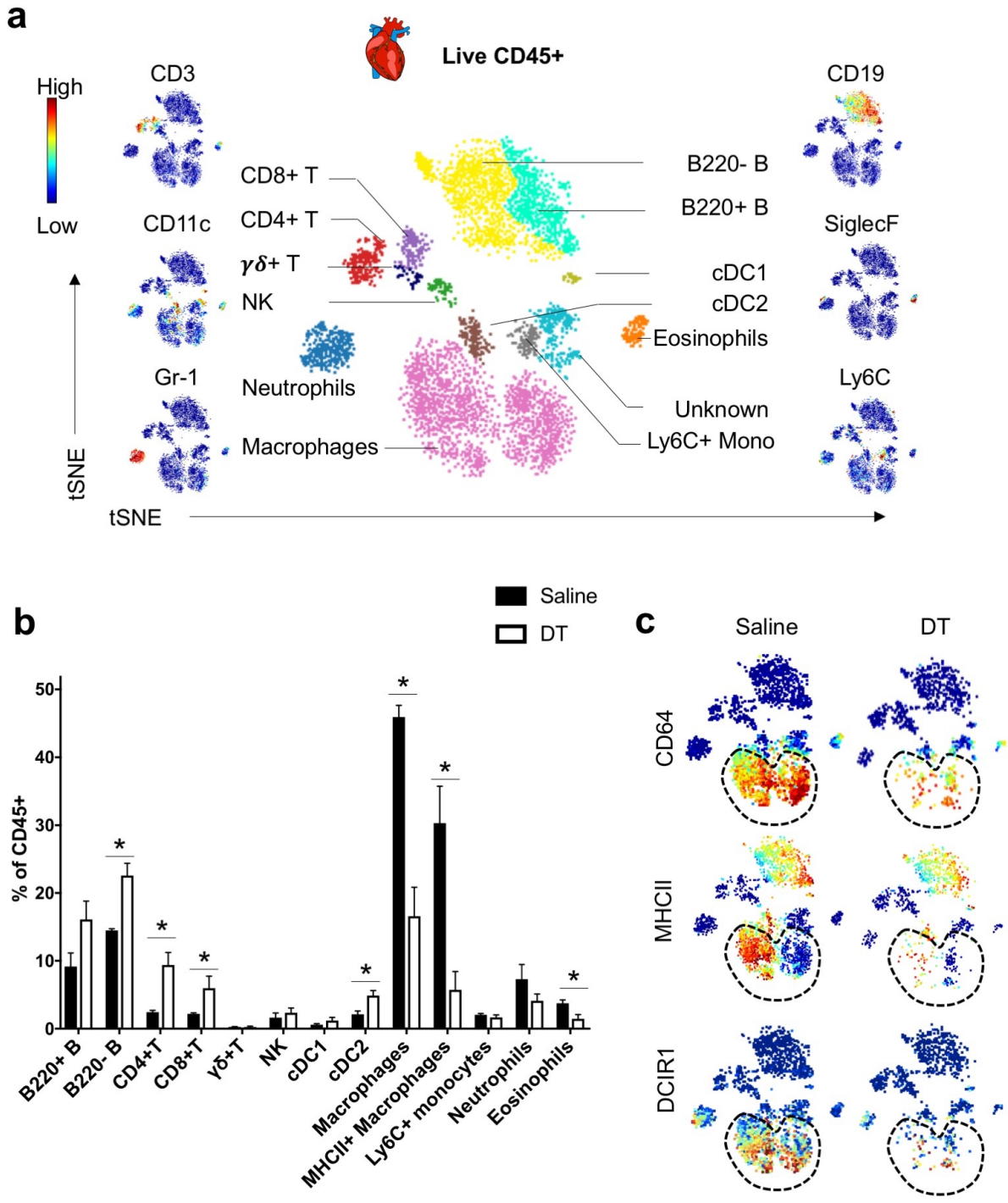


Figure 4.13 In-depth characterisation of macrophage depletion in the heart of the *LysM*^{Cre} *Dcir1*-DTR^{flox} strain by mass cytometry.

a) The viSNE plots of live CD45+ cardiac cells from the saline and 30 ng/g DT-treated *LysM*^{Cre} *Dcir1*-DTR^{flox} mice showing 13 cell clusters and selected marker expression. **b)** The graph displaying the percentage of identified populations by treatment group. **c)** viSNE plots displaying the expression of CD64 and MHCII in live CD45+ cells by treatment. Data are presented as mean±SEM. n=4. Mann-Whitney test. *P<0.05.

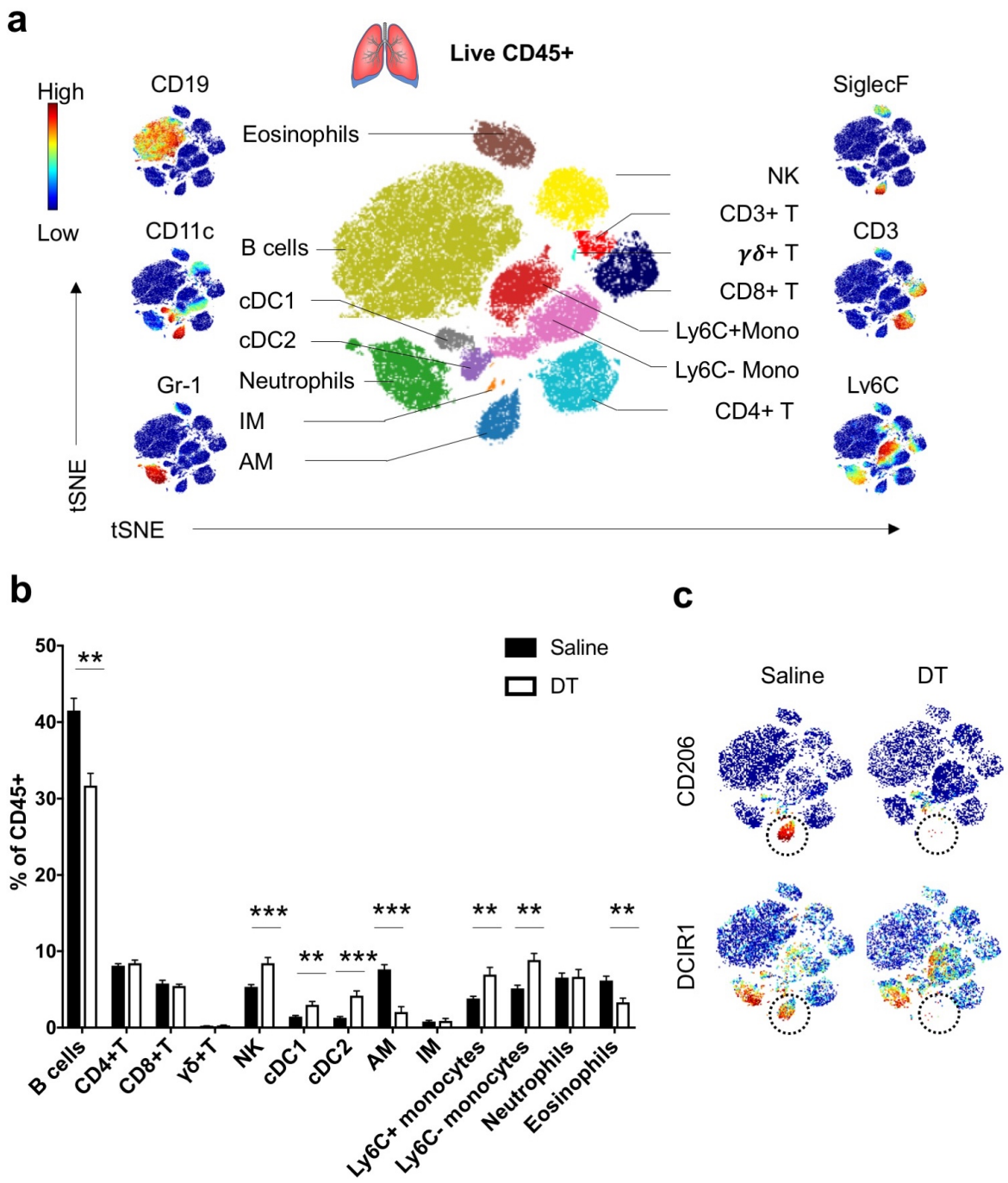


Figure 4.14 In-depth characterisation of macrophage depletion in the lungs of the *LysM*^{Cre} *Dcir1*-DTR^{flox} strain by mass cytometry.

a) The viSNE plots of live CD45+ cells from lungs of the saline and 30 ng/g DT-treated *LysM*^{Cre} *Dcir1*-DTR^{flox} mice showing 14 cell clusters and selected marker expression. **b)** The graph displaying the percentage of identified populations by treatment group. **c)** viSNE plots displaying CD206 expression in live CD45+ cells by treatment group. Data are presented as mean±SEM. n=8. Mann-Whitney test. **P<0.01, ***P<0.001.

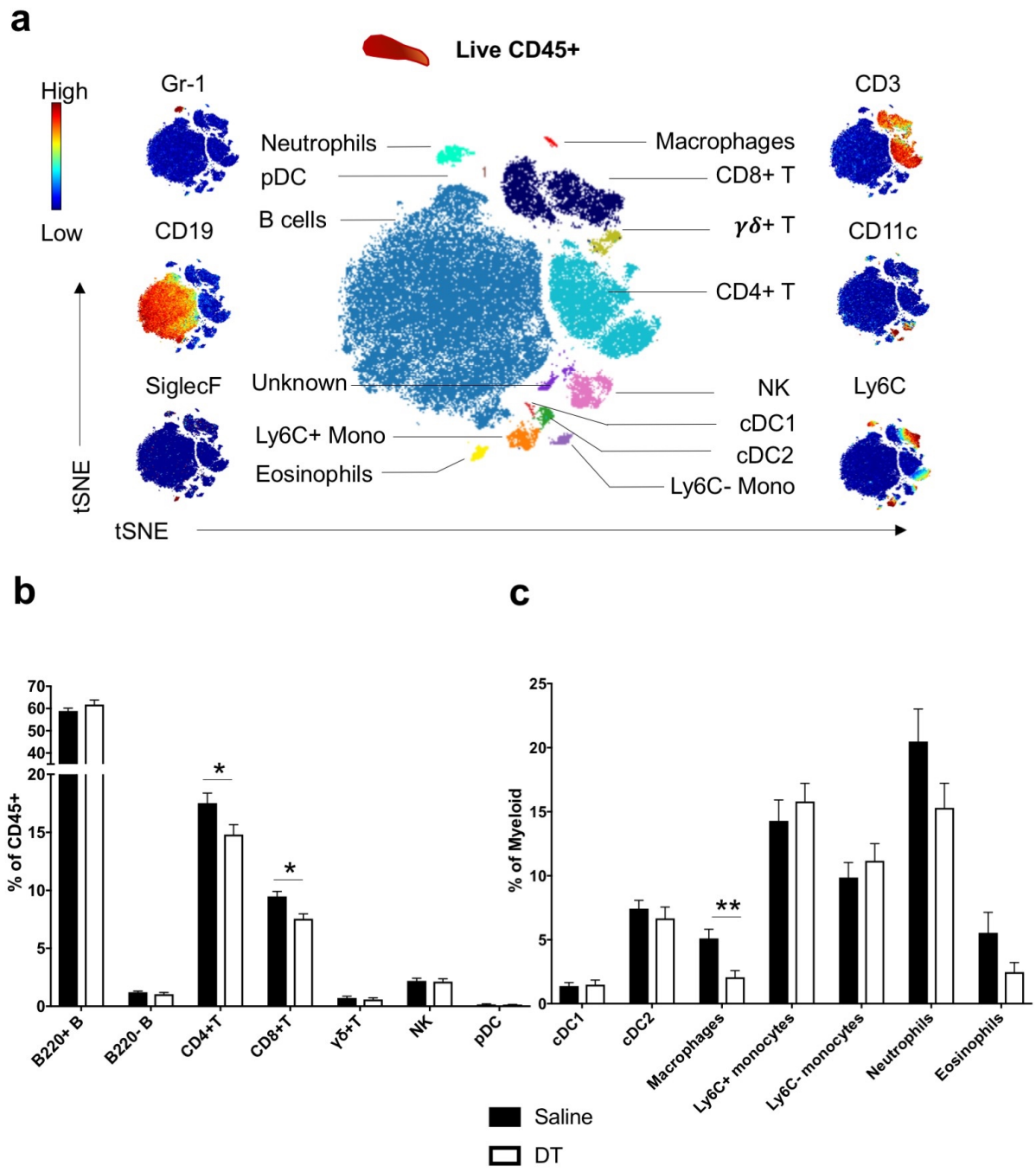


Figure 4.15 In-depth characterisation of macrophage depletion in the spleen of the *LysM*^{Cre} *Dcir1*-DTR^{flox} strain by mass cytometry.

a) The viSNE plots of live CD45+ cells from the spleen of the saline and 30 ng/g DT-treated *LysM*^{Cre} *Dcir1*-DTR^{flox} mice showing 14 cell clusters and selected marker expression. **b)** The graph displaying the percentage of leucocyte populations by treatment group. **c)** The myeloid lineage was further gated and were analysed by viSNE separately and the graph presents the percentage of the myeloid populations in the saline and DT-treated mice. Data are presented as mean±SEM. n=8. Mann-Whitney test. *P<0.05, **P<0.01.

4.2.7. Ablated macrophages are bone marrow-derived in the post-irradiation setting

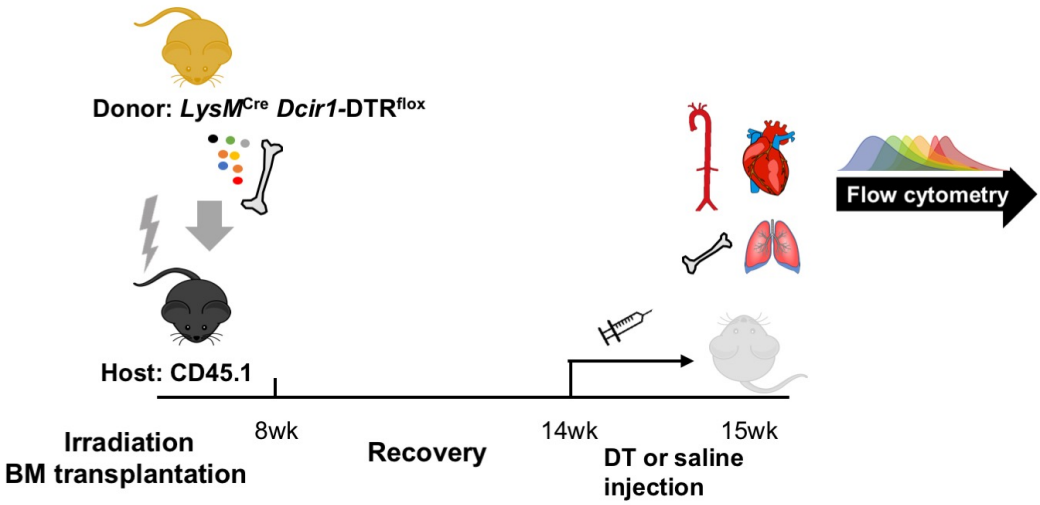
Next, I performed a set of depletion experiments in BM chimera mice to gain further insights in the origin and differentiation of the target macrophage populations. To this end, CD45.1 congenic mice on a C57Bl/6J background were sub-lethally irradiated and received the BM of *LysM*^{Cre} *Dcir1*-DTR^{flox} mice (CD45.2) (**Figure 4.16a**). The mice recovered for 6 weeks and were then subjected to saline or DT treatment three times for a week. A control group of *LysM*^{Cre} *Dcir1*-DTR^{flox} mice that did not undergo irradiation and BM transplantation were also treated with saline or DT to compare the efficacy of DTR-mediated ablation.

Single cells from the aorta, heart, lungs and the BM were retrieved and were analysed by flow cytometry. The chimerism of the mice was calculated based on live single cells expressing CD45.1 (host) and lacking CD45.2 (donor) in all tissues. The reconstitution rates in tissues of chimera mice were 97.4±0.2% in the aorta, 98.5±0.2% in the heart, 96.2±0.3% in the lungs and 99.5±0.0% in the BM (**Figure 4.16b**). In general, the majority of host derived cells which were radio-resistant were CD11b- lymphocyte markers+ MHCII- and low in side scatter in the heart, lungs and BM. In the BM, these cells were positive for CD3, which confirmed that the majority of surviving host cells were T lymphocytes. Interestingly, host-derived radio-resistant macrophages were only found in the aorta, accounting approximately 28.5±1.4% of macrophages in chimeras (**Figure 4.16c**). Newly repopulated aortic macrophages from the donor BM expressed MHCII and DCIR1. While macrophages in the heart and lungs were fully reconstituted in chimera mice over 6 weeks, percentages of macrophages in the aorta and BM were lower than their non-chimera counterparts (**Figure 4.16d,e,f,g**). This

indicated that reconstitution of aortic macrophages required longer than 6 weeks' post-irradiation.

In general, tissue macs were depleted at a lower rate in the DT-treated chimera compared than non-chimeras (% of macrophage ablation in chimeras vs. non-chimera: MHCII+ AoM: 26.2±5.4% (P=0.132) vs. 76.1±3.6% (P<0.01), MHCII+ CM: 57.5±7.7% (P<0.01) vs. 88.4±1.9% (P<0.01), AM: 64.1±10.2% (P<0.05) vs. 98.8±0.2% (P<0.01), BMM: 46.1±13.1% (P<0.01) vs. 95.0±1.3% (P<0.01); **Figure 4.16d,e,f,g**). Newly recruited macrophages in the heart, lungs and BM also acquired DCIR1 expression (**Figure 4.16h**). Therefore, the decreased efficiency of macrophage ablation in all organs suggested that the repopulated macrophages at 6 weeks have not yet acquired gene expression levels of *Dcir1* and *Lyz2* (LysM) at levels needed for ablation.

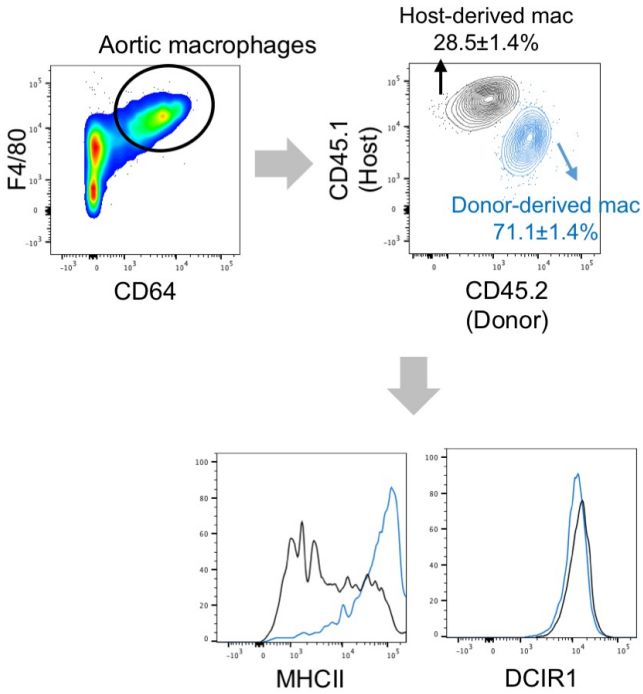
a



b

	Aorta	Heart	Lungs	BM
% Reconstitution	97.4±0.2	98.5±0.2	96.2±0.3	99.5±0.0

c



(Continued on the next page)

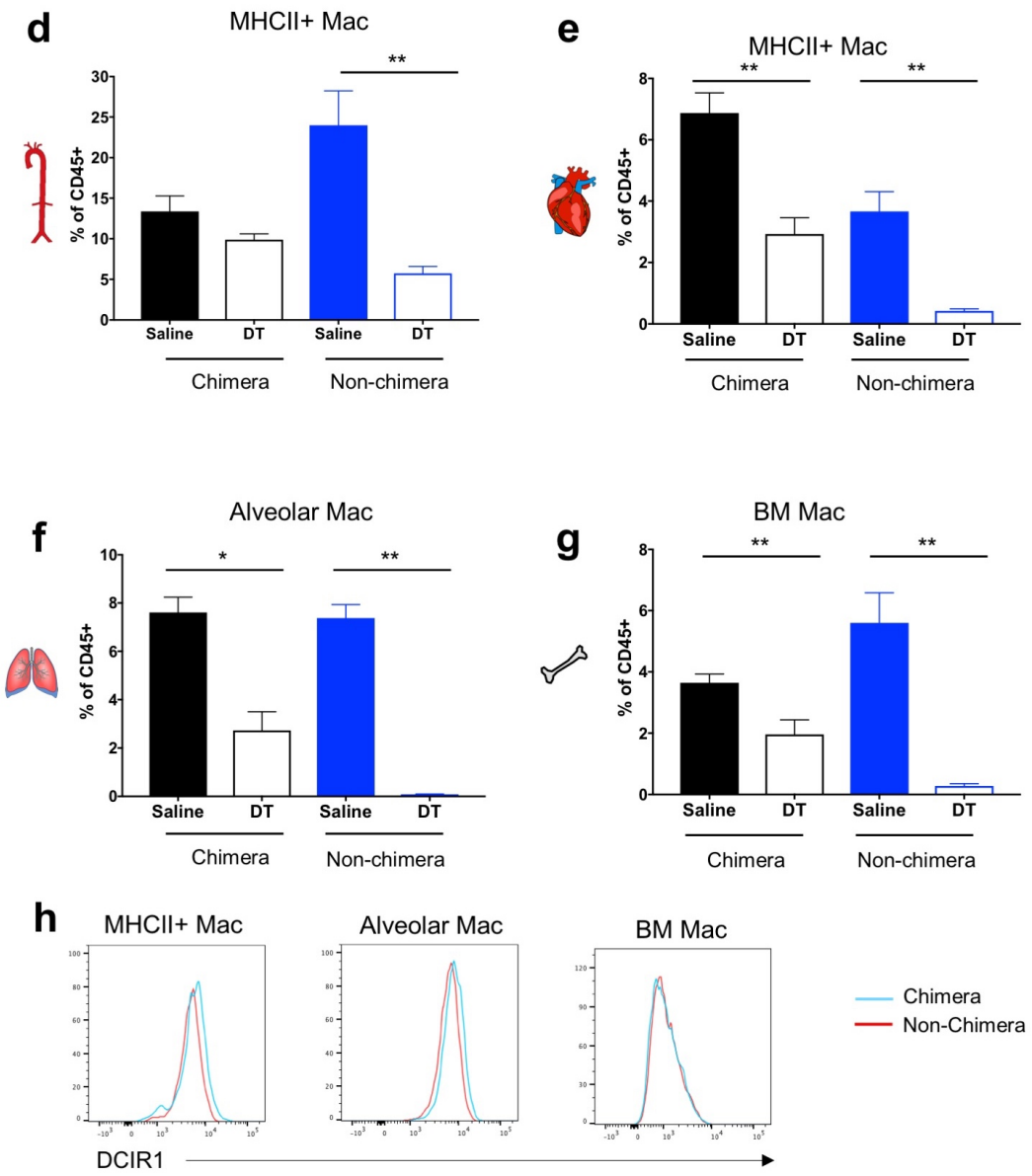


Figure 4.16 Ablation of macrophages from the aorta, heart, lungs and BM of the chimera mice that received the BM from *LysM*^{Cre} *Dcir1*-DTR^{flox} mice.

a) Recipient CD45.1 congenic mice were sub-lethally irradiated and the BM *LysM*^{Cre} *Dcir1*-DTR^{flox} mice was transplanted into the host mice. Following 6 weeks, the chimera mice were subjected to saline or DT treatment for a week. Aortas, hearts, lungs and BM were collected from the chimera. As a control, *LysM*^{Cre} *Dcir1*-DTR^{flox} mice that did not undergo irradiation also received saline or DT treatment for a week and the same organs from the non-chimera mice were also collected. Leucocyte populations in these organs were analysed by flow cytometry. **b)** The reconstitution rates in each organ. **c)** The origin of aortic macrophages on the basis of the expression of host marker CD45.1 and donor marker CD45.2. The MFI of MHCII and DCIR1 is presented in the histogram plot. Percentages of macrophages in the **d)** aorta, **e)** heart, **f)** lungs and **g)** BM. **h)** DCIR1 expression in macrophages in chimera vs. non-chimera mice. Data are presented as mean±SEM. n=6. Mann-Whitney test. *P<0.05, **P<0.01.

To exclude that donor mismatch was a cause for delay in repopulation of the chimera (Jafri et al., 2017), I performed another chimera experiment where all mice were on a CD45.2 background. *LysM*^{Cre} *Dcir1*-DTR^{flox} and *Dcir1*-DTR^{flox} mice were sub-lethally irradiated and received the BM from each other (*LysM*^{Cre} *Dcir1*-DTR^{flox} mice were given the BM from *Dcir1*-DTR^{flox} and vice versa; **Figure 4.17a**). Aortic and cardiac macrophages were replenished at the same level as mice that did not undergo irradiation while the alveolar macrophage niche required longer recovery (**Figure 4.17b**). Macrophage ablation in the aorta and hear was attained at the same rate in comparison with non-chimeras (**Figure 4.17b**). Although full reconstitution was not achieved in alveolar macrophages, DT treatment depleted these cells in chimera mice.

Altogether, I showed that reconstituted macrophages from the BM of *LysM*^{Cre} *Dcir1*-DTR^{flox} mice could be ablated in response to DT treatment. The expression of DCIR1 was not confined only in BM-derived origin of macrophages since it was also expressed by host-derived macrophages that were negative for MHCII expression.

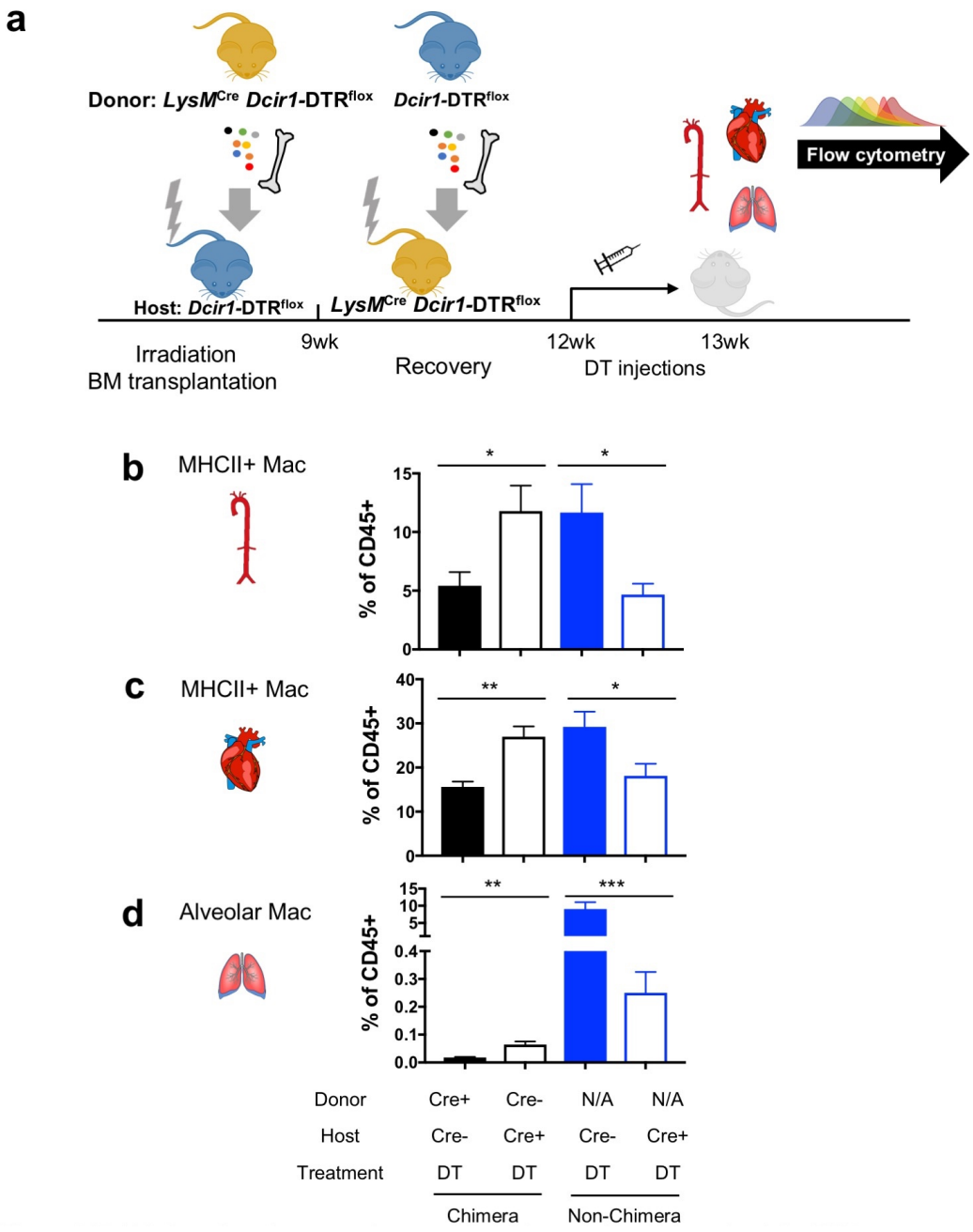


Figure 4.17 Ablation of aortic macrophages of the chimera mice that received the BM from *LysM*^{Cre} *Dcir1*-DTR^{flox} or *Dcir1*-DTR^{flox} mice.

a) *LysM*^{Cre} *Dcir1*-DTR^{flox} or *Dcir1*-DTR^{flox} mice were sub-lethally irradiated and the BM were transplanted as follows. The BM from *LysM*^{Cre} *Dcir1*-DTR^{flox} mice to *Dcir1*-DTR^{flox} mice or the BM from *Dcir1*-DTR^{flox} mice to *LysM*^{Cre} *Dcir1*-DTR^{flox} mice. Following 3 weeks, the chimera mice were subjected to DT treatment for a week. Aortas, hearts, and lungs were collected from the chimera and leucocyte populations were analysed by flow cytometry. *LysM*^{Cre} *Dcir1*-DTR^{flox} or *Dcir1*-DTR^{flox} mice that did not undergo irradiation also received DT treatment and the same tissues were analysed together. The graph shows the percentage of macrophages in the **b)** aorta, **c)** heart and **d)** lungs. Data are presented as mean±SEM. n=6. Mann-Whitney test. *P<0.05, **P<0.01, ***P<0.001.

4.3. DCIR1-mediated macrophage ablation in acute arterial injury model and atherosclerosis

4.3.1. The effect of macrophage depletion on acute arterial injury model

To understand the role of arterial macrophages in the injured artery, a non-occlusive polymer tube (Tygon) was placed around the left common carotid artery of 15-week old WT and *LysM*^{Cre} *Dcir1*-DTR^{flox} mice. After 3 days of recovery, these mice received saline or DT injections 9 times for three weeks (**Figure 4.18a**). The injured artery was cryosectioned and was stained in elastin Van Gieson (EVG) dye to determine the size of artery and neo-intima formation. Casting the artery with Tygon tubing promoted recruitment of blood borne cells on the site of injury and the neo-intima formation in the injured artery. The recruited cells formed the fibrotic tissue surrounding the tubing for three weeks. The upper part of the injured carotid immediately above the Tygon tube was assessed since this area above the tubing developed neo-intima. The aorta, perivascular tissues around the injured artery and deep cervical lymph nodes (DCLN) that are adjacent the injured artery were analysed by flow cytometry.

There were no apparent differences in body weight of three groups during the course of surgery and injections (**Figure 4.18b**). The average of neo-intima, media, the intima/media ratio (IMR) and arterial size was calculated from 10 sections of the carotid tissue, which is distal to the upper part of the cast. There were no differences in the formation of neo-intima, medial area, IMR and arterial size in three experiment groups (**Figure 4.18c,d,e,f,g**).

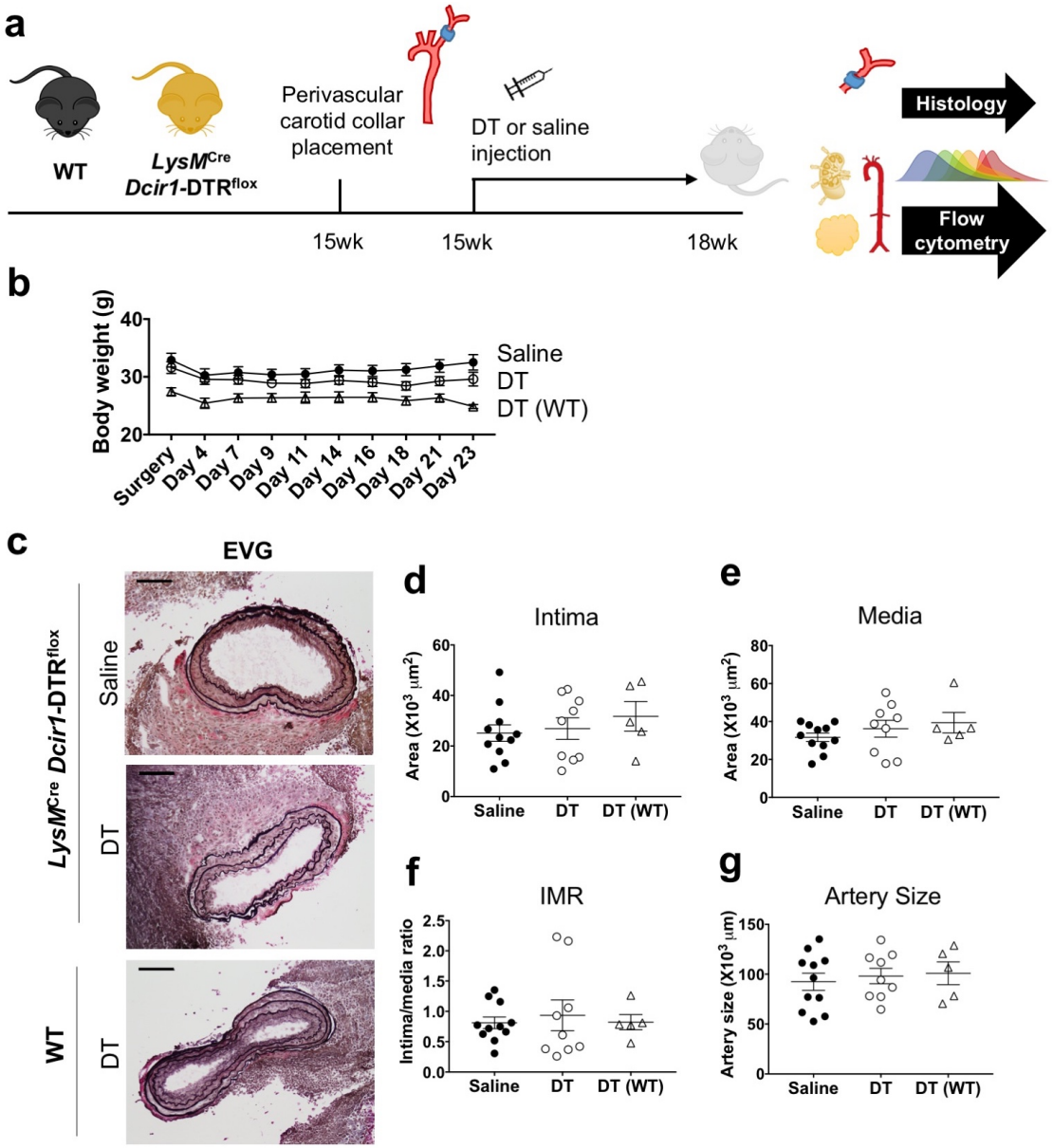


Figure 4.18 The effect of macrophage depletion on perivascular collar-induced injury model using *LysM*^{Cre} *Dcir1*-DTR^{flox} mice.

a) Wild type (WT) *LysM*^{Cre} *Dcir1*-DTR^{flox} mice underwent perivascular collar surgery in the left carotid (described in Materials and Methods) and 3 days after the surgery, the mice received saline or 30 ng/g DT treatment for 3 weeks. The injured carotid arteries were collected for histology. Cells dissociated from aortas, deep cervical lymph nodes (DCLN) and perivascular fibrotic tissues were analysed by flow cytometry. **b)** Body weight of mice that underwent surgery for 23 days. **c)** Sections of injured carotid were stained in elastin Van Gieson (EVG) dye to visualise elastic laminas and neo-intima. The images are representative of 5-11 mice each group and were taken at 20X magnification. Scale bars indicate 100µm. Graphs show the area of **d)** intima and **e)** media and **f)** the ratio of intima/media (IMR). **g)** The arterial size is shown in three groups. Data are presented as mean±SEM. Mann-Whitney test.

During arterial injury-induced inflammation, macrophage ablation was not achieved in the aorta of the DT-injected *LysM*^{Cre} *Dcir1*-DTR^{flox} mice (**Figure 4.19a**). DCIR1 antibody was added in the last experiment to confirm the level of DCIR1 in aortic macrophages of the surgical mice. DCIR1 was detected in aortic macrophages in all mice. However, DCIR1 expression in the DT-treated *LysM*^{Cre} *Dcir1*-DTR^{flox} was moderately lower than two control groups (**Figure 4.19b**). Furthermore, SiglecF is an alveolar macrophage-specific marker and newly recruited alveolar macrophages express less SiglecF (van de Laar et al., 2016, Misharin et al., 2017). In the same experiment, alveolar macrophages from DT-treated *LysM*^{Cre} *Dcir1*-DTR^{flox} mice expressed lower levels of SiglecF relative to two control groups. This observation indicated that DTR-mediated cell depletion occurred in the aorta and lungs and the macrophage pool was replenished by monocytes in 3 weeks. Cells from fibrotic tissues adjoining the injured carotid were also analysed and the showed that DT treatment had no impact on the composition of macrophages, DC, Ly6C+ monocytes, neutrophils and eosinophils (**Figure 4.19c**). The proportion of macrophages and DC from DCLN was also not affected by DT treatment (**Figure 4.19d**).

In summary, DTR-mediated macrophage depletion in the artery did not reduce intimal hyperplasia in an injury model, suggesting that either that DCIR expression was reduced in resident macrophages upon injury hampering their depletion in this particular strain, or that resident vascular macrophages did not have a role in this process.

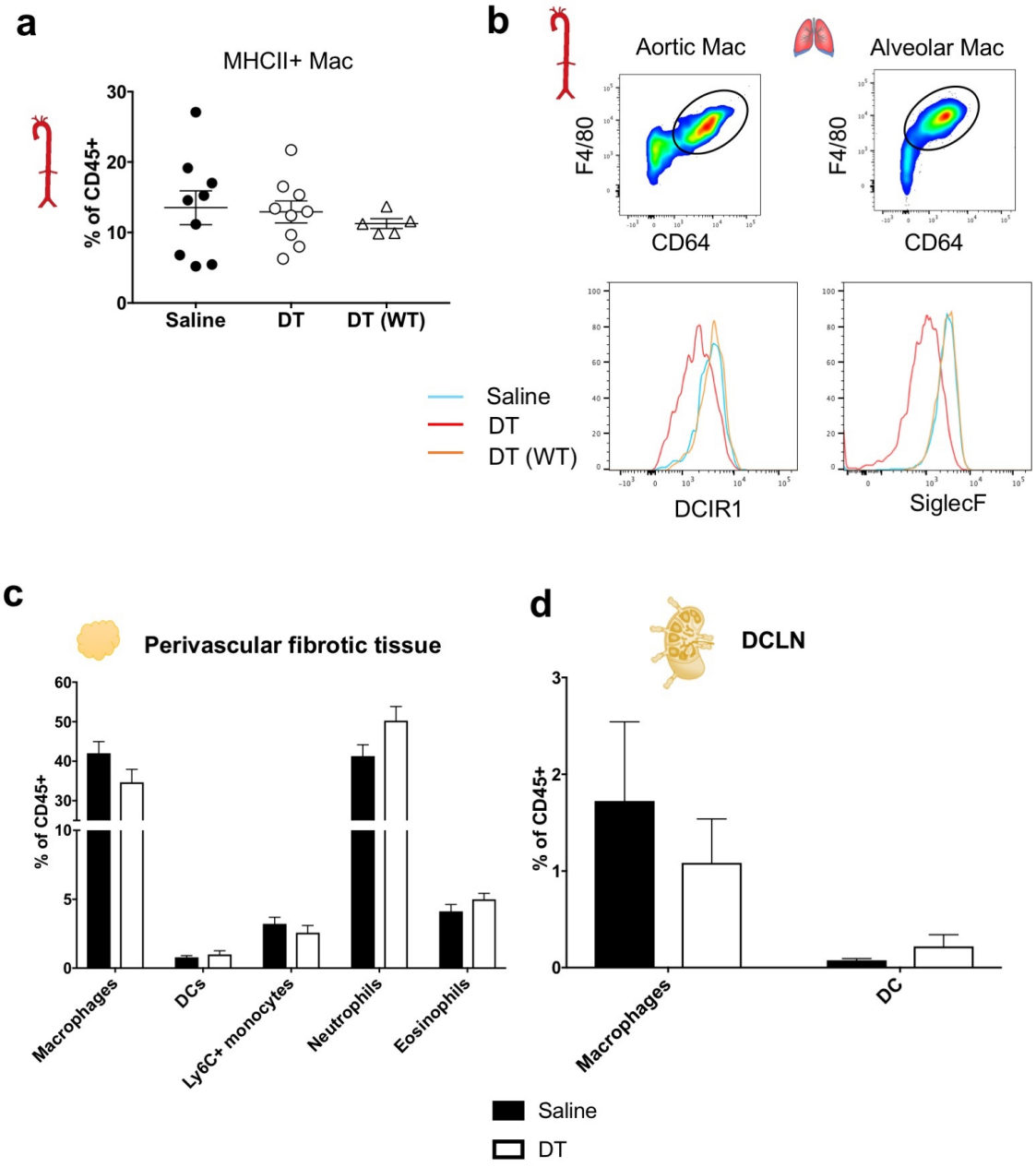


Figure 4.19 Macrophage depletion on perivascular collar-induced injury model using *LysM*^{Cre} *Dcir1*-DTR^{flox} mice.

WT and *LysM*^{Cre} *Dcir1*-DTR^{flox} mice underwent perivascular collar surgery in the left carotid and 3 days after the surgery, the mice received saline or 30 ng/g DT treatment for 3 weeks. Cells dissociated from aortas, deep cervical lymph nodes (DCLN) and perivascular fibrotic tissues were analysed by flow cytometry. **a)** Percentages of macrophages in the aorta. **b)** The expression level of DCIR1 in aortic macrophages and SiglecF in alveolar macrophages in three groups. Percentages of myeloid cell populations in **c)** perivascular fibrotic tissues and **d)** DCLN. Data are presented as mean±SEM. n=8-9 each group. Mann-Whitney test.

4.3.2. Lethality of long term macrophage depletion in atherosclerotic mice

In an effort to assess whether the absence of resident macrophages affects the development of atherosclerosis, the *LysM*^{Cre} *Dcir1*-DTR^{flox} strain was crossed on an *ApoE*$^{-/-}$ background (Materials and Methods Figure 7.3). A set of BM chimera experiments were performed by using *ApoE*$^{-/-}$ mice as a host and *ApoE*$^{-/-}$ *LysM*^{Cre} *Dcir1*-DTR^{flox} (KO HET KI) mice as a donor (**Figure 4.20a**). 8-week old *ApoE*$^{-/-}$ males were sub-lethally irradiated and received the BM from KO HET KI mice. Following 2 weeks, high cholesterol diet (high fat diet (HFD)) was provided to accelerate atherogenesis for 12 weeks. After 6 weeks of HFD, the chimera mice were to receive saline or DT three times weekly for 6 weeks. However, a considerable number of mice reached the critical threshold of 20% of body weight loss, and the experiments were terminated 3 weeks earlier than originally planned (**Table 4.1**). DT-treated mice exhibited difficulty in breathing and two of six mice treated with DT may have suffered from atelectasis (lung collapse), which was confirmed during the dissection. Further analysis suggested alveolar proteinosis as a potential cause of early demise, secondary to the ablation of alveolar macrophages due to the long-term course necessary for atherosclerotic studies. Lesion size and plaque features of the aortic root were examined by histology, and macrophage depletion was also tested by flow cytometry. Summary of the histology and cytometry data is available in **Table 4.2 and 4.3**.

In the aorta, CD206+ “resident” macrophages and their MHCII expressing subset were significantly ablated by DT treatment (Saline vs. DT: resident Mac: 30.2±4.3% vs. 16.9±2.7% ($P<0.05$), MHCII+ Mac: 10.3±1.7% vs. 3.2±0.9% ($P<0.01$); **Figure 4.20b**).

In contrast, “lesional” macrophages expressing CD11c were resistant to DT. Resident macrophage ablation did not induce Ly6C+ monocyte influx in the atherosclerotic aorta (**Figure 4.20c**). The large proportion of AM in the lungs diminished by DT treatment, which may have resulted in lung collapse in the hypercholesterolaemic condition (**Table 4.2**).

Due to the early termination of the experiment, no statistically significant differences were observed in lesion formation in the aortic root of chimera mice (**Figure 4.20d**). The area expressing CD68, CD206, or CD11c within the lesion of the aortic root was not affected by treatment, supporting that lesional macrophages were not depleted in the DT-treated mice (**Figure 4.20e; Table 4.3**). The lipid content and necrotic core size of the aortic roots were also not changed. A non-significant increase in vessel size of the DT-treated mice was observed.

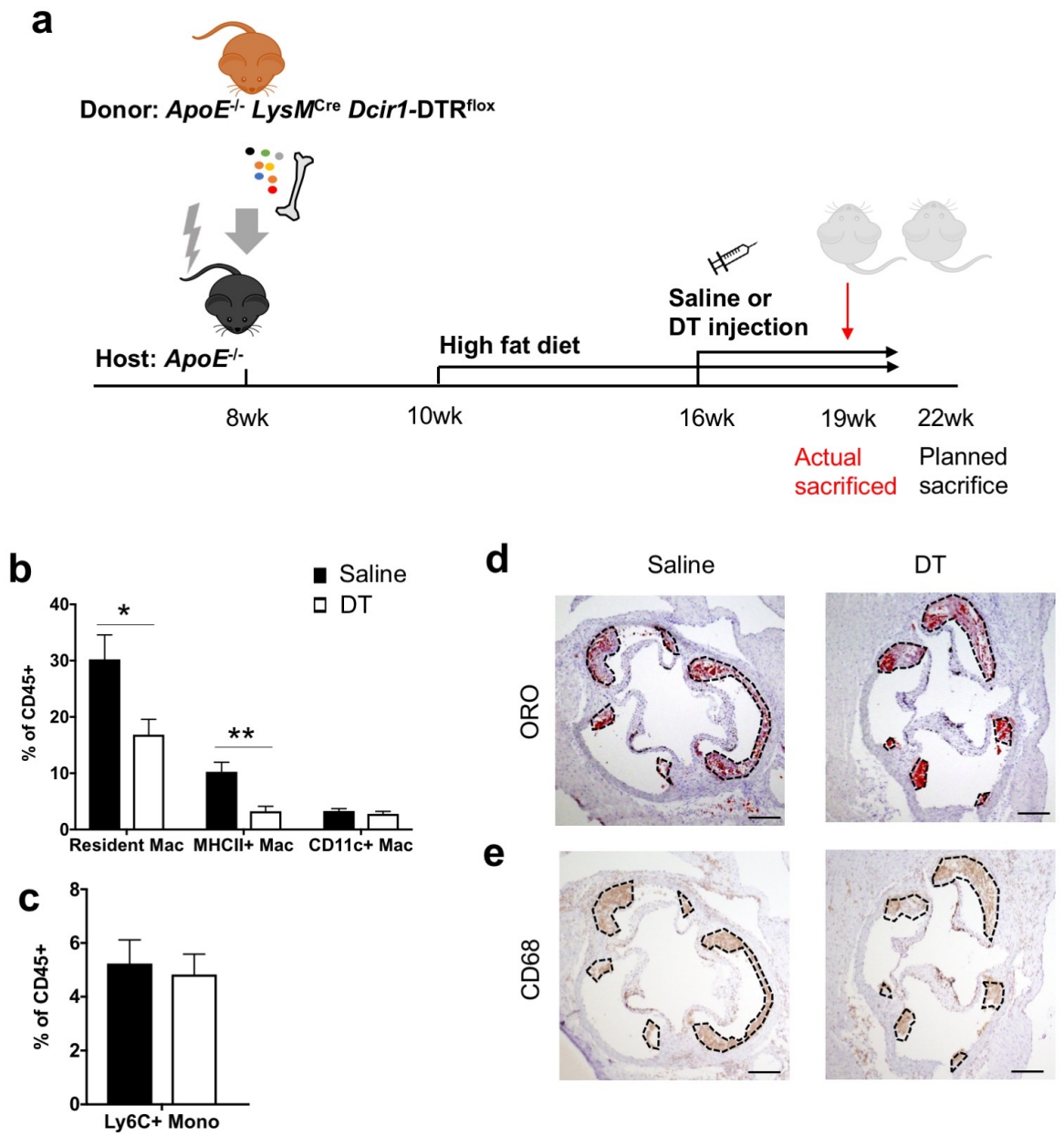


Figure 4.20 The effect of macrophage depletion using *ApoE*$^{-/-}$ mice with the bone marrow of *ApoE*$^{-/-}$ *LysM*^{Cre} *Dcir1*-DTR^{flox} mice.

a) Host *ApoE*$^{-/-}$ mice were irradiated twice and received the BM from *ApoE*$^{-/-}$ *LysM*^{Cre} *Dcir1*-DTR^{flox} (KO HET KI) on the same day. Following 2 weeks, these mice were then put on a high fat diet (HFD) for 12 weeks. Saline or 30ng/g DT treatment started 6 weeks after being fed on HFD for further 6 weeks. Mice were sacrificed 3 weeks earlier than planned due to body weight loss in the DT-treated group. Aortic roots were analysed by histology and aortas, spleens, para-aortic lymph nodes (PALN) and lungs were examined by flow cytometry. **b)** Percentages of resident, MHCII+ resident and recruited macrophages and **c)** Ly6C+ monocytes in the aorta. Data are presented as mean±SEM. n=6 each group. Mann-Whitney test. *P<0.05, **P<0.01. **d)** The lesion in sections of the aortic root was visualised by using Oil Red O (ORO) dye. **e)** macrophage-monocyte contents were detected by immuno-staining with CD68 antibody. Images are taken at 4X magnification. Scale bars indicate 200μm.

	10ng/g		30ng/g		30ng/g	
	Chimera		Chimera		Non-chimera	
	Saline	DT	Saline	DT	Saline	DT
Irradiation	28±1.0	27±0.8	25±0.9	27±0.9	N/A	N/A
DT start	28±0.7	28±0.4	27±0.6	28±0.5	33±1.4	31±0.7
Sacrifice	28±0.6	27±0.2	27±0.5	24±0.9	32±1.7	26±1.4

Table 4.1 Body weight of chimeric *ApoE*$^{-/-}$ mice transplanted by the bone marrow of *ApoE*$^{-/-}$ *LysM*^{Cre} *Dcir1*-DTR^{flox} mice or non-irradiated *ApoE*$^{-/-}$ *LysM*^{Cre} *Dcir1*-DTR^{flox} mice. Unit: gram. 10ng/g n=4-5, 25ng/g n=2, 30ng/g n=6. N/A stands for not applicable.

	10ng/g	25ng/g	30ng/g
Aorta	No depletion	50%	54%
Spleen	No depletion	NT	27%
PALN	No depletion	NT	*58%
Lung	No depletion	50%	87%

Table 4.2 The rates of macrophage depletion by DT treatment in the aorta, spleen, para-aortic lymph nodes (PALN) and lungs in relative to the saline-treated group.

ApoE$^{-/-}$ mice transplanted by the BM of *ApoE*$^{-/-}$ *LysM*^{Cre} *Dcir1*-DTR^{flox} mice were used. 10ng/g n=4-5, 25ng/g n=2, 30ng/g n=6. NT stands for not tested.

X10^3 µm^2	Saline	30ng/g DT	P values
AR size	1254±55	1117±72	0.0649
Lesion area	146±12	160±36	>0.9999
Lipid area	57±6	56±12	0.6991
CD68+ area	80±5	95±19	0.6991
CD206+ area	6±1	9±2	0.3939
CD11c+ area	38±4	47±10	0.7922
Necrotic core size	61±14	67±22	0.8182

Table 4.3 Characterisation of the aortic root section of chimera *ApoE*$^{-/-}$ mice transplanted by the BM of *ApoE*$^{-/-}$ *LysM*^{Cre} *Dcir1*-DTR^{flox} mice.

The area of lesion, lipid, CD68+, CD206+, CD11c+ and necrotic core is quantified within the lesion. Data are presented as mean±SEM. n=6. Mann-Whitney test.

To minimise the phenotype from macrophage depletion, lower doses of DT were also trialled. 10 ng/g DT led to no depletion of macrophages while 25 ng/g DT showed the similar efficacy with 30ng/g DT, resulting in weight loss (**Table 4.2**). Since macrophage depletion caused lung collapse in some of the DT-treated mice, further experiments were performed by introducing DT-resistant monocytes into the trachea after macrophage depletion. *ApoE*$^{-/-}$ *LysM*^{Cre} *Dcir1*-DTR^{flox} (KO HET KI) and *Ldlr*$^{-/-}$ CD45.1 (bone marrow chimeras) mice were used and no signs of lung collapse were observed in these mice (**Figure 4.21a,b**). Although alveolar macrophages were reconstituted and survived from DT injections, I was unable to achieved long-term macrophage depletion by continuing weight loss with DT treatment.

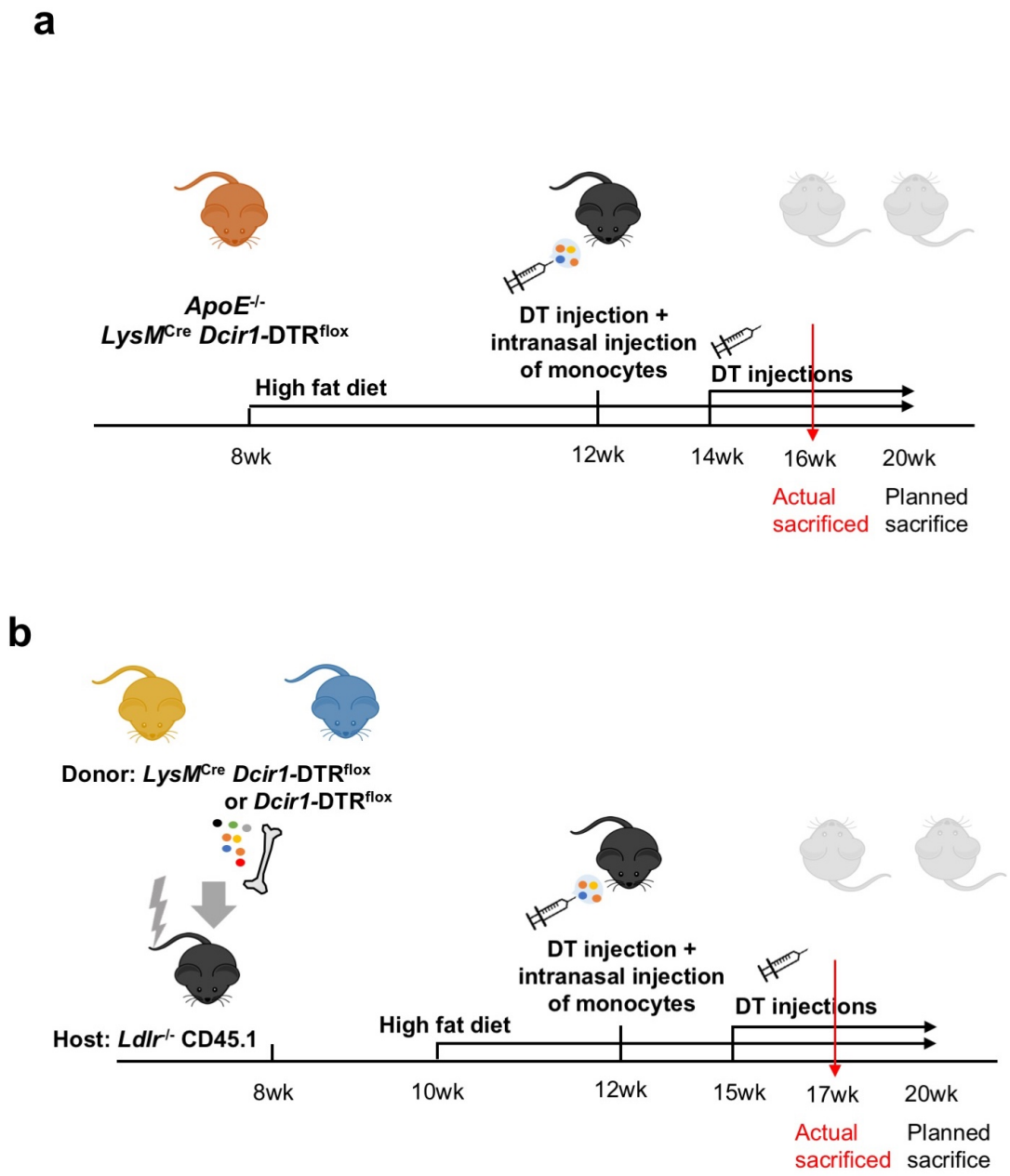


Figure 4.21 Schematic of macrophage depletion in atherosclerotic mice.

a) *ApoE*$^{-/-}$ *LysM*^{Cre} *Dcir1*-DTR^{flox} (KO HET KI and KO WT KI) mice were fed on a high fat diet (HFD) at 8 weeks old and macrophages were depleted at 12 weeks old by one 30 ng/g DT injection. Monocytes from the BM of *ApoE*$^{-/-}$ mice were intranasally introduced to KO HET KI and KO WT KI mice. Saline or DT injections were given at 14 weeks and all mice were sacrificed at 16 weeks. **b)** Host *Ldlr*$^{-/-}$ CD45.1 mice were sub-lethally irradiated and received the BM from *LysM*^{Cre} *Dcir1*-DTR^{flox} HET KI or *Dcir1*-DTR^{flox} mice on the same day. Following 2 weeks, these mice were then put on a for 10 weeks. At the 12-week of age, all mice received DT twice and monocytes from *Dcir1*-DTR^{flox} mice were intranasally introduced to the chimeras. After 3 weeks, these mice were subjected to saline or DT treatment and were sacrificed at the age of 16-week.

4.4. Discussion

The study on the function of resident macrophages is hampered by the lack of specific markers that are not shared by other myeloid populations. In this chapter, I showed that an *in vivo* macrophage depletion strategy based on two markers achieved selective ablation of several subsets of tissue resident macrophages, sparing other myeloid populations.

By using CyTOF, I generated an atlas of leucocyte populations in the aorta, heart, lungs and spleen of the healthy mice. I then carefully documented the DT-mediated macrophage ablation in those tissues with the *LysM*^{Cre} *Dcir1*-DTR^{flox} mouse strain. Successful macrophage depletion in the aorta and heart was attained and this was confined to a macrophage subset expressing high levels of DCIR1 and MHCII. Although the mouse strain was designed for targeting vascular macrophages, macrophage ablation was also effective in several organs including lungs, BM, spleen and peritoneum. In the lungs and peritoneum, DCIR1-mediated depletion was preferentially achieved in embryonically-derived macrophages such as alveolar macrophages and large peritoneal macrophages (Ghosn et al., 2010, Guilliams et al., 2013). In contrast, microglia are derived from embryonic yolk sac progenitors and have no contribution from the foetal liver and bone marrow monocytes in the steady state (Daneman et al., 2010, Ginhoux et al., 2010). The data showed that microglia and brain leucocytes were resistant to DTR-mediated cell ablation, and this can be explained by gene expression data by Immunological Genome Project (ImmGen), showing low levels of *Dcir1* and *LysM* in microglia. Interestingly, interstitial, colonic and liver macrophages were expanded by DT treatment. These macrophages may have been rapidly replenished post macrophage depletion because monocytes have

the capacity to replicate the empty niche (Bain et al., 2014, Scott et al., 2016, Tan and Krasnow, 2016). Furthermore, colonic macrophages in the DT-treated mice exhibited the “recruited” phenotype relative to control mice.

Concomitantly, monocyte influx was also observed in organs including the aorta and lungs in the DT-treated *LysM*^{Cre} *Dcir1*-DTR^{flox} mice, supporting that depleting DCIR1+ macrophages may facilitate the production of chemokines such as monocyte chemoattractant protein 1 (MCP1) to replenish the empty niche of macrophages. Furthermore, I was able to show the concept of “monocyte waterfall”, describing that monocytes differentiate into macrophages lacking DCIR1 and MHCII but expressing CD44, associated with cell recruitment and migration. This finding indicates that DCIR1 maintains tissue resident macrophages, and depletion of DCIR1+ macrophages opens the niche for tissue resident macrophages.

Several studies indicated that MHCII expression was associated with monocyte-derived macrophages in the aorta, heart and the synovium (Epelman et al., 2014, Misharin et al., 2014, Molawi et al., 2014, Ensan et al., 2016). This led to the hypothesis that DCIR1 may be preferentially expressed by monocyte-derived macrophages in the aorta. By using the BM chimera technique, I showed that all newly populated macrophages from the donor BM in the aorta, heart, lungs and BM expressed DCIR1 and MHCII and, were ablated by DT treatment. The efficacy of DT-mediated cell ablation was lower in all these organs relative to non-chimera mice. Although tissue macrophages expressed DCIR1 at the protein level, it may take longer than 6 weeks to exhibit full gene expression signature of the tissue resident phenotype. Thus, DCIR1 expression can be slowly acquired as the repopulated macrophages

adapt to the tissue niche, perhaps under the effect of tissue derived factors, as shown in Chapter 3. In support of this, I showed in this Chapter and Chapter 3 that gene expression of *Dcir1* was high in tissue macrophages compared to other myeloid populations.

I additionally sought to determine the effect of the depletion of tissue resident macrophages in disease settings. Administration of DT for 3 weeks in an arterial injury model in *LysM*^{Cre} *Dcir1*-DTR^{flox} mice did not affect the development of intimal hyperplasia. It can be speculated that macrophage depletion was not observed in the affected vascular tissues, suggesting that the inflammatory insult from injury affected the expression of DCIR1 in the macrophages, hampering ablation. However, relative to control groups, DT-treated mice exhibited lower levels of DCIR1 and SiglecF in aortic macrophages and alveolar macrophages, respectively. This may suggest that the macrophage niche was ablated and was rapidly replenished in surgical mice. In contrast, macrophage depletion was successfully achieved in hyperlipidaemic strains, in particular, vascular macrophages were ablated without affecting lesional macrophages. However, DT administration for 2-3 weeks was detrimental to the health of these mice, probably due to macrophage depletion in several organs. For instance, lung proteinosis is secondary to alveolar macrophage depletion, which was also observed in the DT-treated mice. Whether the longer DT administration period or the higher expression of DCIR1 in hyperlipidaemic mice caused the phenotype remains unknown. Thus, I proposed to study the role of DCIR1 in atherosclerosis using *Dcir1*-deficient hyperlipidaemic mice (Chapter 5).

To conclude, I showed that the *LysM*^{Cre} *Dcir1*-DTR^{flox} mouse strain delivers specific ablation of tissue resident macrophages in the aorta, heart, lungs, spleen, BM and peritoneum in the steady state. Tissue macrophages undergoing DTR-mediated apoptosis may induce the production of chemotactic factors to recruit monocytes to replenish the empty macrophage niche. DCIR1 may play a role in maintaining the long-lived macrophage population in the tissue since newly arrived macrophages acquire the expression of DCIR1 whilst the level is generally lower in monocytes. Thus, high levels of DCIR1 expression is a hallmark of tissue dwelling macrophages and may contribute to their maintenance in tissue and to the regulation of monocyte influx and repopulation rates within the niche.

CHAPTER 5. Dendritic cell immunoreceptor 1 (DCIR1) protects against atherosclerosis by sustaining the vascular macrophage niche

5.1. Introduction

Dendritic cell immunoreceptor (DCIR) is widely expressed by cells of the myeloid lineage and its cytoplasmic domain bears the immunoreceptor tyrosine-based inhibition motif (ITIM), which signals through Src homology region 2 domain-containing phosphatase-1 (SHP1) and SHP2 (Bates et al., 1999, Billadeau and Leibson, 2002). DCIR endocytosis in dendritic cells (DCs) upon activation inhibits Toll-like receptor (TLR) 8- and TLR9-mediated cytokine production (Meyer-Wentrup et al., 2008, Meyer-Wentrup et al., 2009, Massoud et al., 2014). Several studies using *Dcir1*-deficient mice have demonstrated that DCIR1 regulates DC homeostasis in experimental autoimmune diseases including collagen-induced arthritis and multiple sclerosis (Fujikado et al., 2008, Seno et al., 2015). In these models, DCIR1 deficiency aggravates disease severity through modulating the DC-mediated T cell response. In contrast, *Dcir1* deficiency protects mice from malaria and tuberculosis by upregulating inflammation (Maglinao et al., 2013, Troegeler et al., 2017). *Dcir1* deficiency also alleviates hepatitis through inhibiting neutrophil influx in the liver (Ishiguro et al., 2017). Together, this evidence suggests that DCIR1 suppresses immune responses and its role can be either detrimental or protective depending on the nature of inflammation. To date, the role of DCIR1 in macrophage biology is largely unknown and its endogenous ligands and its associated signalling pathways in immune inhibition also remain to be elucidated.

In the previous chapters, I provided evidence that vascular macrophages in the aortic wall can be broadly divided into resident and recruited subsets by single cell analyses. Furthermore, these subsets are differentially compartmentalised within the adventitia and the intima. Adventitial or resident macrophages are thought to maintain

homeostasis in the healthy artery (Lim et al., 2018), but their role in atherosclerosis is still to be investigated. During atherogenesis, the representation of vascular macrophages in the aorta is skewed towards the recruited subsets, which are broadly pro-inflammatory (Chapter 2) (Cole et al., 2018). I have also shown that DCIR1 is highly expressed by vascular macrophages, potentially in response to communication with the local microenvironment. In the murine atherosclerotic aorta, *Dcir1* gene expression distinguishes resident macrophages from recruited macrophages. However, it is still to be determined how the interplay between these two main macrophage populations orchestrates atherogenesis.

In this chapter, I collated gene expression data on murine *Dcir1* and human *Dcir* in the atherosclerotic tissue. I then sought to assess whether *Dcir1* deficiency affects atherogenesis and whether its deficiency has an impact on the phenotype and function of vascular macrophages. To this end, I generated a new mouse strain apolipoprotein E ($ApoE^{-/-}$ $Dcir1^{-/-}$) and performed a comparative study with $ApoE^{-/-}$ mice.

5.2. Atherosclerosis increases *Dcir/Dcir1* expression by recruitment of monocytes and macrophages

One of the hallmarks of atherosclerosis is accumulation of myeloid cells within the vascular wall. Having shown that DCIR1 is highly expressed by resident macrophages, I sought to investigate the kinetics of its expression in the healthy and atherosclerotic aorta. Wild type (WT) mice on a C57BL/6J background, without genetic modification in lipid metabolism, are less susceptible to atherosclerosis (Whitman, 2004). The $ApoE^{-/-}$ mouse strain is hypercholesterolaemic and spontaneously

develops fatty streak in the aorta from 6 weeks of age (Nakashima et al., 1994). A high-fat diet (HFD) accelerates lesion formation in the aorta of *ApoE*$^{-/-}$ mice. Thus, I determined gene expression of *Dcir1* and *Lyz2* (also known as LysM) in whole aortas from WT and *ApoE*$^{-/-}$ mice fed on a normal chow diet at four different age points (6, 12, 35 and 53 weeks). At 6 weeks of age, gene expression of *Dcir1* was already higher in the aorta of *ApoE*$^{-/-}$ compared to WT mice (WT vs. *ApoE*$^{-/-}$: 0.9±0.1 vs. 1.4±0.2 $P<0.05$) and expression in *ApoE*$^{-/-}$ mice continued to increase at 12, 35 and 53 weeks compared to WT (WT vs. *ApoE*$^{-/-}$: 12-week: 0.9±0.1 vs. 1.8±0.4 $P<0.05$, 35-week: 1.5±0.3 vs. 5.7±1.1 $P<0.01$, 53-week: 2.1±0.1 vs. 5.0±0.7 $P<0.01$; **Figure 5.1a**). *Dcir1* expression in the aorta of *ApoE*$^{-/-}$ mice was highest at 35 and 53 weeks (*ApoE*$^{-/-}$: 6-week vs. 35-week $P<0.001$, 6-week vs. 53-week $P<0.001$). Gene expression of *Lyz2* was significantly higher in the aorta of *ApoE*$^{-/-}$ mice at 12, 35 and 53 weeks relative to WT mice (WT vs. *ApoE*$^{-/-}$: 12-week: 2.2±0.6 vs. 7.9±2.7 $P<0.05$, 35-week: 3.6±0.9 vs. 31.3±2.8 $P<0.01$, 53-week: 6.6±0.8 vs. 76.1±12.7. $P<0.01$; **Figure 5.1b**). Arterial *Lyz2* expression gradually increased only in *ApoE*$^{-/-}$ mice with age (*ApoE*$^{-/-}$: 6-week vs. 35-week $P<0.05$, 6-week vs. 53-week $P<0.0001$). Levels of *Dcir1* and *Lyz2* were not significantly altered in the aorta of WT mice with age and taken together with a positive correlation between *Dcir1* and *Lyz2*, the data suggest that *Dcir1* levels correlate with the myeloid influx and atherogenesis.

Next I assessed whether the expression of *Dcir* was also increased in human atherosclerosis. Carotid endarterectomy samples were collected from patients with symptomatic and asymptomatic atherosclerosis at the time of surgery. Atherosclerotic lesions are small and atypical segments in the arterial wall that can be easily identified by macroscopic observation. Whenever “healthy” carotid tissues, adjacent to the

stenosis, were observed, they were collected separately to allow comparisons between “healthy” and atherosclerotic lesions in the same patient to be performed. Gene expression of *Dcir* was significantly higher in plaques from symptomatic patients both in comparison to their matched healthy vessel wall and to lesions from asymptomatic patients (healthy vs. asymptomatic vs. asymptomatic: 0.12±0.05 vs. 0.18±0.04 vs. 0.98±0.33, healthy vs. symptomatic: $P<0.05$, asymptomatic vs. symptomatic: $P<0.05$; **Figure 5.1c**). This may suggest that increased *Dcir* expression correlates with symptomatic disease.

Having shown in Chapter 3 that *Dcir1* is highly expressed in murine macrophages, I ascertained whether DCIR1 was also expressed in macrophages isolated from the human carotid endarterectomies. Gene expression profiling using quantitative real time polymerase chain reaction (qRT-PCR) was performed on CD14+ cells isolated from human carotid endarterectomies by magnetic bead-based cell separation. The data on *Dcir* and *Cd68* expression were extracted for this study. *Dcir* expression in CD14+ atheroma cells was three times higher than human monocyte cell line THP-1 (THP-1 vs. Carotid CD14+: 0.8±0.1 vs. 2.5±0.5 $P=0.0848$; **Figure 5.1d**). Gene expression of monocyte-macrophage marker *Cd68* is also higher in atheroma myeloid cells in comparison to THP-1 (THP-1 vs. Carotid CD14+: 0.8±0.1 vs. 2.2±0.5 $P=0.1333$; **Figure 5.1d**). Finally, we used samples from the Tampere Vascular Study Biobank as a validation cohort in collaboration with Professor Terho Lehtimäki (University of Tampere). In this large cohort, we were able to demonstrate a significant positive correlation between *Dcir* and *Cd68* gene expression in whole extracts of carotid endarterectomies (**Figure 5.1e**).

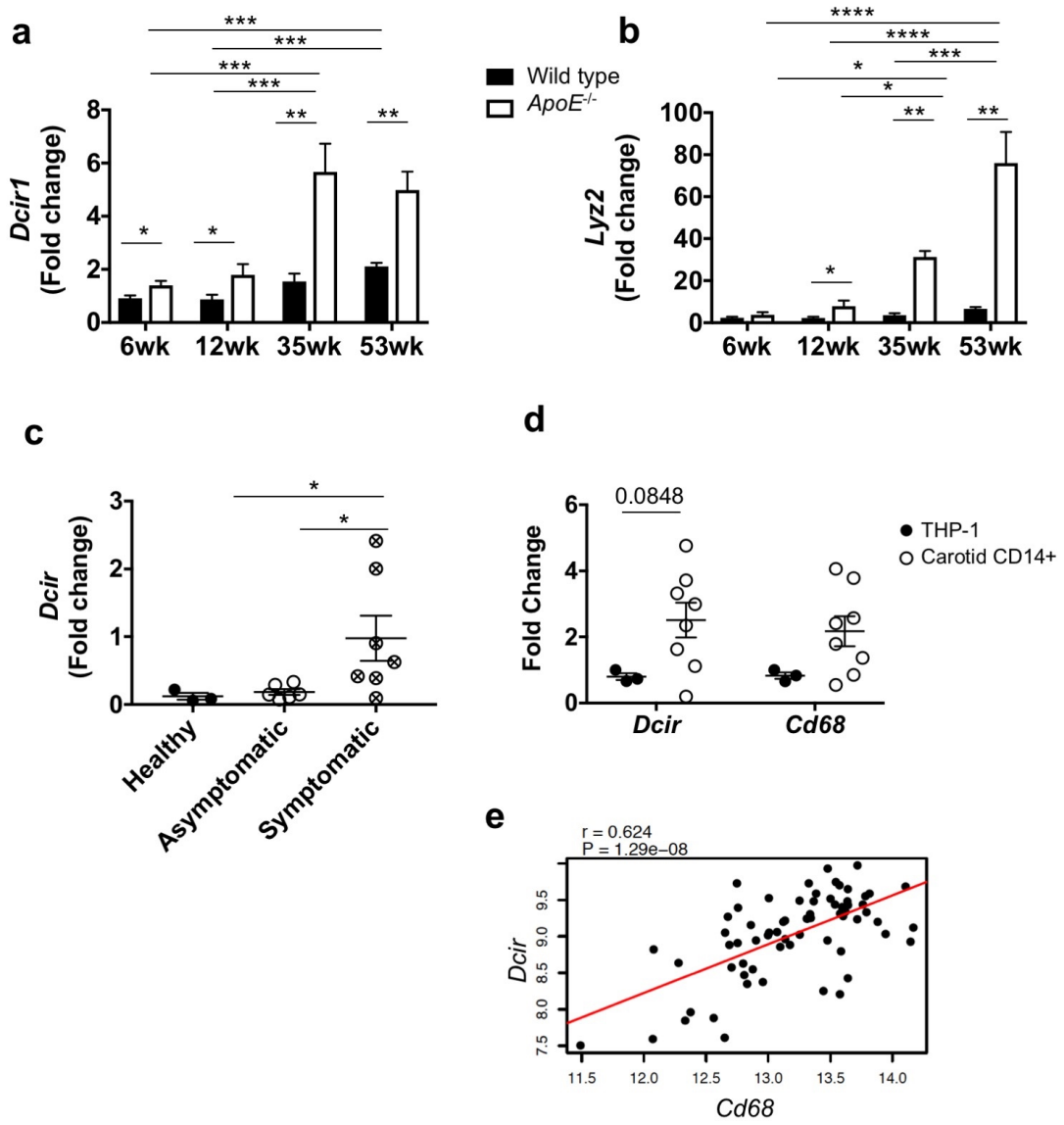


Figure 5.1 The expression of murine *Dcir1* and human *Dcir* in the atherosclerotic tissue.

a, b) Gene expression of *Dcir1* and *Lyz2* in whole aortas of wild type (WT) and *Apolipoprotein E*-deficient (*ApoE*$^{-/-}$) males at 6-, 12-, 35- and 53-week old age. Gene expression is normalised to the housekeeping gene *18S rRNA*. n=5 each. cDNA of murine aortas was obtained from Dr Jennifer Cole (University of Oxford). **c)** Gene expression of *Dcir* in biopsies of carotid endarterectomies from patients with asymptomatic and asymptomatic atherosclerosis and healthy carotid tissues (The data were provided by Dr Joseph Shalhoub (Imperial College London)). Gene expression is normalised to the housekeeping gene *Gapdh*. **d)** Gene expression of *Dcir* and *Cd68* in CD14+ monocytes and macrophages from carotid endarterectomies from patients with atherosclerosis. Human monocyte cell line THP1 was used as a negative control. The data were provided by Dr Leena Viiri (University of Tampere). **e)** A positive correlation between *Dcir* and monocyte-macrophage marker *Cd68* in human carotid endarterectomies from patients with atherosclerosis. This dataset was obtained from Professor Terho Lehtimäki (University of Tampere). Data are presented as mean±SEM. Mann-Whitney test. *P<0.05, **P<0.01, ***<0.001, ****P<0.0001.

5.3. Generation of a *Dcir1*-deficient *ApoE*$^{-/-}$ mouse strain

To examine the role of DCIR1 in murine atherosclerosis, the *Dcir1*$^{-/-}$ mouse stain was obtained from Professor Yoichiro Iwakura (University of Tokyo, Japan). The immune cell composition of the aorta, lungs, spleen, para-aortic lymph nodes and BM of WT and *Dcir1*$^{-/-}$ littermates was determined by flow cytometry at 12-week or 24-week of age (Appendix 1 Table 8.1 and 8.2). In the lungs of 12-week old *Dcir1*$^{-/-}$ mice, interstitial macrophages and cDC2 were decreased in numbers and percentages. In the BM, both the number and percentage of macrophages were decreased in *Dcir1*$^{-/-}$ mice while the neutrophil population was increased. Interestingly, the total number of alveolar macrophages was significantly decreased in the *Dcir1*$^{-/-}$ mice at 24 weeks of age. No other clear differences in the cellular profile between these two strains were observed in the aorta, lungs, spleen and BM in the steady state at 24-weeks of age.

Dcir1$^{-/-}$ mice were crossed with *ApoE*$^{-/-}$ mice to establish the *ApoE*$^{-/-}$ *Dcir1*$^{+/-}$ mouse strain. This strain was then crossed further to generate *ApoE*$^{-/-}$ *Dcir1*$^{-/-}$ and *ApoE*$^{-/-}$ *Dcir1*$^{+/+}$ littermates (named *ApoE*$^{-/-}$ mice thereafter). 8-week old *ApoE*$^{-/-}$ and *ApoE*$^{-/-}$ *Dcir1*$^{-/-}$ mice were fed a normal chow or HFD for 12 weeks and were examined at 20 weeks of age (unless stated otherwise) (**Figure 5.2**). Lesion formation was examined in the aortic root and in the aorta (*en face*). The immune cell composition of the aorta, spleen and para-aortic lymph node (PALN) was analysed by flow cytometry in females and by mass cytometry in males. Single cell RNA sequencing (scRNAseq) was performed on CD11b+ cells from the aorta of 20-week old *ApoE*$^{-/-}$ and *ApoE*$^{-/-}$ *Dcir1*$^{-/-}$ mice.

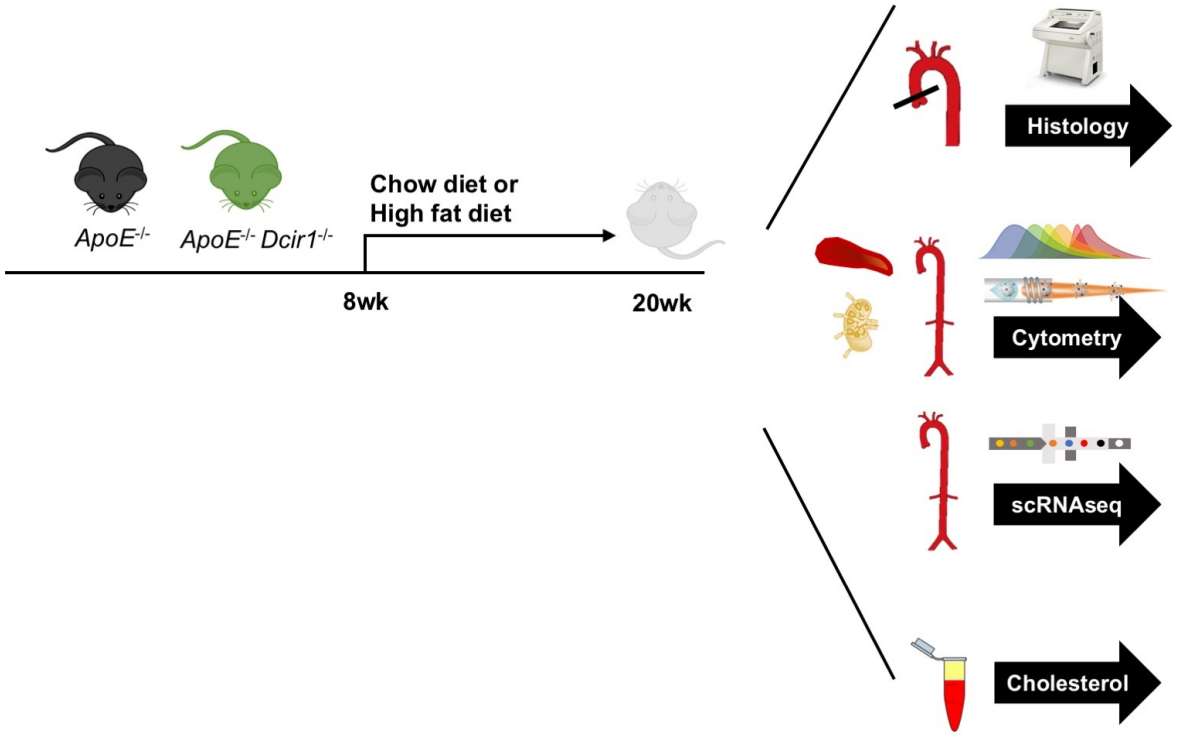


Figure 5.2 Schematic of experimental design and sample processing.

8-week old *ApoE*$^{-/-}$ and *ApoE*$^{-/-}$ *Dcir1*$^{-/-}$ mice were fed on normal (chow) or high fat diet for 12 weeks and were sacrificed at the 20-week of age. Aortic roots were cryo-sectioned to measure lesion development and assess the phenotype of the lesion. In some mice, whole aortas were cut open longitudinally to measure total lesion development. Single cells from aortas, spleens and para-aortic lymph nodes (PALN) were analysed by mass cytometry (CyTOF) in males and flow cytometry in females. In some mice, CD11b+ cells from aortas were isolated by fluorescence-activated cell sorting (FACS) and single cell RNA sequencing (scRNAseq) was performed on the isolated cells. The blood from these animals was collected to measure serum cholesterol levels.

Chow-fed and HFD-fed *ApoE*$^{-/-}$ *Dcir1*$^{-/-}$ males and females did not display any differences in body weight at 20 weeks of age (**Table 5.1**) and *ApoE*$^{-/-}$ and *ApoE*$^{-/-}$ *Dcir1*$^{-/-}$ males showed a similar serum cholesterol profile (**Table 5.2**). This indicates that *Dcir1* deficiency does not influence body weight or levels of cholesterol in serum.

♂	*ApoE*$^{-/-}$	*ApoE*$^{-/-}$ *Dcir1*$^{-/-}$	P values
Chow diet	33.1±0.4	31.9±0.4	0.0761
HFD	34.4±0.9	34.4±0.8	0.9333

♀	*ApoE*$^{-/-}$	*ApoE*$^{-/-}$ *Dcir1*$^{-/-}$	P values
Chow diet	23.8±0.3	23.9±0.4	0.8779
HFD	23.3±0.3	22.8±0.3	0.3202

Table 5.1 Body weight of 20-week old *ApoE*$^{-/-}$ and *ApoE*$^{-/-}$ *Dcir1*$^{-/-}$ mice on a chow or high fat diet.

The unit for body weight is gram. Males n=16-22 each group, females n=14-17 each group. Data are presented as mean±SEM. Mann-Whitney test.

♂	*ApoE*$^{-/-}$	*ApoE*$^{-/-}$ *Dcir1*$^{-/-}$	P values
Chow diet	10.8±0.8	12.0±0.6	0.2545
HFD	12.8±0.7	16.6±1.3	0.0892

Table 5.2 Serum cholesterol levels of 20-week old *ApoE*$^{-/-}$ and *ApoE*$^{-/-}$ *Dcir1*$^{-/-}$ males on a chow or high fat diet.

The unit for cholesterol levels is mg/dL. n=10 each group. Data are presented as mean±SEM. Mann-Whitney test.

5.4. *Dcir1* deficiency exacerbates lesion formation during atherogenesis

Aortic roots from 20-week old *ApoE*$^{-/-}$ and *ApoE*$^{-/-}$ *Dcir1*$^{-/-}$ males were cryo-sectioned to examine lesion formation. Six sections (one taken every 100 μm from the first cusp of the aortic valve) were stained in Oil Red O and haematoxylin to visualise lesion morphology. The stained lesion in the aortic root was quantified and the data are displayed as; lesion area by distance from the start of the aortic sinus, the average absolute lesion size and the average percentage lesional area per aortic root.

Chow-fed *ApoE*$^{-/-}$ and *ApoE*$^{-/-}$ *Dcir1*$^{-/-}$ mice displayed a mild but not statistically significant increase in lesion area in the aortic root (**Figure 5.3a**). However, when fed a HFD, the lesion size in *ApoE*$^{-/-}$ *Dcir1*$^{-/-}$ mice was increased compared to *ApoE*$^{-/-}$ mice and this increase was greatest at points furthest from the start of the aortic sinus (*ApoE*$^{-/-}$ vs. *ApoE*$^{-/-}$ *Dcir1*$^{-/-}$: 400μm: 213.9±18.2 vs. 294.1±26.7 X10^{3}μm^2 P=0.0610, 500μm: 209.9±23 vs. 349.7±33.5 X10^{3}μm^2 P<0.01, 600μm: 190.0±25.9 vs. 370.4±39.9 X10^{3}μm^2 P<0.01; **Figure 5.3b**). In the distal segments of the aortic root of *ApoE*$^{-/-}$ *Dcir1*$^{-/-}$ mice, both absolute lesion size and the percentage of lesion per aortic root were significantly increased compared to *Dcir1*-competent *ApoE*$^{-/-}$ mice (*ApoE*$^{-/-}$ vs. *ApoE*$^{-/-}$ *Dcir1*$^{-/-}$: 205.9±20.6 vs. 338.1± 31.8 X10^{3}μm^2 P<0.01, 17.1±1.5 vs. 24.4±2.0μm^2 P<0.01; **Figure 5.3b**).

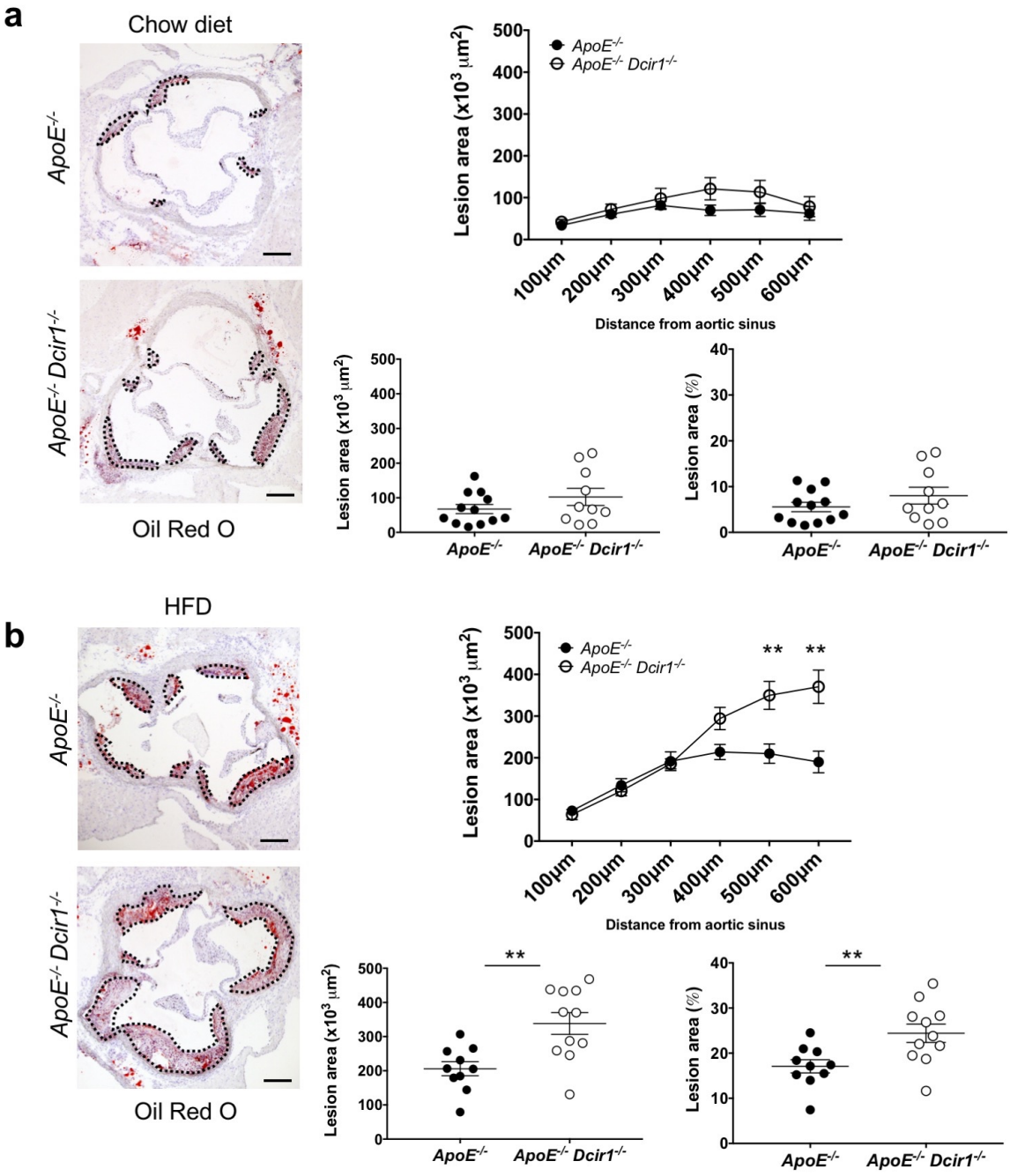


Figure 5.3 Atherosclerotic lesion formation in the aortic root of 20-week old *ApoE*$^{-/-}$ and *ApoE*$^{-/-}$ *Dcir1*$^{-/-}$ mice.

Six aortic root sections at every 100 µm from the first cusp were stained in Oil Red O (ORO) dye and haematoxylin to visualise lipid and nuclei. The lesional area in the aortic root is highlighted in images in a dotted line. **a)** The images are the representation for lesion formation of *ApoE*$^{-/-}$ and *ApoE*$^{-/-}$ *Dcir1*$^{-/-}$ mice fed on chow diet at 400 µm distance. **b)** The images are the representation for lesion formation of HFD- fed *ApoE*$^{-/-}$ and *ApoE*$^{-/-}$ *Dcir1*$^{-/-}$ at 600 µm distance. Lesional areas are presented by distance from the aortic sinus. Graphs show the average of lesional areas and percentages of lesional area per aortic root from 400- 600 µm distance. Data are presented as mean±SEM. Mann-Whitney test.**P<0.01. Images are taken at X4 magnification. Scale bars denote 200µm.

I also examined the development of atherosclerotic plaque in the whole aorta of *ApoE*$^{-/-}$ and *ApoE*$^{-/-}$ *Dcir1*$^{-/-}$ mice fed a HFD for 18 weeks. The whole aortas were fixed, pinned and stained in Sudan IV dye to visualise lipid. *Dcir1* deficiency exacerbated lesion formation in the whole aorta when mice were fed a HFD for 18 weeks, (*ApoE*$^{-/-}$ vs. *ApoE*$^{-/-}$ *Dcir1*$^{-/-}$: 0.05±0.01 vs. 0.10±0.02 X10^6 μm^2 P=0.0952, 6.6±1.3 vs. 13.1±2.1 % P=0.0952; **Figure 5.4**). This study is currently being completed because it was underpowered to achieve statistical significance. Collectively, these data reveal that genetic deletion of *Dcir1* exacerbates lesion formation in the aortic root and the whole aorta in mice with advanced atherosclerosis.

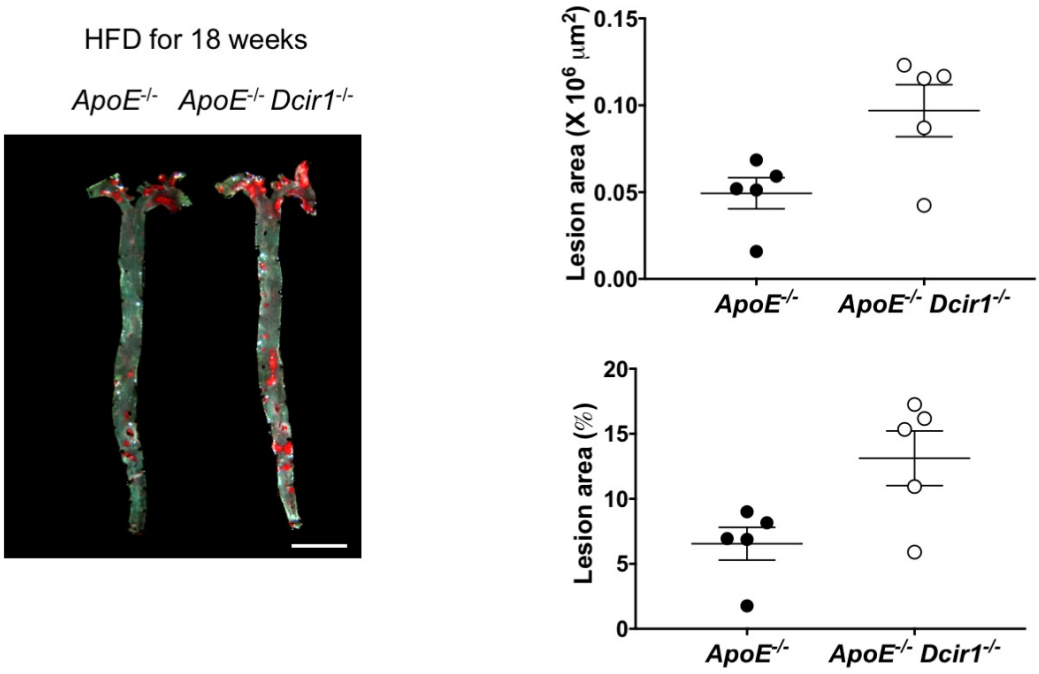


Figure 5.4 Atherosclerotic lesion formation in the whole aorta of *ApoE*$^{-/-}$ and *ApoE*$^{-/-}$ *Dcir1*$^{-/-}$ mice.

Whole aortas were dissected from 26-week old males fed on HFD for for 18 weeks. Aortas were stained in Sudan IV to measure lesion formation. The representative images show the *en face* aorta of *ApoE*$^{-/-}$ and *ApoE*$^{-/-}$ *Dcir1*$^{-/-}$ mice fed on HFD for 18 weeks. The lipid is displayed in red. Graphs show the lesional area and the percentage of lesion size per aorta. Data are presented as mean±SEM. Mann-Whitney test. Non-significant. Images are taken at X0.8 magnifications. The scale bar denotes 5mm.

5.5. *Dcir1* deficiency promotes the development of atherosclerotic plaques with a vulnerable phenotype

During atherogenesis, the arterial wall undergoes a gradual enlargement of the vessel diameter to accommodate lesion growth in a process first described by Glagov et al. as arterial remodelling (Glagov et al., 1987). This is one of the reasons that atherosclerosis can remain undetected for a lengthy period of time throughout life. Failure to undergo this remodelling process can lead to either an increased amount of plaque protruding in the lumen (restrictive remodelling) or to expansive arterial remodelling, where narrowing of the artery is prevented to some extent but is associated with increased inflammation and plaque vulnerability to rupture (Pasterkamp et al., 2004). Importantly, vascular macrophages can regulate vessel wall size through communication with smooth muscle cells (SMCs) (Lim et al., 2018).

No significant differences in the size of artery were observed between chow-fed *ApoE*$^{-/-}$ and *ApoE*$^{-/-}$ *Dcir1*$^{-/-}$ mice. In contrast, the average size of artery in the HFD-fed *ApoE*$^{-/-}$ *Dcir1*$^{-/-}$ mice was significantly larger than in their *ApoE*$^{-/-}$ counterparts (Chow: *ApoE*$^{-/-}$ vs. *ApoE*$^{-/-}$ *Dcir1*$^{-/-}$: 1.1±0.0 vs. 1.2±0.0 X10^{6}µm^{2} P=0.4965; HFD: 1.1±0.0 vs. 1.3±0.1 X10^{6}µm^{2} P<0.05; **Figure 5.5a,b**).

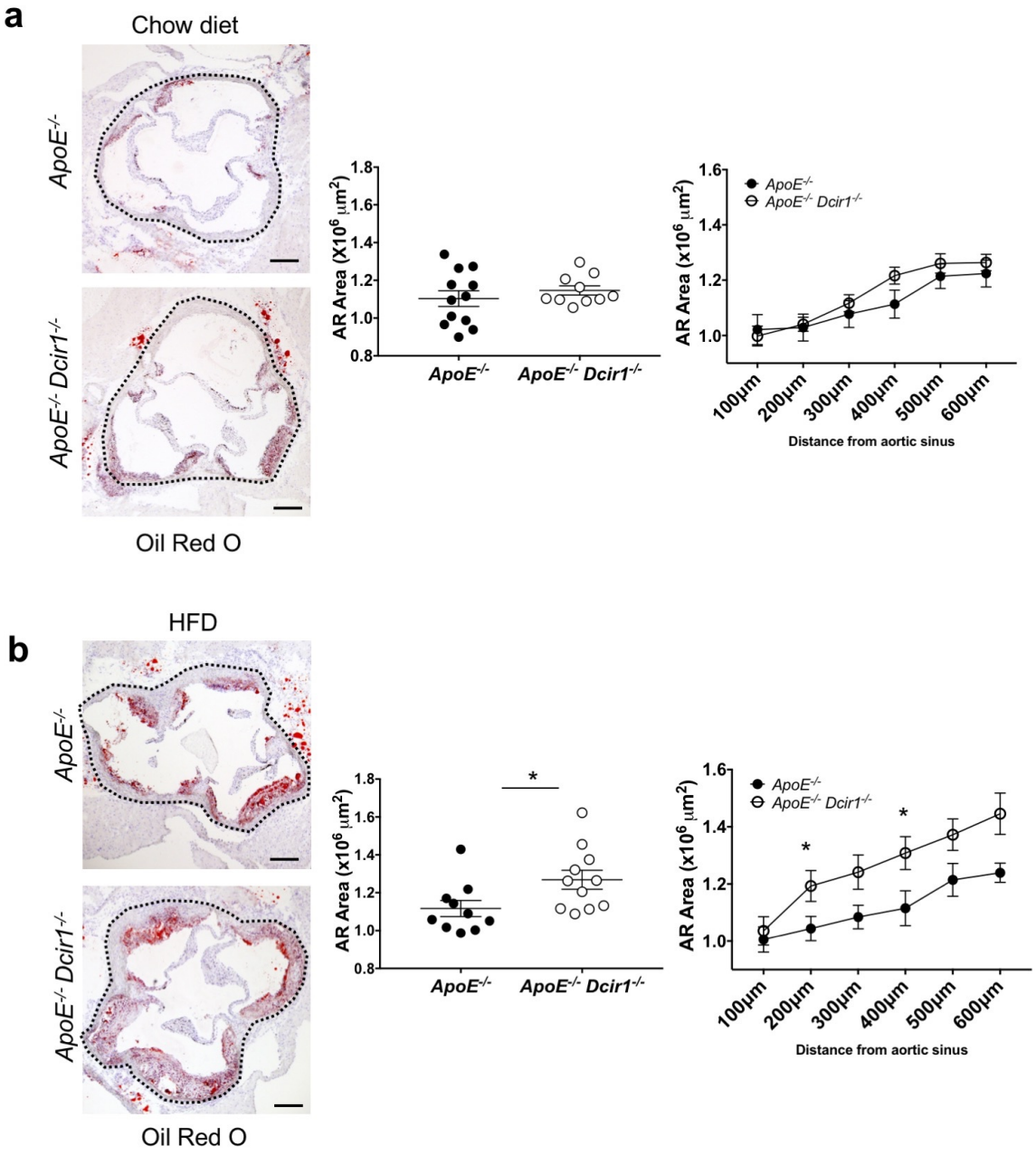


Figure 5.5 The size of aortic roots of 20-week old *ApoE*$^{-/-}$ and *ApoE*$^{-/-}$ *Dcir1*$^{-/-}$ mice.

Six aortic root sections at every 100 µm from the first cusp were stained in Oil Red O (ORO) and haematoxylin to visualise lipid and nuclei. Aortic roots were highlighted in a dotted line. **a)** The images show the aortic root of *ApoE*$^{-/-}$ and *ApoE*$^{-/-}$ *Dcir1*$^{-/-}$ mice fed on a chow diet at 400 µm distance and **b)** the aortic root of HFD-fed *ApoE*$^{-/-}$ and *ApoE*$^{-/-}$ *Dcir1*$^{-/-}$ mice at 600 µm distance. Graphs show average size of the aortic root from 100- 600 µm distance. Aortic root sizes are also presented by distance from the aortic sinus. Data are presented as mean±SEM. Mann-Whitney test.*<0.05. Images are taken at X4 magnification. Scale bars denote 200µm.

Impaired clearance of apoptotic cells, namely efferocytosis, in vascular tissue results in the formation of a necrotic core, a risk factor for the development of plaques with a vulnerable phenotype (Kojima et al., 2017). Necrotic areas within the plaque were visualised by haematoxylin and eosin (H&E) staining and were defined as acellular areas (H&E-free) greater than 3000μm^2 according to the paper by Seimon et al. (Seimon et al., 2009). A marked three-fold increase was observed in necrotic core size in lesions of HFD-fed *ApoE*$^{-/-}$ *Dcir1*$^{-/-}$ animals, compared to *ApoE*$^{-/-}$ mice (*ApoE*$^{-/-}$ vs. *ApoE*$^{-/-}$ *Dcir1*$^{-/-}$: 32.5±8.9 vs. 98.6±18.5 X10^3μm^2 P<0.05; **Figure 5.6b**). A non-statistically significant increase in necrotic core size was also observed in chow fed mice lacking *Dcir1* (*ApoE*$^{-/-}$ vs. *ApoE*$^{-/-}$ *Dcir1*$^{-/-}$: 11.9±3.9 vs. 24.8±10.0 X10^3μm^2 P=0.3333; **Figure 5.6a**).

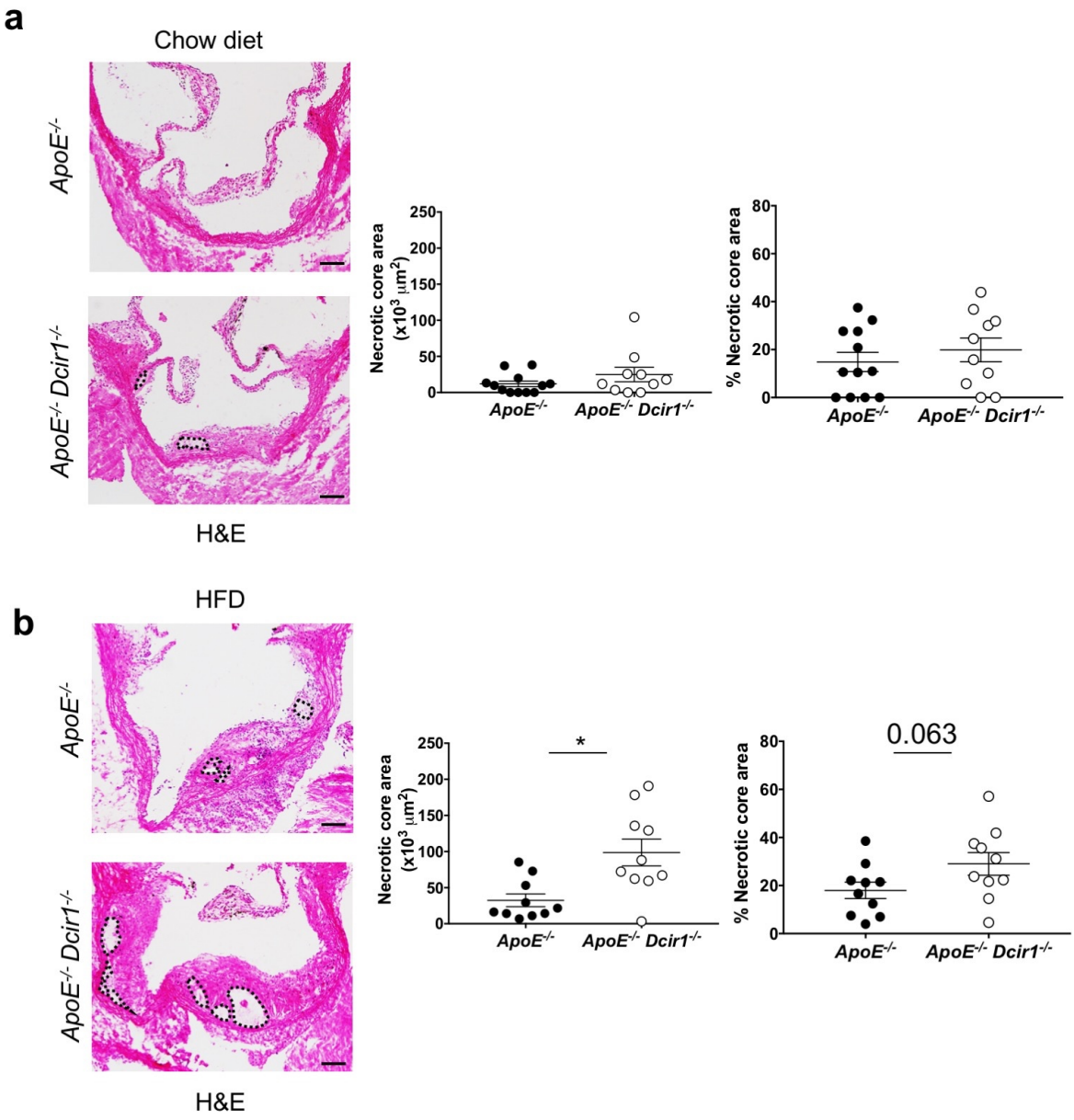


Figure 5.6 Formation of necrotic core in the lesion of 20-week old *ApoE*$^{-/-}$ and *ApoE*$^{-/-}$ *Dcir1*$^{-/-}$ mice.

Aortic root sections were stained in haematoxylin and eosin (H&E) to determine acellular area in the lesion. H&E free areas are accounted for acellular necrotic core. The images are the representation of *ApoE*$^{-/-}$ and *ApoE*$^{-/-}$ *Dcir1*$^{-/-}$ mice fed on a chow diet **a)** and a HFD **b)**. Graphs show the total area of necrotic core and percentages of the necrotic core per lesion. Data are presented as mean±SEM. Mann-Whitney test. P*<0.05. Images are taken at X10 magnification. Scale bars denote 100μm.

Vascular SMCs (VSMCs) play both pro-atherogenic and athero-protective roles in response to signals from the inflamed artery (Doran et al., 2008). In early atherosclerosis, VSMCs proliferate in the media of the artery and drive myeloid cell recruitment. Later in disease, VSMCs migrate into the intima to form a fibrous cap, which protects the plaque from rupture (Bennett et al., 2016). The extracellular matrix produced by VSMCs provides mechanical integrity to the healthy artery. I determined the VSMC content of aortic root lesions by immunostaining using an antibody against alpha SM actin (ASMA). In HFD-fed mice, the total area and percentage of ASMA staining in the media was significantly decreased in *ApoE*$^{-/-}$ *Dcir1*$^{-/-}$ mice compared to *ApoE*$^{-/-}$ mice (*ApoE*$^{-/-}$ vs. *ApoE*$^{-/-}$ *Dcir1*$^{-/-}$: 151.3±10.9 vs. 116.9±11.6 X10^{3}μm^2 P<0.05; 12.2±0.8 vs. 8.4±1.0% P<0.05; **Figure 5.7a**). There was a non-statistically significant trend towards an increase in the ASMA stained area and its percentage in the lesion of HFD-fed *ApoE*$^{-/-}$ *Dcir1*$^{-/-}$ mice compared to *ApoE*$^{-/-}$ mice (*ApoE*$^{-/-}$ vs. *ApoE*$^{-/-}$ *Dcir1*$^{-/-}$: 4.1±1.3 vs. 13.3±4.8 X10^3 μm^2 P=0.0868; **Figure 5.7b**). No significant differences in ASMA staining were observed in chow fed animals. Collectively, loss of DCIR1 might affect SMC behaviour during atherogenesis.

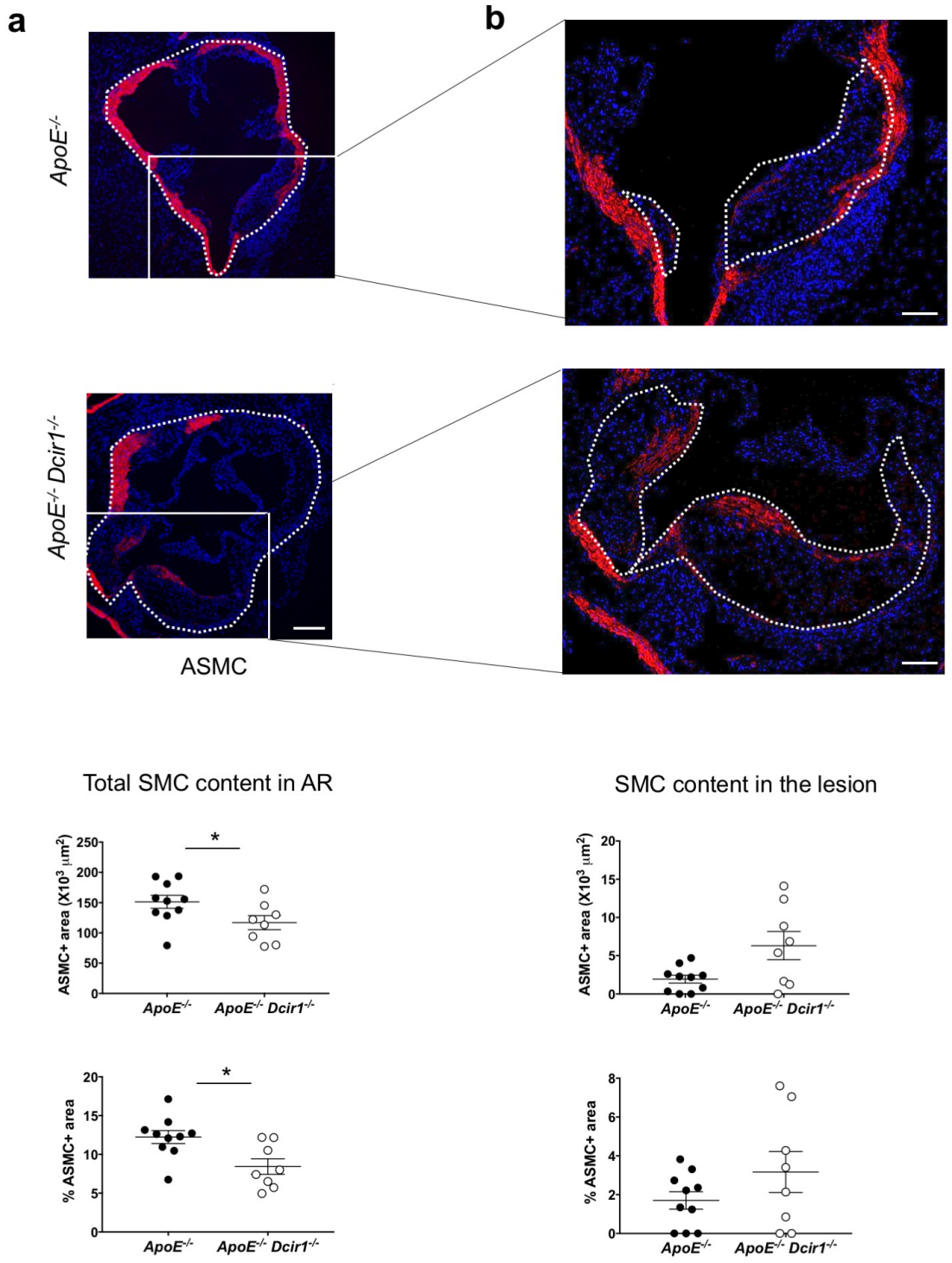


Figure 5.7 Smooth muscle cell content in the aortic root of HFD-fed 20-week old *ApoE*$^{-/-}$ and *ApoE*$^{-/-}$ *Dcir1*$^{-/-}$ mice.

Aortic root sections of *ApoE*$^{-/-}$ and *ApoE*$^{-/-}$ *Dcir1*$^{-/-}$ mice on HFD were immuno-stained with alpha smooth muscle cell actin (ASMC) antibody. The ASMC area is stained in red and blue colour indicates nuclei. **a)** ASMC content in the aortic root (white dotted line) is displayed by area and the percentage. Images are taken at X4 magnification. Scale bars denote 200 µm. **b)** ASMC content and the percentage of ASMC within the lesion of the aortic root (white dotted line). Images are taken at X10 magnification. Scale bars denote 100µm. Data are presented as mean±SEM. Mann-Whitney test. P*<0.05.

VSMCs are the main producer of collagen variants and elastin that form the extracellular matrix (ECM) and support mechanical stability (Barnes and Farndale, 1999). The homeostasis of ECM is sustained through the interaction of lymphatic vessel endothelial hyaluronan receptor (Lyve) 1 and hyaluronan in resident macrophages and VSMCs in the healthy artery (Lim et al., 2018). In atherosclerosis, homeostasis of the ECM is dysregulated, resulting in the accumulation of collagen in the lesion (Adiguzel et al., 2009). In contrast, excessive degradation of collagen can accelerate plaque vulnerability (Rekhter, 1999). To determine levels of collagen, aortic root sections were stained with Picro-Sirius Red dye to visualise total collagen in red under the bright field and type I and type III collagen in orange and green colours under polarised light. A non-statistically significant increase in collagen staining was observed within the lesions in HFD-fed *ApoE*$^{-/-}$ *Dcir1*$^{-/-}$ compared to *ApoE*$^{-/-}$ mice (*ApoE*$^{-/-}$ vs. *ApoE*$^{-/-}$ *Dcir1*$^{-/-}$: total collagen: 79.4±12.4 vs. 132.4 vs. 29.8 X10^{3}µm^2 P=0.2428, type I: 3.4±0.9 vs. 11.1±3.8 X10^{3}µm^2 P=0.1333; **Figure 5.8a,b**).

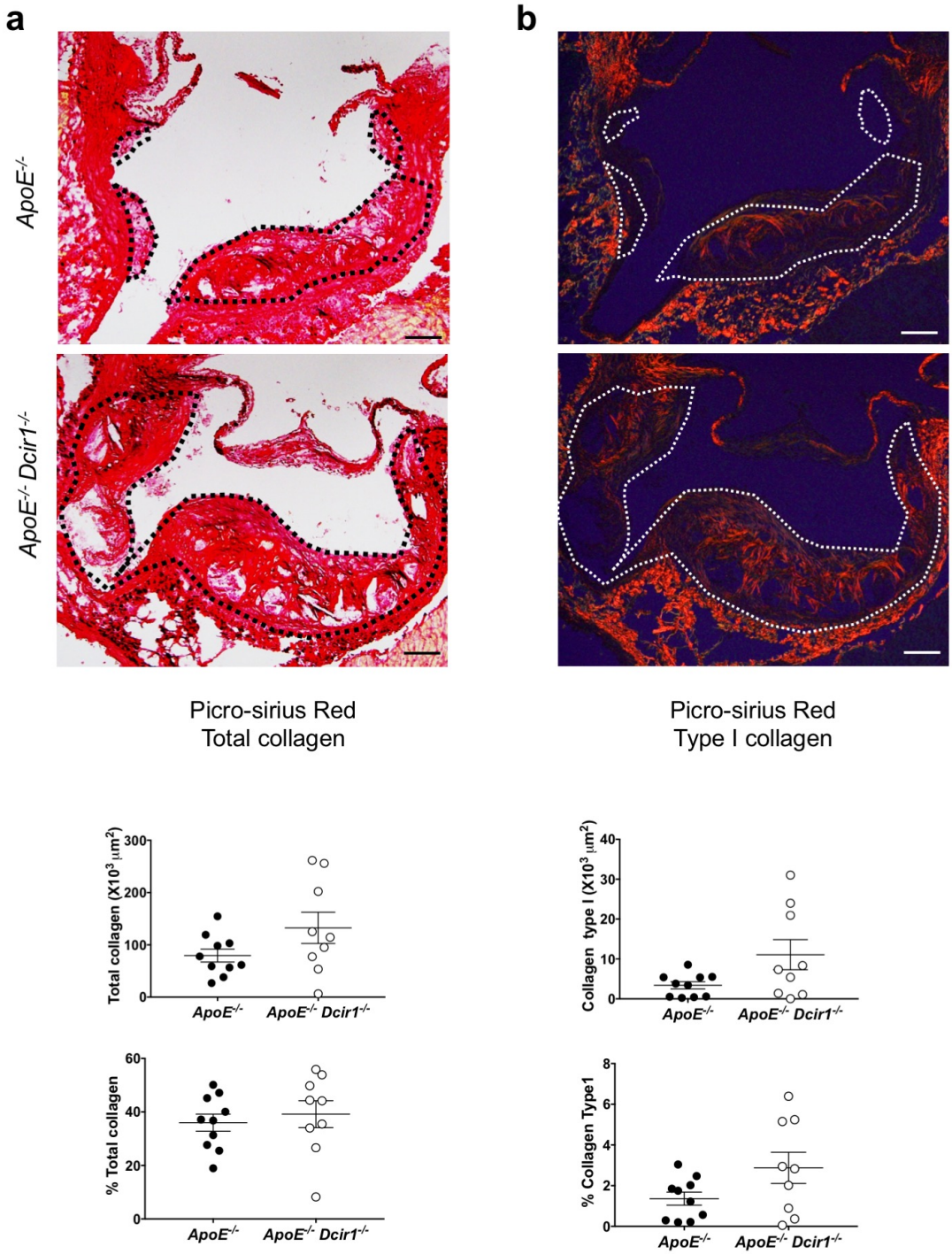


Figure 5.8 Collagen content in the aortic root of HFD-fed 20-week old *ApoE*$^{-/-}$ and *ApoE*$^{-/-}$ *Dcir1*$^{-/-}$ mice.

Aortic root sections of *ApoE*$^{-/-}$ and *ApoE*$^{-/-}$ *Dcir1*$^{-/-}$ mice on HFD were stained in Picro-sirius Red dye. The red colour under the bright field denotes total collagen and the orange colour under the polarised light indicates type I collagen. a) The total collagen content in the lesion of the aortic root (black dotted line). b) Type I collagen content in the lesion of the aortic root (white dotted line). Images are taken at X10 magnification. Scale bars denote 200µm. Data are presented as mean±SEM. Mann-Whitney test. Not-significant.

High-risk plaques are positively associated with a large macrophage content in the atherosclerotic lesion in humans (Fleg et al., 2012). The total CD68 positive area in the lesion was higher in HFD-fed *ApoE*$^{-/-}$ *Dcir1*$^{-/-}$ mice compared to *ApoE*$^{-/-}$ mice (*ApoE*$^{-/-}$ vs. *ApoE*$^{-/-}$ *Dcir1*$^{-/-}$: 134.4±17.7 vs. 195.9±16.1 X10^{3}µm^2 P<0.05; **Figure 5.9a**). Immunostaining for CD64, a macrophage marker, was also increased in HFD-fed *ApoE*$^{-/-}$ *Dcir1*$^{-/-}$ mice compared to *ApoE*$^{-/-}$ mice (*ApoE*$^{-/-}$ vs. *ApoE*$^{-/-}$ *Dcir1*$^{-/-}$: 68.0±9.9 vs. 104.2±10.4 X10^{3}µm^2 P<0.05; **Figure 5.9b**) A non-significant increase in CD11c positive area was present in HFD-fed *ApoE*$^{-/-}$ *Dcir1*$^{-/-}$ mice compared to *ApoE*$^{-/-}$ mice. (*ApoE*$^{-/-}$ vs. *ApoE*$^{-/-}$ *Dcir1*$^{-/-}$: 78.2±12.6 vs. 113.2±10.8 X10^{3}µm^2 P=0.077; **Figure 5.9c**). CD206 staining in the lesion was also significantly increased in HFD-fed *ApoE*$^{-/-}$ *Dcir1*$^{-/-}$ mice compared to *ApoE*$^{-/-}$ mice (*ApoE*$^{-/-}$ vs. *ApoE*$^{-/-}$ *Dcir1*$^{-/-}$: 8.9±2.7 vs. 18.2±4.0 X10^{3}µm^2 P<0.05; **Table 5.3**). No changes were observed in the percentages of CD68, CD64, CD11c or CD206 in the lesion, suggesting that the increase in macrophage content was due to an increase in lesion size rather than heightened inflammation. In the context of the presence of larger necrotic areas in the HFD-fed *ApoE*$^{-/-}$ *Dcir1*$^{-/-}$ mice compared to *ApoE*$^{-/-}$ mice (Figure 5.6), the data on the macrophage content also suggest the possibility of increased macrophage death contributing to this phenotype. No significant changes were observed in chow-fed animals. In summary, *ApoE*$^{-/-}$ *Dcir1*$^{-/-}$ mice develop bigger lesions with larger necrotic cores and increased lesional macrophage content, suggesting that *Dcir1* deficiency promotes plaques susceptible to rupture.

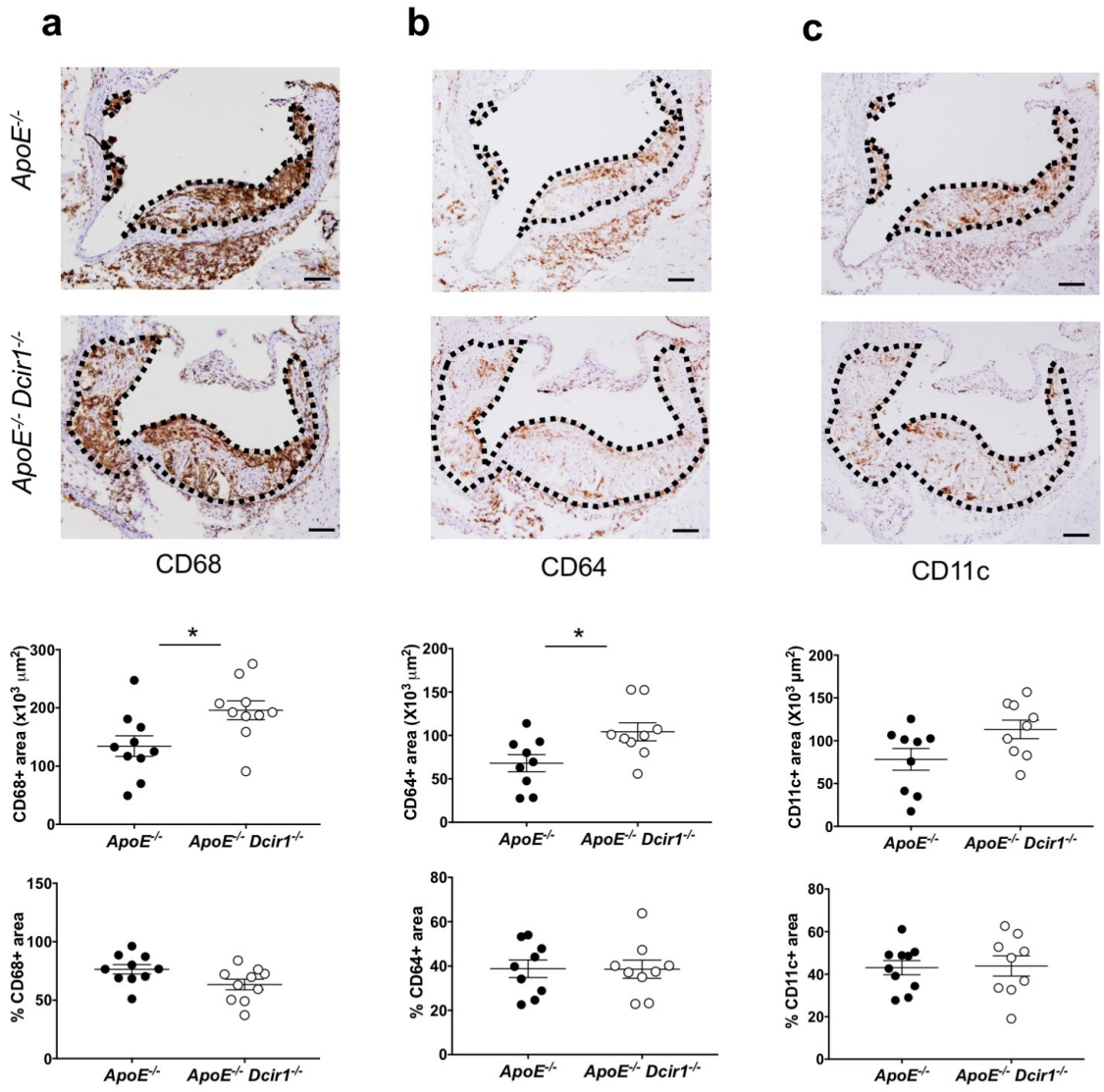


Figure 5.9 Myeloid cell content in the aortic root of HFD-fed 20-week old *ApoE*$^{-/-}$ and *ApoE*$^{-/-}$ *Dcir1*$^{-/-}$ mice.

Aortic root sections of *ApoE*$^{-/-}$ and *ApoE*$^{-/-}$ *Dcir1*$^{-/-}$ mice on HFD were immuno-stained with CD68 (monocyte-macrophage-DC marker), CD11c (macrophage-DC marker) and CD64 (macrophage marker) in brown colour and were counterstained with haematoxylin (purple colour). a) CD68+ area b) CD64+ area and c) CD11c+ area in the lesion of the aortic root. Images are taken at X10 magnification. Scale bars denote 200µm. The total area and the percentage of three markers in the lesion of the aortic root are displayed in dot plots. Data are presented as mean±SEM. Mann-Whitney test. *P<0.05.

♂		*ApoE*$^{-/-}$	*ApoE*$^{-/-}$ *Dcir1*$^{-/-}$	P values
		HFD		
Lipid content	X10^3 μm^2	49.3±5.8	59.0±3.5	0.1431
	% per lesion	30.0±1.9	27.9±1.4	0.3930
VCAM1	X10^3 μm^2	7.3±1.6	10.6±1.9	0.2743
	% per lesion	8.2±1.1	7.3±1.2	0.4598
CD206	X10^3 μm^2	**8.9±2.7**	**18.2±4.0**	**0.0350**
	% per lesion	5.1±1.6	5.4±0.8	0.0503

Table 5.3 Summary of the phenotype of the aortic root lesion from 20-week old *ApoE*$^{-/-}$ and *ApoE*$^{-/-}$ *Dcir1*$^{-/-}$ mice on a high fat diet.

Aortic root sections of *ApoE*$^{-/-}$ and *ApoE*$^{-/-}$ *Dcir1*$^{-/-}$ mice on a HFD were characterised by histology. The content of lipid, VCAM1 and CD206 in the lesion is measured. The average of lipid areas was calculated from sections of 100-600 μm. The area of VCAM1 and CD206 is at 600 μm. n=9-12 each group. Data are presented as mean±SEM. Mann-Whitney test. ND: Not determined. NA: Not applicable.

5.6. DCIR1 sustains the resident macrophage population and limits monocyte influx in the aorta

Single cells from the aorta, spleen and PALN were characterised in 20-week old *ApoE*$^{-/-}$ and *ApoE*$^{-/-}$ *Dcir1*$^{-/-}$ mice either on a chow diet or HFD by mass cytometry (CyTOF) in males and by flow cytometry in females. Total cell numbers of these tissues are summarised in **Table 5.4**. The antibody panel used for CyTOF in this study is available in Materials and Methods Table 7.7.

♂	*ApoE*$^{-/-}$	*ApoE*$^{-/-}$ *Dcir1*$^{-/-}$	P values	*ApoE*$^{-/-}$	*ApoE*$^{-/-}$ *Dcir1*$^{-/-}$	P values
		Chow diet			HFD	
Aorta	0.38±0.04	0.33±0.05	0.2852	0.42±0.09	0.36±0.04	0.9310
Spleen	**41.1±5.48**	**24.3±3.07**	**0.0166**	25.0±4.44	34.8±5.45	0.1906
PALN	0.39±0.07	0.44±0.08	0.5454	0.46±0.09	1.21±0.43	0.1562

♀	*ApoE*$^{-/-}$	*ApoE*$^{-/-}$ *Dcir1*$^{-/-}$	P values	*ApoE*$^{-/-}$	*ApoE*$^{-/-}$ *Dcir1*$^{-/-}$	P values
		Chow diet			HFD	
Aorta	0.45±0.08	0.48±0.10	0.8467	0.57±0.12	0.57±0.10	0.9147
Spleen	32.4±5.09	25.4±3.77	0.6784	28.1±2.45	18.6±2.79	0.0512
PALN	0.80±0.23	0.91±0.26	0.8283	0.59±0.14	0.51±0.15	0.6559

Table 5.4 Cell numbers from the aorta, spleen and para-aortic lymph nodes (PALN) of 20-week old *ApoE*$^{-/-}$ and *ApoE*$^{-/-}$ *Dcir1*$^{-/-}$ mice on a chow or high fat diet.

Males n=10-16, females n=8-10. values are presented as mean±SEM. The unit is in million. Mann-Whitney test.

viSNE clustering was performed on live CD45+ cells from the aorta of mice of the two genotypes. viSNE analysis allowed identification of 13 major leucocyte populations in the atherosclerotic aorta, comprising macrophages, monocytes (Ly6C+CD43-, Ly6C-CD43+ and Ly6C^{low} CD43^{low}), type 1 and 2 conventional DC (cDC1 and cDC2), granulocytes (neutrophils and eosinophils), B cells (B1 B and B2 B) and T cells ($\gamma\delta$+, CD4+ and CD8+) (**Figure 5.10a,b**). Two unknown clusters were also detected; one myeloid population expressing CD11c and CD68 and one lymphoid population expressing CD3 and CD90.2.

As previously shown in Chapter 2, HFD feeding diminished resident populations such as resident macrophages (P=0.1375) and B1 B cells (P<0.05) whilst increasing recruited-phenotype populations such as recruited macrophages (P<0.05), CD11c+ CD68+ MHCII- (P<0.05), Ly6C+ monocytes (P<0.01), neutrophils (P<0.05) and Ly6C+ CD8+ T cells (P<0.01) (**Table 5.5**). In the chow-fed *ApoE*$^{-/-}$ and *ApoE*$^{-/-}$ *Dcir1*$^{-/-}$ animals, there were no significant differences in the immune cell composition of the aorta (**Table 5.5**). However, in HFD-fed conditions, *Dcir1* deletion resulted in a significant increase in the percentages of MHCII+ Ly6C+ monocytes and B2 B cells (*ApoE*$^{-/-}$ vs. *ApoE*$^{-/-}$ *Dcir1*$^{-/-}$: mono: 1.4±0.2 vs. 2.8±0.5% P<0.01, B2 B: 1.9±0.6 vs. 3.0±0.6% P<0.05; **Table 5.5**). Although the percentage of total macrophages per live CD45+ cells was not altered by *Dcir1* deficiency, the immune cell composition in myeloid cell populations was shifted in favour of the recruited (CD11c+) macrophages and monocytes in *ApoE*$^{-/-}$ *Dcir1*$^{-/-}$ mice (**Figure 5.11 a,b)**. An increase in CD11c+ macrophages in HFD-fed *ApoE*$^{-/-}$ *Dcir1*$^{-/-}$ mice was evident as compared to *ApoE*$^{-/-}$ mice (*ApoE*$^{-/-}$ vs. *ApoE*$^{-/-}$ *Dcir1*$^{-/-}$: 13.8±2.4 vs. 22.7±2.2% P<0.05; **Figure 5.11c**). The expansion of CD11c+ macrophages was associated with decrease in the proportion

of resident CD206+ macrophages (*ApoE*$^{-/-}$ vs. *ApoE*$^{-/-}$ *Dcir1*$^{-/-}$: 75.8±3.6 vs. 64.1±3.3% P<0.05). Furthermore, there seemed to be a mild increase in a macrophage population lacking CD11c and CD206.

Consistent with the CyTOF data, a similar phenotypic change in macrophages was detected by flow cytometry. *Dcir1* deficiency diminished the proportion of Lyve1 expressing resident macrophages while increasing the CD11c+ macrophage population (*ApoE*$^{-/-}$ vs. *ApoE*$^{-/-}$ *Dcir1*$^{-/-}$: Lyve1+ mac: 19.3±4.0 v. 6.9±1.6% P<0.05, CD11c+ mac: 7.8±1.6 vs. 12.1±1.3% P=0.0545; **Figure 5.12**).

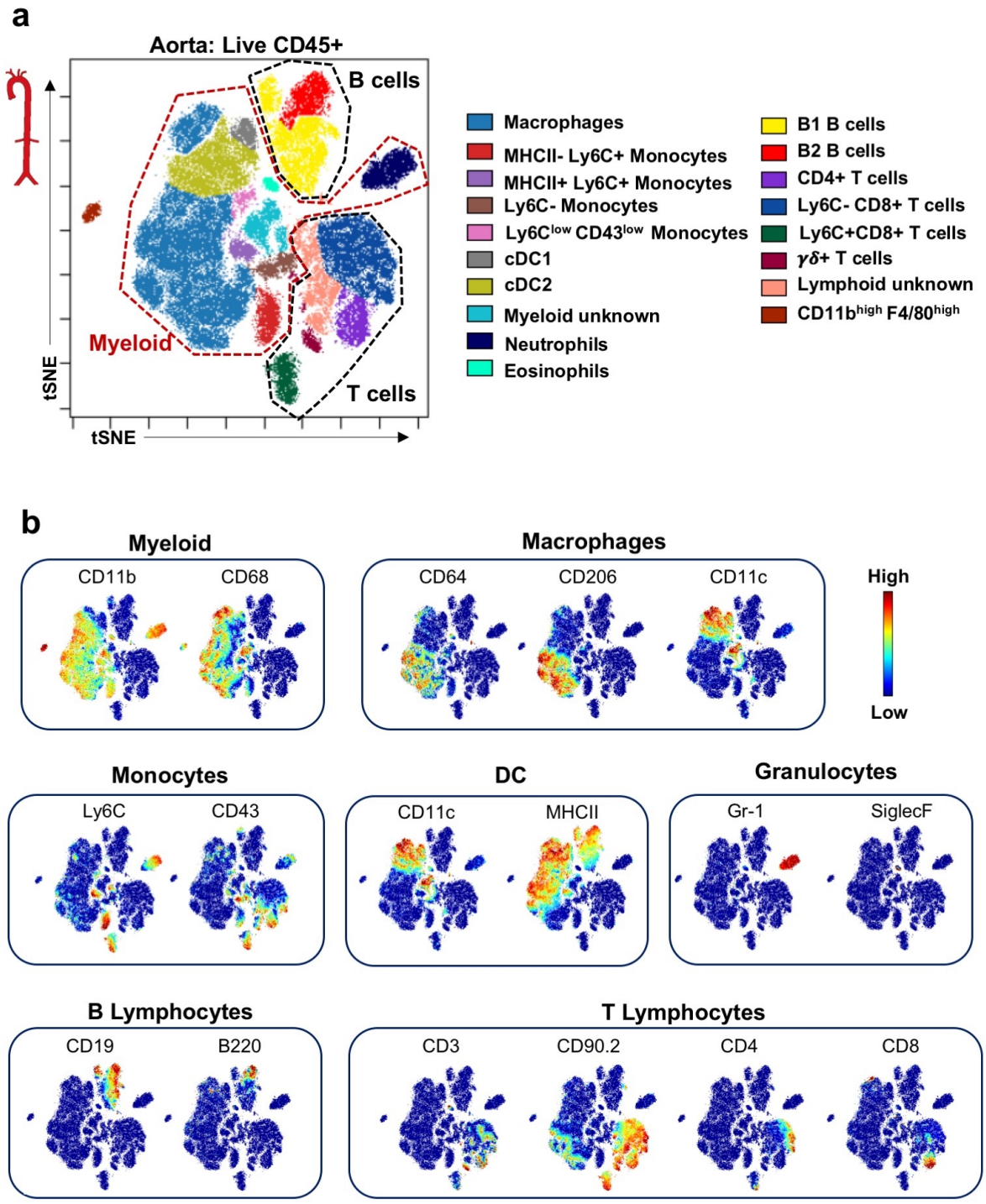


Figure 5.10 The immune cell composition of aortas from 20-week old *ApoE*$^{-/-}$ and *ApoE*$^{-/-}$ *Dcir1*$^{-/-}$ mice by mass cytometry.

Single cells from aortas of *ApoE*$^{-/-}$ and *ApoE*$^{-/-}$ *Dcir1*$^{-/-}$ males on a chow and HFD are analysed by mass cytometry (CyTOF) and multi-dimensional clustering viSNE. **a)** The viSNE image of aortic leucocytes from all mice shows 20 clusters and 17 of which are identified. **b)** Selected marker expressions by cell population.

♂	*ApoE*$^{-/-}$	*ApoE*$^{-/-}$ *Dcir1*$^{-/-}$	P values	*ApoE*$^{-/-}$	*ApoE*$^{-/-}$ *Dcir1*$^{-/-}$	P values
	Chow			HFD		
Macrophages	36.4±3.8	31.1±4.8	0.9926	28.3±5.5	30.5±3.4	0.9999
MHCII- Ly6C+ mono	2.4±0.3	2.5±0.3	0.6163	4.6±0.8	5.2±0.4	0.4359
MHCII+ Ly6C+ mono	0.6±0.2	0.8±0.2	0.0950	**1.4±0.2**	**2.8±0.5**	**0.0089**
Ly6C- mono	2.1±0.3	2.2±0.3	0.4822	2.8±0.4	2.6±0.1	0.8534
Intermediate mono	0.6±0.1	0.6±0.2	0.6245	0.8±0.2	0.8±0.2	0.5787
cDC1	1.6±0.2	1.2±0.1	0.3650	2.3±0.3	2.2±0.2	0.9118
cDC2	6.6±0.9	6.3±1.0	0.9203	7.1±1.3	8.9±1.5	0.3527
Neutrophils	4.2±0.6	3.6±0.7	0.4411	5.5±0.7	6.7±0.6	0.1230
Eosinophils	0.7±0.1	0.9±0.2	0.2449	0.8±0.2	1.1±0.2	0.2176
B1 B	11.9±1.3	10.7±2.4	0.5699	8.0±1.1	6.8±1.4	0.2799
B2 B	1.7±0.4	4.5±2.2	0.4020	**1.9±0.6**	**3.0±0.6**	**0.0433**
CD4+ T	2.9±0.4	3.7±0.7	0.4411	3.9±0.6	5.0±0.6	0.1230
Ly6C- CD8+ T	10.5±1.9	17.2±4.5	0.3650	13.8±3.3	12.7±2.4	0.9705
Ly6C+ CD8+ T	2.4±0.4	3.3±0.5	0.1653	6.8±1.2	4.2±0.9	0.1655
γδ+ T	1.2±0.2	1.2±0.2	0.7639	1.0±0.3	1.5±0.3	0.2176

Table 5.5 The percentage of immune cell populations in the aorta of 20-week old *ApoE*$^{-/-}$ and *ApoE*$^{-/-}$ *Dcir1*$^{-/-}$ mice on chow and high fat diet by mass cytometry.

n=9-11. Data are presented as mean±SEM. Mann-Whitney test.

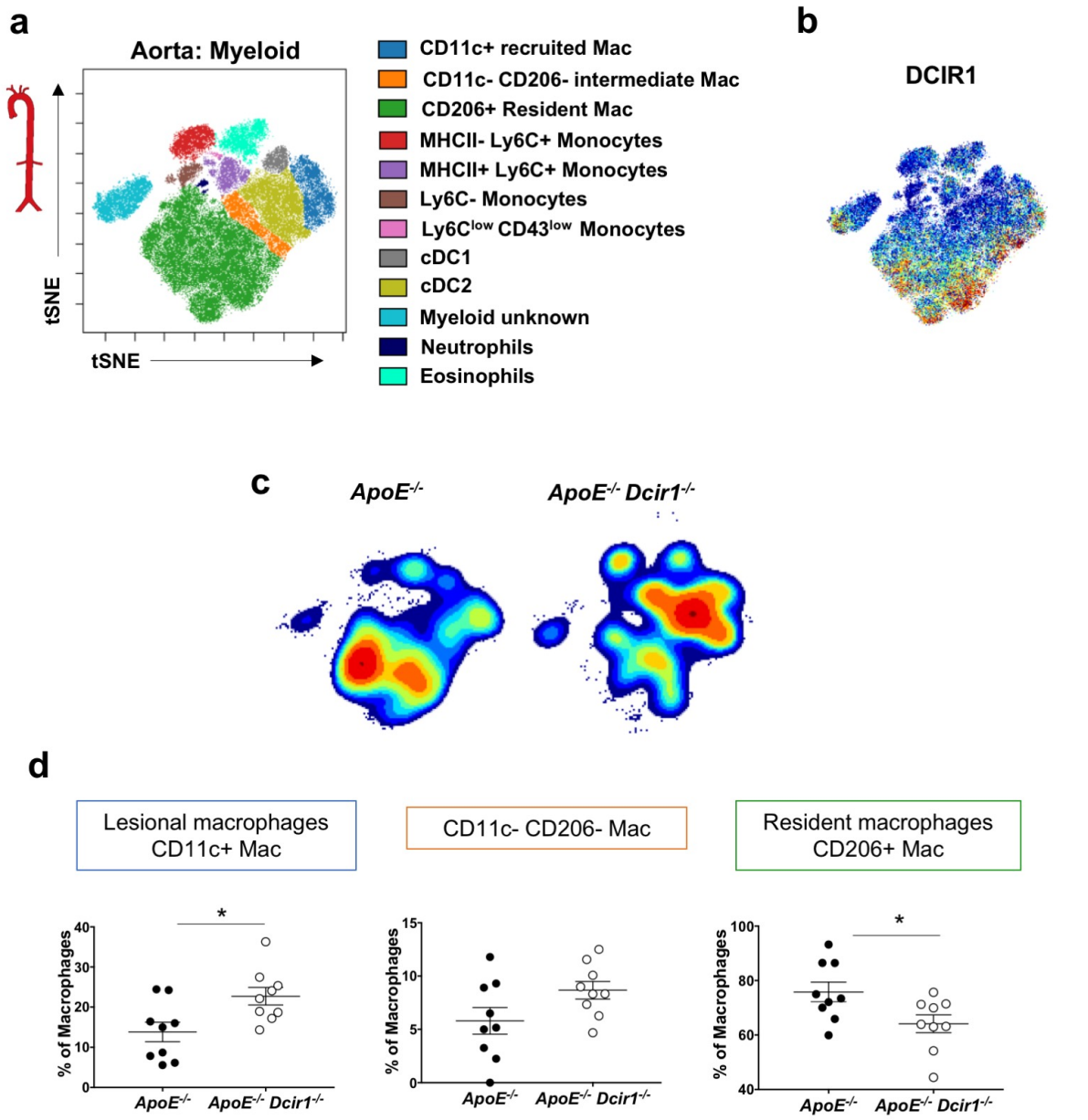


Figure 5.11 The phenotypic changes in macrophages from the aorta of 20-week old HFD-fed *ApoE*$^{-/-}$ and *ApoE*$^{-/-}$ *Dcir1*$^{-/-}$ mice by mass cytometry.

Single cells from aortas of *ApoE*$^{-/-}$ and *ApoE*$^{-/-}$ *Dcir1*$^{-/-}$ males on a chow and HFD are analysed by mass cytometry (CyTOF) and multi-dimensional clustering viSNE. **a)** Myeloid cell populations were gated from the viSNE analysis in Figure 5.10a and were re-analysed based on 21 myeloid markers. **b)** The expression of DCIR1 in myeloid populations. **c)** The representative density plots of the myeloid cells from *ApoE*$^{-/-}$ and *ApoE*$^{-/-}$ *Dcir1*$^{-/-}$ mice. **d)** Percentages of resident (CD206+), intermediate (CD11c- CD206-), lesional (CD11c+) macrophages from the aorta by genotype. Data are presented as mean±SEM. Mann-Whitney test. *P<0.05.

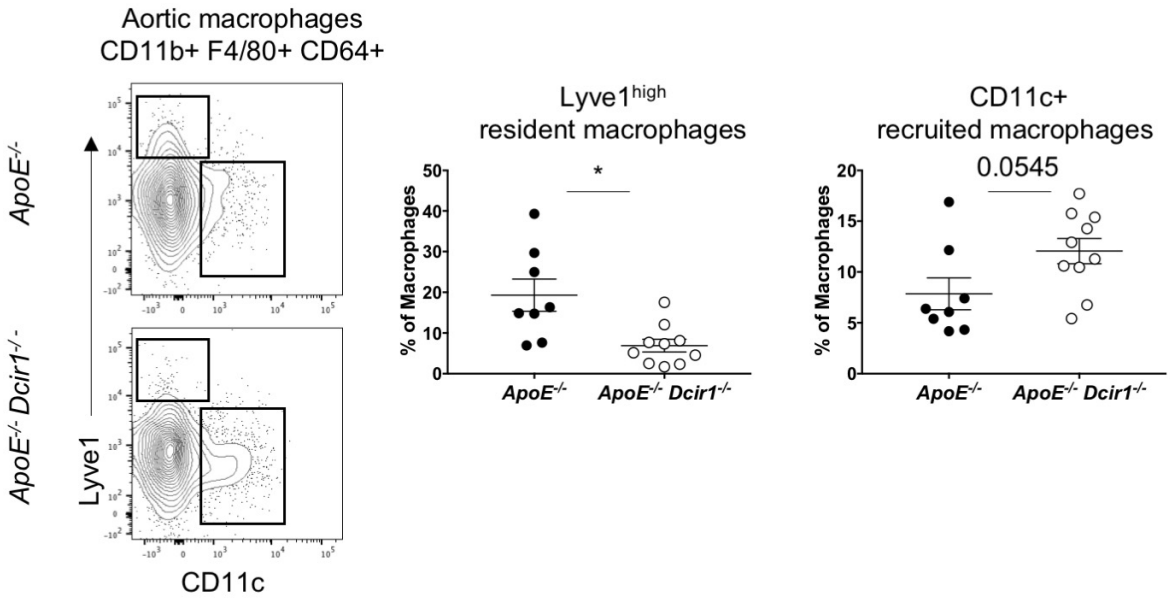


Figure 5.12 The phenotype of macrophages from the aorta of 20-week old HFD-fed *ApoE*$^{-/-}$ and *ApoE*$^{-/-}$ *Dcir1*$^{-/-}$ mice by flow cytometry.

Single cells from aortas are analysed by flow cytometry. Macrophages gated as CD11b+ F4/80+ CD64+ from the live CD45+ are displayed by the expression of Lyve1 (resident) and CD11c (lesional). Percentages of resident (Lyve1+) and lesional (CD11c+) macrophages from the aorta by genotype. Data are presented as mean±SEM. Mann-Whitney test. *P<0.05.

5.7. The effect of DCIR1 on the cellular composition of spleen and para-aortic lymph nodes

The immune cell composition in periphery immune organs including spleen and para-aortic lymph nodes (PALN) was also characterised in 20-week old *ApoE*$^{-/-}$ and *ApoE*$^{-/-}$ *Dcir1*$^{-/-}$ mice either on a chow diet or HFD by mass cytometry (CyTOF). The CyTOF analysis identifies 15 principal leucocyte populations in the spleen (**Table 5.6**). Of note, splenocytes from chow-fed *ApoE*$^{-/-}$ *Dcir1*$^{-/-}$ males have a tendency towards decreased innate immune populations and increased CD4+ T cells relative to their *ApoE*$^{-/-}$ counterparts. Total cell counts of splenocytes in the *ApoE*$^{-/-}$ *Dcir1*$^{-/-}$ strain were lower than in their *ApoE*$^{-/-}$ counterparts (*ApoE*$^{-/-}$ vs. *ApoE*$^{-/-}$ *Dcir1*$^{-/-}$: 41.1±5.5 vs. 24.3±3.1% P<0.05; Table 5.4). Four myeloid cell populations comprising Ly6C+ and Ly6C- monocytes, cDC1 and cDC2 were significantly decreased in the spleen of *ApoE*$^{-/-}$ *Dcir1*$^{-/-}$ mice compared to *ApoE*$^{-/-}$ mice (*ApoE*$^{-/-}$ vs. *ApoE*$^{-/-}$ *Dcir1*$^{-/-}$: Ly6C+ mon: 2.4±0.4 vs. 1.0±0.2% P<0.01, Ly6C- mon: 1.0±0.2 vs. 0.5±0.1% P<0.05, cDC1: 0.4±0.0 vs. 0.2±0.0% P<0.001, cDC2: 1.1±0.2 vs. 0.5±0.1% P<0.05). NK and pDCs in the spleen of *ApoE*$^{-/-}$ *Dcir1*$^{-/-}$ mice were also reduced compared to in *ApoE*$^{-/-}$ counterparts (*ApoE*$^{-/-}$ vs. *ApoE*$^{-/-}$ *Dcir1*$^{-/-}$: NK: 3.2±0.2 vs. 2.3±0.2% P<0.05, pDCs: 0.5±0.1 vs. 0.2±0.1% P<0.05). In contrast, splenic CD4+ T cells were increased in the *Dcir1*-deficient *ApoE*$^{-/-}$ mice relative to *ApoE*$^{-/-}$ mice (*ApoE*$^{-/-}$ vs. *ApoE*$^{-/-}$ *Dcir1*$^{-/-}$: 19.5±1.6 vs. 24.2±1.5% P<0.05). When fed on a HFD, the splenic content of Ly6C+ $\boldsymbol{\gamma\delta}$+ T cells was halved in *ApoE*$^{-/-}$ mice vs *ApoE*$^{-/-}$ *Dcir1*$^{-/-}$ mice. No other significant differences were detected in the spleen of HFD-fed mice.

♂	*ApoE*$^{-/-}$	*ApoE*$^{-/-}$ *Dcir1*$^{-/-}$	P values	*ApoE*$^{-/-}$	*ApoE*$^{-/-}$ *Dcir1*$^{-/-}$	P values
	Chow			HFD		
Macrophages	0.4±0.1	0.2±0.1	0.0533	0.4±0.1	0.5±0.1	0.3054
Ly6C+ mono	**2.4±0.4**	**1.0±0.2**	**0.0040**	1.7±0.3	1.5±0.2	0.9273
Ly6C- mono	**1.0±0.2**	**0.5±0.1**	**0.0297**	1.1±0.2	1.2±0.2	0.7394
cDC1	**0.4±0.0**	**0.2±0.0**	**0.0008**	0.8±0.2	0.4±0.1	0.1717
cDC2	**1.1±0.2**	**0.5±0.1**	**0.0142**	1.0±0.1	1.0±0.1	0.9537
Neutrophils	2.6±0.4	2.5±0.5	0.6201	3.2±0.7	2.8±0.3	0.8100
Eosinophils	0.7±0.1	0.5±0.1	0.5297	0.6±0.1	0.5±0.1	0.6708
B cells	48.7±1.9	47.8±1.4	0.6665	50.2±1.8	51.0±1.8	0.9118
CD4+ T	**19.5±1.6**	**24.2±1.5**	**0.0400**	20.7±1.3	20.5±1.0	>0.9999
Ly6C- CD8+	5.2±0.6	7.8±0.9	0.0503	6.0±0.6	5.5±0.3	0.6986
Ly6C+ CD8+	5.3±0.2	4.8±0.2	0.1685	4.7±0.4	4.5±0.2	0.7394
Ly6C- γδ+ T	0.4±0.1	0.3±0.0	0.4342	0.3±0.0	0.3±0.0	0.3049
Ly6C+ γδ+ T	0.4±0.1	0.3±0.0	0.8134	**0.4±0.1**	**0.2±0.1**	**0.0064**
NK	**3.2±0.2**	**2.3±0.2**	**0.0106**	2.9±0.3	2.8±0.3	0.8534
pDCs	**0.5±0.1**	**0.2±0.1**	**0.0244**	0.5±0.1	0.4±0.1	0.6705

Table 5.6 The percentage of immune cell populations in the spleen of 20-week old *ApoE*$^{-/-}$ and *ApoE*$^{-/-}$ *Dcir1*$^{-/-}$ mice on chow or high fat diet by mass cytometry.

n=9-10. Data are presented as mean±SEM. Mann-Whitney test.

In PALN, there were no significant differences in the proportion of cellular populations between the genotypes in both chow and HFD-fed conditions apart from a DC-macrophage mixed cell population, which was lower in *ApoE*$^{-/-}$ *Dcir1*$^{-/-}$ mice on a chow diet (*ApoE*$^{-/-}$ vs. *ApoE*$^{-/-}$ *Dcir1*$^{-/-}$: 0.6±0.1 vs. 0.2±0.1% P<0.05; **Table 5.7**). In general, *Dcir1* deficiency impacts the homeostasis of myeloid cell populations in peripheral immune organs, suppressing these populations in mild atherosclerosis. However, *Dcir1* deficiency may have less of an impact on myeloid cell populations during disease development although its effect was evident in the aorta, by recruiting monocytes and switching the phenotype of macrophages towards inflammatory.

♂	*ApoE*$^{-/-}$	*ApoE*$^{-/-}$ *Dcir1*$^{-/-}$	P values	*ApoE*$^{-/-}$	*ApoE*$^{-/-}$ *Dcir1*$^{-/-}$	P values
	Chow			HFD		
DC/Mac	**0.6±0.1**	**0.2±0.1**	**0.0105**	0.5±0.1	0.4±0.1	0.3154
B cells	35.4±6.6	33.1±4.9	0.7962	44.0±4.2	48.6±5.9	0.4002
CD4+ T	33.7±4.3	37.5±3.8	0.6048	26.2±2.2	24.5±2.8	0.5490
Ly6C- CD8+ T	13.4±1.3	16.2±1.9	0.4894	12.8±1.2	12.0±1.8	0.6038
Ly6C+ CD8+ T	12.2±1.1	9.0±1.3	0.0503	11.2±0.9	9.0±0.7	0.1333
γδ+ T	0.9±0.3	0.5±0.1	0.4894	0.4±0.1	0.5±0.1	0.9682
NK	1.0±0.1	0.6±0.2	0.0939	0.7±0.1	0.8±1.2	0.4967

Table 5.7 The percentage of immune cell populations in the para-aortic lymph nodes (PALN) of 20-week old *ApoE*$^{-/-}$ and *ApoE*$^{-/-}$ *Dcir1*$^{-/-}$ mice on chow or high fat diet by mass cytometry.

n=9-10. Data are presented as mean±SEM. Mann-Whitney test.

5.8. Characterisation of aortic myeloid cells from *Dcir1*-competent and *Dcir1*-deficient *ApoE*$^{-/-}$ mice using single cell RNA sequencing

To gain insights into how genetic deletion of *Dcir1* shapes the transcriptome profile of myeloid cells in the atherosclerotic aorta, I performed scRNAseq on live CD45+ CD11b+ cells from aortas of 20-week old *ApoE*$^{-/-}$ and *ApoE*$^{-/-}$ *Dcir1*$^{-/-}$ mice fed HFD. First, a novel dimensionality reduction framework, namely the ivis algorithm (developed in collaboration with Dr Ignat Drozdov from Bering Ltd) was adopted for clustering, together with conventional cell clustering methods (tSNE and LargeVis). Gene ontology analysis of biological processes (GO analysis) was also performed to elucidate the functional profiling of the clusters.

Single cell analysis of CD11b+ aortic cells revealed 9 myeloid clusters, including 6 macrophage subsets, neutrophils, Ly6C+ monocytes and DCs, together with 5 unknown clusters (**Figure 5.13a,b,c**). Cluster 2 encompassed Ly6C+ monocytes and exhibited an inflammatory phenotype, expressing pro-inflammatory mediators. The gene expression profile of Cluster 5 had features of polymorphonuclear cells including neutrophils, showing high levels of *S100a8, S100a9, Ly6g* and *Csf3r*. Neutrophils displayed an inflammatory gene signature, expressing *Nfkb* complex genes and *Il1b*. Cluster 11 displayed a DC gene signature of *Ccr7, Cd40, Cd86, H2-Ab1* (MHCII) and *Dpp4*. Clusters representing less than 3% of total cells were also found; 2 of these expressed T cell markers (Cluster 10 and 12) and Cluster 13 expressed endothelial cell-associated genes.

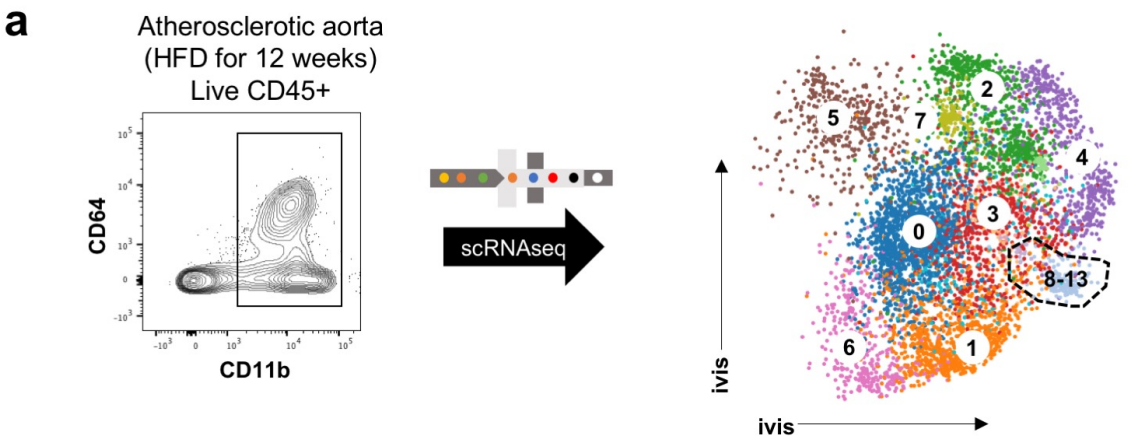
The 6 macrophage clusters were identified and comprised 3 CD206+ “resident” and 3 CD11c+ “recruited” macrophage subsets (**Figure 5.13a,b,c**). First, Cluster 0

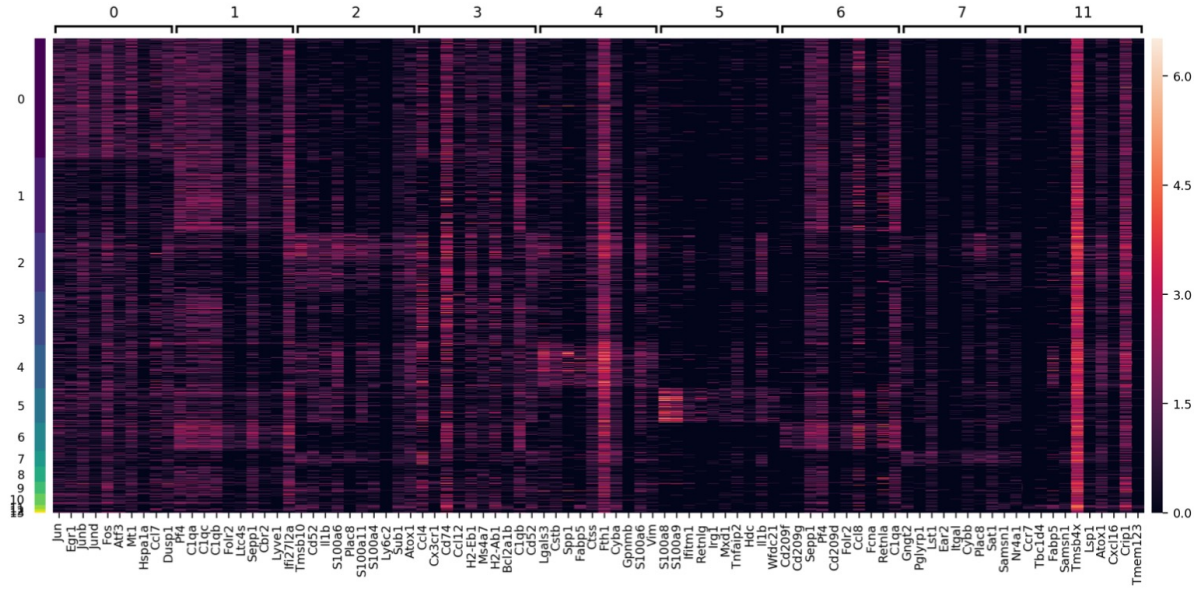
expressed haem oxygenase 1 (HO1; gene name: *hmox1*) and resident macrophage markers (*Lyve1, Mrc1, CD163*). Oxidised phospholipids within the murine atherosclerotic plaque drive a unique phenotype of macrophages, by promoting redox-regulatory gene expression via nuclear factor erythroid 2–related factor (Nrf) 2 (Kadl et al., 2010). The gene expression profile of cluster 0 suggested that this subset may represent Mox macrophages. In addition, Clusters 1 and 6 represented CD206+ CD209b- macrophage and CD206+ CD209b+ macrophage subsets, respectively. These three clusters presented the features of resident macrophages, such as the expression of resident macrophage markers including *Lyve1, Mrc1* and *CD163*. The data from the GO analysis indicated that these CD206+ clusters were also associated with functions such as angiogenesis (Cluster 0: CD206+ HO1+ macrophages), cholesterol clearance (Cluster 1: CD206+ CD209b- macrophages) and maintenance of proliferation of vascular endothelial cells and VSMCs (Cluster 6: CD206+ CD209b+ macrophages **Figure 5.13d**). Clusters 1 and 6 were identifiable in the CyTOF analysis, however, Cluster 0 was not clearly identifiable due to the scarce success of the HO1 antibody.

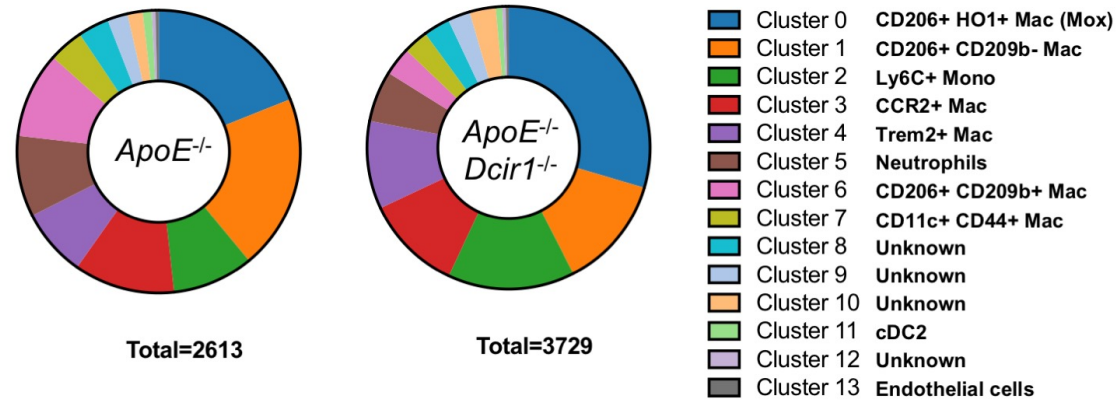
The additional 3 clusters of macrophages identified in this single cell genomics analysis of CD11b+ aortic cells were similar to the subsets identified in the CyTOF analysis. First, CCR2+ macrophages (Cluster 3) exhibited high expression levels of the chemokine receptors CCR2 and CX3CR1. Cluster 4 and Cluster 7 expressed high levels of CD11c and CD44. Of relevance, Clusters 3 and 4 expressed Trem2, a marker expressed by infiltrating and inflammatory macrophages and Trem2^{high} macrophages in human and murine atherosclerotic aortas were previously identified (Turnbull et al., 2006, Cochain et al., 2018). These 3 latter clusters shared a variety of genes involved

in chemotaxis and immune responses according to the GO analysis, indicating they might be recruited subsets.

When the representation of each cluster was compared across the 2 genotypes, aortas of *ApoE*$^{-/-}$ *Dcir1*$^{-/-}$ mice were found to be enriched in CD206+ HO1+ Mac (Cluster 0), Cluster 2 (Ly6C+ Mono) and Cluster 4 (Trem2+ Mac) (**Figure 5.13c**). *Dcir1* deficiency in the atherosclerotic aorta decreased Cluster 1 (CD206+ CD209b- Mac), Cluster 5 (neutrophils) and Cluster 6 (CD206+ CD209b+ Mac). The proportion of Cluster 3 (CCR2+ Mac), Cluster 7 (CD11c+ CD44+ Mac) and Cluster 11 (cDC2) were not altered by *Dcir1* deletion.







(Continued on the next page)

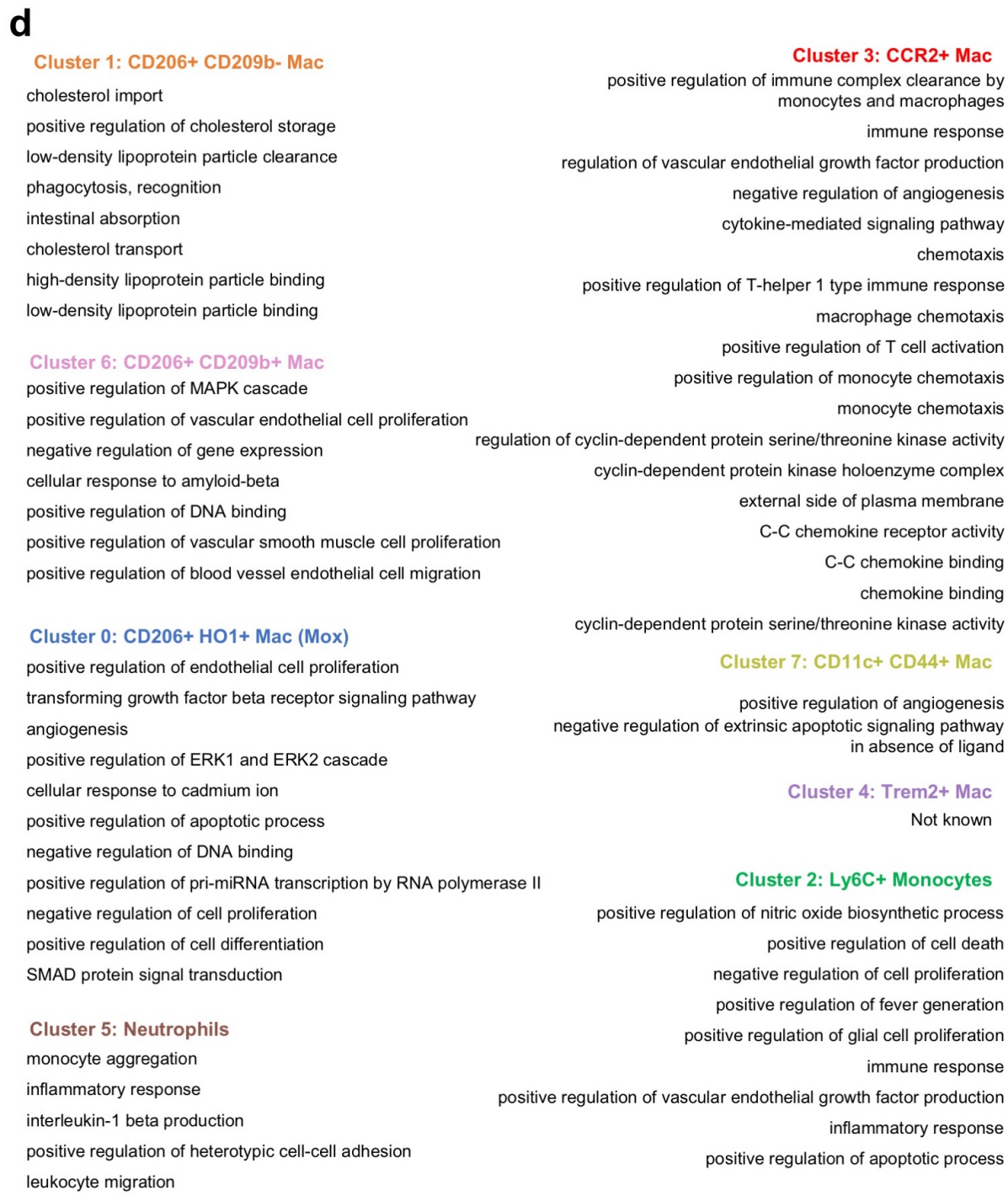


Figure 5.13 Single cell RNA sequencing identifies 9 myeloid populations in CD11b+ cells from aorta of *ApoE*$^{-/-}$ and *ApoE*$^{-/-}$ *Dcir1*$^{-/-}$ mice.

a) Live CD45+ CD11b+ cells were isolated from aortas of 8 *ApoE*$^{-/-}$ and *9 ApoE*$^{-/-}$ *Dcir1*$^{-/-}$ females fed on HFD. Single cells were then sequenced by using 10X Genomics platform. The transcriptomic data from single cells were analysed using ivis, which identifies 11 clusters. **b)** The heatmap of 14 clusters showing top 10 genes each. **c)** The proportion of all clusters by genetype. **d)** Gene ontology analysis of biological processes (GO analysis) was applied to all clusters to relate the gene expression profile to cellular functions. The data of 8 identified myeloid subsets are shown.

5.9. Discussion

In Chapter 2, I showed that the progression of atherogenesis triggers radical changes in the vascular myeloid cell composition: an increase in monocyte and recruited macrophages and a decrease in resident macrophages. Monocyte influx is strongly associated with initiation of atherosclerosis and Ly6C+ monocytes differentiate into macrophages which sustains their proliferation in the lesion (Swirski et al., 2007, Robbins et al., 2013). The atherogenic micro-environment shapes the phenotype of macrophages, which range from inflammation, lipid-handling, redox regulation, haemorrhage remodelling, phagocytosis and anti-inflammation (Moore et al., 2013). The regulators of these myeloid cell dynamics associated with atherogenesis are unknown.

In Chapters 2 and 4, I highlighted that *Dcir1* was highly expressed by vascular macrophages and discriminated the resident population from the recruited counterpart. Here, I also showed that human *Dcir* and murine *Dcir1* expression was increased in the atherosclerotic tissue and presented a strong association with macrophage markers. I generated *ApoE*$^{-/-}$ and *ApoE*$^{-/-}$ *Dcir1*$^{-/-}$ mice to investigate whether *Dcir1* deficiency affects atherogenesis. Histological assessments on the aortic root lesions of these mice demonstrated that *Dcir1* deficiency exacerbated lesion development in advanced atherosclerosis (high fat feeding for 12 weeks). When both strains were further challenged by feeding HFD for 18 weeks, *ApoE*$^{-/-}$ *Dcir1*$^{-/-}$ mice developed significantly larger plaques across the whole aorta relative to *ApoE*$^{-/-}$ mice. DCIR1 exerted more of an effect in the advanced stages of disease and its loss had the limited effect on early lesions modelled in chow-diet fed *ApoE*$^{-/-}$ mice.

A significant difference in lesional necrotic core formation was evident in hyperlipidaemic mice deficient in *Dcir1* compared to their littermates. Lesional necrotic core size was three times larger in the absence of *Dcir1*, suggesting that DCIR1 has an important role in regulating the formation of the necrotic core. Mechanisms associated with necrotic core formation include increased apoptosis and/or defective efferocytosis (Thorp and Tabas, 2009). The scRNAseq data on aortic myeloid cells indicated that *Dcir1* deficiency resulted in expansion of CD206+ HO1+ (Mox) macrophages undergoing apoptosis. Although Mox macrophages express the resident marker CD206, HO1 expression is widely found in the lesional area, indicating that this subset might reside in the lesion and are possibly responsible for the accumulation of necrotic cores. The presence of enhanced apoptosis of macrophages in the lesion could be confirmed by *in situ* TUNEL staining to ascertain the role of DCIR1 in efferocytosis.

A second feature of *Dcir1* deletion in atherogenesis was the striking change in the representation of myeloid cell subsets within the aorta. Mice lacking *Dcir1* exhibited an increased recruitment of inflammatory monocytes in the aorta, in particular Ly6C+ monocytes expressing MHCII. There was also a significant increase in CD11c+ CD44+ macrophages and CD206+ HO1+ (Mox) macrophages in the aorta of *ApoE*$^{-/-}$ *Dcir1*$^{-/-}$ mice. A decrease in two resident macrophage subsets, CD206+ CD209b+ and CD206+ CD209b- cells, was observed in *ApoE*$^{-/-}$ *Dcir1*$^{-/-}$ mice. Altogether, DCIR1 may regulate the balance between recruited and resident macrophages.

To date, studies using scRNAseq and mass cytometry have demonstrated several macrophage subsets in the atherosclerotic lesion. Cochain et al. introduced three

subsets comprising inflammatory ("recruited"), resident-like and Trem2^{high} macrophages (Cochain et al., 2018) and Kim et al. recently separated recruited macrophages into foam cells and an inflammatory subset (Kim et al., 2018). Winkels et al. and Cole et al. utilised mass cytometry and concomitantly showed recruited and resident macrophages (Cole et al., 2018, Winkels et al., 2018). I initially introduced 4 macrophage subsets including 2 recruited (CD11c+ and CCR2+ subsets) and 2 resident (CD206+ CD209b+ and CD206+ CD209b- subsets) phenotypes by scRNAseq in Chapter 2. Here, I further identified 6 subsets, consisting of 4 currently known populations (CD11c+, Trem2+, CD206+ CD209b- and CD206+ HO1+ (Mox)) and novel subsets CCR2+ recruited and CD206+ CD209b+ resident macrophages. Of these macrophages, *Dcir1* was highly expressed by two resident subsets: CD206+ CD209b- and CD206+ CD209b+.

DCIR1 may limit the growth and instability of atherosclerotic plaques by restricting monocyte influx to the artery and their differentiation into lesional macrophages. The findings in Chapter 4 also supported this hypothesis by showing that ablation of aortic resident macrophages promoted influx of Ly6C+ monocytes, which potentially give rise to Ly6C+ CD44+ macrophages. Several studies using *Dcir1*$^{-/-}$ mice in murine disease models also suggested that DCIR1 may modulate myeloid cell homeostasis (Fujikado et al., 2008, Seno et al., 2015). Thus, my results also support the idea that DCIR1 maintains survival and phenotype of resident macrophages during arterial inflammation, and controls the recruitment of monocytes to tissues.

Vascular Lyve1+ macrophages sustain arterial homeostasis by degrading excessive collagen and absence of Lyve1+ macrophages increases stiffness and the size of the

artery (Lim et al., 2018). *Dcir1* deficiency resulted in expansive arterial remodelling and profound changes in the VSMC compartment. According to the histological features of the aortic root from *ApoE*$^{-/-}$ *Dcir1*$^{-/-}$ mice on HFD, the VSMC area was decreased in the arterial media and the artery size was enlarged. The GO analysis also supported the finding that CD206+ CD209b+ macrophages, that regulate proliferation of VSMC and express high levels of *Dcir1*, were reduced in the aorta of *ApoE*$^{-/-}$ *Dcir1*$^{-/-}$ mice. Future work could focus on detecting co-localisation of VSMC and aortic CD206+ CD209b+ macrophages *in situ* and the potential interaction of these cells could be investigated through *in vitro* co-culture. Thus, DCIR1 plays an important role in modulating arterial remodelling during atherogenesis, by supporting resident macrophages and their connections with SMC.

In summary, DCIR1 maintains survival of resident vascular macrophages and inhibits monocyte recruitment to the artery during atherogenesis. *Dcir1* deficiency results in diminished resident macrophages, which in turn promotes recruitment of monocytes and accumulation of lesional macrophages. This cellular shift may accelerate lesion formation and drive plaque instability.

CHAPTER 6. Final Discussion

Macrophages are long lived phagocytic cells that reside in the specific tissue niche, supporting tissue homeostasis (Gordon and Pluddemann, 2017). For instance, vascular macrophages are located in the adventitial layer of the artery where they regulate vessel wall remodelling via communication with smooth muscle cells (SMCs) (Lim et al., 2018). Vascular macrophages originate from embryonic precursors and are postnatally replaced by monocytes (Ensan et al., 2016). They self-maintain via C-X3-C motif chemokine ligand (CX3CL1) and macrophage colony-stimulating factor (MCSF) after birth (Ensan et al., 2016, Lim et al., 2018).

During atherogenesis, cardiovascular risk factors such as hypercholesterolaemia promote recruitment of monocytes to the intimal space of the aorta where they differentiate into macrophages (Swirski et al., 2007). These intimal (or recruited) macrophages acquire scavenger receptors and differentiate into various subsets in response to atherogenic signals (Robbins et al., 2013). The establishment of macrophages within the arterial intima in early atherosclerosis is dependent on the recruitment of monocytes from the circulating blood (Boring et al., 1998, Combadiere et al., 2003, Lesnik et al., 2003, Combadiere et al., 2008). It has been proposed that the recruited macrophages can self-renew through their acquired scavenger receptors in advanced atherosclerosis (Robbins et al., 2013).

Several macrophage subsets have been described in atherosclerotic lesions including inflammatory (M1), oxidised phospholipid-induced (Mox), haemorrhage-induced (Mhem and M(hb)) and anti-inflammatory (M2) macrophages (Figure 1.3) (Chinetti-Gbaguidi et al., 2015, Park et al., 2017). However, the role of resident vascular macrophages in atherosclerosis is unknown. In this thesis, I characterised

macrophage subsets in the healthy and atherosclerotic artery with single cell technologies, and identified new subsets and their dynamics in atherogenesis. Furthermore, I demonstrated the essential role of dendritic cell immunoreceptor (DCIR) 1 in resident macrophage biology and its protective role in atherosclerosis.

6.1. Characterisation of macrophage subsets in the atherosclerotic aorta

In order to delineate vascular macrophage subsets in healthy and atherosclerotic mice, I adopted mass cytometry and single cell genomics. I showed that healthy murine aortas contain a significant complement of macrophages, the majority of which reside in the adventitia in the steady state (Figure 2.5). Vascular macrophages were readily identifiable as they expressed CD64, while dendritic cells (DCs) did not (Figure 2.2). Vascular resident macrophages in the healthy and atherosclerotic aorta expressed CD206 and Lyve1 (Figure 4.12, Figure 2.5, Figure 2.8). I identified for the first time 3 subsets within CD206+ macrophages: 1) CD206^{high} CD169+ CD209b+ 2) CD206^{high} CD169+ CD209b- and 3) CD206+ CD169- CD209b- (Figure 2.5) (Cole et al., 2018) **(Figure 6.1)**. Further analysis with single cell RNA sequencing (scRNAseq) on macrophages from the atherosclerotic aorta confirmed the existence of a subset of macrophages expressing CD206, Lyve1 and CD209b (resident subset 1; hereafter CD209b+ macrophages). The transcriptomic data identified a new CD206+ subset expressing haem oxygenase 1 (HO) 1+ (resident subset 3; hereafter HO1+ macrophages) (Figure 2.7). According to the Gene Ontology (GO) enrichment analysis which identifies potential function based on the transcriptomic profile, CD209b+ macrophages support humoral immune responses and complement activation. HO1+ macrophages may be involved in responses to tissue damage and extracellular

signal–regulated kinases (ERK) signalling, suggesting equivalent function to that of oxidised phospholipid-induced macrophages (Mox).

Moreover, I defined 3 subsets of vascular macrophages with a “recruited” phenotype in atherosclerosis: by using mass cytometry and scRNAseq: 1) CD11c+ CD44+ MHCII+, 2) CD11c+ CD44+ MHCII- and 3) CCR2+ subsets. Single cell genomics confirmed the existence of an inflammatory macrophage subset bearing CD11c and CD44 and a CCR2+ subset. The GO analysis suggests that CD11c+ macrophages are capable of chemotaxis, lipid localisation and production of cytokines (Figure 2.7). The CCR2+ subset is associated with wound healing, phagocytosis and reactive oxygen species metabolic processes, which suggests the potential representation of anti-inflammatory macrophages (Rahman et al., 2017).

CD11c+ macrophages are virtually absent in the normal intima and vessel wall, and are largely increased during atherogenesis (Figure 2.3). I demonstrated that CD11c expression was predominantly detected in the intima bearing lesions while CD206 was strongly expressed in the adventitia. The macrophage marker CD64 overlaid with CD11c expression in the intima, provided evidence that CD11c+ macrophages are associated with atherosclerosis. Although the presence of CD11c+ myeloid cells in the intima of the atherosclerotic artery was reported by several research groups (Wu et al., 2009, Paulson et al., 2010, Koltsova et al., 2012), it was challenging to distinguish CD11c+ macrophages from DCs due to the lack of multi-parametric analysis. In the paper by Cole et al. we were the first to use mass cytometry to delineate macrophages from DCs in the murine aorta (Cole et al., 2018). Our group previously showed that interferon regulatory factor (IRF5) directly regulates CD11c gene expression in

macrophages and global deletion of IRF5 diminishes CD11c+ macrophages in the atherosclerotic aorta (Seneviratne et al., 2017). In contrast to resident macrophages, CD11c+ macrophages may rely on granulocyte-macrophage colony-stimulating factor (GMCSF), in keeping with published studies (Subramanian et al., 2015, Zhu et al., 2009) (Figure 2.8). I presented two distinct morphologies of CD11c+ macrophages, consisting of both foamy and round macrophages (Figure 2.9). A very recent paper also showed that aortic CD11c+ macrophages can be further separated into foam cells and inflammatory macrophages, which supports the heterogeneity of this subset (Kim et al., 2018).

Finally, my work showed for the first time that the number of resident vascular macrophages significantly declines during atherogenesis while recruited macrophage subsets establish themselves in the growing intimal lesion (Figure 2.3). These data suggest that the balance between lesional and resident macrophages can determine the severity of atherosclerosis. However, the mechanisms regulating these myeloid cell dynamics in atherosclerosis are yet to be discovered.

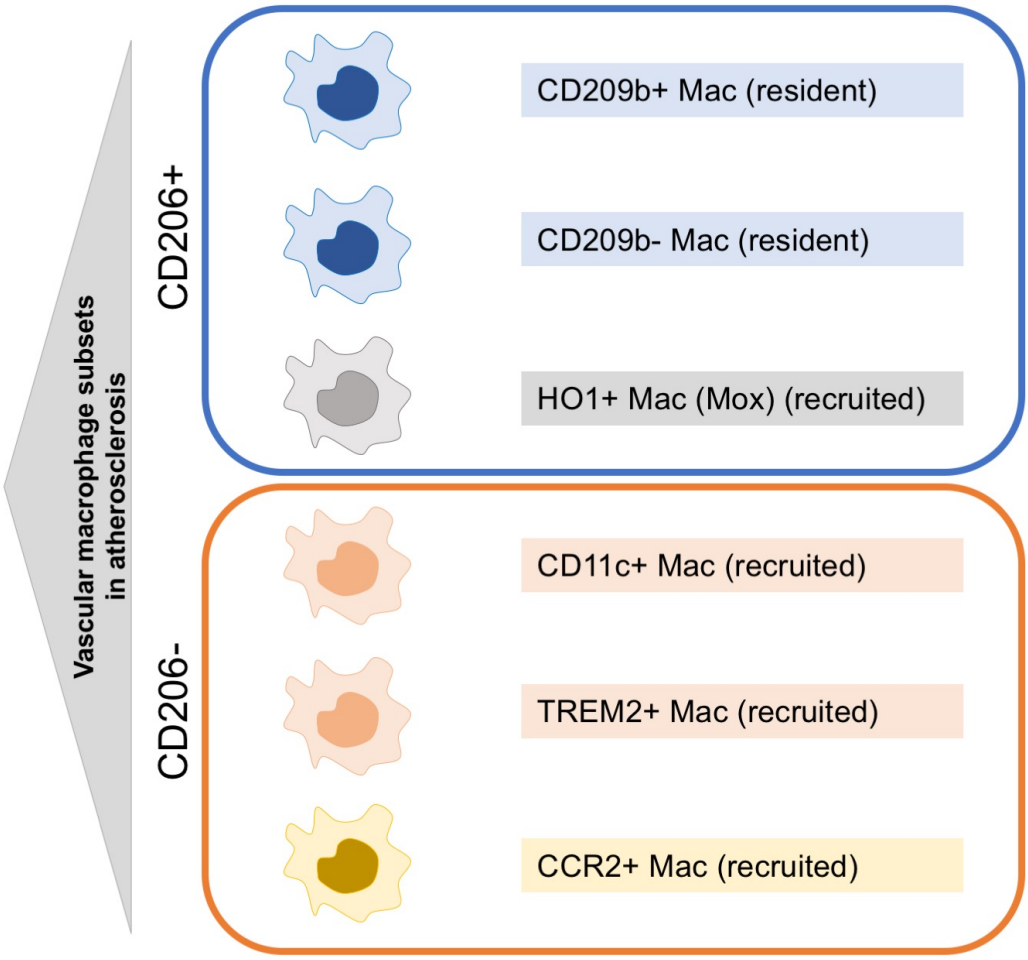


Figure 6.1 Macrophage subsets in the atherosclerotic aorta.

Schematic of macrophage subsets including three resident (CD206+) and three recruited (CD206-) subpopulations in the atherosclerotic aorta.

6.2. DCIR1 expression levels define tissue resident macrophages

DCIR is a C-type lectin receptor that bears an immunoreceptor tyrosine-based inhibition motif (ITIM) in the cytoplasmic domain (Bates et al., 1999). In humans, there is only one isoform of DCIR whereas in mice, 4 isoforms exist. Murine DCIR1 most resembles the expression pattern of human DCIR compared to the 3 other isoforms. The function of DCIR1 has mostly been studied in DCs, however, its role in macrophage biology is largely unknown. Moreover, the study of its biology has been hampered by high levels of cross reactivity between commercial DCIR1 antibodies and other isoforms.

I initially determined human *Dcir* and murine *Dcir1* expression *in vitro,* and demonstrated that both *Dcir* and *Dcir1* were inhibited by inflammatory signals (lipopolysaccharide (LPS), Interferon (IFN) γ and both) in macrophages (Figure 3.1; Figure 3.3). Human *Dcir* was increased by T helper (Th) 2-derived cytokines interleukin (IL)-4 and IL-13 whereas murine *Dcir1* remained unchanged by Th2 cytokines. This indicates that human DCIR and murine DCIR1 are present in macrophages and may behave differently in response to different infections.

I mapped DCIR1 expression in all myeloid cell types using mass cytometry and quantitative PCR, and demonstrated that resident macrophages expressed high levels of DCIR1 at the gene and protein levels relative to other myeloid cells (Figure 3.6, Figure 3.7, Figure 3.8 and Figure 4.4). In support of the expression studies, I was able to achieve the selective ablation of tissue resident macrophages by using *LysM*^{Cre} *Dcir1*-DTR^{flox} mice, including MHCII+ aortic and cardiac macrophages as well as

alveolar, BM, splenic and peritoneal macrophages (Figure 4.10). This finding is in keeping with the observation that tissue environmental cues lead to the upregulation of *Dcir1* (Figure 3.9), and that DCIR1 maintains the levels of CD206 expression in MCSF-derived macrophages (Figure 3.4). Moreover, *Dcir1*$^{-/-}$ mice displayed lower numbers of alveolar macrophages in the steady state (Table 8.3). My data indicated that DCIR1 might be used to identify resident macrophage populations and as such it could represent a pan-resident macrophage marker. In addition, the tissue environmental cues may induce *Dcir1* gene expression in macrophages (Figure 3.9). Finally, the *LysM*^{Cre} *Dcir1*-DTR^{flox} mouse model that I characterised could be a useful tool to study the function of resident macrophage populations.

Depletion of tissue resident macrophages in *LysM*^{Cre} *Dcir1*-DTR^{flox} mice was associated with an increase in the recruitment of monocytes in the affected tissues. The data support the concept that ablation of resident macrophages opens the niche to BM-derived monocytes for repopulation (Guilliams and Scott, 2017) (Figure 4.11). Although macrophage ablation was not attained in the colonic and liver macrophages, the number of macrophages and monocytes was increased by DT treatment, potentially indicating that rapidly repopulated macrophages from monocytes may mask the depletion (Figure 4.11). Additional time points before and after 7 days should be investigated to identify the timing of depletion and replenishment at these sites. Several studies demonstrated that monocytes can fully replicate the transcriptomic profiles and functions of tissue macrophages relative to embryonic precursors (Scott et al., 2016, van de Laar et al., 2016). In order to follow the repopulation and differentiation of macrophages in these organs, I performed bone marrow chimera studies, demonstrating that repopulated macrophages gradually re-acquire key tissue-

specific markers including DCIR1 as they adapt to their niche (Figure 4.16, Figure 4.17).

Repeated ablation of macrophages was lethal in atherosclerotic mice, potentially due to alveolar proteinosis, a known consequence of depleting alveolar macrophages (Trapnell et al., 2003). Although alveolar macrophages in this strain were rescued by introducing DT-resistant monocytes, long term treatment with DT was still detrimental to these mice. Thus, to determine the role of DCIR1 in the homeostasis of the myeloid niche, I decided to examine *Dcir1*-deficient atherosclerotic mice.

6.3. DCIR1 protects against atherosclerosis by maintaining the resident macrophage niche in the aorta

DCIR1 is an immune regulatory molecule that plays both protective and detrimental roles in autoimmune disorders and infectious diseases, respectively (Fujikado et al., 2008, Maglinao et al., 2013, Seno et al., 2015, Ishiguro et al., 2017, Troegeler et al., 2017). To date, the role of DCIR1 in atherosclerosis has not been elucidated. To determine whether global deletion of *Dcir1* affects the pathogenesis of atherosclerosis, I generated *Dcir1*-deficient *ApoE*$^{-/-}$ mice and conducted a comparative study with *ApoE*$^{-/-}$ mice. Indeed, DCIR1 protects against atherosclerosis, whereby *ApoE*$^{-/-}$ *Dcir1*$^{-/-}$ mice exhibited enlargement in arterial size and large necrotic core formation in the lesion ((Figure 5.3 to Figure 5.6). Accordingly, there was a decline in CD206+ resident macrophages in the aorta of *ApoE*$^{-/-}$ *Dcir1*$^{-/-}$ mice (Figure 5.11, Figure 5.12), which supports the finding that DCIR1 maintains CD206 expression in BMDM (Figure 3.4).

Conversely, *ApoE*$^{-/-}$ *Dcir1*$^{-/-}$ mice show increased monocyte influx and a concomitant increase in recruited macrophages in the aorta (Table 5.5, Figure 5.11, Figure 5.12).

The scRNAseq analysis of aortic CD11b+ cells from *ApoE*$^{-/-}$ and *ApoE*$^{-/-}$ *Dcir1*$^{-/-}$ mice identified additional macrophage subsets to that found in Chapter 2; these include 3 subsets of resident macrophages and 3 subsets of lesional macrophages (Figure 5.13). The resident population comprises 1) CD209b+, 2) CD209b- and 3) HO1+ macrophages and the recruited counterpart consists of 1) CD11c+ CD44+, 2) CCR2+ and 3) triggering receptor expressed on myeloid cells (Trem) 2+ subsets. This dataset confirms a reduction in CD209b+ and CD209b- resident macrophages in the aorta of *ApoE*$^{-/-}$ *Dcir1*$^{-/-}$ mice. In particular, HO1+ macrophages (Mox) (Kadl et al., 2010), TREM2+ macrophages (Cochain et al., 2018) and inflammatory monocytes were increased in the aorta of mice lacking DCIR1. Taken together, my data indicate that DCIR1 maintains the homeostasis of resident vascular macrophages in atherosclerosis. The absence of DCIR1 promotes recruitment of monocytes to the atherosclerotic aorta and enhances lesion growth and necrotic core formation, thus mimicking human high risk atherosclerotic lesions.

6.4. Future perspectives

My study identified DCIR1 as a marker and regulator of tissue resident macrophages in mice. DCIR1 was shown to regulate CD206 expression in MCSF-derived macrophage cultures (Figure 3.4) and limit TLR9 signalling (Table 3.5). To understand whether and how DCIR1 regulates broader macrophage programming, the BM of CD45.1 WT and *Dcir1*$^{-/-}$ CD45.2 mice could be cultured together with MCSF and

scRNAseq could be performed. Furthermore, a competitive BM chimera study using CD45.1 as host with mixed BM from CD45.1.2 WT and *Dcir1*$^{-/-}$ CD45.2 could provide evidence whether *Dcir1*-competent macrophages dominantly take over the niche relative to *Dcir1* knock-out macrophages. In addition, further extrapolation of the single cell genomics data generated in my study will shed light on functional studies of macrophages, enabling identification of novel markers for targeting each macrophage subset.

To date, the ligand for murine DCIR1 remains unknown, limiting the range of signalling analyses that can be performed. The identification of DCIR1 ligands could be achieved by generating a recombinant fusion protein that consists of the carbohydrate-binding domain of the *Dcir1* gene and human Fc protein. This DCIR1-fusion protein could capture the potential ligands in the supernatant from these tissues and the candidates could be identified by mass spectrometry. This fusion protein could also be utilised to locate potential ligands in the tissue section. The identification of specific ligands would enable further investigation into the downstream signalling pathway of DCIR1 in macrophage biology, and offer the means to target and activate resident macrophages.

6.5. Concluding remarks

This thesis provides an in-depth characterisation of vascular macrophage subpopulations in the healthy and atherosclerotic aorta. DCIR1 defines resident vascular macrophages and is employed by the majority of tissue resident macrophages as a survival mechanism. Tissue macrophages acquire DCIR1

expression via communication with the local microenvironment. In contrast, inflammatory signals inhibit DCIR1 expression in macrophages, enabling macrophage activation and increasing the threshold of TLR-dependent responses. In atherosclerosis, DCIR1 plays a protective role through sustaining survival of vascular macrophages and limiting monocyte infiltration. This study highlights that DCIR1 regulates the balance between resident and recruited macrophage subsets in the atherosclerotic aorta (**Figure 6.2**).

In conclusion, DCIR1 is a potent regulator of myeloid homeostasis by maintaining tissue resident macrophage pools in various organs. In atherosclerosis, its loss unfavourably alters myeloid cell dynamics enhancing the recruitment of monocytes and pathogenic macrophage subsets and worsening disease evolution. DCIR, as a modulator for macrophage phenotype, could enable development of tools for resident macrophage targeting and activation in diseases.

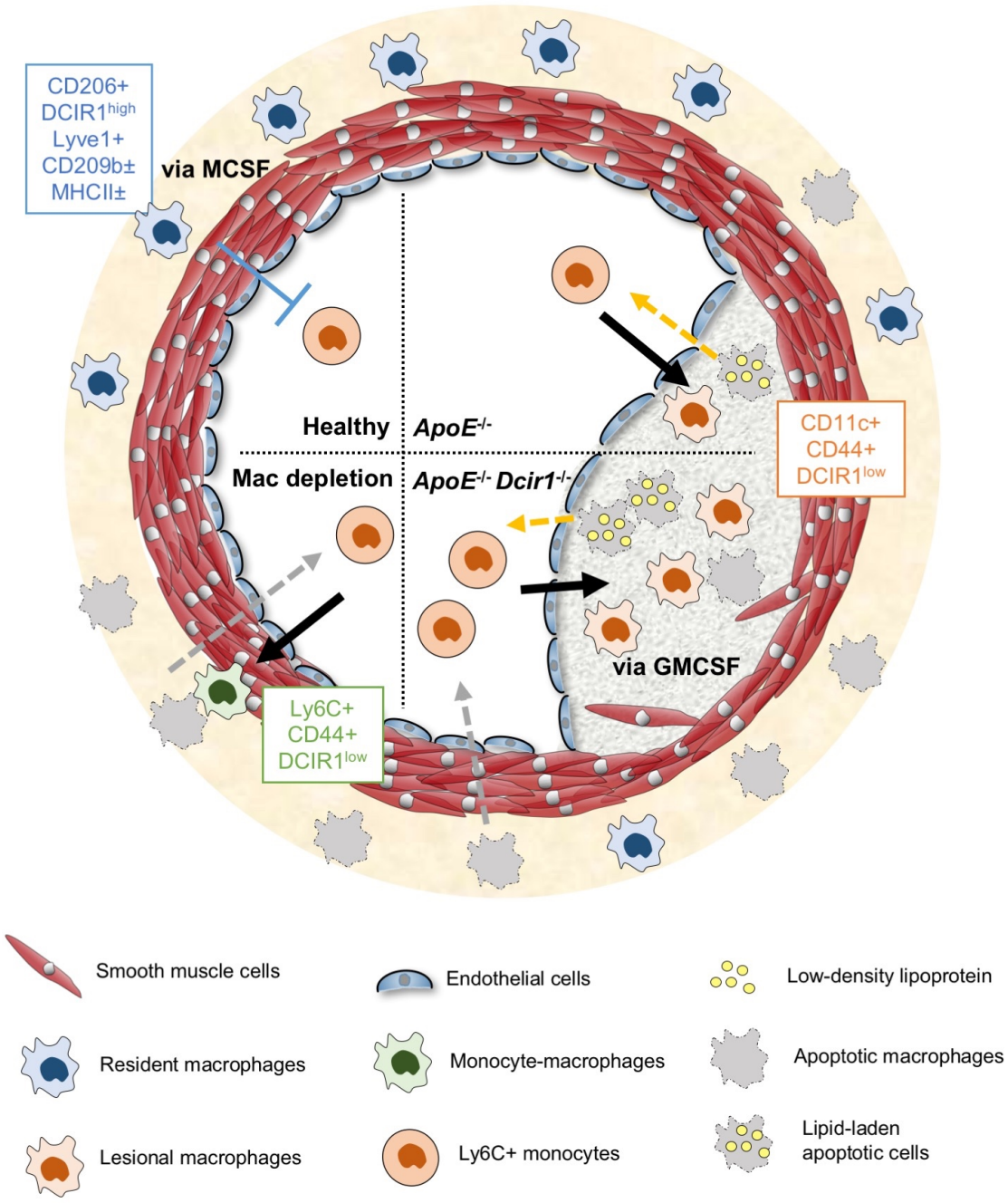


Figure 6.2 The proposed role of DCIR1 in vascular macrophages and atherosclerosis.

Resident vascular macrophages predominantly reside in the adventitia (the outermost layer) in the steady state and express high levels of DCIR1. The DCIR1-mediated cell ablation in vascular macrophages promotes the recruitment of Ly6C+ monocytes to replenish the macrophage niche. During atherosclerosis, monocytes are recruted in the intimal and differentiate into lesional macrophages which perform immune responses and lipid uptake. *Dcir1* deficiency results in a reduction in vascular macrophages and an increase in Ly6C+ monocytes and lesional macrophages, consequently responsible for the exacerbation of atherosclerosis.

CHAPTER 7. Materials and Methods

7.1. List of antibodies

Antibodies used for all experiments are listed in **Table 7.1**. Reagents that were made in-house are also listed in **Table 7.2**. The detail of commercially available reagents is indicated in each method sections.

Table 7.1 Antibodies used in experiments.

IF stands for immunofluorescence, CyTOF for cytometry by time-of-flight, FC for flow cytometry, IHC for immunohistochemistry, WB for Western blot.

Targets	Synonyms	Species	Clone	Company	Used for
ACTA	α-smooth muscle	Mouse	1A4	Sigma	IF/CyTOF
Annexin V	Annexin A5	Mouse	Polyclonal	eBiosciences	FC
B220	CD45R	Mouse	RA3-6B2	Fluidigm	CyTOF
B220	CD45R	Mouse	RA3-6B2	Biolegend	FC
CCR2	CD192	Mouse	SA203G11	Biolegend	FC
CD103	ITGAE	Mouse	2 E7	Biolegend	FC
CD115	CSF1R	Mouse	ASF98	Fluidigm	CyTOF
CD115	CSF1R	Mouse	ASF98	Biolegend	FC
CD11b	ITGAM/Mac1	Mouse	M1/70	Fluidigm	CyTOF
CD11b	ITGAM/Mac1	Mouse	M1/70	Biolegend	FC
CD11c	ITGAX	Mouse	N418	Fluidigm	CyTOF
CD11c	ITGAX	Mouse	N418	Biolegend	FC
CD11c	ITGAX	Mouse	N418	BioRad	FC/IHC
CD14		Mouse	M14-23	Biolegend	FC
CD14		Human	63D3	Biolegend	FC
CD15	SSEA1	Human	HI98	Biolegend	FC
CD150	SLAMF1	Mouse	TC15-12-F12.2	Biolegend	FC
CD16	FcγRIII	Human	3G8	Biolegend	FC
CD16/32	FcγRIII/II	Mouse	2.4G2	BD Biosciences	FC
CD163	Group B SR	Human	GHI/61	Biolegend	FC
CD169	Siglec1	Mouse	3D6.112	Biolegend	FC/CyTOF
CD172a	SIRPα	Mouse	SIRPa	Biolegend	CyTOF
CD19	B4	Mouse	6D5	Fluidigm	CyTOF
CD19	B4	Mouse	6D5	Biolegend	FC
CD206	MMR/MRC1	Mouse	C068C2	Biolegend	FC/CyTOF
CD206	MMR/MRC1	Mouse	MR5D3	BioRad	IF/IHC
CD209b	SIGNR1	Mouse	22D1	eBiosciences	FC/CyTOF
CD24	HSA	Mouse	M1/69	Fluidigm	CyTOF
CD26	DPP4	Mouse	DPP-4	Biolegend	CyTOF
CD3	T3	Mouse	17A2	Biolegend	FC
CD3	T3	Human	SP34-2	BD Biosciences	FC
CD31	PECAM1	Mouse	390	Biolegend	CyTOF
CD34	gp105-120	Mouse	RAM34	eBiosciences	FC
CD4		Mouse	RM4-5	Fluidigm	CyTOF
CD4		Mouse	RM4-5	Biolegend	FC
CD40	Bp50/TNFSF5	Mouse	1C10	Biolegend	FC
CD40	Bp50/TNFSF5	Human	5C3	Biolegend	FC
CD43	Ly48	Mouse	S11	Biolegend	FC/CyTOF
CD44	HCAM	Mouse	IM7	Fluidigm	CyTOF
CD44	HCAM	Mouse	IM7	Biolegend	FC
CD45	PTPRC	Mouse	30-F11	Fluidigm	CyTOF
CD45	PTPRC	Mouse	30-F11	Biolegend	FC
CD45.1		Mouse	A20	Fluidigm	CyTOF
CD45.1		Mouse	A20	Biolegend	FC
CD45.2		Mouse	104	Fluidigm	CyTOF
CD45.2		Mouse	104	Biolegend	FC
CD62L	L-selectin	Mouse	MEL-14	Biolegend	FC
CD64	FcγRI	Mouse	X54-5/7.1	Fluidigm	CyTOF
CD64	FcγRI	Mouse	X54-5/7.1	Biolegend	FC

Targets	Synonyms	Species	Clone	Company	Used for
CD64	FcγRI	Mouse	X54-5/7.1	Biolegend	FC
CD64	FcγRI	Mouse	AT152-9	BioRad	IF/IHC
CD68	Macrosialin	Mouse	FA-11	Biolegend	FC/CyTOF
CD68	Macrosialin	Mouse	FA-11	BioRad	IHC
CD8a	Lyt2/Ly2	Mouse	53-6.7	Fluidigm	CyTOF
CD8a	Lyt2/Ly2	Mouse	53-6.7	Biolegend	FC
CD90.2	Thy1.2	Mouse	30-H12	Biolegend	CyTOF
CX3CR1	Fractalkine receptor	Mouse	SA011F11	Biolegend	FC/CyTOF
DCAR	CLEC4B	Mouse	349214	R&D systems	FC
DCIR	CLEC4A	Human	9E8 -	Biolegend	FC
DCIR	CLEC4A	Human	9E8 -	eBiosciences	FC
DCIR1	CLEC4A2	Mouse	320507	R&D systems	FC
DCIR1	CLEC4A2	Mouse	TKKT	Prof. Matsumoto (Univ. of Tokyo)	FC/CyTOF/ WB
F4/80	EMR1/Ly71	Mouse	BM8	Fluidigm	CyTOF
F4/80	EMR1/Ly71	Mouse	BM8	Biolegend	FC
FcεRIα		Mouse	MAR-1	Biolegend	FC
GFP		Mouse	5F12.4	Fluidigm	CyTOF
GFP		Mouse	5F12.4	eBiosciences	FC
GFP		Mouse	FM264G	Biolegend	FC
GFP		Mouse	Polyclonal	Abcam	IF
IL-7Ra	CD127	Mouse	A7R34	Biolegend	CyTOF
iNOS	NOS2	Mouse	CXNFT	Fluidigm	CyTOF
iNOS	NOS2	Mouse	CXNFT	eBiosciences	FC
Ly6C		Mouse	HK1.4	Fluidigm	CyTOF
Ly6C		Mouse	HK1.4	Biolegend	FC
Ly6G		Mouse	1A8	Biolegend	FC
Ly6G/C	Gr1	Mouse	RB6-8C5	Fluidigm	CyTOF
Lyve1	XLKD1	Mouse	223322	R&D systems	FC
Lyve1		Mouse	ALY7	eBiosciences	FC/CyTOF
MerTK	MER	Mouse	108928	R&D systems	FC/CyTOF
MHCII	I-A/I-E	Mouse	M5/114.15.2	Fluidigm	CyTOF
MHCII	I-A/I-E	Mouse	M5/114.15.2	Biolegend	FC
MHCII	I-A/I-E	Mouse	M5/114.15.2	BD Biosciences	FC
NK1.1	CD161	Mouse	PK136	Fluidigm	CyTOF
NK1.1	CD161	Mouse	PK136	Biolegend	FC
NKp46	CD335	Mouse	29A1.4	Fluidigm	CyTOF
NKp46	CD335	Mouse	29A1.4	Biolegend	FC
Sca-1	Ly6A/E	Mouse	D7	Biolegend	FC
SiglecF	CD170	Mouse	E50-2440	BD Biosciences	FC
SiglecH		Mouse	551	Biolegend	CyTOF
STAT5		Human/mouse	89/Stat5	BD Biosciences	FC
STAT5 (Phospho)		Human/mouse	47/Stat5(pY694)	BD Biosciences	FC
STAT6		Human/mouse	23/Stat6	BD Biosciences	FC
STAT6 (Phospho)		Human/mouse	18/P-Stat6	BD Biosciences	FC
Surfactant Protein A		Mouse	Polyclonal	Abcam	WB
Surfactant Protein D		Human/mouse	EP9191	Abcam	WB
TCR$\boldsymbol{\beta}$		Mouse	H57-597	Fluidigm	CyTOF
TCR$\boldsymbol{\gamma\delta}$		Mouse	GL3	Biolegend	CyTOF
Ter119	Ly76	Mouse	TER-119	Biolegend	FC
Tim4	TIMD4	Mouse	F31-5G3	Biolegend	FC/CyTOF
XCR1	GPR5	Mouse	ZET	Biolegend	CyTOF

Name	Regent type	Company	Used for
Biotinylated Goat Anti-Hamster IgG	Secondary antibody	AbD Serotec	IHC
Biotinylated Rabbit Anti-Rat IgG	Secondary antibody	AbD Serotec	IHC
Goat-Anti-Rat IgG-AF488	Secondary antibody	Invitrogen	IF
Goat-Anti-Hamster IgG-AF568	Secondary antibody	Invitrogen	IF
Streptavidin	Secondary antibody	BD Biosciences	FC
Horseradish peroxidase (HRP)-conjugated antibody	Secondary antibody	Invitrogen	WB
Rat Anti-mouse CD16/32	Mouse FC block	BD Biosciences	FC

Table 7.2 Buffers and solutions made in-house.

Solution	Composition
50X TAE	242g Tris-base, 57.1ml Glacial Acetic Acid, 18.6g, 100mM EDTA in 1L dH_20
FACS buffer	1% w/v FBS in PBS
Oil Red O	1% w/v Oil red O (Sigma-Aldrich) in 100% isopropanol 1% w/v dextrin (Sigma-Aldrich) in dH_20 3:2 (Oil red O:Dextrin solution)
Sudan IV	0.5% w/v Sudan Fat Red (Sigma-Aldrich) in equal parts 70% ethanol and 100% acetone
Brewer's thioglycollate solution	4% w/v Brewer's thioglycollate (Sigma-Aldrich) in dH_20 Autoclaved and matured for at least 1 month in the fridge
PBS-T	0.1% Tween20 (Sigma-Aldrich) in PBS
5% BSA in PBS-T	5% w/v BSA in PBS-T
3X Sample buffer	0.5M Tris-HCL, 20% SDS (Sigma-Aldrich), 30% Glycerol Phenol Red in dH_20 1.25mM DTT was freshly added each time.

7.2. Mice

7.2.1. Maintenance of Mice

All mouse strains were on a C57BL/6J background. A list of mouse strains is available in **Table 7.3**. New mouse strains generated in-house are described in **Figure 7.1, 7.2, 7.3** and **7.4**. Mice were housed under specific-pathogen free conditions and were studied according to UK Home Office regulations and institutional guidelines. UK Home office regulations conform to the guidelines from Directive 2010/63/EU of the European Parliament on the protection of animals used for scientific purposes.

Table 7.3 List of mouse strains used in experiments.

Mouse strain	Generated by / purchased from	Used for	
ApoE$^{-/-}$	Charles River Laboratories UK	Atherosclerosis research/Bone marrow culture	
ApoE$^{-/-}$ *Dcir1*$^{-/-}$	Bred in-house	Atherosclerosis research	See Figure 7.1
ApoE$^{-/-}$ *LysM*^{Cre}+ *Dcir1*-DTR^{flox}	Bred in-house	Atherosclerosis research	See Figure 7.3
C57BL/6J (wild type)	Charles River Laboratories UK	Bone marrow culture/ Arterial injury model	
CD45.1	Oxford Biological Science Building	Monocyte adoptive transfer/ Bone marrow chimera	
Dcir1$^{-/-}$	Prof. Iwakura, University of Tokyo	Bone marrow culture	See Figure 7.1
Dcir1-DTR^{flox}	Gen0way	Bone marrow culture/Arterial injury model/Macrophage depletion	See Figure 7.2
Ldlr$^{-/-}$ CD45.1	Bred in-house	Atherosclerosis research	See Figure 7.4
LysM^{Cre}+ *Dcir1*-DTR^{flox}	Bred in-house	Bone marrow culture/Arterial injury model/Macrophage depletion	See Figure 7.2

7.2.2. Generation of mouse strains

7.2.2.1. Generation of *Dcir1*$^{-/-}$ and *ApoE*$^{-/-}$ *Dcir1*$^{-/-}$ mouse strains

Cryopreserved embryos from *Dcir1*$^{-/-}$ mice were thawed and viable embryos were implanted into a pseudo-pregnant female. *Dcir1*$^{-/-}$ mice were then bred with *ApoE*$^{-/-}$ mice to generate the *ApoE*$^{-/-}$ *Dcir1*$^{-/-}$ mouse colony (**Figure 7.1**).

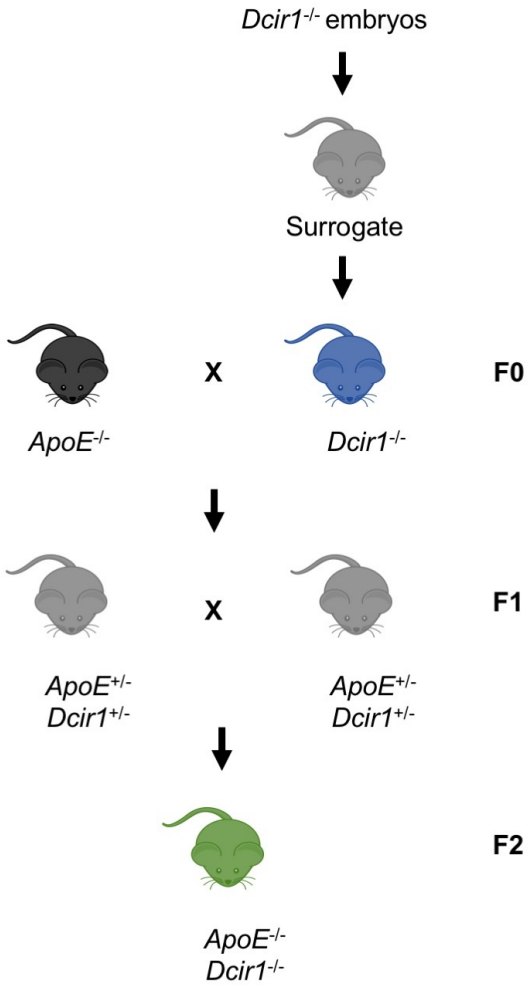


Figure 7.1 Breeding strategy to generate an *ApoE*$^{-/-}$ *Dcir1*$^{-/-}$ mouse colony.

F numbers represent the breeding generation.

7.2.2.2. Breeding plans for *Dcir1*-DTR^{flox} knock-in and *LysM*^{Cre}+ *Dcir1*-DTR^{flox} mice

A construct containing *loxP* sequences, neomycin, *DTR (Hbegf)* and *egfp* was inserted upstream of exon 8 of the *Dcir1* gene (**Figure 7.2**). Neomycin including a stop codon can be deleted by Cre-*loxP* recombination. This gene modification does not affect the function of DCIR1. *Dcir1*-DTR^{flox} heterozygous mice were generated by Gen0way (France) and were bred with each other to obtain homozygous animals in-house. *Dcir1*-DTR^{flox} homozygous mice were further crossed with *LysM*^{Cre}+ homozygous mice to establish the transcription of *DTR (Hbegf)* and *egfp*. *Dcir1*-DTR^{flox} mice expressing *LysM*^{Cre} (both heterozygous and homozygous) were tested in this study. For atherosclerosis research, *LysM*^{Cre}+ heterozygous *Dcir1*-DTR^{flox} homozygous mice were used to preserve LysM activity.

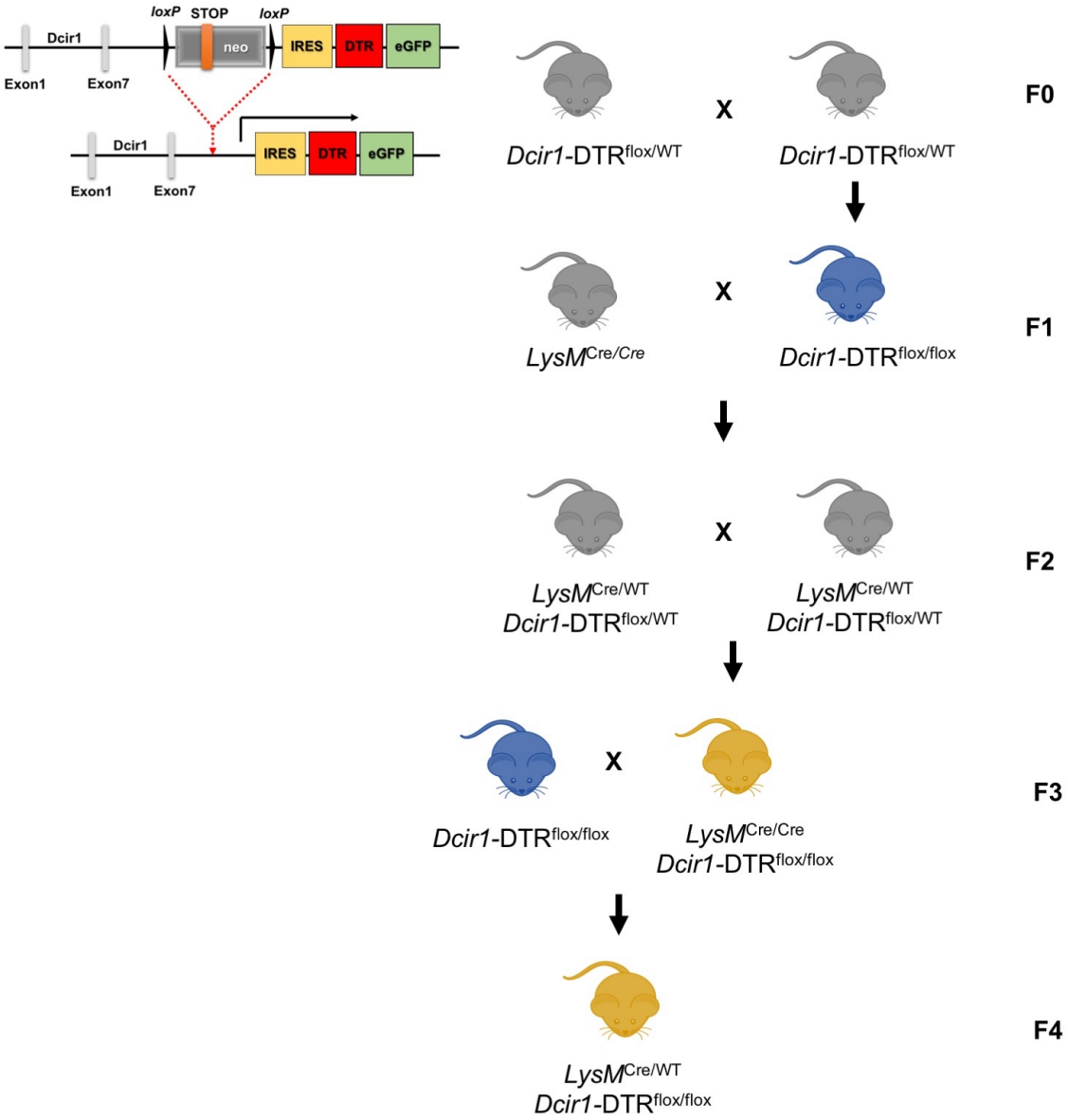


Figure 7.2 Generation of *Dcir1*-DTR^{flox} knock-in and *LysM*^{Cre} *Dcir1*-DTR^{flox} mice for *Dcir1*-mediated cell ablation.

F numbers represent the breeding generation.

7.2.2.3. Establishment of triple mutant *ApoE*$^{-/-}$ *LysM*^{Cre}+ *Dcir1*-DTR^{flox} mice

To establish a triple mutant mouse colony, *Dcir1*-DTR^{flox} mice were bred with *ApoE*$^{-/-}$ mice. Heterozygous animals were crossed with each other to obtain *ApoE*$^{-/-}$ *Dcir1*-DTR^{flox} mice. Separately, *ApoE*$^{+/-}$ *LysM*^{Cre}+ *Dcir1*-DTR^{flox} were generated by crossing *ApoE*$^{-/-}$ and *LysM*^{Cre}+ *Dcir1*-DTR^{flox} mice. *ApoE*$^{-/-}$ *Dcir1*-DTR^{flox} and *ApoE*$^{+/-}$ *LysM*^{Cre}+ heterozygous *Dcir1*-DTR^{flox} were then crossed to obtain *ApoE*$^{-/-}$ *LysM*^{Cre}+ heterozygous *Dcir1*-DTR^{flox}, which then were bred with each other to produce littermates. I then continued pairing *ApoE*$^{-/-}$ *LysM*^{Cre}+ heterozygous *Dcir1*-DTR^{flox} and *ApoE*$^{-/-}$ *Dcir1*-DTR^{flox} mice to produce littermates for experiments (**Figure 7.3**).

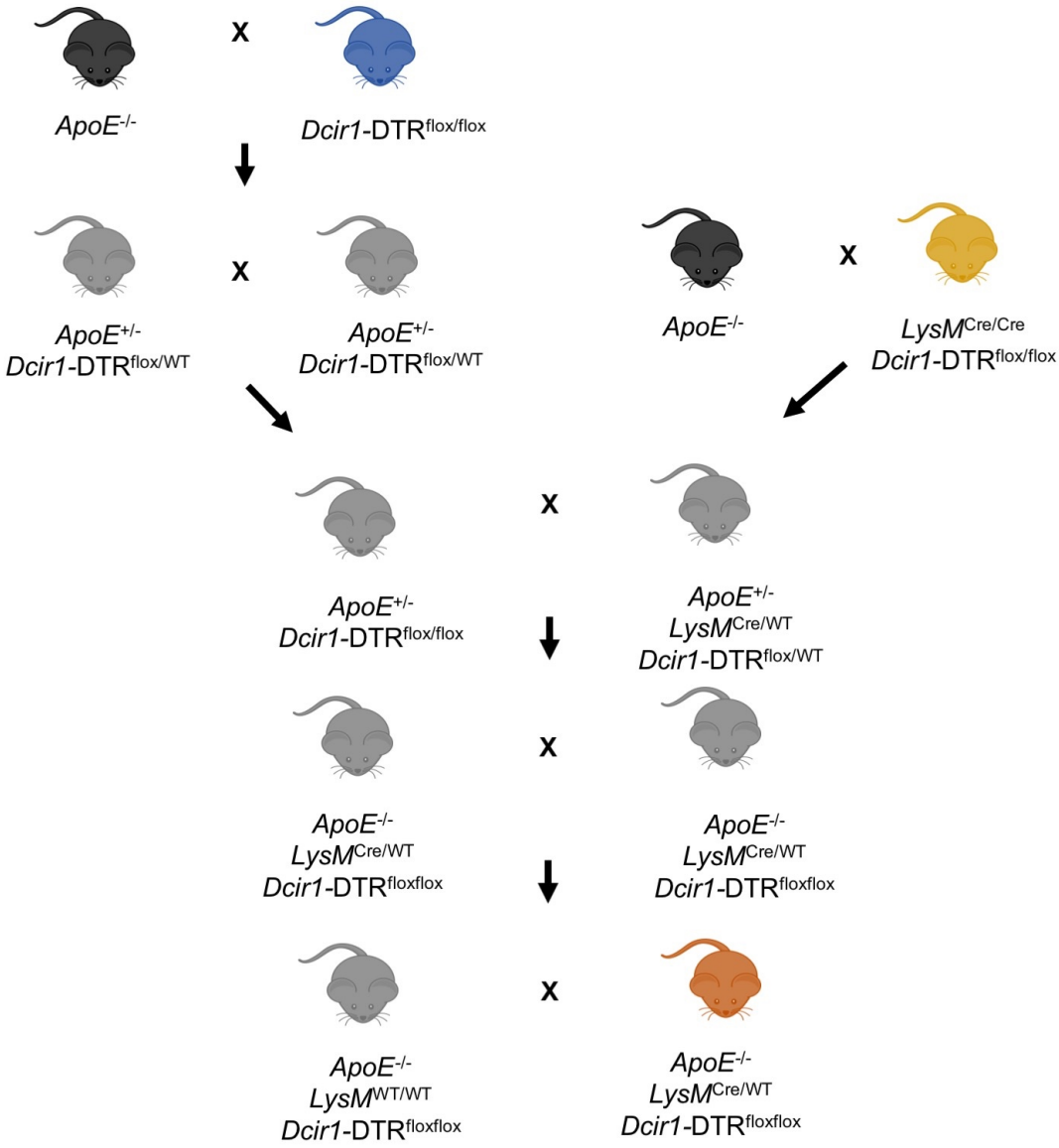


Figure 7.3 Breeding strategy to generate an *ApoE*$^{-/-}$ *LysM*^{Cre} *Dcir1*-DTR^{flox} littermate.

F numbers represent the breeding generation.

7.2.2.4. Breeding strategy of *Ldlr*$^{-/-}$ on a CD45.1 background

Ldlr$^{-/-}$ mice were purchased from Jackson Laboratories (USA) and were crossed with CD45.1 purchased from the Oxford Biological Science Building (University of Oxford). *Ldlr*$^{+/-}$ Heterozygous animals were then crossed with each other to obtain *Ldlr*$^{-/-}$ mice on CD45.1 mouse (**Figure 7.4**).

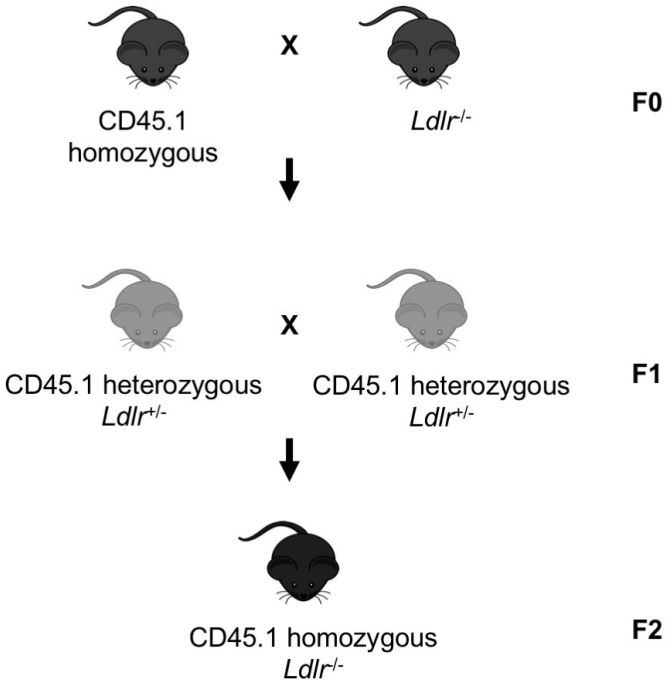


Figure 7.4 Breeding strategy to produce *Ldlr*$^{-/-}$ mice on a CD45.1 background.

F numbers represent the breeding generation.

7.2.3. Genotyping

7.2.3.1. DNA extraction

Genomic DNA was extracted from the ear biopsies using REDExtract-N-Amp™ Tissue PCR Kit (Sigma-Aldrich) according to manufacturer's instructions. In brief, the tissue was mixed with 25μl of Extraction solution and then with 5.25μl of Tissue Preparation solution. The tissue was vigorously mixed by vortexing and was then incubated for 10 minutes at room temperature. Samples were heated at 95°C for 3 minutes and 25μl of Neutralisation solution B was added immediately. Finally, samples were briefly mixed by vortexing and were stored at 4°C.

7.2.3.2. Polymerase Chain Reaction (PCR)

For the detection of genomic DNA (gDNA), PCR using Extract-N-Amp™ PCR ReadyMix™ (Sigma-Aldrich) was used according to the manufacturer's instructions. The Knock-in gDNA band of *Dcir1*-DTR^{flox} allele was amplified using the Expand™ Long Template PCR system (Sigma-Aldrich) according to the manufacturer's instructions. All gDNA bands were visualised in 1% agarose gel (ThermoFisher Scientific) with SYBR DNA gel stain (ThermoFisher Scientific) in TAE buffer. Primer sequences, the expected size of gDNA band and PCR reaction conditions are listed in **Table 7.4** and **7.5**. Representative images of genotyping results are depicted in **Figure 7.5 to 7.7**.

7.2.3.3. Blood preparation and flow cytometry

Mice on a CD45.1 background were bled from the tail vein using a 25G needle and the blood drops were collected in 100μl Alsever's solution (Sigma-Aldrich). Samples were then washed with PBS and red blood cells were lysed using Red Blood Cell lysis buffer (Sigma-Aldrich) for 5 minutes at room temperature. Cells were washed twice

with PBS and stained with CD45.1 and CD45.2 antibodies for 30 minutes at 4°C. The stained cells were washed twice and were fixed in 200μl 1X BD CellFix (BD Biosciences) for 10 minutes at 4°C.

Table 7.4 Sequences of primers used for genotyping.

Strain	Wild type	Common	Mutant
LysM^{Cre}	TTACAGTCGGCCAG GCTGAC	CTTGGGCTGCCAGA ATTTCTC	CCCAGAAATGCCAG ATTACG
Dcir1-DTR^{flow} WT	ATCACTGGGATCTTG GACACTCATGC	N/A	GGGGTGGGATTAGA T AAATGCCTGC
Dcir1-DTR^{flow} KI	GCAAAAAGTTCCATG TGTGTCCATAAGG	N/A	CCTCATTCTCAGGCT TGGTTCATCTTG
ApoE$^{-/-}$	GCCTAGCCGAGGGA GAGCCG	TGTGACTTGGGAGCT CTGCAGC	GCCGCCCCGACTGC ATCT
Dcir1$^{-/-}$	CAAAATTCTGTCAAG CGTAGAGGGG	AAGTGTCCCCTCTTG TACTCTGTG	CATTATACGAAGTTA TCTCGAGTCGC
Ldlr$^{-/-}$	GCGATGGATACACT CACTGC	CCATATGCATCCCCA GTCTT	AATCCATCTTGTTCA ATGGCCGATC

Table 7.5 Parameters for reverse transcription PCR of genotyping assays.

Strain		Cycles				
	Denaturing	Denaturing	Annealing	Extension	Cycles	Completion
LysM^{Cre}	95°C 300s	94°C 30s	62°C 60s	72°C 60s	X35	72°C 120s
Dcir1-DTR^{flow} WT	95°C 120s	94°C 30s	65°C 60s	68°C 300s	X35	68°C 480s
Dcir1-DTR^{flow} KI	95°C 120s	94°C 30s	65°C 60s	68°C 60s	X35	68°C 480s
ApoE$^{-/-}$	94°C 180s	94°C 30s	60°C 60s	72°C 45s	X30	72°C 600s
Dcir1$^{-/-}$	94°C 180s	94°C 30s	60°C 60s	72°C 45s	X30	72°C 600s
Ldlr$^{-/-}$	94°C 180s	94°C 30s	60°C 45s	72°C 45s	X35	72°C 120s

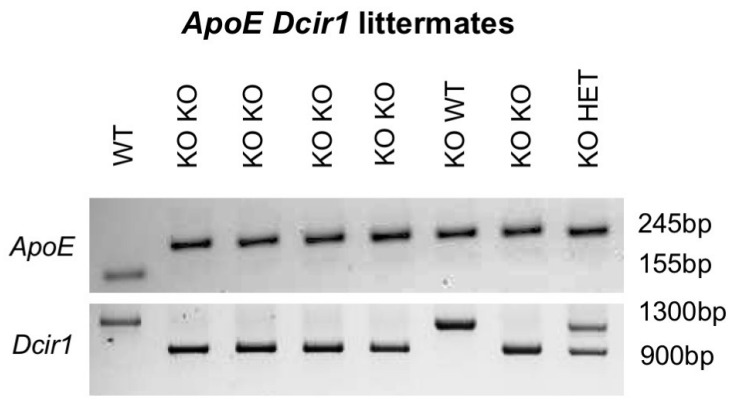


Figure 7.5 Genotyping of *ApoE*$^{-/-}$ *Dcir1*$^{+/-}$ littermate mice.

Gel electrophoresis showing PCR products of *ApoE and Dcir1* genes. *ApoE* WT band: 155bp, KO band: 245bp. *Dcir1* WT band: 1300bp and KO band: 900bp.

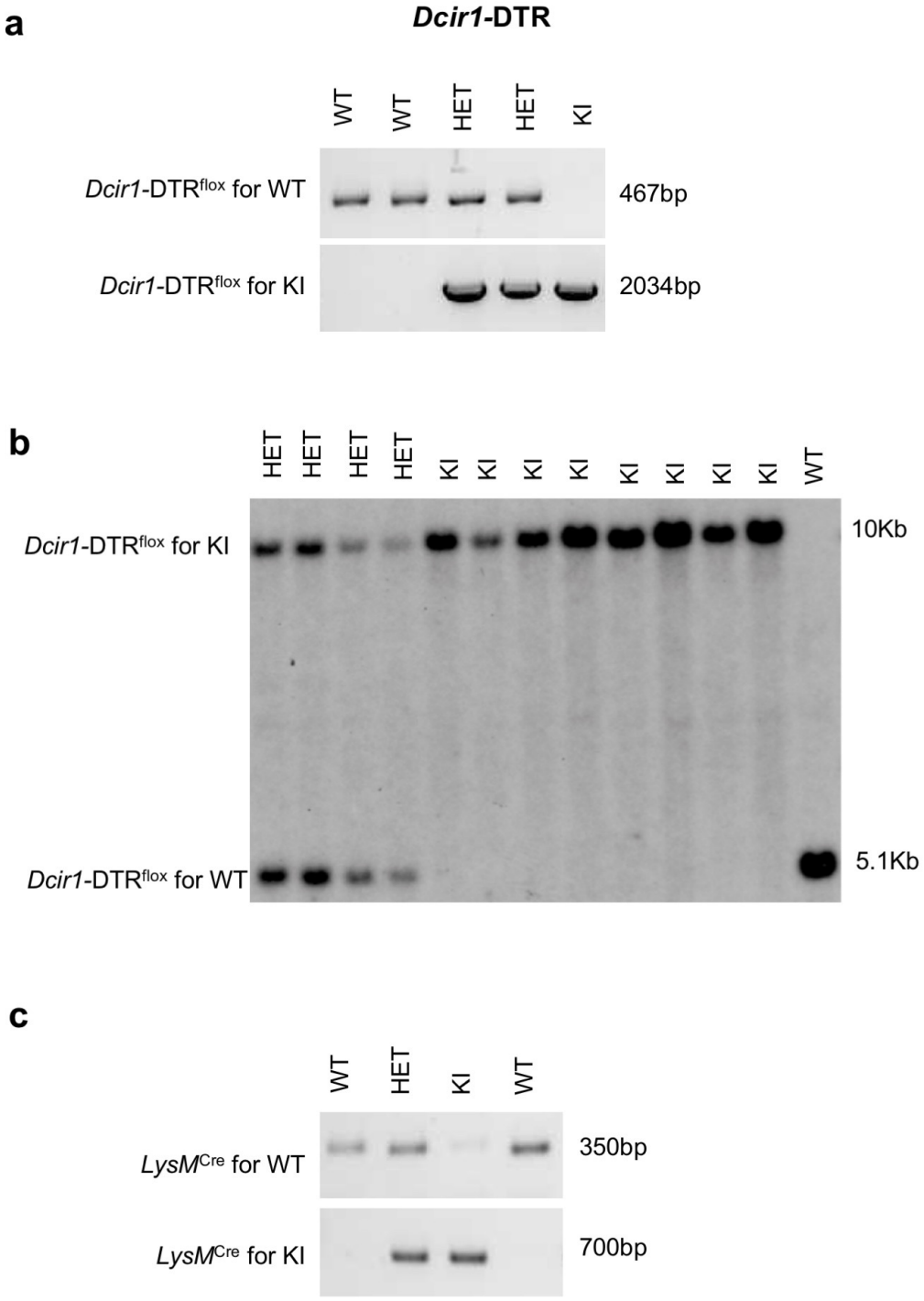


Figure 7.6 Genotyping of *Dcir1*-DTR^{flox} knock-in and *LysM*^{Cre}*Dcir1*-DTR^{flox} mice.

a) PCR for *Dcir1*-DTR^{flox} Knock-in. **b)** Southern blot for for *Dcir1*-DTR^{flox} Knock-in. **c)** PCR for *LysM*^{Cre} mice.

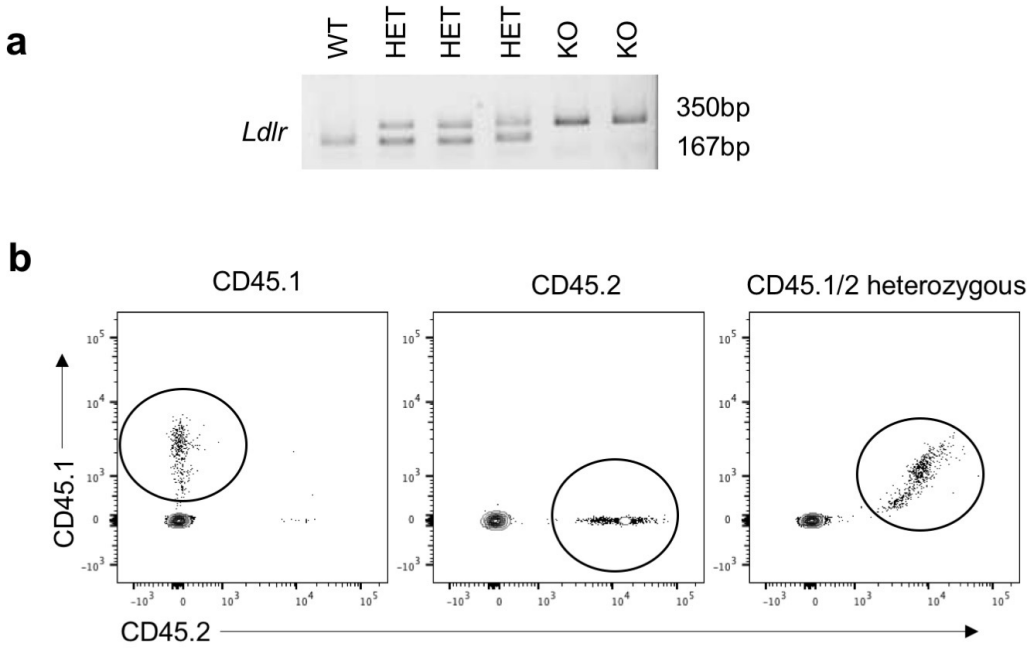


Figure 7.7 Genotyping of *Ldlr*$^{-/-}$ mice on a CD45.1 background.

a) Gel electrophoresis showing PCR products of the *Ldlr* gene. WT band: 167bp, KO band: 350bp. **b)** Detection of CD45 isoforms (CD45.1 and CD45.2) by flow cytometry.

7.2.4. *In vivo* Experimental procedures

Mice were euthanised in most experiments by intraperitoneal injection of barbiturate overdose (Merial). Some mice for bone marrow (BM) culture, BM donors, peritonitis models and single cell RNA sequencing (scRNAseq) were sacrificed by residual CO_2 inhalation for 5 minutes. Blood was collected by cardiac puncture and mice were perfused with saline to remove excessive blood.

7.2.4.1. Diphtheria toxin-mediated cell ablation

Diphtheria toxin (DT, Sigma-Aldrich) was reconstituted in sterile saline at 1mg/ml. C57BL/6, *Dcir1*-DTR^{flox}, *LysM*^{Cre}+ *Dcir1*-DTR^{flox}. *ApoE*$^{-/-}$ *LysM*^{Cre}+ *Dcir1*-DTR^{flox} and *ApoE*$^{-/-}$ chimera mice received diphtheria toxin (DT) or saline intraperitoneally. Some mice received DT or saline intravenously. DT concentrations, route of administration and length of treatment are specified in each experiment.

7.2.4.2. Thioglycollate-induced peritonitis

0.5ml of 4% brewer's thioglycollate (TG) solution (Sigma-Aldrich) was injected intraperitoneally. For neutrophil assays, peritoneal cells were harvested 4 hours after the injection. 5ml of saline was injected intraperitoneally into the mice and the small part was cut in the abdomen for collecting cells in the peritoneum. Macrophages were collected in the same manner 4 days after the injection of TG.

7.2.4.3. Arterial injury using perivascular tygon collar

Under brief anaesthesia with isoflurane, 15-week old C57BL/6, *Dcir1*-DTR^{flox} and *LysM*^{Cre}+ *Dcir1*-DTR^{flox} mice were ligated with a non-occlusive tube of tygon (length: 2.5 mm; internal diameter: 510 μm; Cole-Parmer) around the left carotid artery (**Figure 7.8**). The mice were allowed to recover from surgery for 3-4 days and were subjected to intraperitoneal injection of DT three times weekly for three weeks. Mice were

euthanised and the collar was carefully removed. The arteries were then snap-frozen in optimal cutting temperature (OCT) embedding medium (Tissue-Tek, Sakura) and were stored at -80°C. Deep cervical lymph nodes, fibrotic tissues around the injured carotid artery and aortas were collected and were analysed using flow cytometry.

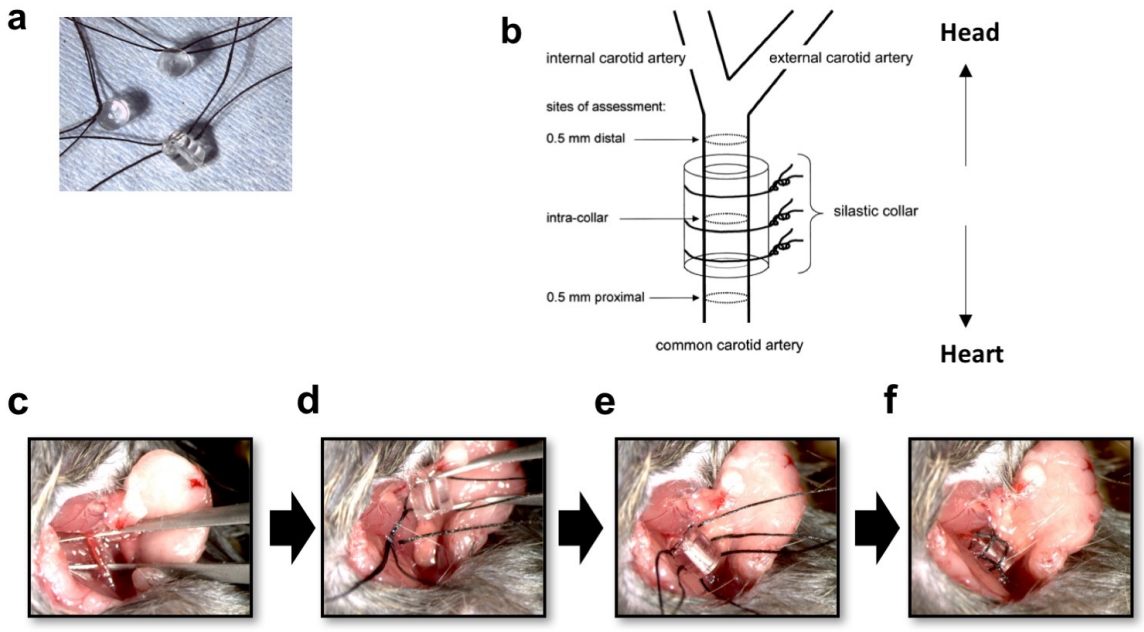


Figure 7.8 Surgical placement of a Tygon collar on a mouse carotid artery.

a) Perivascular collars (2.5mm Tygon tubing; internal bore diameter: 510µm). **b)** Murine Common left carotid artery. **c)** A sagittal anterior neck incision was made to expose common left carotid artery. **d)** the ligatures were passed through under the artery. **e)** The collar was placed around the vessel. **f)** The collar was tied with ligatures.

7.2.4.4. Generation of bone marrow chimera mice

Recipient mice were sub-lethally irradiated twice with a 4-hour interval using an X-ray irradiator (Gulmay; 1.8Gy/min, 210KV, 13mA for 3min, table height: 400mm). The irradiated mice received 3-5X10^6 bone marrow cells by tail vein injection 1 hour after the last irradiation. 1% antibiotic (Baytril, Bayer) in autoclaved drinking water was given for 2 weeks.

7.2.4.5. Intranasal adoptive transfer of monocytes

Recipient mice were anaesthetised with isoflurane and received 0.1X10^6 monocytes in a volume of 50μl by intranasal inhalation.

7.2.4.6. Feeding high fat diet

ApoE$^{-/-}$, *Ldlr*$^{-/-}$ CD45.1 or *ApoE*$^{-/-}$ *LysM*^{Cre}+ *Dcir1*-DTR^{flox} mice were fed on a high fat diet (HFD) at 12-week old for 12 weeks (Chapter 2) or at 8-week old for 12 weeks or 18weeks (Chapter 4 and Chapter 5). HFD was purchased from Special Diets Services (UK) consisting of (w/w) cocoa butter (15%), cholesterol (0.25%), maize starch (10%), casein (20%), sucrose (40.5%), cellulose (5.95%), corn oil (1%), 50% choline chloride (2%), methionine (0.2%) and mineral mixture (5.1%).

7.2.5. Single cell dissociation from murine tissues

Tissue processing was performed with 5% FBS in RPMI unless stated.

7.2.5.1. The bone marrow

Femurs and tibias were disinfected in 70% ethanol for 1min. The bone ends were removed and the bone marrow was flushed out using a blunt 26G cannula (Biochrome) and a 10ml syringe filled with medium. Erythrocytes were lysed using Red Cell Lysis Buffer (Sigma-Aldrich) at room temperature for 2 minutes. The cells were then washed

with medium, were resuspended with medium and were filtered through a 70μm cell strainer (Greiner Bio-One). The red cell lysis step was omitted for the BM for transplantation into irradiated mice.

Neutrophil isolation from the BM was performed using a Neutrophil isolation kit (Miltenyi Biotech) according to the manufacturer's instructions. Monocytes were isolated from the bone marrow using a murine monocyte isolation kit (Miltenyi Biotech).

7.2.5.2. Blood

To collect leucocytes, 700μl of whole blood was added to 700μl Alsever's solution (Sigma-Aldrich) and erythrocytes were lysed by 2 minute-incubation with 1ml Red Cell Lysis Buffer (Sigma-Aldrich) at room temperature.

7.2.5.3. Spleen and lymph nodes

Spleen and lymph nodes were mechanically disrupted by pushing through a 70μm cell strainer. For spleen, erythrocytes were lysed using Red Cell Lysis Buffer (Sigma-Aldrich) at room temperature for 2 minutes.

7.2.5.4. Aorta

Aortas were cut into small pieces and were placed in the appropriate enzyme mixture (collagenase I, collagenase XI, hyaluronidase, DNase I) and were digested at 37°C for 45-50 minutes (**Table 7.6**). The cells were retrieved by passing aortic tissues through a 70μm cell strainer.

For separating aortic layers into the intima/media and the adventitia, the whole aorta was pre-incubated with collagenase II and elastase at 37°C for 10 minutes (**Table 7.6**). The adventitia layer was stripped off from the inner tube (the intima and media) by pulling with two pairs of fine forceps.

7.2.5.5. Lung and heart

Tissues were cut into small pieces and were placed in the appropriate enzyme mixture (collagenase IV, DNase I for the lung; collagenase II, DNase I for the heart) and were digested at 37°C for 40 minutes for the lung and 30 minutes for the heart (**Table 7.6**). The cells were retrieved by passing tissues through a 70μm cell strainer. Erythrocytes were lysed using Red Cell Lysis Buffer (Sigma-Aldrich) at room temperature for 2 minutes.

7.2.5.6. Liver

Liver tissues were cut into small pieces and were placed in the appropriate enzyme mixture (collagenase VIII, and DNase I) and were digested at 37°C for 40 minutes (**Table 7.6**). The cells were retrieved by passing tissues through a 70μm cell strainer. Hepatocytes were removed after two low speed spins at 54 Xg force for 2 minutes and the supernatant containing Kupffer cells and leucocytes was collected.

7.2.5.7. Colon

Dissected colons were cut open longitudinally and were then finely cut into small pieces in Hanks' Balanced Salt Solution (HBSS). Tissues were vigorously vortexed and were incubated at 37 °C for 30 minutes (**Table 7.6**). Epithelial cells in the supernatant were discarded from the tissues by using a 70μm cell strainer and the remaining tissues were digested again in the appropriate enzyme mixture (collagenase VIII, and DNase I) for a further 40 minutes. Single cells were retrieved by mechanical dissociation through a 70um cell strainer.

7.2.5.8. Brain

Brains were cut into small pieces and were placed in the appropriate enzyme mixture (collagenase D, and DNase I) and were digested at 37°C for 30 minutes (**Table 7.6**).

Leucocytes and microglia were enriched by separating them from myelin and cell debris by density gradient centrifugation using Percoll (Sigma-Aldrich) using three gradients (30%/37%/70%). The interface between 37% and 70% containing most of leucocytes in the bottom of the 15ml Falcon tube (Corning) was collected.

7.2.5.9. Fibrotic tissues

Perivascular tissues from the injured carotid artery were cut into pieces and were placed in the appropriate enzyme mixture (collagenase IV, and DNase I) and were digested at 37°C for 30 minutes (**Table 7.6**). The cells were retrieved by passing tissues through a 70μm cell strainer.

Table 7.6 Concentrations of enzymes for tissue dissociation.

All enzymes were purchased from Sigma-Aldrich and DNase I for the aorta digestion was from ThermoFisher Scientific.

Tissue	Enzyme	mg per 10ml	Incubation time (min)
Aorta	Collagenase Type I	36	45-50
	Collagenase Type XI	1	
	Hyaluronidase	1.5	
	DNase I	*3ul	
Intima/adventitia	Collagenase Type II	5.1	10
	Elastase	4.7	
Lungs	Collagenase Type IV	4	40
	DNase I	1.5	
Heart	Collagenase Type II	10	30
	DNase I	1.5	
Liver	Collagenase VIII	10	40
	DNase I	1.5	
Colon	Collagenase VIII	10	40
	DNase I	1.5	
Brain	Collagenase D	10	30
	DNase I	1.5	
Fibrotic tissues	Collagenase Type IV	5	30
	DNase I	1.5	

7.3. *In vitro* cell culture

7.3.1. Murine bone marrow cell culture

Bone marrow cells were cultured in RPMI-1640 (Gibco), 10% FBS, 10 units/ml penicillin (Gibco), 0.1mg/ml streptomycin (Gibco), 2.5µg/ml amphotericin B (Gibco) and 50µM 2-mercaptoethanol (Gibco), together with 20ng/ml GMCSF (Peprotech), 100ng/ml MCSF (Peprotech) or 20ng/ml GCSF (Peprotech). $5x10^6$ cells per 10cm dish were cultured with 10ml complete medium and the medium was refreshed every 2 to 3 days. For macrophage activation, adherent cells were scraped using a Cell Lifter Blade (Corning) after 4-6 days and were re-plated with the medium containing appropriate stimuli. Ligand concentrations used for macrophage priming are 100ng/ml LPS (Enzo Life Sciences), 100ng/ml IFNγ (Biolegend), 20ng/ml IL-4 (Peprotech), 20ng/ml IL-13 (Peprotech), 100ng/ml FSL-1 (Invivogen), 10ng/ml Poly I:C high molecular weight (Invivogen), 20ng/ml CpG ODN 2395 (Invivogen), 20ng/ml IL-10 (Peprotech).

7.3.2. Human monocyte-derived macrophage culture

Human monocytes were separated and purified by centrifugal elutriation. Briefly, human PBMC were obtained by density centrifugation through Ficoll of a single-donor platelet depleted residue (North London Blood Transfusion Service, Colindale, UK). PBMC were then centrifugally elutriated in 1% FBS in RPMI in a JE6 elutriator (Beckman). Monocytes separated by this method were assessed for purity by FACSCan (Becton Dickinson) and were greater than 80%. $1x10^7$ monocytes were cultured with 20ng/ml GMCSF (Peprotech) or 100ng/ml MCSF (Peprotech) in 10cm dishes in RPMI-1640 + 10% FBS for 4-5 days.

7.3.3. Ligand assay

Heart, lungs and aorta were dissected and were rinsed in PBS to remove the excessive blood. Finely cut tissues were placed in DMEM containing 1% FBS, 10 units/ml penicillin (Gibco), 0.1mg/ml streptomycin (Gibco), and were then transferred to an insert containing 0.5 μm-sized pores (Greiner Bio-One). This insert allows migration of small molecules such as cytokines and growth factors while blocking cell migration. The inserts were placed in the 6 well plate where RAW264.6 cells were seeded a day before and tissues and cells were co-cultured at 37 °C for 24 hours. The insert containing the tissues was removed and the cells were washed in PBS. Cells were stained and were analysed by flow cytometry or were lysed in 700μl RLT buffer (Qiagen) for gene expression assay.

7.4. Nucleic acid assays

7.4.1. Quantitative Real Time Polymerase Chain Reaction (qRT-PCR)

Total RNA was extracted from cell lysates in RLT buffer using an RNeasy Mini kit (Qiagen) according to the manufacturer's instructions. 50ng/ml of RNA was synthesised into cDNA using a High Capacity cDNA Reverse Transcription kit (Applied Biosystems). A pre-amplification step was performed according to the manufacturer's instructions using appropriate TaqMan assays (Applied Biosystems) and TaqMan Pre-Amp Master Mix (Applied Biosystems). The TaqMan assays are listed in **Table 7.7**. The pre-amplified cDNA, TaqMan Assays and TaqMan Gene Expression Master Mix (Applied Biosystems) were used for qPCR in a 384-well plate and the reaction was run by Viia7 Real Time PCR system (Applied Biosystems) according to the

manufacturer's instructions. The data were analysed using a comparative ΔΔ cycle threshold (CT) method (Livak and Schmittgen, 2001).

Table 7.7 List of TaqMan assays used for quantitative real time PCR in this study.

All probes were purchased from Applied Biosystems.

Gene	Assay ID
18S rRNA	Hs99999901_s1
Clec4a	Hs01087625_m1
Clec4a1	Mm01184185_m1
Clec4a2	Mm04210363_mH
Clec4a3	Mm00462705_m1
Clec4a4	Mm04203490_m1
Clec4b1	Mm01184151_g1
Clec4d	Mm00501738_m1
Clec4e	Mm01183703_m1
Clec7a	Mm01183349_m1
egfp	Mr04097229_mr
Hbegf	Hs00181813_m1
Il12b	Mm01288993_m1
Irf4	Mm00516431_m1
Irf5	Mm00494477_m1
Lyz2	Mm01612741_m1
Mrc1	Mm00485148_m1
Nos2	Mm00440502_m1
Pparg	Mm01184322_m1
Tgfb1	Mm01178820_m1
Tnf	Mm00443258_m1

7.4.2. Single cell RNA sequencing

7.4.2.1. Sample processing

Single cell suspensions of the aorta were sorted using FACSAriaIII (BD Biosciences) as follows. For chapter 2, live CD45+ CD11b+ F4/80+ $CD64^{low\ to\ high}$ cells of 20-week old HFD-fed *ApoE*$^{-/-}$ females were used. For chapter 5, live CD45+ CD11b+ cells were sorted from 20-week old HFD-fed *ApoE*$^{-/-}$ and *ApoE*$^{-/-}$ *Dcir1*$^{-/-}$ females. Sample processing of FACS-sorted cells was performed by Oxford Genomics Centre, Wellcome Centre for Human Genetics. Briefly, cells were washed in PBS with 0.04% BSA and were resuspended before capturing single cells in droplets on a Chromium 10x Genomics platform. Library generation for 10x Genomics v2 chemistry was performed following the Chromium Single Cell 3' Reagents Kits (User Guide: CG00052).

Quantification of cDNA was performed using a Qubit dsDNA HS Assay Kit (Life Technologies Q32851) and high-sensitivity DNA tapestation (Agilent. 5067-5584). Quantification of the library construction was performed using Qubit dsDNA HS Assay Kit (Life Technologies Q32851) and high-sensitivity DNA tapestation (Agilent. 5067-5584).

Libraries were sequenced on an Illumina HiSeq4000 platform to achieve an average of 50,000 or more reads per cell. The raw sequence data were generated in a FASTQ file format and the alignment data were generated in a BAM file format.

7.4.2.2. Data analysis

The sequencing data were analysed by Dr Ignat Drozdov (Bering Limited) as a collaboration. Raw gene counts across multiple biological samples were pooled using the CellRanger command line interface. Reads were subsampled from higher depth

libraries until they all had an equal number of confidently mapped reads per cell. Integrated raw gene matrix was passed to SCANPY (Wolf et al., 2018) for pre-processing and quality control. Quality control pipeline removed n=1,467,497 cells that have fewer than 200 expressed genes and n=14,872 genes that were detected in fewer than 3 cells. Cells with greater than 5% mitochondrial gene expression were also excluded from the analysis. The count matrix was log-normalised and scaled to unit variance, whilst mitochondrial and cell count effects were removed using a linear regression.

Structure-preserving dimensionality reduction was achieved using three algorithms including tSNE (Maaten and Hinton, 2008), LargeVis (Tang et al., 2016) and ivis, which was built by Dr Ignat Drozdov (Bering Limited; unpublished).

7.5. Protein assays

7.5.1. Flow cytometry

Cells were stained with LIVE/DEAD fixable aqua dye (ThermoFisher Scientific) for 10 minutes at room temperature and were then washed with 1% FBS in PBS. Non-specific binding of antibodies was blocked using anti-mouse CD16/32 (BD Biosciences) at 4°C for 10 minutes, followed by incubating with fluorochrome-conjugated antibodies recognising cell surface markers for 30 minutes at 4°C. Following by two wash steps, cells were fixed using either BD fix (BD Biosciences) for 10 minutes at 4°C or Foxp3/Transcription Factor Staining Buffer Set (eBiosciences) for intracellular staining. For intracellular staining, fixed cells were washed and were stained with fluorochrome-conjugated antibodies against intracellular markers. Cell acquisition was performed using an LSRII (BD Biosciences) or a Fortessa (BD Biosciences) flow cytometer.

7.5.2. Mass cytometry

Some metal-conjugated antibodies were purchased from Fluidigm. Some purified unlabelled antibodies were conjugated in-house using the Maxpar X8 Metal Labelling Kit (Fluidigm) according to the manufacturer's instructions. All antibodies were titrated to determine the optimal staining concentration. Single cells from murine tissues were first stained with a rhodium DNA intercalator (Fluidigm) to distinguish live or dead cells followed by barcoding using the palladium-based 20-Plex Pd Barcoding Kit (Fluidigm) according to the manufacturer's instructions. Barcoded cells were then combined into a single tube prior to addition of anti-mouse CD16/32 (BD Biosciences) and staining with metal-conjugated antibodies for 30min at 4°C (**Table 7.8**). The cells were then washed and were permeabilised using the Foxp3/Transcription Factor Staining Buffer Set (eBiosciences) for 40-60 minutes at 4°C prior to staining with antibodies against intracellular markers for 30 min at 4°C. Finally, the stained cells were incubated with an Iridium DNA intercalator (Fluidigm) in Maxpar fix and perm buffer (Fluidigm) for 18-24 hours at 4°C. Prior to acquisition, cells were washed twice with cell staining buffer (Fluidigm) followed by two washes with water (Fluidigm) and filtered through 40μm cell strainer before introducing into a Helios mass cytometer (Fluidigm).

7.5.3. Mass cytometry data processing and analysis

Data were in an fcs file format. All fcs files in the experiment were normalised and were then debarcoded using the normalisation and debarbarcoding tools within the Helios software. These fcs files were then uploaded to Cytobank (www.cytobank.org) for all gating and further analysis using the automated dimensionality reduction algorithm viSNE.

Table 7.8 List of antibodies used for mass cytometry.

	Chapter 2	Chapter 3	Chapter 4
Metal Label	**Antigen**		
141Pr	Ly-6G/C	Ly-6G/C	Ly-6G/C
142Nd	CD11c	CD11c	CD11c
143Nd	IL-17ra	Tim4	IL-17ra
144Nd	XCR1	XCR1	XCR1
145Nd	TCR$\gamma\delta$	TCR$\gamma\delta$	TCR$\gamma\delta$
146Nd	CX3CR1	CX3CR1	CX3CR1
147Sm	CD45	CD45	CD45
148Nd	CD11b	CD11b	CD11b
149Sm	CD19	CD19	CD19
150Nd	CD24	CD24	CD24
151Eu	CD64	CD64	CD64
152Sm	CD3e	CD3e	CD3e
153Eu	NKp46	NKp46	NKp46
154Sm	CD31	-	CD103
155Gd	ACTA 2	-	Lyve1
156Gd	CD169	CD169	CD43
158Gd	CD206	CD206	CD206
159Tb	F4/80	F4/80	F4/80
160Gd	CD26	DCIR1	DCIR1
161Dy	CD103	CD103	iNOS
162Dy	Ly6C	Ly6C	Ly6C
163Dy	CCR2	CCR2	CCR2
164Dy	CD172a	CD172a	CD172a
165Ho	NK1.1	Lyve1	NK1.1
166Er	CD209b	CD209b	CD209b
167Er	SIGLECF	SIGLECF	SIGLECF
168Er	CD8a	CD8a	CD8a
169Tm	TCRβ	TCRβ	TCRβ
170Er	CD90.2	MerTK	CD90.2
171Yb	CD44	CD44	CD44
172Yb	CD4	CD4	CD4
173Yb	SIGLECH	SIGLECH	SIGLECH
174Yb	MHCII	MHCII	MHCII
175Lu	CD68	CD68	CD68
176Yb	CD45R	CD45R	CD45R

7.5.4. Enzyme-linked immunosorbent assay (ELISA)

Murine IL-6 and IL-10 were measured in the supernatant from macrophage culture. 96-well EIA/RIA plates (Corning) were coated with 1μg/ml Capture antibody for murine IL-6 (BD Pharmingen) overnight at 4˚C. Non-specific binding was blocked with 2% BSA in PBS for 2 hours at room temperature. To generate a standard curve, serial dilutions of murine IL-6 standard (PeproTech) were used at 1:3 from 10,000 to 4.5pg/ml. Supernatant samples were also diluted as appropriate and added to the plate, together with the standards. The samples were incubated overnight at 4˚C and treated with 0.5μg/ml biotinylated antibody (BD Pharmingen) for 1 hour at room temperature, followed by streptavidin-horseradish peroxidase (R&D Systems) at a 1:400 dilution for 1 hour at room temperature. 3,3', 5,5'-Tetramethylbenzidine (TMB; Kirkegaard & Perry Laboratories) was added and incubated at room temperature for up to 20 minutes. The reaction was stopped by adding 1.1M sulphuric acid. The plate was read using a Multiskan Ascent multiplate reader at 450 nm.

7.5.5. Immunoblotting

Up to $2X10^6$ cells were lysed in 250-500 μl Pierce IP lysis buffer (ThermoFisher Scientific). Protein lysates were diluted in 1X Sample buffer and denatured by heating for 10 minutes at 95°C. The lysates were separated by molecular weight in 4-12% Mini-PROTEAN TGX precast gels (BioRad). Protein samples were transferred onto polyvinylidene difluoride (PVDF) membranes by Trans-Blot Turbo (BioRad). Membranes were transferred to 5 % BSA in PBS-Tween20 to block non-specific binding for 1 hour at room temperature. The membranes were treated with primary antibodies overnight at 4°C. The membranes were washed in PBS-Tween20 and were treated with HRP-conjugated secondary antibodies for 1 hour at room temperature.

Finally, protein bands were visualised using a chemilluminescence substrate (SuperSignal™ West Femto Maximum Sensitivity Substrate; Thermo Fisher Scientific) in a G:BOX Chemi gel doc (Syngene).

7.6. Serum cholesterol assay

The blood was taken by cardiac puncture and was centrifuged at 6000rpm for 30 minutes at 4°C in a Heraeus Primo R centrifuge (Thermo Scientific). The serum was collected in aliquots and were stored at -80°C. To measure levels of cholesterol in murine blood serum, the enzymatic endpoint method was adopted to calculate the concentration of cholesterol based on the standard. A cholesterol standard (Randox) was serially diluted 1: 2 with dH_20 and dH_20 was used as blank. Murine serum was diluted 1:5 and 1:10 with dH_20. 200µl of cholesterol detection reagent (Randox) was added to each well and the plate was incubated for 10 minutes at 37°C. All tests were performed in duplicate. Optical density (OD) of each well was measured by SPECTROstar Nano (BMG Labtech) at 540nm and 640nm wavelengths. The OD from the 540nm reading was subtracted from the 620nm, followed by subtracting the blank OD. The standard curve was generated using GraphPad Prism software and the concentrations of sample wells were interpolated based on the standard curve. Serum cholesterol levels were calculated in mg/dL by multiplying by the dilution factor and by 38.7; the mean values from two wells of each dilution were used for calculation.

7.7. Histology

7.7.1. May-Grünwald Giemsa stain

Flow cytometer-sorted aortic macrophages and DCs were cytospun onto a slide (Shandon; ThermoFisher Scientific) by using a Shandon Cytospin 3 (ThermoFisher

Scientific) at 400rpm for 5 minutes. The slides were air-dried and were stained in the May-Grünwald solution (Sigma-Aldrich) for 5 minutes. The slides were then washed in PBS for 1 minute twice and were then stained in the Giemsa solution (1:20 in dH_20; Sigma-Aldrich) for 15 minutes. The slides were briefly washed in dH_20, were air-dried and were mounted with DPX mountant (Sigma-Aldrich) with cover glasses (VWR).

7.7.2. Perivascular cast-treated carotid artery analysis

Perivascular cast-treated carotid arteries were cryosectioned at 5µm thickness in a CM3050S cryostat (Leica) and 5 sections were collected onn s slide (Superfrost Plus Adhesion microscope slides; ThermoFisher Scientific). Sections were collected from the distal end of the collar enclosed artery. The slides were air-dried and were then stored at -80°C.

7.7.3. Elastin Van Gieson (EVG)

Slides were selected to represent the artery immediately distal to the collar. Eight alternate slides were taken for Elastic Van Gieson staining, according to the manufacturer's instructions (Sigma-Aldrich). In brief, slides were fixed in 4% paraformaldehyde (PFA) for 8 minutes and were then stained in working elastin solution for 10 minutes. The slides were differentiated in ferric chloride solution for 2 to 3 minutes. The slides were counter-stained with Van Gieson solution for 30 seconds and were dehydrated in ethanol and xylene, followed by mounting with DPX mountant (Sigma-Aldrich) with cover glasses (VWR).

7.7.4. Aorta *en face* analysis and Sudan IV staining

Dissected aortas were fixed in 4% PFA at 4°C at least overnight and were cut open longitudinally from the iliac arteries to the aortic root. They were then pinned flat onto a black paraffin wax board using black insect pins (Interfocus). The mounted aortas were washed in PBS followed by a wash in 70% ethanol for 5 minutes. The aortas were then stained in Sudan IV solution for 6 min with gentle agitation. The stained aorta was then differentiated in 80% ethanol for 1 min and moved to clean 80% ethanol for 2 more minutes. The aortas were transferred into PBS until imaging.

7.7.5. Aortic root section

To section the aortic root, the heart was cut transversely below the aorta and the top of the heart was frozen in OCT (Tissue-Tek, Sakura) in a biopsy processing cassette mould (Tissue-Tek, Sakura) at -80°C. OCT-embedded tissues were cryosectioned in a CM3050 cryostat (Leica) and the sections were collected on Superfrost Plus Adhesion microscope slides (Thermo Scientific, USA). For aortic roots, five-micrometer cryosections were taken of the aortic root for the entire region of the valve leaflets and 3 sections were collected on a slide. Slides at 100 µm intervals were selected to stain with Oil red O (ORO) while other slides were retained for other staining. All slides were air-dried and stored at -20°C.

7.7.6. Oil Red O (ORO)

Oil Red O (ORO) stains lipid red in the atherosclerotic lesion. Aortic root section slides were air-dried for 30 minutes and fixed in 4% PFA for 10 minutes. After rinsing slides in PBS for 5 minutes and 60% isopropanol for 1 minute, slides were stained in the ORO solution for 15 minutes. After washing in deionised water, sections were then

counterstained with Harris haematoxylin (Sigma-Aldrich) for 30 seconds and were rinsed in running deionised water. Finally, the stained slides were immediately mounted with aqueous Kaier's Glycergel mounting medium (Merck Millipore) with cover glasses (VWR).

7.7.7. Haematoxylin and Eosin staining

Haematoxylin and Eosin (H&E) staining was used to visualise necrotic areas in the lesion within the aortic root. The staining procedure was performed using the Tissue-Tek Prisma/Film automated slide stainer (Sakura) and the Tissue-Tek Glas^{TM} g2 coverslipper (Sakura). The slides were air dried for 30 minutes, fixed in 4% PFA for 10 minutes, and rinsed in deionised water for 5 minutes. The slides were stained with Harris haematoxylin (Sigma-Aldrich) for 8 minutes, washed in running tap water for 5 minutes, and differentiated with 0.3% acid alcohol for 2 minutes. Following washing in water, the slides were counterstained with the eosin solution (Sigma-Aldrich) for 2 minutes and rinsed again in water. Finally, the stained slides were dehydrated through three graded ethanol solutions for 1 minute each and were cleared in two changes of xylene for 1 minute each. The slides were finally mounted in DPX mountant (Sigma-Aldrich) and cover glasses (VWR). The areas in the lesion free from H&E stain and bigger than 3000 μm^2 were designated to be necrotic core.

7.7.8. Picro-sirius Red

Collagen in the aortic root was quantified using the Picro-Sirius Red stain kit (Abcam) according to the manufacturer's instructions. Collagen appears in red under the bright field and Type I and III collagen is shown in orange and green, respectively under the polarised light. The slides were air dried for 30 minutes, fixed in 4% PFA for 10 minutes

and rinsed in deionised water. The slides were stained in Picro-Sirius Red dye solution for 1 hour and rinsed in two changes of acetic acid solution. Finally, the stained slides were dehydrated through three graded ethanol solutions for 1 minute each and were cleared in two changes of xylene for 1 minute each. The slides were finally mounted in DPX mountant (Sigma-Aldrich) and cover glasses (VWR).

7.7.9. Avidin-Biotin Complex (ABC) staining

Selected slides were air-dried for 30 minutes. A circle was drawn around the tissue section by using the ImmEdge hydrophobic barrier pen (Vector Laboratories) to keep the reagent within the section. The slides were fixed in ice-cold acetone (VWR) for 10 minutes and were air-dried again for 30 seconds. The slides were then washed in PBS for 5 minutes and were blocked with 10% serum (rabbit or goat serum from Abcam; the same species in which the secondary antibody was raised) for 1 hour. After washing in PBS, Avidin and Biotin solutions (Vector Laboratories) were used to block endogenous avidin and biotin for 15 minutes each. The slides were incubated with a primary antibody diluted in PBS for 1 hour and were washed in PBS. The slides were then incubated with a biotinylated secondary antibody (Vector Laboratories) diluted by 1:400 in PBS for 1 hour. After two washing steps, the slides were then treated with 0.3% hydrogen peroxide (Sigma-Aldrich) for 15 minutes to block endogenous peroxidase activity. The slides were then washed and were incubated with an ABC-Elite-Standard Kit for Peroxidase (Vector Laboratories) for 40 minutes. After two washing steps, the slides were treated with DAB (3,3'-diaminobenzidine) HRP substrate solution (Vector Laboratories) for 1-5 minutes depending on the intensity of the signal. The slides were then washed in PBS, counter-stained in Harris haematoxylin solution (Sigma-Aldrich) for 30 seconds and washed in deionised water.

The slides were dehydrated in 70% ethanol for 1 minute and 100% ethanol for 1 minute. Finally, the slides were air-dried and were mounted using Histomount (National Diagnostics) and cover glasses (VWR).

7.7.10. Immunofluorescence (IF)

The slides were air-dried for 30 minutes. A circle was drawn around the tissue section by using the ImmEdge hydrophobic barrier pen (Vector Laboratories) to keep the reagent within the section. The slides were fixed in ice-cold acetone (VWR) for 10 minutes and were air-dried again for 30 seconds. The slides were then washed in PBS for 5 minutes and were blocked with 10% serum for 1 hour. After washing steps in PBS, the slides were treated with a primary antibody or two antibodies for co-staining for 1 hour and were washed in PBS twice. The slides were then incubated with secondary antibody conjugated with AF488 or AF568 for 1 hour in the dark. The slides were then washed in PBS followed by dipping in deionised water briefly to remove salt. The slides were then mounted with Fluoromount-G with DAPI (ThermoFisher Scientific) and were kept at 4°C.

7.7.11. Imaging and analysis of the cryosectioned tissue

Section images from the stained slides were taken using the Olympus BX51 at 4X, 10X or 20X magnification depending on the size of the tissue, For the cellular morphology, images were taken at 40X. *En face* aorta images were taken using the Leica M60 dissection microscope at X0.8 magnifications.

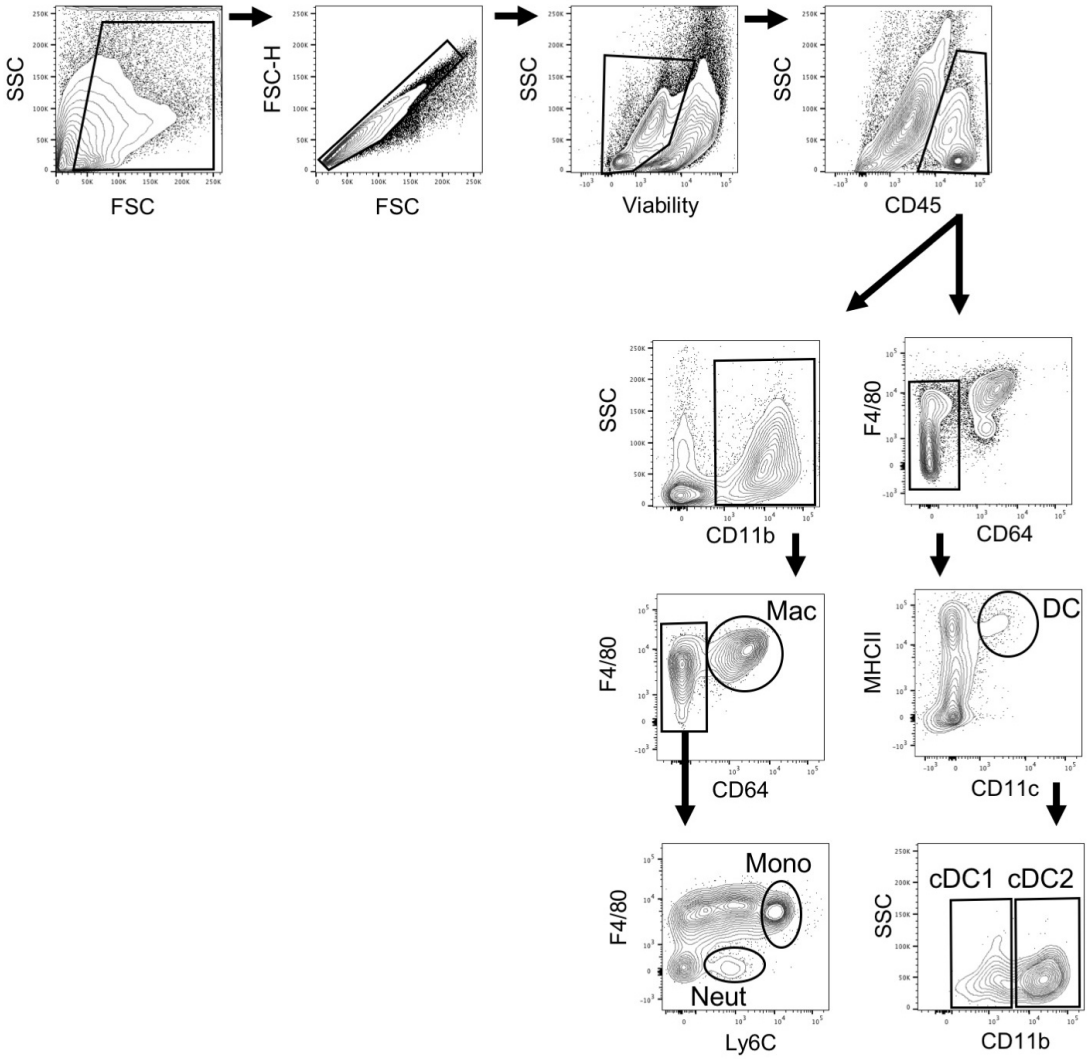
Images were randomized for blind analysis. Quantification of stained images were analysed using Clemex software.

7.8. Statistical analysis

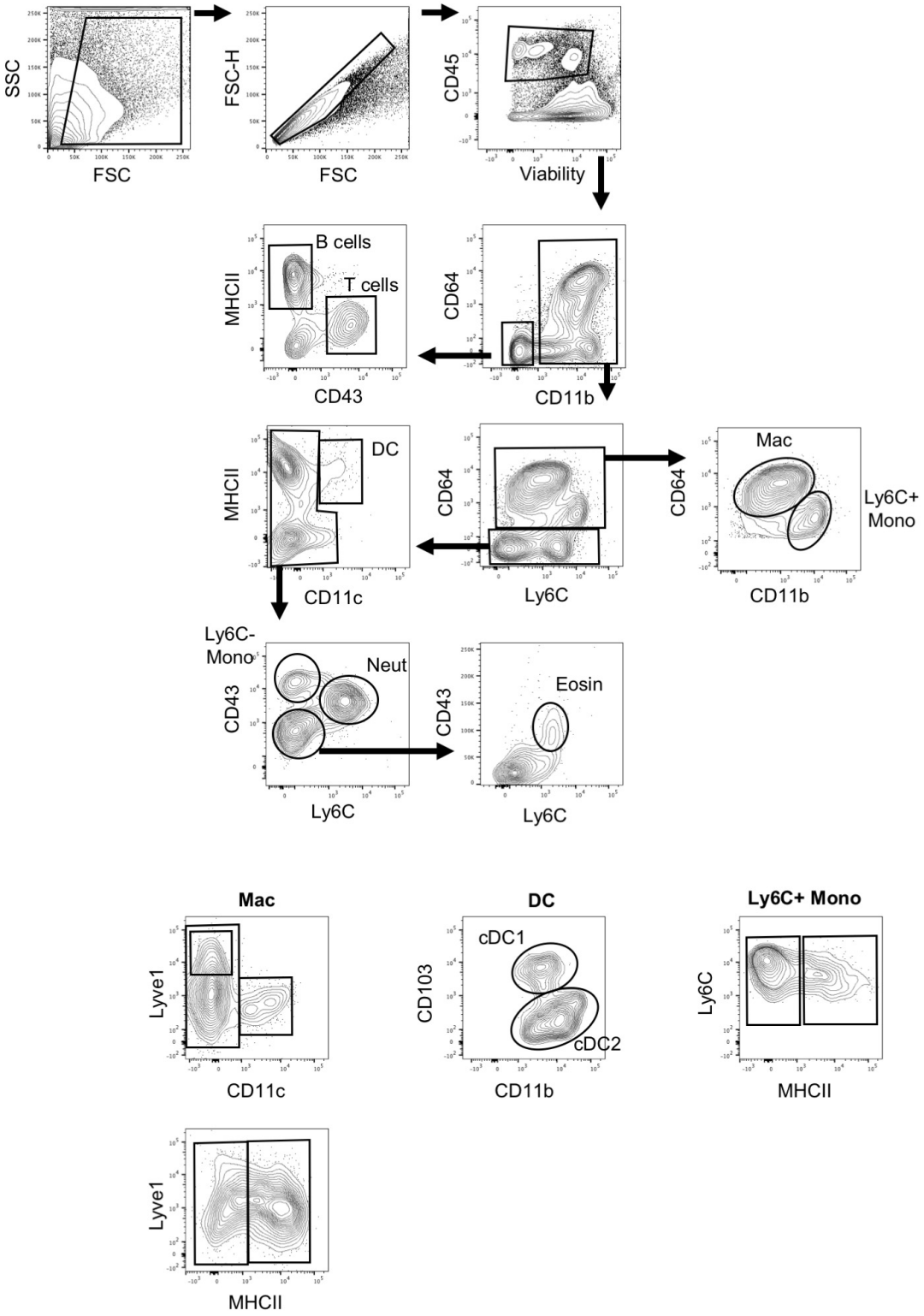
Data were analysed with GraphPad Prism (version 7.0d) software and were presented as Mean ± SEM. Mann-Whitney test or multiple t test was performed as appropriate. Differences were considered statistically significant where P values were below 0.05.

Appendix 1: Supplemental data

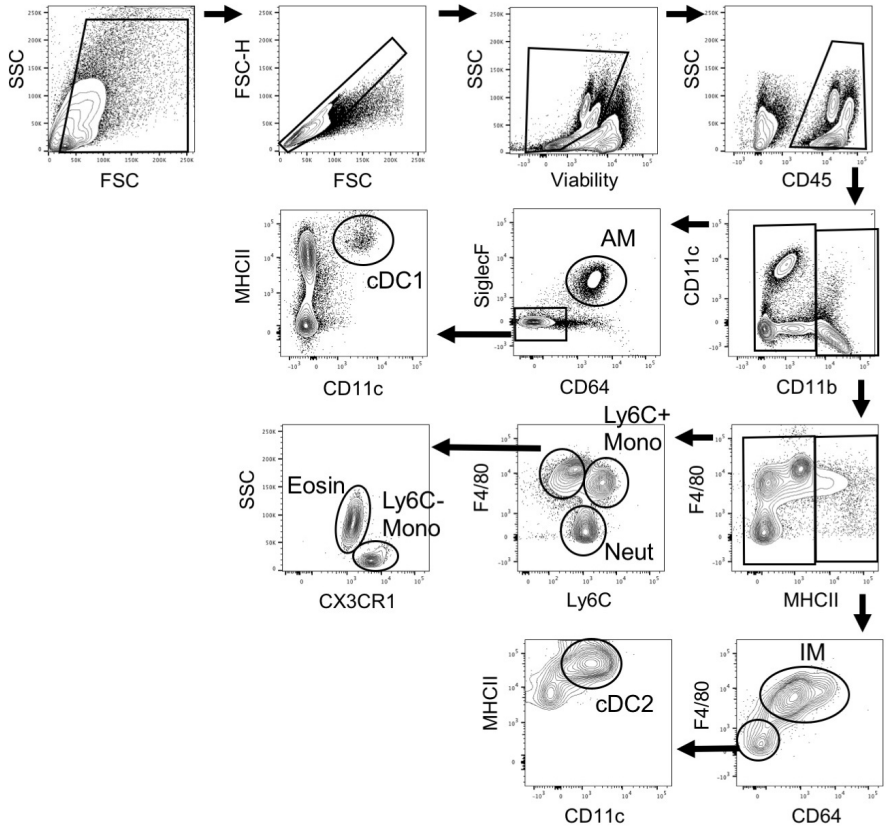
Appendix Figure 8. 1 Gating strategy for myeloid cell populations in the healthy aorta and heart.



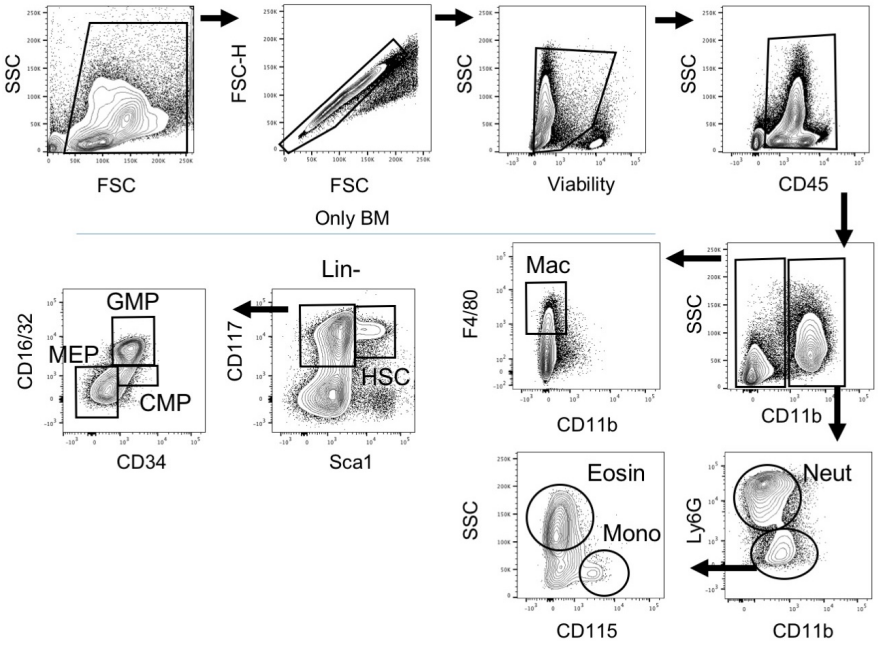
Appendix Figure 8. 2 Gating strategy for leucocyte populations in the atherosclerotic aorta.



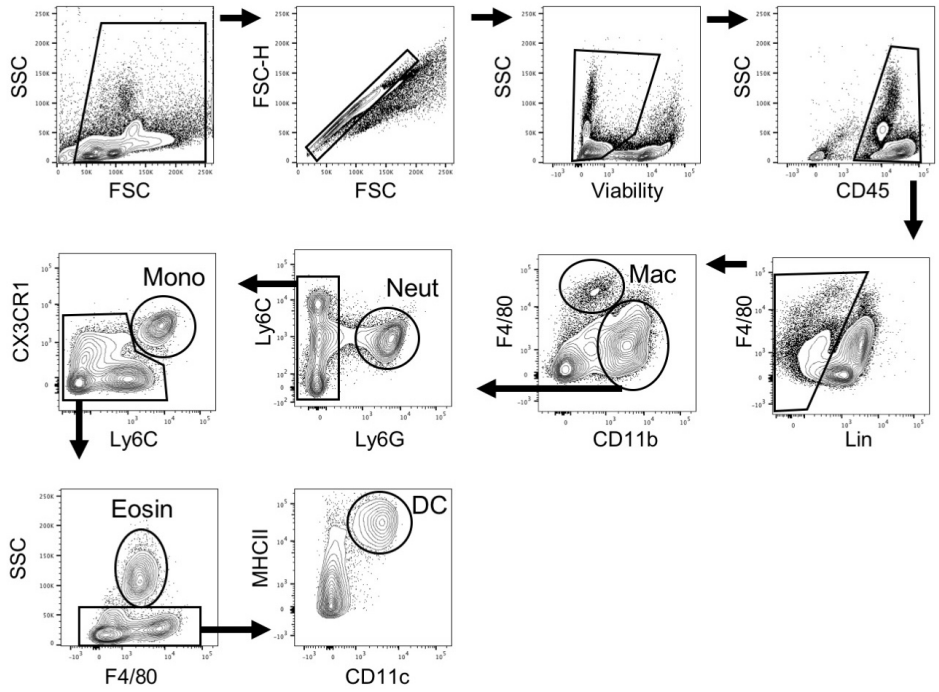
Appendix Figure 8. 3 Gating strategy for myeloid cell populations in the lungs.



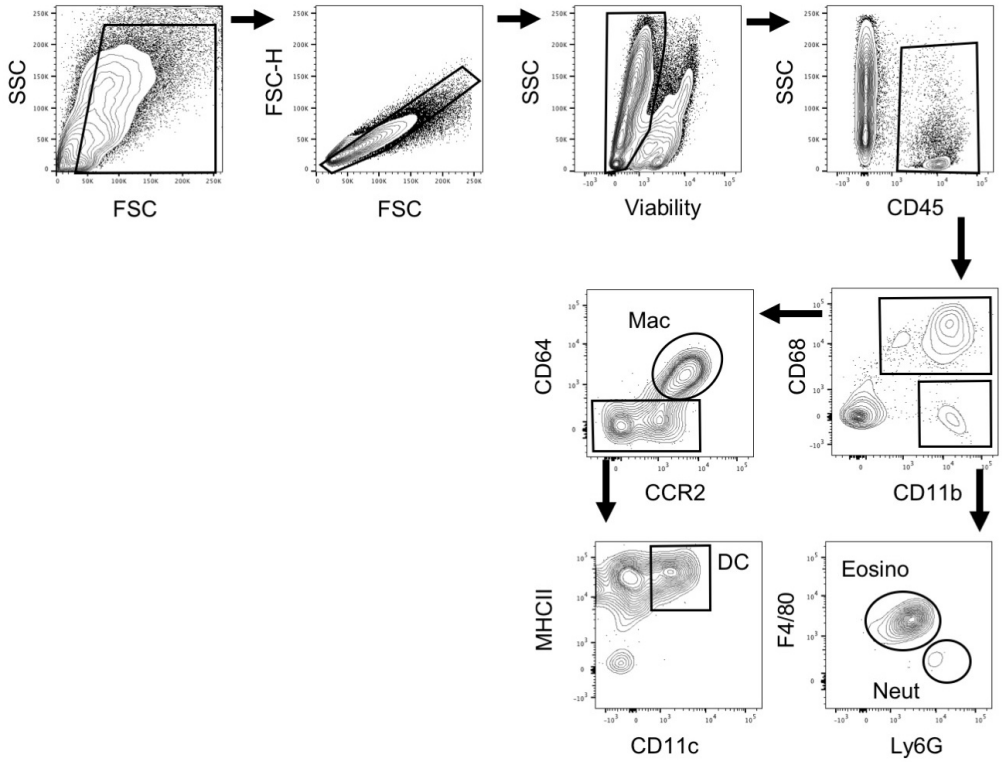
Appendix Figure 8. 4 Gating strategy for myeloid cell populations in the BM and blood.



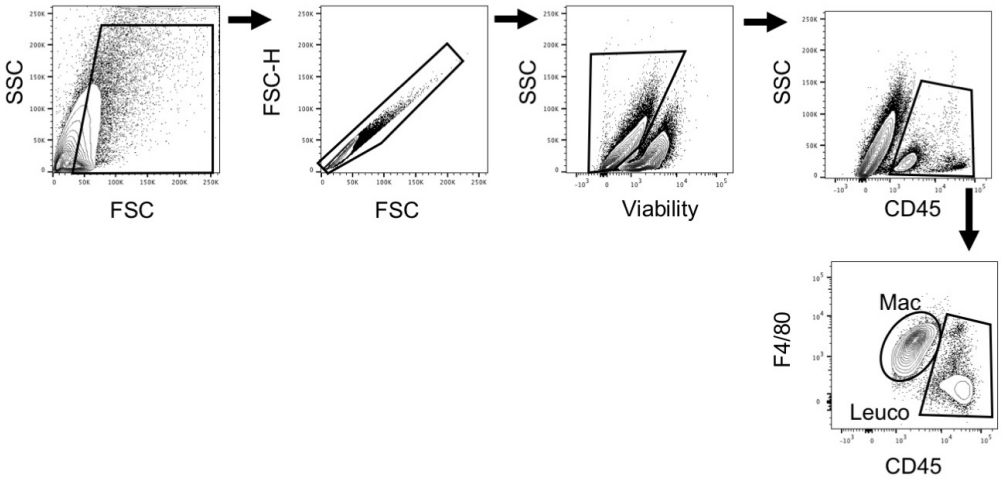
Appendix Figure 8. 5 Gating strategy for myeloid cell populations in the spleen.



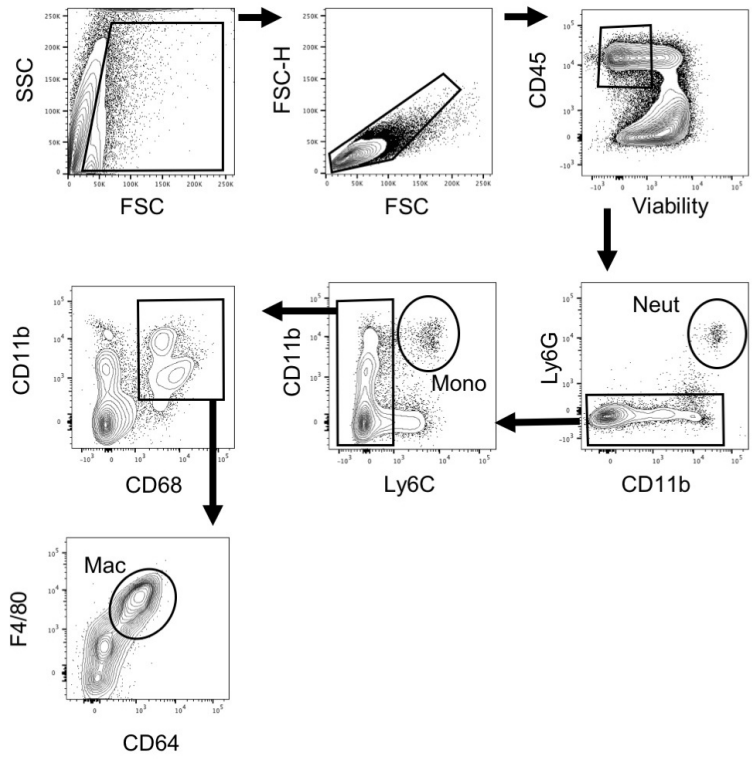
Appendix Figure 8. 6 Gating strategy for myeloid cell populations in the colon.



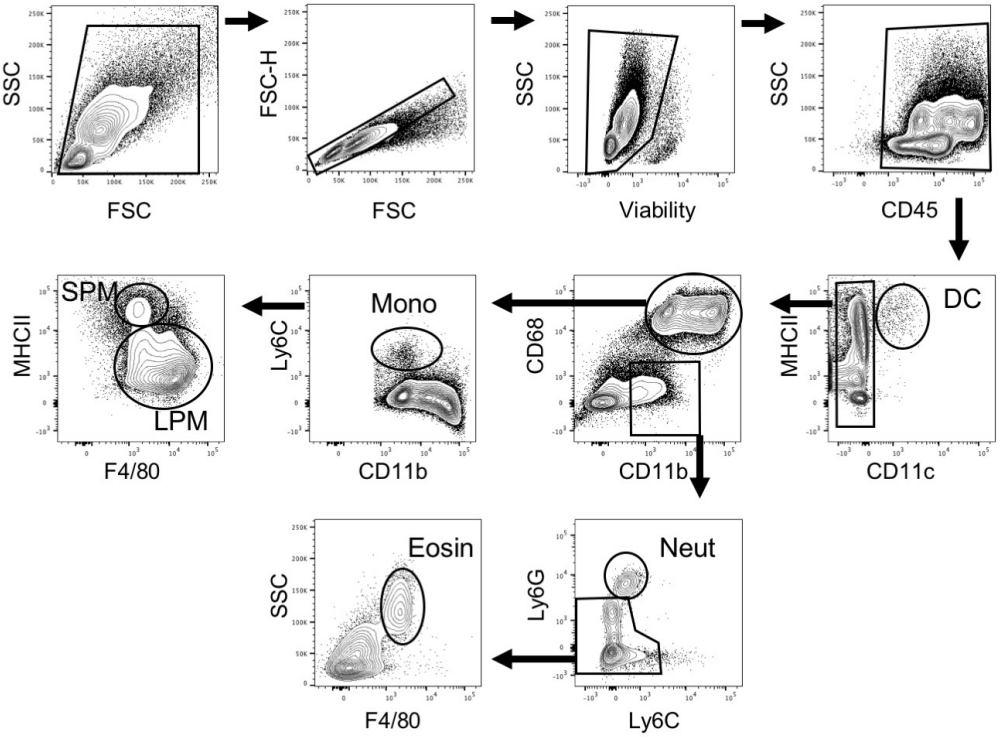
Appendix Figure 8. 7 Gating strategy for myeloid cell populations in the brain.



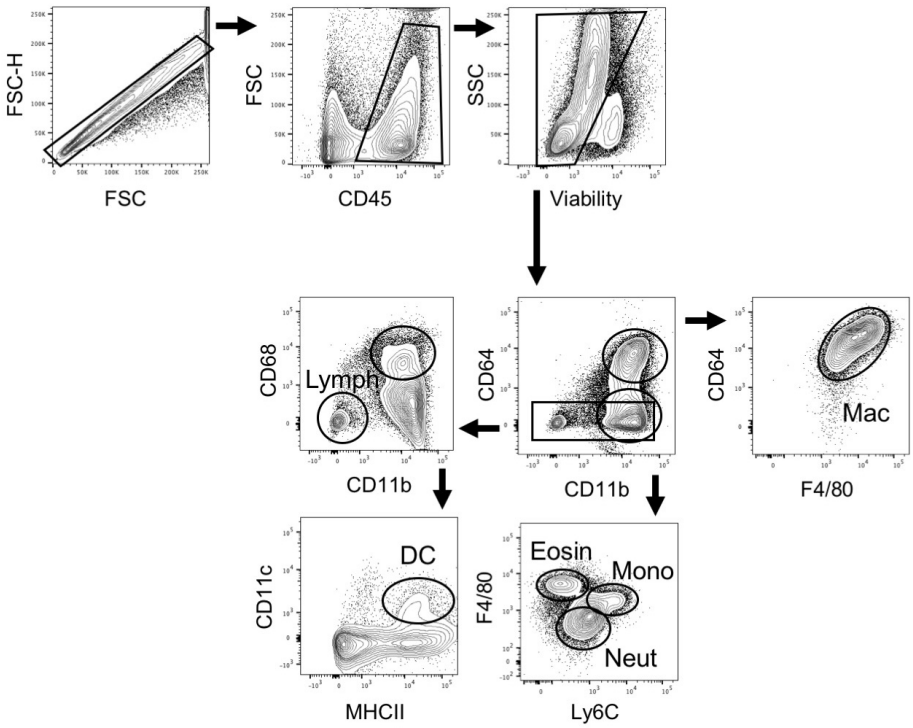
Appendix Figure 8. 8 Gating strategy for myeloid cell populations in the liver.



Appendix Figure 8. 9 Gating strategy for myeloid cell populations in the peritoneum.



Appendix Figure 8. 10 Gating strategy for leucocyte cell populations in the perivascular fibrotic tissue.



Appendix Table 8. 1 The percentage of leucocyte populations in the aorta, lungs, spleen and BM of wild type and *Dcir1*$^{-/-}$ mice at 12 weeks old.

Percentages are calculated per live CD45+ cells. n=3-4. Data are presented as mean±SEM. Multiple t test.

	Population	WT		KO		P value	
		No.	%	No.	%	No.	%
Aorta	Ly6C+ monocytes	390±268	3.2±1.5	199±44	2.6±0.4	n.s.	n.s.
	Macrophages	2999±444	33.9±6.0	2980±747	36.1±5.3	n.s.	n.s.
	Neutrophils	684±38	6.6±0.9	403±91	5.2±0.4	n.s.	n.s.
	cDC1	62±16	0.7±0.2	40±9	0.5±0.1	n.s.	n.s.
	cDC2	107±36	1.1±0.4	48±14	0.6±0.1	n.s.	n.s.
	B cells	1395±534	12.1±3.5	916±253	11.8±1.8	n.s.	n.s.
	T cells	859±335	8.2±0.9	725±223	9.3±1.5	n.s.	n.s.
Lungs	Ly6C+ monocytes	12833±2706	7.0±0.9	9636±403	5.5±0.3	n.s.	n.s.
	AM	18110±1427	10.4±1.7	18686±937	10.7±0.4	n.s.	n.s.
	IM	**1832±187**	**1.0±0.0**	**1086±47**	**0.6±0.0**	**0.0440**	**0.0011**
	Neutrophils	23445±4722	12.8±1.3	25604±3726	14.7±2.4	n.s.	n.s.
	cDC1	1632±235	0.9±0.0	1038±71	0.6±0.0	n.s.	0.0444
	cDC2	**2417±140**	**1.4±0.1**	**1519±108**	**0.9±0.1**	**0.0277**	**0.0291**
	B cells	48461±3681	27.43.1	51254±5695	29.0±2.1	n.s.	n.s.
	T cells	33683±7193	18.3±1.6	30355±1349	17.3±0.7	n.s.	n.s.
Spleen	Ly6C+ monocytes	3644±823	1.1±0.3	4480±1022	1.3±0.3	n.s.	n.s.
	Macrophages	328±46	0.1±0.0	1782±989	0.5±0.3	n.s.	n.s.
	Neutrophils	11488±2780	3.6±1.1	13053±2640	3.8±0.7	n.s.	n.s.
	DC	2337±187	0.7±0.1	2167±180	0.6±0.1	n.s.	n.s.
	B cells	135868±16724	41.5±4.5	157630±7102	46.5±1.3	n.s.	n.s.
	T cells	144534±24784	43.8±6.1	121796±5326	36.2±2.6	n.s.	n.s.
BM	Ly6C+ monocytes	8088±969	5.6±0.6	7618±319	4.9±0.2	n.s.	n.s.
	Macrophages	**3563±423**	**2.5±0.3**	**1749±96**	**1.1±0.1**	**0.0226**	**0.0278**
	Neutrophils	**67572±1493**	**46.9±0.3**	**89861±2038**	**57.6±0.8**	**0.0026**	**0.0006**
	B cells	17329±3393	12.0±2.3	10167±491	6.5±0.4	n.s.	n.s.
	T cells	6054±636	4.2±0.5	4291±193	2.8±0.1	n.s.	n.s.
	pDC	3731±779	2.6±0.6	2380±272	1.5±0.2	n.s.	n.s.
	HSC	4219±544	0.4±0.1	4896±536	0.4±0.0	n.s.	n.s.
	CMPs	5104±327	0.4±0.0	5226±402	0.4±0.0	n.s.	n.s.
	GMPs	16799±363	1.4±0.0	16986±2867	1.4±0.2	n.s.	n.s.
	MEPs	9480±381	0.8±0.0	8107±336	0.7±0.0	n.s.	n.s.

Appendix Table 8. 2 The percentage of leucocyte populations in the aorta and lungs of wild type and *Dcir1*$^{-/-}$ mice at 24 weeks old.

Percentages are calculated per live CD45+ cells. Data are presented as mean±SEM. Mann-Whitney t test.

	Population	WT		KO		P value	
		No.	%	No.	%	No.	%
Aorta	Ly6C+ monocytes	65±26	1.0±0.3	69±35	0.9±0.4	n.s.	n.s.
	Macrophages	2551±385	43.5±5.3	2841±645	40.0±5.2	n.s.	n.s.
	Neutrophils	270±70	4.3±0.6	208±52	2.9±0.4	n.s.	n.s.
	DC	180±18	3.1±0.3	170±26	2.5±0.2	n.s.	n.s.
	B cells	405±121	6.3±1.1	459±103	6.8±1.8	n.s.	n.s.
	T cells	1477±405	24.2±3.8	2075±270	32.2±6.5	n.s.	n.s.
Lungs	Ly6C+ monocytes	2221±344	3.3	1780±231	3.3	n.s.	n.s.
	Ly6C- monocytes	1911±204	2.9	1261±130	2.4	n.s.	n.s.
	AM	**8314±219**	**12.6**	**6284±517**	**12.2**	**0.0286**	**n.s.**
	IM	538±165	0.8	329±48	0.6	n.s.	n.s.
	Neutrophils	5188±556	7.7	4583±432	8.6	n.s.	n.s.
	Eosinophils	2374±464	3.5	1850±231	3.4	n.s.	n.s.
	cDC1	700±74	1.1	685±47	1.3	n.s.	n.s.
	cDC2	481±76	0.7	489±99	0.9	n.s.	n.s.
	B cells	22408±526	33.8	18272±3709	32.3	n.s.	n.s.
	T cells	18140±981	27.3	15772±2439	28.5	n.s.	n.s.

Appendix 2: Abbreviations

ApoE	Apolipoprotein E
BAL	Brochoalveolar lavage
BCR	B cell receptor
BM	Bone marrow
BMDM	Bone marrow-derived macrophages
BSA	Bovine serum albumin
CCL	C-C chemokine ligand
CCR	C-C chemokine receptor
CD	Cluster of differentiation
cDC	Conventional dendritic cell
CLR	C-type lectin receptor
CMP	Common myeloid progenitors
Collectins	Collagen-containing C-type lectins
CRD	Carbohydrate recognition domains
CVD	Cardiovascular disease
CX3CL	C-X3-C motif chemokine ligand
CX3CR	C-X3-C motif chemokine receptor
CXCR	C-X-C motif chemokine receptor
CyTOF	Cytometry by time of flight
DAMP	Damage associated molecular pattern
DC	Dendritic cells
DC-SIGN	Dendritic cell-specific intercellular adhesion molecule-3-grabbing non-integrin
DCAR	Dendritic cell immunoactivating receptor
DCIR	Dendritic cell immunoreceptor
DCLN	Deep cervical lymph nodes
DMEM	Dulbecco’s Modified Eagle’s Medium
DNA	Deoxyribonucleic acid
DT	Diphtheria toxin
DTR	Diphtheria toxin receptor
ECM	Extracellular matrix
ERK	Extracellular signal–regulated kinase
EVG	Elastin Van Gieson
FACS	Fluorescence activated cell sorting
FBS	Foetal bovine serum
Fc	Fragment crystallizable region
FSC	Forward scatter
GCSF	Granulocyte-colony stimulating factor
GFP	Green fluorescence protein
GMCSF	Granulocyte macrophage colony stimulating factor
GMP	granulocyte/macrophage progenitors
GO	Gene Ontology
GRO-α	Growth-regulated oncogene α
HBSS	Hanks' Balanced Salt Solution
HFD	High fat diet

HIV-1	Human immunodeficiency virus 1
HSC	Haematopoietic stem cells
ICAM1	Intercellular adhesion molecule 1
IFN	Interferon
IL	Interleukin
IMR	Intima/media ratio
iNOS	Inducible nitric oxide synthase
IRES	Internal ribosome entry site
IRF	Interferon regulatory factor
ITAM	Immunoreceptor tyrosine-based activation motif
ITIM	Immunoreceptor tyrosine-based inhibition motif
kDa	Kilodalton
KI	Knock in
KLF2	Krüppel-like factor
KO	Knock out
LDL	Low density lipoprotein
LDLR	Low density lipoprotein receptor
LPS	Lipopolysaccharide
LXR	Liver X receptor
Ly6C	Lymphocyte antigen 6C
Ly6G	Lymphocyte antigen 6G
Lyve1	Lymphatic vessel endothelial hyaluronan receptor 1
MCP	Monocyte chemoattractant protein
MCSF	Macrophage-colony stimulating factor
MEP	Megakaryocyte/erythrocyte progenitors
MerTK	C-mer proto-oncogene tyrosine kinase
MFI	Mean fluorescence intensity
MHC	Major histocompatibility complex
MMP	Matrix metalloproteinase
MNC	Mononuclear cells
MR	Mannose receptor
NFκB	Nuclear factor kappa light polypeptide gene enhancer in B cells
NK	Natural killer
NLRP	NACHT, LRR and PYD domains-containing protein
NO	Nitric oxide
Nrf2	Nuclear factor (erythroid-derived 2)-like 2
ORO	Oil Red O
oxLDL	Oxidised low density lipoprotein
PALN	Para-aortic lymph node
PAMP	Pathogen associated molecular pattern
PBS	Phosphate buffered saline
PCR	Polymerase chain reaction
pDC	Plasmacytoid dendritic cell
PFA	Paraformaldehyde
PMN	Polymorphonuclear cells

PPAR	Peroxisome proliferator-activated receptor
PPR	Pattern recognition receptor
qRT-RCS	Quantitative real time polymerase chain reaction
RA	Rheumatoid arthritis
RBC	Red blood cell
RNA	Ribonucleic acid
RPM	Revolutions per minute
RPMI	Roswell Park Memorial Institute medium
scRNAseq	Single cell RNA sequencing
SEM	Standard error of the mean
SHIP	SH2-domain-containing inositol polyphosphate 5' phosphatase
SHP	Src homology region 2 domain-containing phosphatase
Siglec	Sialic acid binding immunoglobulin-like lectin
SIGN-R1	Specific ICAM-3 grabbing nonintegrin-related 1
SLE	Systemic lupus erythematous
SMC	Smooth muscle cell
SP	Surfactant protein
SR	Scavenger receptor
SSC	Side scatter
STAT	Signal transducers and activators of transcription
t SNE	t-Distributed Stochastic Neighbor Embedding
TCR	T cell receptor
TG	Thioglycollate
Th	T helper cell
TLR	Toll-like receptor
TNF	Tumour necrosis factor
Treg	Regulatory T cell
Trem	Triggering receptor expressed on myeloid cells
VCAM1	Vascular cell adhesion molecule 1
WT	Wild type
XCR	C-motif chemokine receptor

Appendix 3: Published material

Abstracts presented at scientific conferences

- British Atherosclerosis Society 2018 (*Awarded the best poster prize)
- British Society for Immunology 2018
- British Atherosclerosis Society 2017 (*Awarded the best poster prize)
- Keystone Symposia 2017 (Mononuclear Phagocytes in Health, Immune Defense and Disease (D3))

Published material

PARK, I., KASSITERIDI, C. & MONACO, C. 2017. Functional diversity of macrophages in vascular biology and disease. *Vascul Pharmacol,* 99**,** 13-22.

COLE, J. E.*, **PARK, I.*,** AHERN, D. J., KASSITERIDI, C., DANSO ABEAM, D., GODDARD, M. E., GREEN, P., MAFFIA, P. & MONACO, C. 2018. Immune cell census in murine atherosclerosis: cytometry by time of flight illuminates vascular myeloid cell diversity. *Cardiovasc Res,* 114**,** 1360-1371.

*Co-first authors

Appendix 4: Bibliography

ADIGUZEL, E., AHMAD, P. J., FRANCO, C. & BENDECK, M. P. 2009. Collagens in the progression and complications of atherosclerosis. *Vasc Med,* 14**,** 73-89.

AJAMI, B., BENNETT, J. L., KRIEGER, C., TETZLAFF, W. & ROSSI, F. M. 2007. Local self-renewal can sustain CNS microglia maintenance and function throughout adult life. *Nat Neurosci,* 10**,** 1538-43.

AKIRA, S., UEMATSU, S. & TAKEUCHI, O. 2006. Pathogen recognition and innate immunity. *Cell,* 124**,** 783-801.

AVERILL, L. E., MEAGHER, R. C. & GERRITY, R. G. 1989. Enhanced monocyte progenitor cell proliferation in bone marrow of hyperlipemic swine. *Am J Pathol,* 135**,** 369-77.

BABAEV, V. R., YANCEY, P. G., RYZHOV, S. V., KON, V., BREYER, M. D., MAGNUSON, M. A., FAZIO, S. & LINTON, M. F. 2005. Conditional knockout of macrophage PPARgamma increases atherosclerosis in C57BL/6 and low-density lipoprotein receptor-deficient mice. *Arterioscler Thromb Vasc Biol,* 25**,** 1647-53.

BACK, M. & HANSSON, G. K. 2015. Anti-inflammatory therapies for atherosclerosis. *Nat Rev Cardiol,* 12**,** 199-211.

BACK, M. R., CAREW, T. E. & SCHMID-SCHOENBEIN, G. W. 1995. Deposition pattern of monocytes and fatty streak development in hypercholesterolemic rabbits. *Atherosclerosis,* 116**,** 103-15.

BAIN, C. C., BRAVO-BLAS, A., SCOTT, C. L., GOMEZ PERDIGUERO, E., GEISSMANN, F., HENRI, S., MALISSEN, B., OSBORNE, L. C., ARTIS, D. & MOWAT, A. M. 2014. Constant replenishment from circulating monocytes maintains the macrophage pool in the intestine of adult mice. *Nat Immunol,* 15**,** 929-37.

BARNES, M. J. & FARNDALE, R. W. 1999. Collagens and atherosclerosis. *Exp Gerontol,* 34**,** 513-25.

BATES, E. E., FOURNIER, N., GARCIA, E., VALLADEAU, J., DURAND, I., PIN, J. J., ZURAWSKI, S. M., PATEL, S., ABRAMS, J. S., LEBECQUE, S., GARRONE, P. & SAELAND, S. 1999. APCs express DCIR, a novel C-type lectin surface receptor containing an immunoreceptor tyrosine-based inhibitory motif. *J Immunol,* 163**,** 1973-83.

BENDALL, S. C., SIMONDS, E. F., QIU, P., AMIR EL, A. D., KRUTZIK, P. O., FINCK, R., BRUGGNER, R. V., MELAMED, R., TREJO, A., ORNATSKY, O. I., BALDERAS, R. S., PLEVRITIS, S. K., SACHS, K., PE'ER, D., TANNER, S. D. & NOLAN, G. P. 2011. Single-cell mass cytometry of differential immune and drug responses across a human hematopoietic continuum. *Science,* 332**,** 687-96.

BENNETT, M. R., SINHA, S. & OWENS, G. K. 2016. Vascular Smooth Muscle Cells in Atherosclerosis. *Circ Res,* 118**,** 692-702.

BILLADEAU, D. D. & LEIBSON, P. J. 2002. ITAMs versus ITIMs: striking a balance during cell regulation. *J Clin Invest,* 109**,** 161-8.

BLOEM, K., VUIST, I. M., VAN DEN BERK, M., KLAVER, E. J., VAN DIE, I., KNIPPELS, L. M., GARSSEN, J., GARCIA-VALLEJO, J. J., VAN VLIET, S. J. & VAN KOOYK, Y. 2014. DCIR interacts with ligands from both endogenous and pathogenic origin. *Immunol Lett,* 158**,** 33-41.

BLOEM, K., VUIST, I. M., VAN DER PLAS, A. J., KNIPPELS, L. M., GARSSEN, J., GARCIA-VALLEJO, J. J., VAN VLIET, S. J. & VAN KOOYK, Y. 2013. Ligand binding and signaling of dendritic cell immunoreceptor (DCIR) is modulated by the glycosylation of the carbohydrate recognition domain. *PLoS One,* 8**,** e66266.

BOISVERT, W. A., SPANGENBERG, J. & CURTISS, L. K. 1995. Treatment of severe hypercholesterolemia in apolipoprotein E-deficient mice by bone marrow transplantation. *J Clin Invest,* 96**,** 1118-24.

BORING, L., GOSLING, J., CLEARY, M. & CHARO, I. F. 1998. Decreased lesion formation in CCR2-/- mice reveals a role for chemokines in the initiation of atherosclerosis. *Nature,* 394**,** 894-7.

BOUHLEL, M. A., DERUDAS, B., RIGAMONTI, E., DIEVART, R., BROZEK, J., HAULON, S., ZAWADZKI, C., JUDE, B., TORPIER, G., MARX, N., STAELS, B. & CHINETTI-GBAGUIDI, G. 2007. PPARgamma activation primes human monocytes into alternative M2 macrophages with anti-inflammatory properties. *Cell Metab,* 6**,** 137-43.

BOYLE, J. J., JOHNS, M., KAMPFER, T., NGUYEN, A. T., GAME, L., SCHAER, D. J., MASON, J. C. & HASKARD, D. O. 2012. Activating transcription factor 1 directs Mhem atheroprotective macrophages through coordinated iron handling and foam cell protection. *Circ Res,* 110**,** 20-33.

BOYLE, J. J., JOHNS, M., LO, J., CHIODINI, A., AMBROSE, N., EVANS, P. C., MASON, J. C. & HASKARD, D. O. 2011. Heme induces heme oxygenase 1 via Nrf2: role in the homeostatic macrophage response to intraplaque hemorrhage. *Arterioscler Thromb Vasc Biol,* 31**,** 2685-91.

BRINKMANN, V., REICHARD, U., GOOSMANN, C., FAULER, B., UHLEMANN, Y., WEISS, D. S., WEINRAUCH, Y. & ZYCHLINSKY, A. 2004. Neutrophil extracellular traps kill bacteria. *Science,* 303**,** 1532-5.

BUCH, T., HEPPNER, F. L., TERTILT, C., HEINEN, T. J., KREMER, M., WUNDERLICH, F. T., JUNG, S. & WAISMAN, A. 2005. A Cre-inducible diphtheria toxin receptor mediates cell lineage ablation after toxin administration. *Nat Methods,* 2**,** 419-26.

BUTCHER, M. J., HERRE, M., LEY, K. & GALKINA, E. 2011. Flow cytometry analysis of immune cells within murine aortas. *J Vis Exp*.

CHARO, I. F. & TAUB, R. 2011. Anti-inflammatory therapeutics for the treatment of atherosclerosis. *Nat Rev Drug Discov,* 10**,** 365-76.

CHINETTI-GBAGUIDI, G., BARON, M., BOUHLEL, M. A., VANHOUTTE, J., COPIN, C., SEBTI, Y., DERUDAS, B., MAYI, T., BORIES, G., TAILLEUX, A., HAULON, S., ZAWADZKI, C., JUDE, B. & STAELS, B. 2011. Human atherosclerotic plaque alternative macrophages display low cholesterol handling but high phagocytosis because of distinct activities of the PPARgamma and LXRalpha pathways. *Circ Res,* 108**,** 985-95.

CHINETTI-GBAGUIDI, G., COLIN, S. & STAELS, B. 2015. Macrophage subsets in atherosclerosis. *Nat Rev Cardiol,* 12**,** 10-7.

CHO, K. W., MORRIS, D. L. & LUMENG, C. N. 2014. Flow cytometry analyses of adipose tissue macrophages. *Methods Enzymol,* 537**,** 297-314.

CHO, K. Y., MIYOSHI, H., KURODA, S., YASUDA, H., KAMIYAMA, K., NAKAGAWARA, J., TAKIGAMI, M., KONDO, T. & ATSUMI, T. 2013. The phenotype of infiltrating macrophages influences arteriosclerotic plaque vulnerability in the carotid artery. *J Stroke Cerebrovasc Dis,* 22**,** 910-8.

CHOI, J. H., CHEONG, C., DANDAMUDI, D. B., PARK, C. G., RODRIGUEZ, A., MEHANDRU, S., VELINZON, K., JUNG, I. H., YOO, J. Y., OH, G. T. & STEINMAN, R. M. 2011. Flt3 signaling-dependent dendritic cells protect against atherosclerosis. *Immunity,* 35**,** 819-31.

CLAUSEN, B. E., BURKHARDT, C., REITH, W., RENKAWITZ, R. & FORSTER, I. 1999. Conditional gene targeting in macrophages and granulocytes using LysMcre mice. *Transgenic Res,* 8**,** 265-77.

CLINTON, S. K., UNDERWOOD, R., HAYES, L., SHERMAN, M. L., KUFE, D. W. & LIBBY, P. 1992. Macrophage colony-stimulating factor gene expression in vascular cells and in experimental and human atherosclerosis. *Am J Pathol,* 140**,** 301-16.

COCHAIN, C., VAFADARNEJAD, E., ARAMPATZI, P., PELISEK, J., WINKELS, H., LEY, K., WOLF, D., SALIBA, A. E. & ZERNECKE, A. 2018. Single-Cell RNA-Seq Reveals the Transcriptional Landscape and Heterogeneity of Aortic Macrophages in Murine Atherosclerosis. *Circ Res,* 122**,** 1661-1674.

COEN, M., GABBIANI, G. & BOCHATON-PIALLAT, M. L. 2011. Myofibroblast-mediated adventitial remodeling: an underestimated player in arterial pathology. *Arterioscler Thromb Vasc Biol,* 31**,** 2391-6.

COLE, J. E., PARK, I., AHERN, D. J., KASSITERIDI, C., DANSO ABEAM, D., GODDARD, M. E., GREEN, P., MAFFIA, P. & MONACO, C. 2018. Immune cell census in murine atherosclerosis: cytometry by time of flight illuminates vascular myeloid cell diversity. *Cardiovasc Res,* 114**,** 1360-1371.

COLLINS, A. R., MEEHAN, W. P., KINTSCHER, U., JACKSON, S., WAKINO, S., NOH, G., PALINSKI, W., HSUEH, W. A. & LAW, R. E. 2001. Troglitazone inhibits formation of early atherosclerotic lesions in diabetic and nondiabetic low density lipoprotein receptor-deficient mice. *Arterioscler Thromb Vasc Biol,* 21**,** 365-71.

COMBADIERE, C., POTTEAUX, S., GAO, J. L., ESPOSITO, B., CASANOVA, S., LEE, E. J., DEBRE, P., TEDGUI, A., MURPHY, P. M. & MALLAT, Z. 2003. Decreased atherosclerotic lesion formation in CX3CR1/apolipoprotein E double knockout mice. *Circulation,* 107**,** 1009-16.

COMBADIERE, C., POTTEAUX, S., RODERO, M., SIMON, T., PEZARD, A., ESPOSITO, B., MERVAL, R., PROUDFOOT, A., TEDGUI, A. & MALLAT, Z. 2008. Combined inhibition of CCL2, CX3CR1, and CCR5 abrogates Ly6C(hi) and Ly6C(lo) monocytosis and almost abolishes atherosclerosis in hypercholesterolemic mice. *Circulation,* 117**,** 1649-57.

CYBULSKY, M. I. & GIMBRONE, M. A., JR. 1991. Endothelial expression of a mononuclear leukocyte adhesion molecule during atherogenesis. *Science,* 251**,** 788-91.

CYBULSKY, M. I., IIYAMA, K., LI, H., ZHU, S., CHEN, M., IIYAMA, M., DAVIS, V., GUTIERREZ-RAMOS, J. C., CONNELLY, P. W. & MILSTONE, D. S. 2001. A major role for VCAM-1, but not ICAM-1, in early atherosclerosis. *J Clin Invest,* 107**,** 1255-62.

DAHLOF, B. 2010. Cardiovascular disease risk factors: epidemiology and risk assessment. *Am J Cardiol,* 105**,** 3A-9A.

DAISSORMONT, I. T., CHRIST, A., TEMMERMAN, L., SAMPEDRO MILLARES, S., SEIJKENS, T., MANCA, M., ROUSCH, M., POGGI, M., BOON, L., VAN DER LOOS, C., DAEMEN, M., LUTGENS, E., HALVORSEN, B., AUKRUST, P., JANSSEN, E. & BIESSEN, E. A. 2011. Plasmacytoid dendritic cells protect

against atherosclerosis by tuning T-cell proliferation and activity. *Circ Res,* 109**,** 1387-95.

DANEMAN, R., ZHOU, L., KEBEDE, A. A. & BARRES, B. A. 2010. Pericytes are required for blood-brain barrier integrity during embryogenesis. *Nature,* 468**,** 562-6.

DAUGHERTY, A. 2002. Mouse models of atherosclerosis. *Am J Med Sci,* 323**,** 3-10.

DAVIES, L. C., JENKINS, S. J., ALLEN, J. E. & TAYLOR, P. R. 2013. Tissue-resident macrophages. *Nat Immunol,* 14**,** 986-95.

DEL FRESNO, C., IBORRA, S., SAZ-LEAL, P., MARTINEZ-LOPEZ, M. & SANCHO, D. 2018. Flexible Signaling of Myeloid C-Type Lectin Receptors in Immunity and Inflammation. *Front Immunol,* 9**,** 804.

DORAN, A. C., MELLER, N. & MCNAMARA, C. A. 2008. Role of smooth muscle cells in the initiation and early progression of atherosclerosis. *Arterioscler Thromb Vasc Biol,* 28**,** 812-9.

EDELSON, J. D., MACFADDEN, D. K., KLEIN, M. & REBUCK, A. S. 1985. Autofluorescence of alveolar macrophages: problems and potential solutions. *Med Hypotheses,* 17**,** 403-7.

ENSAN, S., LI, A., BESLA, R., DEGOUSEE, N., COSME, J., ROUFAIEL, M., SHIKATANI, E. A., EL-MAKLIZI, M., WILLIAMS, J. W., ROBINS, L., LI, C., LEWIS, B., YUN, T. J., LEE, J. S., WIEGHOFER, P., KHATTAR, R., FARROKHI, K., BYRNE, J., OUZOUNIAN, M., ZAVITZ, C. C., LEVY, G. A., BAUER, C. M., LIBBY, P., HUSAIN, M., SWIRSKI, F. K., CHEONG, C., PRINZ, M., HILGENDORF, I., RANDOLPH, G. J., EPELMAN, S., GRAMOLINI, A. O., CYBULSKY, M. I., RUBIN, B. B. & ROBBINS, C. S. 2016. Self-renewing resident arterial macrophages arise from embryonic CX3CR1(+) precursors and circulating monocytes immediately after birth. *Nat Immunol,* 17**,** 159-68.

EPELMAN, S., LAVINE, K. J., BEAUDIN, A. E., SOJKA, D. K., CARRERO, J. A., CALDERON, B., BRIJA, T., GAUTIER, E. L., IVANOV, S., SATPATHY, A. T., SCHILLING, J. D., SCHWENDENER, R., SERGIN, I., RAZANI, B., FORSBERG, E. C., YOKOYAMA, W. M., UNANUE, E. R., COLONNA, M., RANDOLPH, G. J. & MANN, D. L. 2014. Embryonic and adult-derived resident cardiac macrophages are maintained through distinct mechanisms at steady state and during inflammation. *Immunity,* 40**,** 91-104.

FINN, A. V., NAKANO, M., POLAVARAPU, R., KARMALI, V., SAEED, O., ZHAO, X., YAZDANI, S., OTSUKA, F., DAVIS, T., HABIB, A., NARULA, J., KOLODGIE, F. D. & VIRMANI, R. 2012. Hemoglobin directs macrophage differentiation and prevents foam cell formation in human atherosclerotic plaques. *J Am Coll Cardiol,* 59**,** 166-77.

FLEG, J. L., STONE, G. W., FAYAD, Z. A., GRANADA, J. F., HATSUKAMI, T. S., KOLODGIE, F. D., OHAYON, J., PETTIGREW, R., SABATINE, M. S., TEARNEY, G. J., WAXMAN, S., DOMANSKI, M. J., SRINIVAS, P. R. & NARULA, J. 2012. Detection of high-risk atherosclerotic plaque: report of the NHLBI Working Group on current status and future directions. *JACC Cardiovasc Imaging,* 5**,** 941-55.

FLORNES, L. M., BRYCESON, Y. T., SPURKLAND, A., LORENTZEN, J. C., DISSEN, E. & FOSSUM, S. 2004. Identification of lectin-like receptors expressed by antigen presenting cells and neutrophils and their mapping to a novel gene complex. *Immunogenetics,* 56**,** 506-17.

FUJIKADO, N., SAIJO, S., YONEZAWA, T., SHIMAMORI, K., ISHII, A., SUGAI, S., KOTAKI, H., SUDO, K., NOSE, M. & IWAKURA, Y. 2008. Dcir deficiency

causes development of autoimmune diseases in mice due to excess expansion of dendritic cells. *Nat Med,* 14**,** 176-80.

GALKINA, E., KADL, A., SANDERS, J., VARUGHESE, D., SAREMBOCK, I. J. & LEY, K. 2006. Lymphocyte recruitment into the aortic wall before and during development of atherosclerosis is partially L-selectin dependent. *J Exp Med,* 203**,** 1273-82.

GAUTIER, E. L., SHAY, T., MILLER, J., GRETER, M., JAKUBZICK, C., IVANOV, S., HELFT, J., CHOW, A., ELPEK, K. G., GORDONOV, S., MAZLOOM, A. R., MA'AYAN, A., CHUA, W. J., HANSEN, T. H., TURLEY, S. J., MERAD, M., RANDOLPH, G. J. & IMMUNOLOGICAL GENOME, C. 2012. Gene-expression profiles and transcriptional regulatory pathways that underlie the identity and diversity of mouse tissue macrophages. *Nat Immunol,* 13**,** 1118-28.

GEISSMANN, F., JUNG, S. & LITTMAN, D. R. 2003. Blood monocytes consist of two principal subsets with distinct migratory properties. *Immunity,* 19**,** 71-82.

GETZ, G. S. & REARDON, C. A. 2016. Do the Apoe-/- and Ldlr-/- Mice Yield the Same Insight on Atherogenesis? *Arterioscler Thromb Vasc Biol,* 36**,** 1734-41.

GHOSN, E. E., CASSADO, A. A., GOVONI, G. R., FUKUHARA, T., YANG, Y., MONACK, D. M., BORTOLUCI, K. R., ALMEIDA, S. R., HERZENBERG, L. A. & HERZENBERG, L. A. 2010. Two physically, functionally, and developmentally distinct peritoneal macrophage subsets. *Proc Natl Acad Sci U S A,* 107**,** 2568-73.

GINHOUX, F., GRETER, M., LEBOEUF, M., NANDI, S., SEE, P., GOKHAN, S., MEHLER, M. F., CONWAY, S. J., NG, L. G., STANLEY, E. R., SAMOKHVALOV, I. M. & MERAD, M. 2010. Fate mapping analysis reveals that adult microglia derive from primitive macrophages. *Science,* 330**,** 841-5.

GLAGOV, S., WEISENBERG, E., ZARINS, C. K., STANKUNAVICIUS, R. & KOLETTIS, G. J. 1987. Compensatory enlargement of human atherosclerotic coronary arteries. *N Engl J Med,* 316**,** 1371-5.

GLEISSNER, C. A., SHAKED, I., ERBEL, C., BOCKLER, D., KATUS, H. A. & LEY, K. 2010. CXCL4 downregulates the atheroprotective hemoglobin receptor CD163 in human macrophages. *Circ Res,* 106**,** 203-11.

GORDON, S. & PLUDDEMANN, A. 2017. Tissue macrophages: heterogeneity and functions. *BMC Biol,* 15**,** 53.

GORDON, S., PLUDDEMANN, A. & MARTINEZ ESTRADA, F. 2014. Macrophage heterogeneity in tissues: phenotypic diversity and functions. *Immunol Rev,* 262**,** 36-55.

GOSSELIN, D., LINK, V. M., ROMANOSKI, C. E., FONSECA, G. J., EICHENFIELD, D. Z., SPANN, N. J., STENDER, J. D., CHUN, H. B., GARNER, H., GEISSMANN, F. & GLASS, C. K. 2014. Environment drives selection and function of enhancers controlling tissue-specific macrophage identities. *Cell,* 159**,** 1327-40.

GUILLIAMS, M., DE KLEER, I., HENRI, S., POST, S., VANHOUTTE, L., DE PRIJCK, S., DESWARTE, K., MALISSEN, B., HAMMAD, H. & LAMBRECHT, B. N. 2013. Alveolar macrophages develop from fetal monocytes that differentiate into long-lived cells in the first week of life via GM-CSF. *J Exp Med,* 210**,** 1977-92.

GUILLIAMS, M., GINHOUX, F., JAKUBZICK, C., NAIK, S. H., ONAI, N., SCHRAML, B. U., SEGURA, E., TUSSIWAND, R. & YONA, S. 2014. Dendritic cells, monocytes and macrophages: a unified nomenclature based on ontogeny. *Nat Rev Immunol,* 14**,** 571-8.

GUILLIAMS, M. & SCOTT, C. L. 2017. Does niche competition determine the origin of tissue-resident macrophages? *Nat Rev Immunol,* 17**,** 451-460.

GUO, J., DE WAARD, V., VAN ECK, M., HILDEBRAND, R. B., VAN WANROOIJ, E. J., KUIPER, J., MAEDA, N., BENSON, G. M., GROOT, P. H. & VAN BERKEL, T. J. 2005. Repopulation of apolipoprotein E knockout mice with CCR2-deficient bone marrow progenitor cells does not inhibit ongoing atherosclerotic lesion development. *Arterioscler Thromb Vasc Biol,* 25**,** 1014-9.

GUO, J., WU, X., TOO, C. L., YIN, F., LU, X., HE, J., LI, R., LIU, X., MURAD, S., PADYUKOV, L. & LI, Z. 2012. A replication study confirms the association of dendritic cell immunoreceptor (DCIR) polymorphisms with ACPA - negative RA in a large Asian cohort. *PLoS One,* 7**,** e41228.

HANNA, R. N., CARLIN, L. M., HUBBELING, H. G., NACKIEWICZ, D., GREEN, A. M., PUNT, J. A., GEISSMANN, F. & HEDRICK, C. C. 2011. The transcription factor NR4A1 (Nur77) controls bone marrow differentiation and the survival of Ly6C- monocytes. *Nat Immunol,* 12**,** 778-85.

HASHIMOTO, D., CHOW, A., NOIZAT, C., TEO, P., BEASLEY, M. B., LEBOEUF, M., BECKER, C. D., SEE, P., PRICE, J., LUCAS, D., GRETER, M., MORTHA, A., BOYER, S. W., FORSBERG, E. C., TANAKA, M., VAN ROOIJEN, N., GARCIA-SASTRE, A., STANLEY, E. R., GINHOUX, F., FRENETTE, P. S. & MERAD, M. 2013. Tissue-resident macrophages self-maintain locally throughout adult life with minimal contribution from circulating monocytes. *Immunity,* 38**,** 792-804.

HAYES, E. M., TSAOUSI, A., DI GREGOLI, K., JENKINSON, S. R., BOND, A. R., JOHNSON, J. L., BEVAN, L., THOMAS, A. C. & NEWBY, A. C. 2014. Classical and Alternative Activation and Metalloproteinase Expression Occurs in Foam Cell Macrophages in Male and Female ApoE Null Mice in the Absence of T and B Lymphocytes. *Front Immunol,* 5**,** 537.

HOBBS, H. H., BROWN, M. S. & GOLDSTEIN, J. L. 1992. Molecular genetics of the LDL receptor gene in familial hypercholesterolemia. *Hum Mutat,* 1**,** 445-66.

HORCKMANS, M., RING, L., DUCHENE, J., SANTOVITO, D., SCHLOSS, M. J., DRECHSLER, M., WEBER, C., SOEHNLEIN, O. & STEFFENS, S. 2017. Neutrophils orchestrate post-myocardial infarction healing by polarizing macrophages towards a reparative phenotype. *Eur Heart J,* 38**,** 187-197.

HOVING, J. C., WILSON, G. J. & BROWN, G. D. 2014. Signalling C-type lectin receptors, microbial recognition and immunity. *Cell Microbiol,* 16**,** 185-94.

HSU, Y., OKADA, R., NISHIMURA, T., KAWASAKI, N., YAMAMOTO, K. & MATSUMOTO, N. 2017. DCIR3 and DCIR4 are co-expressed on inflammatory and patrolling monocytes. *Biochem Biophys Res Commun,* 494**,** 440-445.

HULSMANS, M., CLAUSS, S., XIAO, L., AGUIRRE, A. D., KING, K. R., HANLEY, A., HUCKER, W. J., WULFERS, E. M., SEEMANN, G., COURTIES, G., IWAMOTO, Y., SUN, Y., SAVOL, A. J., SAGER, H. B., LAVINE, K. J., FISHBEIN, G. A., CAPEN, D. E., DA SILVA, N., MIQUEROL, L., WAKIMOTO, H., SEIDMAN, C. E., SEIDMAN, J. G., SADREYEV, R. I., NAXEROVA, K., MITCHELL, R. N., BROWN, D., LIBBY, P., WEISSLEDER, R., SWIRSKI, F. K., KOHL, P., VINEGONI, C., MILAN, D. J., ELLINOR, P. T. & NAHRENDORF, M. 2017. Macrophages Facilitate Electrical Conduction in the Heart. *Cell,* 169**,** 510-522 e20.

HUTTER, J., ERIKSSON, M., JOHANNSSEN, T., KLOPFLEISCH, R., VON SMOLINSKI, D., GRUBER, A. D., SEEBERGER, P. H. & LEPENIES, B. 2014.

Role of the C-type lectin receptors MCL and DCIR in experimental colitis. *PLoS One,* 9**,** e103281.

INGERSOLL, M. A., SPANBROEK, R., LOTTAZ, C., GAUTIER, E. L., FRANKENBERGER, M., HOFFMANN, R., LANG, R., HANIFFA, M., COLLIN, M., TACKE, F., HABENICHT, A. J., ZIEGLER-HEITBROCK, L. & RANDOLPH, G. J. 2010. Comparison of gene expression profiles between human and mouse monocyte subsets. *Blood,* 115**,** e10-9.

ISHIBASHI, S., BROWN, M. S., GOLDSTEIN, J. L., GERARD, R. D., HAMMER, R. E. & HERZ, J. 1993. Hypercholesterolemia in low density lipoprotein receptor knockout mice and its reversal by adenovirus-mediated gene delivery. *J Clin Invest,* 92**,** 883-93.

ISHIGURO, T., FUKAWA, T., AKAKI, K., NAGAOKA, K., TAKEDA, T., IWAKURA, Y., INABA, K. & TAKAHARA, K. 2017. Absence of DCIR1 reduces the mortality rate of endotoxemic hepatitis in mice. *Eur J Immunol,* 47**,** 704-712.

JAFRI, S., MOORE, S. D., MORRELL, N. W. & ORMISTON, M. L. 2017. A sex-specific reconstitution bias in the competitive CD45.1/CD45.2 congenic bone marrow transplant model. *Sci Rep,* 7**,** 3495.

JANEWAY, C. A. 1999. *Immunobiology,* Edinburgh, Churchill Livingstone.

JIANG, C., TING, A. T. & SEED, B. 1998. PPAR-gamma agonists inhibit production of monocyte inflammatory cytokines. *Nature,* 391**,** 82-6.

JOHNSON, J. L. 2017. Metalloproteinases in atherosclerosis. *Eur J Pharmacol,* 816**,** 93-106.

JONGSTRA-BILEN, J., HAIDARI, M., ZHU, S. N., CHEN, M., GUHA, D. & CYBULSKY, M. I. 2006. Low-grade chronic inflammation in regions of the normal mouse arterial intima predisposed to atherosclerosis. *J Exp Med,* 203**,** 2073-83.

KADL, A., MEHER, A. K., SHARMA, P. R., LEE, M. Y., DORAN, A. C., JOHNSTONE, S. R., ELLIOTT, M. R., GRUBER, F., HAN, J., CHEN, W., KENSLER, T., RAVICHANDRAN, K. S., ISAKSON, B. E., WAMHOFF, B. R. & LEITINGER, N. 2010. Identification of a novel macrophage phenotype that develops in response to atherogenic phospholipids via Nrf2. *Circ Res,* 107**,** 737-46.

KAMEDA, Y., HANAYAMA, M., KISHIMOTO, A., KUME, M., YAMAMOTO, K. & MATSUMOTO, N. 2016. Dendritic cell inhibitory receptor 4 (DCIR4) is preferentially expressed on inflammatory and patrolling monocytes. *Biochem Biophys Res Commun,* 480**,** 215-221.

KANAZAWA, N., OKAZAKI, T., NISHIMURA, H., TASHIRO, K., INABA, K. & MIYACHI, Y. 2002. DCIR acts as an inhibitory receptor depending on its immunoreceptor tyrosine-based inhibitory motif. *J Invest Dermatol,* 118**,** 261-6.

KANAZAWA, N., TASHIRO, K., INABA, K. & MIYACHI, Y. 2003. Dendritic cell immunoactivating receptor, a novel C-type lectin immunoreceptor, acts as an activating receptor through association with Fc receptor gamma chain. *J Biol Chem,* 278**,** 32645-52.

KEARNEY, P. M., WHELTON, M., REYNOLDS, K., MUNTNER, P., WHELTON, P. K. & HE, J. 2005. Global burden of hypertension: analysis of worldwide data. *Lancet,* 365**,** 217-23.

KIM, C. J., KHOO, J. C., GILLOTTE-TAYLOR, K., LI, A., PALINSKI, W., GLASS, C. K. & STEINBERG, D. 2000. Polymerase chain reaction-based method for quantifying recruitment of monocytes to mouse atherosclerotic lesions in vivo: enhancement by tumor necrosis factor-alpha and interleukin-1 beta. *Arterioscler Thromb Vasc Biol,* 20**,** 1976-82.

KIM, K., SHIM, D., LEE, J. S., ZAITSEV, K., WILLIAMS, J. W., KIM, K. W., JANG, M. Y., SEOK JANG, H., YUN, T. J., LEE, S. H., YOON, W. K., PRAT, A., SEIDAH, N. G., CHOI, J., LEE, S. P., YOON, S. H., NAM, J. W., SEONG, J. K., OH, G. T., RANDOLPH, G. J., ARTYOMOV, M. N., CHEONG, C. & CHOI, J. H. 2018. Transcriptome Analysis Reveals Nonfoamy Rather Than Foamy Plaque Macrophages Are Proinflammatory in Atherosclerotic Murine Models. *Circ Res,* 123**,** 1127-1142.

KISHIMOTO, A., WATANABE, M., TERAUCHI, K., KOJIMA, T., KAMEDA, Y., YAMAMOTO, K. & MATSUMOTO, N. 2015. Ubiquitous versus restricted expression of the two mouse dendritic cell C-type lectin receptors, DCIR1 and DCAR2, among myeloid cells. *Biochem Biophys Res Commun,* 467**,** 383-8.

KLECHEVSKY, E., FLAMAR, A. L., CAO, Y., BLANCK, J. P., LIU, M., O'BAR, A., AGOUNA-DECIAT, O., KLUCAR, P., THOMPSON-SNIPES, L., ZURAWSKI, S., REITER, Y., PALUCKA, A. K., ZURAWSKI, G. & BANCHEREAU, J. 2010. Cross-priming CD8+ T cells by targeting antigens to human dendritic cells through DCIR. *Blood,* 116**,** 1685-97.

KOJIMA, Y., VOLKMER, J. P., MCKENNA, K., CIVELEK, M., LUSIS, A. J., MILLER, C. L., DIRENZO, D., NANDA, V., YE, J., CONNOLLY, A. J., SCHADT, E. E., QUERTERMOUS, T., BETANCUR, P., MAEGDEFESSEL, L., MATIC, L. P., HEDIN, U., WEISSMAN, I. L. & LEEPER, N. J. 2016. CD47-blocking antibodies restore phagocytosis and prevent atherosclerosis. *Nature,* 536**,** 86-90.

KOJIMA, Y., WEISSMAN, I. L. & LEEPER, N. J. 2017. The Role of Efferocytosis in Atherosclerosis. *Circulation,* 135**,** 476-489.

KOLACZKOWSKA, E. & KUBES, P. 2013. Neutrophil recruitment and function in health and inflammation. *Nat Rev Immunol,* 13**,** 159-75.

KOLTSOVA, E. K., GARCIA, Z., CHODACZEK, G., LANDAU, M., MCARDLE, S., SCOTT, S. R., VON VIETINGHOFF, S., GALKINA, E., MILLER, Y. I., ACTON, S. T. & LEY, K. 2012. Dynamic T cell-APC interactions sustain chronic inflammation in atherosclerosis. *J Clin Invest,* 122**,** 3114-26.

KRAUSGRUBER, T., BLAZEK, K., SMALLIE, T., ALZABIN, S., LOCKSTONE, H., SAHGAL, N., HUSSELL, T., FELDMANN, M. & UDALOVA, I. A. 2011. IRF5 promotes inflammatory macrophage polarization and TH1-TH17 responses. *Nat Immunol,* 12**,** 231-8.

KUNJATHOOR, V. V., FEBBRAIO, M., PODREZ, E. A., MOORE, K. J., ANDERSSON, L., KOEHN, S., RHEE, J. S., SILVERSTEIN, R., HOFF, H. F. & FREEMAN, M. W. 2002. Scavenger receptors class A-I/II and CD36 are the principal receptors responsible for the uptake of modified low density lipoprotein leading to lipid loading in macrophages. *J Biol Chem,* 277**,** 49982-8.

LAMBERT, A. A., GILBERT, C., RICHARD, M., BEAULIEU, A. D. & TREMBLAY, M. J. 2008. The C-type lectin surface receptor DCIR acts as a new attachment factor for HIV-1 in dendritic cells and contributes to trans- and cis-infection pathways. *Blood,* 112**,** 1299-307.

LAMBRECHT, B. N. 2006. Alveolar macrophage in the driver's seat. *Immunity,* 24**,** 366-8.

LAVIN, Y., WINTER, D., BLECHER-GONEN, R., DAVID, E., KEREN-SHAUL, H., MERAD, M., JUNG, S. & AMIT, I. 2014. Tissue-resident macrophage enhancer landscapes are shaped by the local microenvironment. *Cell,* 159**,** 1312-26.

LAWRENCE, T. & NATOLI, G. 2011. Transcriptional regulation of macrophage polarization: enabling diversity with identity. *Nat Rev Immunol,* 11**,** 750-61.

LEHNERT, B. E., VALDEZ, Y. E. & HOLLAND, L. M. 1985. Pulmonary macrophages: alveolar and interstitial populations. *Exp Lung Res,* 9**,** 177-90.

LESNIK, P., HASKELL, C. A. & CHARO, I. F. 2003. Decreased atherosclerosis in CX3CR1-/- mice reveals a role for fractalkine in atherogenesis. *J Clin Invest,* 111**,** 333-40.

LESSNER, S. M., PRADO, H. L., WALLER, E. K. & GALIS, Z. S. 2002. Atherosclerotic lesions grow through recruitment and proliferation of circulating monocytes in a murine model. *Am J Pathol,* 160**,** 2145-55.

LI, A. C., BROWN, K. K., SILVESTRE, M. J., WILLSON, T. M., PALINSKI, W. & GLASS, C. K. 2000. Peroxisome proliferator-activated receptor gamma ligands inhibit development of atherosclerosis in LDL receptor-deficient mice. *J Clin Invest,* 106**,** 523-31.

LIAO, X., SHARMA, N., KAPADIA, F., ZHOU, G., LU, Y., HONG, H., PARUCHURI, K., MAHABELESHWAR, G. H., DALMAS, E., VENTECLEF, N., FLASK, C. A., KIM, J., DOREIAN, B. W., LU, K. Q., KAESTNER, K. H., HAMIK, A., CLEMENT, K. & JAIN, M. K. 2011. Kruppel-like factor 4 regulates macrophage polarization. *J Clin Invest,* 121**,** 2736-49.

LIM, H. Y., LIM, S. Y., TAN, C. K., THIAM, C. H., GOH, C. C., CARBAJO, D., CHEW, S. H. S., SEE, P., CHAKAROV, S., WANG, X. N., LIM, L. H., JOHNSON, L. A., LUM, J., FONG, C. Y., BONGSO, A., BISWAS, A., GOH, C., EVRARD, M., YEO, K. P., BASU, R., WANG, J. K., TAN, Y., JAIN, R., TIKOO, S., CHOONG, C., WENINGER, W., POIDINGER, M., STANLEY, R. E., COLLIN, M., TAN, N. S., NG, L. G., JACKSON, D. G., GINHOUX, F. & ANGELI, V. 2018. Hyaluronan Receptor LYVE-1-Expressing Macrophages Maintain Arterial Tone through Hyaluronan-Mediated Regulation of Smooth Muscle Cell Collagen. *Immunity,* 49**,** 326-341 e7.

LINTON, M. F., ATKINSON, J. B. & FAZIO, S. 1995. Prevention of atherosclerosis in apolipoprotein E-deficient mice by bone marrow transplantation. *Science,* 267**,** 1034-7.

LIU, M., WU, X., LIU, X., HE, J., SU, Y., GUO, J. & LI, Z. 2015. Contribution of dendritic cell immunoreceptor (DCIR) polymorphisms in susceptibility of systemic lupus erythematosus and primary Sjogren's syndrome. *Hum Immunol,* 76**,** 808-11.

LIU, P., YU, Y. R., SPENCER, J. A., JOHNSON, A. E., VALLANAT, C. T., FONG, A. M., PATTERSON, C. & PATEL, D. D. 2008. CX3CR1 deficiency impairs dendritic cell accumulation in arterial intima and reduces atherosclerotic burden. *Arterioscler Thromb Vasc Biol,* 28**,** 243-50.

LIVAK, K. J. & SCHMITTGEN, T. D. 2001. Analysis of relative gene expression data using real-time quantitative PCR and the 2(-Delta Delta C(T)) Method. *Methods,* 25**,** 402-8.

LLOYD-JONES, D. M. 2010. Cardiovascular risk prediction: basic concepts, current status, and future directions. *Circulation,* 121**,** 1768-77.

LORENTZEN, J. C., FLORNES, L., EKLOW, C., BACKDAHL, L., RIBBHAMMAR, U., GUO, J. P., SMOLNIKOVA, M., DISSEN, E., SEDDIGHZADEH, M., BROOKES, A. J., ALFREDSSON, L., KLARESKOG, L., PADYUKOV, L. & FOSSUM, S. 2007. Association of arthritis with a gene complex encoding C-type lectin-like receptors. *Arthritis Rheum,* 56**,** 2620-32.

LUM, H. & MALIK, A. B. 1994. Regulation of vascular endothelial barrier function. *Am J Physiol,* 267**,** L223-41.

MAATEN, L. J. P. V. D. & HINTON, G. E. 2008. Visualizing High-Dimensional Data Using t-SNE. *Journal of Machine Learning Research***,** 2579-2605.

MACRITCHIE, N., GRASSIA, G., SABIR, S. R., MADDALUNO, M., WELSH, P., SATTAR, N., IALENTI, A., KUROWSKA-STOLARSKA, M., MCINNES, I. B., BREWER, J. M., GARSIDE, P. & MAFFIA, P. 2012. Plasmacytoid dendritic cells play a key role in promoting atherosclerosis in apolipoprotein E-deficient mice. *Arterioscler Thromb Vasc Biol,* 32**,** 2569-79.

MAGLINAO, M., KLOPFLEISCH, R., SEEBERGER, P. H. & LEPENIES, B. 2013. The C-type lectin receptor DCIR is crucial for the development of experimental cerebral malaria. *J Immunol,* 191**,** 2551-9.

MANTOVANI, A., BISWAS, S. K., GALDIERO, M. R., SICA, A. & LOCATI, M. 2013. Macrophage plasticity and polarization in tissue repair and remodelling. *J Pathol,* 229**,** 176-85.

MANTOVANI, A., SOZZANI, S., LOCATI, M., ALLAVENA, P. & SICA, A. 2002. Macrophage polarization: tumor-associated macrophages as a paradigm for polarized M2 mononuclear phagocytes. *Trends Immunol,* 23**,** 549-55.

MARTINEZ, F. O. & GORDON, S. 2014. The M1 and M2 paradigm of macrophage activation: time for reassessment. *F1000Prime Rep,* 6**,** 13.

MASSOUD, A. H., YONA, M., XUE, D., CHOUIALI, F., ALTURAIHI, H., ABLONA, A., MOURAD, W., PICCIRILLO, C. A. & MAZER, B. D. 2014. Dendritic cell immunoreceptor: a novel receptor for intravenous immunoglobulin mediates induction of regulatory T cells. *J Allergy Clin Immunol,* 133**,** 853-63 e5.

MCCORMACK, F. X. & WHITSETT, J. A. 2002. The pulmonary collectins, SP-A and SP-D, orchestrate innate immunity in the lung. *J Clin Invest,* 109**,** 707-12.

MERAD, M., SATHE, P., HELFT, J., MILLER, J. & MORTHA, A. 2013. The dendritic cell lineage: ontogeny and function of dendritic cells and their subsets in the steady state and the inflamed setting. *Annu Rev Immunol,* 31**,** 563-604.

MEYER-WENTRUP, F., BENITEZ-RIBAS, D., TACKEN, P. J., PUNT, C. J., FIGDOR, C. G., DE VRIES, I. J. & ADEMA, G. J. 2008. Targeting DCIR on human plasmacytoid dendritic cells results in antigen presentation and inhibits IFN-alpha production. *Blood,* 111**,** 4245-53.

MEYER-WENTRUP, F., CAMBI, A., JOOSTEN, B., LOOMAN, M. W., DE VRIES, I. J., FIGDOR, C. G. & ADEMA, G. J. 2009. DCIR is endocytosed into human dendritic cells and inhibits TLR8-mediated cytokine production. *J Leukoc Biol,* 85**,** 518-25.

MICHA, R., IMAMURA, F., WYLER VON BALLMOOS, M., SOLOMON, D. H., HERNAN, M. A., RIDKER, P. M. & MOZAFFARIAN, D. 2011. Systematic review and meta-analysis of methotrexate use and risk of cardiovascular disease. *Am J Cardiol,* 108**,** 1362-70.

MILLS, C. D., KINCAID, K., ALT, J. M., HEILMAN, M. J. & HILL, A. M. 2000. M-1/M-2 macrophages and the Th1/Th2 paradigm. *J Immunol,* 164**,** 6166-73.

MISHARIN, A. V., CUDA, C. M., SABER, R., TURNER, J. D., GIERUT, A. K., HAINES, G. K., 3RD, BERDNIKOVS, S., FILER, A., CLARK, A. R., BUCKLEY, C. D., MUTLU, G. M., BUDINGER, G. R. & PERLMAN, H. 2014. Nonclassical Ly6C(-) monocytes drive the development of inflammatory arthritis in mice. *Cell Rep,* 9**,** 591-604.

MISHARIN, A. V., MORALES-NEBREDA, L., REYFMAN, P. A., CUDA, C. M., WALTER, J. M., MCQUATTIE-PIMENTEL, A. C., CHEN, C. I., ANEKALLA, K. R., JOSHI, N., WILLIAMS, K. J. N., ABDALA-VALENCIA, H., YACOUB, T. J., CHI, M., CHIU, S., GONZALEZ-GONZALEZ, F. J., GATES, K., LAM, A. P., NICHOLSON, T. T., HOMAN, P. J., SOBERANES, S., DOMINGUEZ, S., MORGAN, V. K., SABER, R., SHAFFER, A., HINCHCLIFF, M., MARSHALL,

S. A., BHARAT, A., BERDNIKOVS, S., BHORADE, S. M., BARTOM, E. T., MORIMOTO, R. I., BALCH, W. E., SZNAJDER, J. I., CHANDEL, N. S., MUTLU, G. M., JAIN, M., GOTTARDI, C. J., SINGER, B. D., RIDGE, K. M., BAGHERI, N., SHILATIFARD, A., BUDINGER, G. R. S. & PERLMAN, H. 2017. Monocyte-derived alveolar macrophages drive lung fibrosis and persist in the lung over the life span. *J Exp Med,* 214**,** 2387-2404.

MITAMURA, T., UMATA, T., NAKANO, F., SHISHIDO, Y., TOYODA, T., ITAI, A., KIMURA, H. & MEKADA, E. 1997. Structure-function analysis of the diphtheria toxin receptor toxin binding site by site-directed mutagenesis. *J Biol Chem,* 272**,** 27084-90.

MOHANTA, S., YIN, C., WEBER, C., HU, D. & HABENICHT, A. J. 2016. Aorta Atherosclerosis Lesion Analysis in Hyperlipidemic Mice. *Bio Protoc,* 6.

MOLAWI, K., WOLF, Y., KANDALLA, P. K., FAVRET, J., HAGEMEYER, N., FRENZEL, K., PINTO, A. R., KLAPPROTH, K., HENRI, S., MALISSEN, B., RODEWALD, H. R., ROSENTHAL, N. A., BAJENOFF, M., PRINZ, M., JUNG, S. & SIEWEKE, M. H. 2014. Progressive replacement of embryo-derived cardiac macrophages with age. *J Exp Med,* 211**,** 2151-8.

MOORE, K. J., SHEEDY, F. J. & FISHER, E. A. 2013. Macrophages in atherosclerosis: a dynamic balance. *Nat Rev Immunol,* 13**,** 709-21.

MOORE, K. J. & TABAS, I. 2011. Macrophages in the pathogenesis of atherosclerosis. *Cell,* 145**,** 341-55.

MOSSER, D. M. & EDWARDS, J. P. 2008. Exploring the full spectrum of macrophage activation. *Nat Rev Immunol,* 8**,** 958-69.

MURPHY, A. J., AKHTARI, M., TOLANI, S., PAGLER, T., BIJL, N., KUO, C. L., WANG, M., SANSON, M., ABRAMOWICZ, S., WELCH, C., BOCHEM, A. E., KUIVENHOVEN, J. A., YVAN-CHARVET, L. & TALL, A. R. 2011. ApoE regulates hematopoietic stem cell proliferation, monocytosis, and monocyte accumulation in atherosclerotic lesions in mice. *J Clin Invest,* 121**,** 4138-49.

NAGLICH, J. G., ROLF, J. M. & EIDELS, L. 1992. Expression of functional diphtheria toxin receptors on highly toxin-sensitive mouse cells that specifically bind radioiodinated toxin. *Proc Natl Acad Sci U S A,* 89**,** 2170-4.

NAKASHIMA, Y., PLUMP, A. S., RAINES, E. W., BRESLOW, J. L. & ROSS, R. 1994. ApoE-deficient mice develop lesions of all phases of atherosclerosis throughout the arterial tree. *Arterioscler Thromb,* 14**,** 133-40.

NERLOV, C. & GRAF, T. 1998. PU.1 induces myeloid lineage commitment in multipotent hematopoietic progenitors. *Genes Dev,* 12**,** 2403-12.

NJOROGE, J. M., MITCHELL, L. B., CENTOLA, M., KASTNER, D., RAFFELD, M. & MILLER, J. L. 2001. Characterization of viable autofluorescent macrophages among cultured peripheral blood mononuclear cells. *Cytometry,* 44**,** 38-44.

OLSON, M. C., SCOTT, E. W., HACK, A. A., SU, G. H., TENEN, D. G., SINGH, H. & SIMON, M. C. 1995. PU. 1 is not essential for early myeloid gene expression but is required for terminal myeloid differentiation. *Immunity,* 3**,** 703-14.

PARK, I., KASSITERIDI, C. & MONACO, C. 2017. Functional diversity of macrophages in vascular biology and disease. *Vascul Pharmacol,* 99**,** 13-22.

PASSLICK, B., FLIEGER, D. & ZIEGLER-HEITBROCK, H. W. 1989. Identification and characterization of a novel monocyte subpopulation in human peripheral blood. *Blood,* 74**,** 2527-34.

PASTERKAMP, G., DE KLEIJN, D. P. & BORST, C. 2000. Arterial remodeling in atherosclerosis, restenosis and after alteration of blood flow: potential mechanisms and clinical implications. *Cardiovasc Res,* 45**,** 843-52.

PASTERKAMP, G., GALIS, Z. S. & DE KLEIJN, D. P. 2004. Expansive arterial remodeling: location, location, location. *Arterioscler Thromb Vasc Biol,* 24**,** 650-7.

PATTLE, R. E. 1955. Properties, function and origin of the alveolar lining layer. *Nature,* 175**,** 1125-6.

PAULSON, K. E., ZHU, S. N., CHEN, M., NURMOHAMED, S., JONGSTRA-BILEN, J. & CYBULSKY, M. I. 2010. Resident intimal dendritic cells accumulate lipid and contribute to the initiation of atherosclerosis. *Circ Res,* 106**,** 383-90.

PINTO, A. R., PAOLICELLI, R., SALIMOVA, E., GOSPOCIC, J., SLONIMSKY, E., BILBAO-CORTES, D., GODWIN, J. W. & ROSENTHAL, N. A. 2012. An abundant tissue macrophage population in the adult murine heart with a distinct alternatively-activated macrophage profile. *PLoS One,* 7**,** e36814.

PITSILOS, S., HUNT, J., MOHLER, E. R., PRABHAKAR, A. M., PONCZ, M., DAWICKI, J., KHALAPYAN, T. Z., WOLFE, M. L., FAIRMAN, R., MITCHELL, M., CARPENTER, J., GOLDEN, M. A., CINES, D. B. & SACHAIS, B. S. 2003. Platelet factor 4 localization in carotid atherosclerotic plaques: correlation with clinical parameters. *Thromb Haemost,* 90**,** 1112-20.

PLUMP, A. S., SMITH, J. D., HAYEK, T., AALTO-SETALA, K., WALSH, A., VERSTUYFT, J. G., RUBIN, E. M. & BRESLOW, J. L. 1992. Severe hypercholesterolemia and atherosclerosis in apolipoprotein E-deficient mice created by homologous recombination in ES cells. *Cell,* 71**,** 343-53.

QIAO, J. H., TRIPATHI, J., MISHRA, N. K., CAI, Y., TRIPATHI, S., WANG, X. P., IMES, S., FISHBEIN, M. C., CLINTON, S. K., LIBBY, P., LUSIS, A. J. & RAJAVASHISTH, T. B. 1997. Role of macrophage colony-stimulating factor in atherosclerosis: studies of osteopetrotic mice. *Am J Pathol,* 150**,** 1687-99.

RAHMAN, K., VENGRENYUK, Y., RAMSEY, S. A., VILA, N. R., GIRGIS, N. M., LIU, J., GUSAROVA, V., GROMADA, J., WEINSTOCK, A., MOORE, K. J., LOKE, P. & FISHER, E. A. 2017. Inflammatory Ly6Chi monocytes and their conversion to M2 macrophages drive atherosclerosis regression. *J Clin Invest,* 127**,** 2904-2915.

RAJAVASHISTH, T., QIAO, J. H., TRIPATHI, S., TRIPATHI, J., MISHRA, N., HUA, M., WANG, X. P., LOUSSARARIAN, A., CLINTON, S., LIBBY, P. & LUSIS, A. 1998. Heterozygous osteopetrotic (op) mutation reduces atherosclerosis in LDL receptor- deficient mice. *J Clin Invest,* 101**,** 2702-10.

REKHTER, M. D. 1999. Collagen synthesis in atherosclerosis: too much and not enough. *Cardiovasc Res,* 41**,** 376-84.

RICHARD, M., THIBAULT, N., VEILLEUX, P., BRETON, R. & BEAULIEU, A. D. 2003. The ITIM-bearing CLECSF6 (DCIR) is down-modulated in neutrophils by neutrophil activating agents. *Biochem Biophys Res Commun,* 310**,** 767-73.

RICHARD, M., VEILLEUX, P., ROULEAU, M., PAQUIN, R. & BEAULIEU, A. D. 2002. The expression pattern of the ITIM-bearing lectin CLECSF6 in neutrophils suggests a key role in the control of inflammation. *J Leukoc Biol,* 71**,** 871-80.

RICOTE, M., LI, A. C., WILLSON, T. M., KELLY, C. J. & GLASS, C. K. 1998. The peroxisome proliferator-activated receptor-gamma is a negative regulator of macrophage activation. *Nature,* 391**,** 79-82.

RIDKER, P. M. 2010. Statin therapy for low-LDL, high-hsCRP patients: from JUPITER to CORONA. *Clin Chem,* 56**,** 505-7.

RIDKER, P. M., EVERETT, B. M., THUREN, T., MACFADYEN, J. G., CHANG, W. H., BALLANTYNE, C., FONSECA, F., NICOLAU, J., KOENIG, W., ANKER, S. D., KASTELEIN, J. J. P., CORNEL, J. H., PAIS, P., PELLA, D., GENEST, J.,

CIFKOVA, R., LORENZATTI, A., FORSTER, T., KOBALAVA, Z., VIDA-SIMITI, L., FLATHER, M., SHIMOKAWA, H., OGAWA, H., DELLBORG, M., ROSSI, P. R. F., TROQUAY, R. P. T., LIBBY, P., GLYNN, R. J. & GROUP, C. T. 2017. Antiinflammatory Therapy with Canakinumab for Atherosclerotic Disease. *N Engl J Med*.

ROBBINS, C. S., HILGENDORF, I., WEBER, G. F., THEURL, I., IWAMOTO, Y., FIGUEIREDO, J. L., GORBATOV, R., SUKHOVA, G. K., GERHARDT, L. M., SMYTH, D., ZAVITZ, C. C., SHIKATANI, E. A., PARSONS, M., VAN ROOIJEN, N., LIN, H. Y., HUSAIN, M., LIBBY, P., NAHRENDORF, M., WEISSLEDER, R. & SWIRSKI, F. K. 2013. Local proliferation dominates lesional macrophage accumulation in atherosclerosis. *Nat Med,* 19**,** 1166-72.

ROSENFELD, M. E., YLA-HERTTUALA, S., LIPTON, B. A., ORD, V. A., WITZTUM, J. L. & STEINBERG, D. 1992. Macrophage colony-stimulating factor mRNA and protein in atherosclerotic lesions of rabbits and humans. *Am J Pathol,* 140**,** 291-300.

ROSS, R. 1999. Atherosclerosis--an inflammatory disease. *N Engl J Med,* 340**,** 115-26.

SABATINE, M. S., GIUGLIANO, R. P., KEECH, A. C., HONARPOUR, N., WIVIOTT, S. D., MURPHY, S. A., KUDER, J. F., WANG, H., LIU, T., WASSERMAN, S. M., SEVER, P. S., PEDERSEN, T. R., COMMITTEE, F. S. & INVESTIGATORS 2017. Evolocumab and Clinical Outcomes in Patients with Cardiovascular Disease. *N Engl J Med,* 376**,** 1713-1722.

SAITO, M., IWAWAKI, T., TAYA, C., YONEKAWA, H., NODA, M., INUI, Y., MEKADA, E., KIMATA, Y., TSURU, A. & KOHNO, K. 2001. Diphtheria toxin receptor-mediated conditional and targeted cell ablation in transgenic mice. *Nat Biotechnol,* 19**,** 746-50.

SANCHO, D. & REIS E SOUSA, C. 2012. Signaling by myeloid C-type lectin receptors in immunity and homeostasis. *Annu Rev Immunol,* 30**,** 491-529.

SATOH, T., TAKEUCHI, O., VANDENBON, A., YASUDA, K., TANAKA, Y., KUMAGAI, Y., MIYAKE, T., MATSUSHITA, K., OKAZAKI, T., SAITOH, T., HONMA, K., MATSUYAMA, T., YUI, K., TSUJIMURA, T., STANDLEY, D. M., NAKANISHI, K., NAKAI, K. & AKIRA, S. 2010. The Jmjd3-Irf4 axis regulates M2 macrophage polarization and host responses against helminth infection. *Nat Immunol,* 11**,** 936-44.

SCHNEIDER, C., NOBS, S. P., KURRER, M., REHRAUER, H., THIELE, C. & KOPF, M. 2014. Induction of the nuclear receptor PPAR-gamma by the cytokine GM-CSF is critical for the differentiation of fetal monocytes into alveolar macrophages. *Nat Immunol,* 15**,** 1026-37.

SCOTT, C. L., ZHENG, F., DE BAETSELIER, P., MARTENS, L., SAEYS, Y., DE PRIJCK, S., LIPPENS, S., ABELS, C., SCHOONOOGHE, S., RAES, G., DEVOOGDT, N., LAMBRECHT, B. N., BESCHIN, A. & GUILLIAMS, M. 2016. Bone marrow-derived monocytes give rise to self-renewing and fully differentiated Kupffer cells. *Nat Commun,* 7**,** 10321.

SEIMON, T. A., WANG, Y., HAN, S., SENOKUCHI, T., SCHRIJVERS, D. M., KURIAKOSE, G., TALL, A. R. & TABAS, I. A. 2009. Macrophage deficiency of p38alpha MAPK promotes apoptosis and plaque necrosis in advanced atherosclerotic lesions in mice. *J Clin Invest,* 119**,** 886-98.

SENEVIRATNE, A. N., EDSFELDT, A. O., COLE, J. E., KASSITERIDI, C., SWART, M., PARK, I., GREEN, P., KHOYRATTY, T. E., SALIBA, D. G., GODDARD, M. E., SANSOM, S. N., GONCALVES, I., KRAMS, R., UDALOVA, I. A. &

MONACO, C. 2017. Interferon Regulatory Factor 5 Controls Necrotic Core Formation in Atherosclerotic Lesions by Impairing Efferocytosis. *Circulation*.

SENO, A., MARUHASHI, T., KAIFU, T., YABE, R., FUJIKADO, N., MA, G., IKARASHI, T., KAKUTA, S. & IWAKURA, Y. 2015. Exacerbation of experimental autoimmune encephalomyelitis in mice deficient for DCIR, an inhibitory C-type lectin receptor. *Exp Anim,* 64**,** 109-19.

SHARMA, N., LU, Y., ZHOU, G., LIAO, X., KAPIL, P., ANAND, P., MAHABELESHWAR, G. H., STAMLER, J. S. & JAIN, M. K. 2012. Myeloid Kruppel-like factor 4 deficiency augments atherogenesis in ApoE-/- mice--brief report. *Arterioscler Thromb Vasc Biol,* 32**,** 2836-8.

SHAW, T. N., HOUSTON, S. A., WEMYSS, K., BRIDGEMAN, H. M., BARBERA, T. A., ZANGERLE-MURRAY, T., STRANGWARD, P., RIDLEY, A. J. L., WANG, P., TAMOUTOUNOUR, S., ALLEN, J. E., KONKEL, J. E. & GRAINGER, J. R. 2018. Tissue-resident macrophages in the intestine are long lived and defined by Tim-4 and CD4 expression. *J Exp Med,* 215**,** 1507-1518.

SHI, J., HUA, L., HARMER, D., LI, P. & REN, G. 2018a. Cre Driver Mice Targeting Macrophages. *Methods Mol Biol,* 1784**,** 263-275.

SHI, X., YKEMA, M. R., HAZENOOT, J., TEN BLOEMENDAAL, L., MANCINI, I., ODIJK, M., DE HAAN, P. & BOSMA, P. J. 2018b. Cre Recombinase Mediates the Removal of Bacterial Backbone to Efficiently Generate rSV40. *Mol Ther Methods Clin Dev,* 9**,** 225-233.

SMYTHIES, L. E., SELLERS, M., CLEMENTS, R. H., MOSTELLER-BARNUM, M., MENG, G., BENJAMIN, W. H., ORENSTEIN, J. M. & SMITH, P. D. 2005. Human intestinal macrophages display profound inflammatory anergy despite avid phagocytic and bacteriocidal activity. *J Clin Invest,* 115**,** 66-75.

SRIKAKULAPU, P. & MCNAMARA, C. A. 2017. B cells and atherosclerosis. *Am J Physiol Heart Circ Physiol,* 312**,** H1060-H1067.

STEIN, M., KESHAV, S., HARRIS, N. & GORDON, S. 1992. Interleukin 4 potently enhances murine macrophage mannose receptor activity: a marker of alternative immunologic macrophage activation. *J Exp Med,* 176**,** 287-92.

STERNBERG, N. & HAMILTON, D. 1981. Bacteriophage P1 site-specific recombination. I. Recombination between loxP sites. *J Mol Biol,* 150**,** 467-86.

STOGER, J. L., GIJBELS, M. J., VAN DER VELDEN, S., MANCA, M., VAN DER LOOS, C. M., BIESSEN, E. A., DAEMEN, M. J., LUTGENS, E. & DE WINTHER, M. P. 2012. Distribution of macrophage polarization markers in human atherosclerosis. *Atherosclerosis,* 225**,** 461-8.

STONEMAN, V., BRAGANZA, D., FIGG, N., MERCER, J., LANG, R., GODDARD, M. & BENNETT, M. 2007. Monocyte/macrophage suppression in CD11b diphtheria toxin receptor transgenic mice differentially affects atherogenesis and established plaques. *Circ Res,* 100**,** 884-93.

SUBRAMANIAN, M., THORP, E. & TABAS, I. 2015. Identification of a non-growth factor role for GM-CSF in advanced atherosclerosis: promotion of macrophage apoptosis and plaque necrosis through IL-23 signaling. *Circ Res,* 116**,** e13-24.

SWIRSKI, F. K., LIBBY, P., AIKAWA, E., ALCAIDE, P., LUSCINSKAS, F. W., WEISSLEDER, R. & PITTET, M. J. 2007. Ly-6Chi monocytes dominate hypercholesterolemia-associated monocytosis and give rise to macrophages in atheromata. *J Clin Invest,* 117**,** 195-205.

SWIRSKI, F. K., PITTET, M. J., KIRCHER, M. F., AIKAWA, E., JAFFER, F. A., LIBBY, P. & WEISSLEDER, R. 2006. Monocyte accumulation in mouse atherogenesis

is progressive and proportional to extent of disease. *Proc Natl Acad Sci U S A,* 103**,** 10340-10345.

TABAS, I. 2005. Consequences and therapeutic implications of macrophage apoptosis in atherosclerosis: the importance of lesion stage and phagocytic efficiency. *Arterioscler Thromb Vasc Biol,* 25**,** 2255-64.

TACKE, F., ALVAREZ, D., KAPLAN, T. J., JAKUBZICK, C., SPANBROEK, R., LLODRA, J., GARIN, A., LIU, J., MACK, M., VAN ROOIJEN, N., LIRA, S. A., HABENICHT, A. J. & RANDOLPH, G. J. 2007. Monocyte subsets differentially employ CCR2, CCR5, and CX3CR1 to accumulate within atherosclerotic plaques. *J Clin Invest,* 117**,** 185-94.

TAKEUCHI, O. & AKIRA, S. 2010. Pattern recognition receptors and inflammation. *Cell,* 140**,** 805-20.

TAMOUTOUNOUR, S., HENRI, S., LELOUARD, H., DE BOVIS, B., DE HAAR, C., VAN DER WOUDE, C. J., WOLTMAN, A. M., REYAL, Y., BONNET, D., SICHIEN, D., BAIN, C. C., MOWAT, A. M., REIS E SOUSA, C., POULIN, L. F., MALISSEN, B. & GUILLIAMS, M. 2012. CD64 distinguishes macrophages from dendritic cells in the gut and reveals the Th1-inducing role of mesenteric lymph node macrophages during colitis. *Eur J Immunol,* 42**,** 3150-66.

TAN, S. Y. & KRASNOW, M. A. 2016. Developmental origin of lung macrophage diversity. *Development,* 143**,** 1318-27.

TANG, J., LIU, J., ZHANG, M. & MEI, Q. 2016. Visualizing Large-scale and High-dimensional Data. *Proceedings of the 25th International Conference on World Wide Web***,** 287-297.

THOMAS, A. C., EIJGELAAR, W. J., DAEMEN, M. J. & NEWBY, A. C. 2015. Foam Cell Formation In Vivo Converts Macrophages to a Pro-Fibrotic Phenotype. *PLoS One,* 10**,** e0128163.

THOMAS, G. D., HAMERS, A. A. J., NAKAO, C., MARCOVECCHIO, P., TAYLOR, A. M., MCSKIMMING, C., NGUYEN, A. T., MCNAMARA, C. A. & HEDRICK, C. C. 2017. Human Blood Monocyte Subsets: A New Gating Strategy Defined Using Cell Surface Markers Identified by Mass Cytometry. *Arterioscler Thromb Vasc Biol*.

THORP, E. & TABAS, I. 2009. Mechanisms and consequences of efferocytosis in advanced atherosclerosis. *J Leukoc Biol,* 86**,** 1089-95.

TOKIEDA, S., KOMORI, M., ISHIGURO, T., IWAKURA, Y., TAKAHARA, K. & INABA, K. 2015. Dendritic cell immunoreceptor 1 alters neutrophil responses in the development of experimental colitis. *BMC Immunol,* 16**,** 64.

TOYONAGA, K., TORIGOE, S., MOTOMURA, Y., KAMICHI, T., HAYASHI, J. M., MORITA, Y. S., NOGUCHI, N., CHUMA, Y., KIYOHARA, H., MATSUO, K., TANAKA, H., NAKAGAWA, Y., SAKUMA, T., OHMURAYA, M., YAMAMOTO, T., UMEMURA, M., MATSUZAKI, G., YOSHIKAI, Y., YANO, I., MIYAMOTO, T. & YAMASAKI, S. 2016. C-Type Lectin Receptor DCAR Recognizes Mycobacterial Phosphatidyl-Inositol Mannosides to Promote a Th1 Response during Infection. *Immunity,* 45**,** 1245-1257.

TRAPNELL, B. C., WHITSETT, J. A. & NAKATA, K. 2003. Pulmonary alveolar proteinosis. *N Engl J Med,* 349**,** 2527-39.

TROEGELER, A., MERCIER, I., COUGOULE, C., PIETRETTI, D., COLOM, A., DUVAL, C., VU MANH, T. P., CAPILLA, F., POINCLOUX, R., PINGRIS, K., NIGOU, J., RADEMANN, J., DALOD, M., VERRECK, F. A., AL SAATI, T., LUGO-VILLARINO, G., LEPENIES, B., HUDRISIER, D. & NEYROLLES, O. 2017. C-type lectin receptor DCIR modulates immunity to tuberculosis by

sustaining type I interferon signaling in dendritic cells. *Proc Natl Acad Sci U S A,* 114**,** E540-E549.

TURNBULL, I. R., GILFILLAN, S., CELLA, M., AOSHI, T., MILLER, M., PICCIO, L., HERNANDEZ, M. & COLONNA, M. 2006. Cutting edge: TREM-2 attenuates macrophage activation. *J Immunol,* 177**,** 3520-4.

UTO, T., FUKAYA, T., TAKAGI, H., ARIMURA, K., NAKAMURA, T., KOJIMA, N., MALISSEN, B. & SATO, K. 2016. Clec4A4 is a regulatory receptor for dendritic cells that impairs inflammation and T-cell immunity. *Nat Commun,* 7**,** 11273.

VAN DE LAAR, L., SAELENS, W., DE PRIJCK, S., MARTENS, L., SCOTT, C. L., VAN ISTERDAEL, G., HOFFMANN, E., BEYAERT, R., SAEYS, Y., LAMBRECHT, B. N. & GUILLIAMS, M. 2016. Yolk Sac Macrophages, Fetal Liver, and Adult Monocytes Can Colonize an Empty Niche and Develop into Functional Tissue-Resident Macrophages. *Immunity,* 44**,** 755-68.

VAN FURTH, R. 1981. Current view of the mononuclear phagocyte system. *Haematol Blood Transfus,* 27**,** 3-10.

VAN FURTH, R. & COHN, Z. A. 1968. The origin and kinetics of mononuclear phagocytes. *J Exp Med,* 128**,** 415-35.

VAN LAMMEREN, G. W., REICHMANN, B. L., MOLL, F. L., BOTS, M. L., DE KLEIJN, D. P., DE VRIES, J. P., PASTERKAMP, G. & DE BORST, G. J. 2011. Atherosclerotic plaque vulnerability as an explanation for the increased risk of stroke in elderly undergoing carotid artery stenting. *Stroke,* 42**,** 2550-5.

VIRMANI, R., KOLODGIE, F. D., BURKE, A. P., FARB, A. & SCHWARTZ, S. M. 2000. Lessons from sudden coronary death: a comprehensive morphological classification scheme for atherosclerotic lesions. *Arterioscler Thromb Vasc Biol,* 20**,** 1262-75.

WARNATSCH, A., IOANNOU, M., WANG, Q. & PAPAYANNOPOULOS, V. 2015. Inflammation. Neutrophil extracellular traps license macrophages for cytokine production in atherosclerosis. *Science,* 349**,** 316-20.

WEBER, C., MEILER, S., DORING, Y., KOCH, M., DRECHSLER, M., MEGENS, R. T., ROWINSKA, Z., BIDZHEKOV, K., FECHER, C., RIBECHINI, E., VAN ZANDVOORT, M. A., BINDER, C. J., JELINEK, I., HRISTOV, M., BOON, L., JUNG, S., KORN, T., LUTZ, M. B., FORSTER, I., ZENKE, M., HIERONYMUS, T., JUNT, T. & ZERNECKE, A. 2011. CCL17-expressing dendritic cells drive atherosclerosis by restraining regulatory T cell homeostasis in mice. *J Clin Invest,* 121**,** 2898-910.

WHITMAN, S. C. 2004. A practical approach to using mice in atherosclerosis research. *Clin Biochem Rev,* 25**,** 81-93.

WINKELS, H., EHINGER, E., VASSALLO, M., BUSCHER, K., DINH, H. Q., KOBIYAMA, K., HAMERS, A. A. J., COCHAIN, C., VAFADARNEJAD, E., SALIBA, A. E., ZERNECKE, A., PRAMOD, A. B., GHOSH, A. K., ANTO MICHEL, N., HOPPE, N., HILGENDORF, I., ZIRLIK, A., HEDRICK, C. C., LEY, K. & WOLF, D. 2018. Atlas of the Immune Cell Repertoire in Mouse Atherosclerosis Defined by Single-Cell RNA-Sequencing and Mass Cytometry. *Circ Res,* 122**,** 1675-1688.

WOLF, F. A., ANGERER, P. & THEIS, F. J. 2018. SCANPY: large-scale single-cell gene expression data analysis. *Genome Biol,* 19**,** 15.

WOLINSKY, H. & GLAGOV, S. 1967. Nature of species differences in the medial distribution of aortic vasa vasorum in mammals. *Circ Res,* 20**,** 409-21.

WONG, K. L., YEAP, W. H., TAI, J. J., ONG, S. M., DANG, T. M. & WONG, S. C. 2012. The three human monocyte subsets: implications for health and disease. *Immunol Res,* 53**,** 41-57.

WU, H., GOWER, R. M., WANG, H., PERRARD, X. Y., MA, R., BULLARD, D. C., BURNS, A. R., PAUL, A., SMITH, C. W., SIMON, S. I. & BALLANTYNE, C. M. 2009. Functional role of CD11c+ monocytes in atherogenesis associated with hypercholesterolemia. *Circulation,* 119**,** 2708-17.

XUE, J., SCHMIDT, S. V., SANDER, J., DRAFFEHN, A., KREBS, W., QUESTER, I., DE NARDO, D., GOHEL, T. D., EMDE, M., SCHMIDLEITHNER, L., GANESAN, H., NINO-CASTRO, A., MALLMANN, M. R., LABZIN, L., THEIS, H., KRAUT, M., BEYER, M., LATZ, E., FREEMAN, T. C., ULAS, T. & SCHULTZE, J. L. 2014. Transcriptome-based network analysis reveals a spectrum model of human macrophage activation. *Immunity,* 40**,** 274-88.

YONA, S., KIM, K. W., WOLF, Y., MILDNER, A., VAROL, D., BREKER, M., STRAUSS-AYALI, D., VIUKOV, S., GUILLIAMS, M., MISHARIN, A., HUME, D. A., PERLMAN, H., MALISSEN, B., ZELZER, E. & JUNG, S. 2013. Fate mapping reveals origins and dynamics of monocytes and tissue macrophages under homeostasis. *Immunity,* 38**,** 79-91.

YUN, T. J., LEE, J. S., MACHMACH, K., SHIM, D., CHOI, J., WI, Y. J., JANG, H. S., JUNG, I. H., KIM, K., YOON, W. K., MIAH, M. A., LI, B., CHANG, J., BEGO, M. G., PHAM, T. N., LOSCHKO, J., FRITZ, J. H., KRUG, A. B., LEE, S. P., KELER, T., GUIMOND, J. V., HADDAD, E., COHEN, E. A., SIROIS, M. G., EL-HAMAMSY, I., COLONNA, M., OH, G. T., CHOI, J. H. & CHEONG, C. 2016. Indoleamine 2,3-Dioxygenase-Expressing Aortic Plasmacytoid Dendritic Cells Protect against Atherosclerosis by Induction of Regulatory T Cells. *Cell Metab,* 24**,** 886.

ZHANG, S. H., REDDICK, R. L., PIEDRAHITA, J. A. & MAEDA, N. 1992. Spontaneous hypercholesterolemia and arterial lesions in mice lacking apolipoprotein E. *Science,* 258**,** 468-71.

ZHU, S. N., CHEN, M., JONGSTRA-BILEN, J. & CYBULSKY, M. I. 2009. GM-CSF regulates intimal cell proliferation in nascent atherosclerotic lesions. *J Exp Med,* 206**,** 2141-9.

Acknowledgements

My DPhil was a journey that provided excitement and challenges along the way. First of all, I would like to express my deepest gratitude to Professor Claudia Monaco for the wonderful opportunity to pursue my DPhil in her laboratory. I very much enjoyed the numerous discussions throughout my project and I am very grateful for her continuous encouragement and direction.

I would like to thank Jennifer Cole for teaching me valuable techniques and her guidance on my project. I would also like to thank Mike Goddard for teaching me *in vivo* work and for his great support in countless procedures. I would also like to express my thanks to Natacha Zanin, for her input in the 'signalling network' part of my project and for being such great company. To Christina Kassiteridi, for sharing her experience in FACS and for going through our DPhil journey together. To Trish Green, for her warm care and help. I am very grateful to all past and present members of the Monaco group for providing me with advice and warm support: Lea Dib, Alice Robinson, Maarten Swart, Henk Schipper, Rachel Edwards, Ismail Cassimjee, Andreas Edsfeldt and Anusha Seneviratne. Special thanks to Dave Ahern and Warren Baker for their great help with CyTOF and to Jon Webber for his expertise in sorting aortic cells. I am very grateful to the Kennedy Trust for awarding me a studentship to pursue my DPhil at the Kennedy Institute of Rheumatology. I would also like to acknowledge Professor Afsie Sabokbar and Professor Andy Carr for their generous support for the NDORMS student committee.

Finally, I would like to thanks my Korean and English families for the love, support and constant encouragement. To my ugly Martin Attwood, for being the best thing that has ever happened in my life.

한국에서 응원해준 가족들에게도 감사의 마음 전합니다